



Lead-free Piezoelectric Microgenerator for Energy Autonomous Wireless Sensors

Namanu Panayanthatta

► To cite this version:

Namanu Panayanthatta. Lead-free Piezoelectric Microgenerator for Energy Autonomous Wireless Sensors. Micro and nanotechnologies/Microelectronics. Université Grenoble Alpes [2020-..], 2022. English. NNT : 2022GRALT017 . tel-03702754

HAL Id: tel-03702754

<https://theses.hal.science/tel-03702754>

Submitted on 23 Jun 2022

HAL is a multi-disciplinary open access archive for the deposit and dissemination of scientific research documents, whether they are published or not. The documents may come from teaching and research institutions in France or abroad, or from public or private research centers.

L'archive ouverte pluridisciplinaire **HAL**, est destinée au dépôt et à la diffusion de documents scientifiques de niveau recherche, publiés ou non, émanant des établissements d'enseignement et de recherche français ou étrangers, des laboratoires publics ou privés.

THÈSE

Pour obtenir le grade de

DOCTEUR DE L'UNIVERSITÉ GRENOBLE ALPES

Spécialité : NANO ELECTRONIQUE ET NANO TECHNOLOGIES

Arrêté ministériel : 25 mai 2016

Présentée par

Namanu PANAYANTHATTA

Thèse dirigée par **Edwige BANO**, Enseignant-chercheur,
Université Grenoble Alpes
et co-encadrée par **Laurent MONTES**, Maître de Conférence

préparée au sein du **Laboratoire Institut de Microélectronique,
Electromagnétisme et Photonique - Laboratoire
d'hyperfréquences et de caractérisation**
dans l'**École Doctorale Electronique, Electrotechnique,
Automatique, Traitement du Signal (EEATS)**

**Microgenerateurs piezoelectriques sans plomb
pour capteurs autonomes sans fils**

**Lead-free Piezoelectric Microgenerator for
Energy Autonomous Wireless Sensors**

Thèse soutenue publiquement le **15 mars 2022**,
devant le jury composé de :

Madame Edwige BANO

PROFESSEUR DES UNIVERSITES, GRENOBLE INP, Directrice de
thèse

Monsieur Daniel ALQUIER

PROFESSEUR DES UNIVERSITES, Université de Tours, Rapporteur

Monsieur Alain GIANI

PROFESSEUR DES UNIVERSITES, Université de Montpellier,
Rapporteur

Monsieur Skandar BASROUR

PROFESSEUR DES UNIVERSITES, Université Grenoble Alpes,
Président



Acknowledgments

I would like to sincerely thank numerous people who not only helped me in the scientific and technical part but also in my personal and career development. Firstly, I would like to thank my supervisors, Laurent Montes and Edwige Bano for their constant support and for their ideas to guide and improve my work. I would especially thank Laurent and Edwige for their care during the COVID-19 pandemic period.

I also wish to especially thank the jury members for being part of my committee, for their expertise, and for their helpful comments. I would like to thank Skandar Basrour who accepted the presidency of the jury, and Daniel Alquier and Alain Giani who accepted to review my manuscript and gave important comments and suggestions.

I also take this opportunity to thank Roberto La Rosa, my supervisor in ST Microelectronics Catania, for his constant support and guidance. Also, I express my special thanks to Sanjay Mathur, University of Cologne, and Michael Lallart, INSA Lyon for the supervision during the secondments.

I thank the director IMEP-LaHC, for hosting me at the laboratory. A special thought goes to all support staff especially Xavier Mescot with AFM and electrical measurement setups, Martine Gri for wire bonding, Nicolas with PCB fabrication. A special thanks to Anais for the financial management and arranging numerous trips and secondments during the work. I also express my thanks to Dalhila and Brigitte for administrative and technical support.

I also take this opportunity to again thank Skandar Basrour for the facilities at TIMA laboratory, and Gaetan for technical support.

I would like to thank Auserine Bartaszyte, the project co-ordinator, and all my colleagues of the ITN-ENHANCE project, for the collaborations, and for the thoughts and wonderful time spent during the several events and project meetings. I thank my friends and colleagues in ST

Microelectronics, especially Daniele and Giuseppe for the interesting discussions during lunch and coffee breaks.

I would like to thank all my friends and colleagues in IMEP-LaHC, especially Militiadis, Balraj, Alfa, Angelikki, Byda, Camille, Maxim and Andrez for the wonderful time spent together, and for the fruitful discussion and thoughts. Thank you guys for encouraging me, and helping me with every aspect of my thesis. Dear Prof. Daniel Alquier, Dear Prof. Alain Giani, Dear Prof. Skandar Basrour, Dear Prof. Edwige Bano, Dear Prof. Laurent Montes,

Special thanks to my parents Narayanan and Santha and my sister Saranya, who is always my motivation to push my limits and excel in my life.

Lead-free Piezoelectric Microgenerator for Energy Autonomous Wireless Sensors

Contents

General Introduction	1
Thesis Overview.....	1
Thesis Structure.....	2
Context	3
1 On the interest of ambient energy harvesting.....	6
1.1 Energy Harvesting at Microscale.....	6
1.2 Power requirement of WSNs.....	7
1.3 Ambient power sources for Energy harvesting	9
1.3.1 Vibration Energy Harvesting (ViEH).....	11
1.3.2 Piezoelectric Energy Harvesting (PEH).....	18
1.3.3 Piezoelectric Vibration Energy Harvesters	19
1.4 Power Management circuits for PEH.....	26
1.5 Summary	28
2 Electromechanical characterization of piezoelectric materials.....	30
2.1 Piezoelectric Materials	30
2.2 Piezoelectric constituent equations	32
2.3 Classification of Piezoelectric Materials:	32
2.4 Poling of Piezoelectric Materials.....	33
2.5 Ferroelectric Hysteresis Loop and Butterfly Loop	34
2.5.1 Ferroelectric Hysteresis Loop.....	34

2.5.2	Butterfly loop.....	35
2.6	Key Properties of Piezoelectric Materials	36
2.6.1	Piezoelectric coefficients	36
2.6.2	Youngs Modulus.....	36
2.6.3	Dielectric Permittivity	37
2.6.4	The electromechanical coupling factor, K_{ij}	37
2.7	Towards Lead free Piezoelectric ceramics.....	38
2.8	Piezoresponse Force Microcopy (PFM)	39
2.8.1	Choice of AFM tip and operating frequency.....	42
2.8.2	Calibration of vertical deflection sensitivity	42
2.8.3	Measuring d_{ij} coefficients	43
2.9	PFM Characterization of Lithium Tantalate (LT) samples.....	44
2.9.1	On the interest of Lithium Tantalate	44
2.9.2	LT samples and topography	44
2.9.3	Domain polarization of LT samples	45
2.10	PFM study of Sodium Potassium Niobate (KNN) thin films.....	49
2.10.1	Introduction.....	49
2.10.2	KNN cantilever dimensions and topography	50
2.10.3	Piezoresponse characterization of KNN films by PFM.....	51
2.11	External Poling of KNN PTF	54
2.11.1	Poling process:.....	54
2.11.2	PFM study of the poled KNN PTF	56
2.12	PFM study of Sodium Potassium Niobate (KNN) thin films doped with Tantalum	65
2.12.1	Introduction.....	65
2.12.2	Piezoresponse characterization of KNNT film by PFM.....	66
2.12.3	Conclusion	68
2.13	PFM study of Sodium Potassium Niobate (KNN) and KNN-Ta doped (KNNT) fibres	69
2.13.1	Introduction.....	69
2.13.2	Experimental setup and procedure	70

2.13.3	Topography of KNN fibers	70
2.13.4	PFM study of the KNN fibres before poling.....	71
2.13.5	Radial Poling of KNN fibres	72
2.13.6	PFM study of KNNT (KNN doped with 10% Ta) Fibers.....	75
2.13.7	Conclusion	80
2.14	Comparison of the Figure of Merit of the cantilevers.....	81
2.15	Summary	83
3	Piezoelectric Microgenerator based on lead-free Lithium Niobate single crystal.....	85
3.1	Introduction	85
3.2	Microgenerator geometry and Fabrication process.....	87
3.3	Dynamic Electrical Characterization	89
3.4	Estimation of Mechanical Quality Factor (Q_m) based on impedance curve.....	90
3.5	Electromechanical coupling coefficient (k_{33} and k_{31}).....	92
3.6	Design of Proof mass	92
3.7	Equivalent Circuit model of Piezoelectric Energy Harvester (PEH)	95
3.7.1	Experimental Parameter Identification	97
3.7.2	Analysis of the impedance of the equivalent circuit in SPICE	99
3.8	Estimation of the mechanical quality factor (Q_m) and coupling coefficient K with proof mass	100
3.9	Optimal load resistance for maximum output power	101
3.9.1	Theoretical prediction	101
3.9.2	Experimental determination of optimal load	102
3.9.3	Optimal load by LT-SPICE	102
3.10	Output Voltage and RMS power of the harvester	103
3.11	Test Results and Analysis	104
3.12	Power harvesting circuit for Piezoelectric Energy Harvester.....	106
3.13	A novel three-terminal harvester concept with Maximum Power Point Tracking (MPPT) for ultra-low power applications.....	108

3.13.1	Introduction.....	108
3.13.2	Theory and working principle	111
3.13.3	Design considerations	113
3.13.4	The feasibility study of 3 terminal harvester.....	113
3.13.5	Bending-Mode Resonance Frequency.....	114
3.13.6	Finite element Analysis.....	115
3.13.7	Boundary Conditions.....	116
3.13.8	Experimental results.....	118
3.13.9	Measurement of Open circuit voltage	119
3.13.10	Conclusion	121
3.14	Summary	122
4	Energy Autonomous Wireless Vibration Sensor based on Piezoelectric Microgenerator	124
4.1	Introduction	124
4.2	System description.....	127
4.3	Piezoelectric Energy Harvester Design	129
4.4	Energy Autonomous Wireless Vibration Sensor Working Principle.....	132
4.5	Experimental Results	136
4.6	Conclusions	141
	Conclusion and Perspectives.....	143
	References.....	162

ABBREVIATIONS

<i>Alternating Current</i>	<i>AC</i>
<i>Atomic Force Microscopy</i>	<i>AFM</i>
<i>Application-Specific Integrated Circuit</i>	<i>ASIC</i>
<i>Bluetooth Low Energy</i>	<i>BLE</i>
<i>Base Station</i>	<i>BS</i>
<i>Complementary Metal Oxide Semiconductor</i>	<i>CMOS</i>
<i>cyclic transparent optical polymer</i>	<i>CYTOP</i>
<i>Double synchronized switch harvesting</i>	<i>DSSH</i>
<i>Energy Autonomous Wireless Vibration Sensor</i>	<i>EAWVS</i>
<i>Electrostatic energy harvesters</i>	<i>EEHs</i>
<i>Electromagnetic Energy Harvesters</i>	<i>EMEHs</i>
<i>Full-Bridge Rectifiers</i>	<i>FBR</i>
<i>Finite Element Method</i>	<i>FEM</i>
<i>Fractional Open-Circuit</i>	<i>FOC</i>
<i>Figure of Merit</i>	<i>FoM</i>
<i>General-Purpose Input/Output</i>	<i>GPIO</i>
<i>Near Field Communication</i>	<i>NFC</i>
<i>High Temperature</i>	<i>HT</i>
<i>Integrated Circuit</i>	<i>IC</i>
<i>inverse optical lever sensitivity</i>	<i>inv-OLS</i>
<i>Internet of Things</i>	<i>IoT</i>
<i>Sodium Potassium Niobate</i>	<i>KNN</i>
<i>Sodium Potassium Niobate Tantalate</i>	<i>KNNT</i>
<i>Liquid Crystal Display</i>	<i>LCD</i>
<i>Lock-in Amplifier</i>	<i>LIA</i>
<i>Lithium Niobate</i>	<i>LN</i>
<i>Limit of Detection</i>	<i>LOD</i>
<i>Lateral Piezoresponse Force Microcopy</i>	<i>LPFM</i>
<i>Lithium tantalate</i>	<i>LT</i>
<i>Micro Electro Mechanical Systems</i>	<i>MEMS</i>

<i>Metal Oxide Semiconductor Field Effect Transistor</i>	<i>MOSFET</i>
<i>Maximum Power Point Tracking</i>	<i>MPPT</i>
<i>Printed Circuit Board</i>	<i>PCB</i>
<i>Polydimethylsiloxane</i>	<i>PDMS</i>
<i>Piezoelectric Energy Harvesters</i>	<i>PEH</i>
<i>Piezoresponse Force Microcopy</i>	<i>PFM</i>
<i>Piezoelectric Thin Films</i>	<i>PTF</i>
<i>Piezoelectric Materials</i>	<i>PM</i>
<i>Power-Management Circuit</i>	<i>PMC</i>
<i>Power Management IC</i>	<i>PMIC</i>
<i>Poly(methyl methacrylate)</i>	<i>PMMA</i>
<i>Periodically Poled Lithium Niobate</i>	<i>PPLN</i>
<i>Piezo-Response</i>	<i>PR</i>
<i>Position Sensitive Photodetector</i>	<i>PSD</i>
<i>Piezoelectric Thin Films</i>	<i>PTFs</i>
<i>Programmable Voltage Detector</i>	<i>PVD</i>
<i>Polyvinylidene fluoride</i>	<i>PVDF</i>
<i>Lead Zirconate Tantalate</i>	<i>PZT</i>
<i>Radio Frequency</i>	<i>RF</i>
<i>Root Mean Square</i>	<i>RMS</i>
<i>Single Degree of Freedom</i>	<i>SDOF</i>
<i>Standard Energy Transfer</i>	<i>SET</i>
<i>System-on-Chip</i>	<i>SoC</i>
<i>Silicon on Insulator</i>	<i>SOI</i>
<i>Scanning Probe Microscopy</i>	<i>SPM</i>
<i>Synchronized Switch Harvesting on Inductor</i>	<i>SSHI</i>
<i>Vi-Energy Harvester</i>	<i>ViEH</i>
<i>Vibrational Energy Harvesters</i>	<i>Vi-EH</i>
<i>Vertical Piezoresponse Force Microcopy</i>	<i>VPFM</i>
<i>Wireless Sensor Nodes</i>	<i>WSNs</i>

General Introduction

This chapter discusses the overall outlook of this thesis from the framework of the EU ITN-ENHANCE project. The main objectives and goals of this thesis are laid out.

Thesis Overview

The overall aim of this Ph.D. work under the ITN-ENHANCE project is the investigation of the electrical power harvested from ambient vibrations at relatively low frequencies (< 500 Hz) using lead-free materials for low-power sensors or actuators that are used in automotive. The “Internet of Things” IoT [1]–[3] concept comprises “smart structures” with autonomous self-powered sensors, actuators, and associated low-power electronics circuits that are spread across a network of Wireless Sensor Nodes (WSNs) that can sense and share data among one another and the master unit. The global IoT market is evaluated to be nearly 250 billion Euros in 2019, and with the growing interest in areas such as smart structures, precision farming, autonomous vehicles, and Artificial Intelligence (AI), the market is projected to reach nearly 1,200 billion Euros by 2027 [4]. IoT has an overall impact of up to 9.3 trillion Euros in 2020 in the economic world.

To achieve fully autonomous status for the WSNs, it is very important that they are powered independently and, therefore, it is needed to replace the depleted energy in the batteries. Harnessing and storing the ambient energy available in the environment to power such WSNs would help to replace batteries needed for the autonomous WSNs. In this situation, the use of ubiquitous ambient mechanical vibrations to generate electricity for powering the WSNs is a promising choice compared to the conventional battery-based powering system that needs intermittent replacement. Further, the battery-less approach helps to reduce the environmental issues caused by batteries. Among various techniques to convert vibrations to electricity namely piezoelectric, electromagnetic, and electrostatic based techniques, [5]–[8] the piezoelectric energy harvesting is more convenient for micro-energy harvesting due to the high energy density ($300\mu\text{W}/\text{cm}^2/\text{g}^2$) in practical applications, material deposition compatibility with MEMS process [9]. However, state of the art Piezoelectric Energy Harvesters (PEHs) are mostly based on lead-

based materials such as PZT[10] which contains Pb, a toxic element that does not comply with REACH (Registration, Evaluation, Authorization and Restriction of Chemicals) and RoHS (Restriction of Hazardous Substances) regulations[11]. For this reason, there is a growing need in the electronics industry to explore new environment-friendly materials and processes for next-generation "green" PEHs based on lead-free materials[11]. In this thesis, the piezoelectric energy harvesting solutions based on lead-free materials for powering battery-free and energy-autonomous sensors, are therefore explored.

Thesis Structure

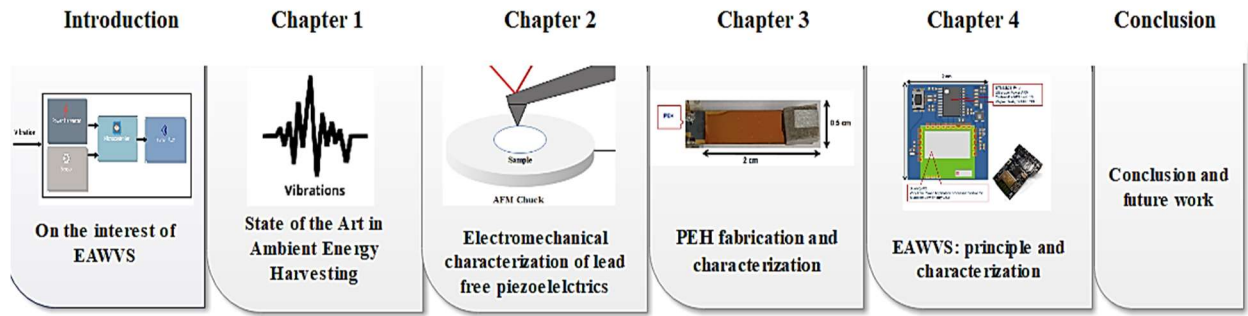


Figure 1: Thesis structure

The structure of this thesis from material to device design, realization and characterization is divided into six chapters and the outline of each one is as follows:

- **General Introduction:** sets the overall outlook of this thesis and discusses the main objectives and goals.
- **Chapter 1:** gives a literature review, identifying the current state-of-the-art energy harvesting devices at the microscale with a focus on vibration energy harvesting and the challenges that this thesis will address. Different applications and energy sources for harvesting are discussed before going into further detail into piezoelectric energy harvesting. Strategies and outlooks toward a lead-free piezoelectric energy harvester are laid out.
- **Chapter 2:** This chapter focuses on the microscale characterization of new lead-free piezoelectric materials deposited by a sol-gel process. Lithium Tantalate, Sodium Potassium Niobate, Tantalum doped Sodium Potassium Niobate thin films and fibres are studied and their electromechanical properties and energy harvesting Figures of Merit (FoM) are compared with Lithium Niobate single crystal. The techniques that have been

used to characterize the piezoelectric properties, morphologies such as Atomic Force Microscopy (AFM) are detailed. Also, a brief discussion on the processing and deposition of these piezoelectric materials is discussed.

- **Chapter 3:** Discusses the fabrication and characterization of a lead-free microgenerator based on a lead-free Lithium Niobate single crystal wafer. In this chapter, we develop an electromechanical equivalent circuit model of the piezoelectric energy harvester and in addition, the voltage conditioning and device interfacing for controlled and stable DC output is discussed. An efficient architecture to maximize the power transferred to the load with a Maximum Power Point Tracking (MPPT) is also investigated, with a specific focus on low power circuits.
- **Chapter 4:** The application of the harvester to power a battery-free IoT WSN based on Bluetooth Low Energy-(BLE) connectivity with ambient vibration is demonstrated. In addition, the operating principle and system implementation of the Energy Autonomous Wireless Sensor (EAWVS) based on the STM32 [12] microcontroller is detailed. The ability of the harvester in sensing input acceleration is demonstrated. Finally, the application scenario of the EAWVS is laid out.
- **Conclusion and perspectives:** Finally, the overall findings of the thesis are laid out and the perspectives are discussed briefly.

Context

With the increasing need for comfort and functionalities, the new generation of cars usually requires more sophisticated sensing and communication systems. The sensors and actuators, based on Micro Electro Mechanical Systems (MEMS), are widely used to control various sections of automobiles, such as the rotors, shafts, powertrain, and chassis control, advanced areas of driver assistance systems[13]–[16]. Low-power MEMS sensors, based on silicon technology, became the devices of choice offering cost-effective solutions and high yield in the automotive and aerospace industry. Currently, the need of the hour in the car industry is to reduce the total weight of cars and fuel consumption, to reduce carbon emissions. For instance, the reduction in car weight by 100 kg cuts the CO₂ emission by 4-6 g/km (in 2020, the standard for the average value of CO₂ emission by cars fabricated in the EU is 95 g/km). To supply the required power, as well as to transmit the output signal from these sensors, vehicles require a complex web of wires (several kilometers in length) [17]. These wires often contribute around 50 kg, and in addition, create complexity in

installation and maintenance[17]. Significant maintenance costs are related to wiring and contact problems. Further, the wire connections are prone to damage to solder from heat, close to the engine side.

Therefore, the EU-ENHANCE project focus on the development of power sources for autonomous self-powered wireless sensors that can be handy in places that are difficult to reach or have harsh working conditions. One of the best possible ways to implement such install and forget type sensor concept is, by harnessing the power from the ambient environment, such as vibrations, thermal or solar energies.

Piezoelectric Energy Harvesters (PEHs) are an attractive choice for the powering of autonomous sensor networks due to the prospect of integration with electronic circuits & sensor nodes [18]. Recently, the miniaturization of harvesters using MEMS technology with thin piezoelectric films or nanocomposites attracted interest to power small low power systems. Also, it is necessary to ensure that the operating frequency of these harvesters is in the range of ambient vibration in the environment ($<500\text{Hz}$). This means along with ensuring high FoM of materials, it is equally necessary to have an appropriate design of mechanical and electrical parts to have better performance of the energy harvesting system. To obtain high power output from piezoelectric harvesters, a high electromechanical coupling K^2 value is required. Currently, most of such PEHs with higher K^2 are employing bulk $\text{PbZr}_{1-x}\text{Ti}_x\text{O}_3$ (PZT), and piezoelectric bulk composites [10]. Higher K^2 ensures that the input mechanical energy is efficiently converted to usable electrical energy by the material. However, in the future, PZT has to be replaced by lead-free materials, even for thin films due to growing environmental concerns.

ENHANCE project, therefore, focus on the development of energy harvesters for automotive sensors based on lead-free piezoelectric materials. However, project results could also be important for other industries such as aerospace and heavy industries. Ferroelectric lead-free material, such as LiNbO_3 (LN) shows FoM similar to that of PZT [19]. Moreover, LN is compatible with high-temperature applications (up to 500°C) [20]. Bismuth Ferrite (BFO) is also a potential candidate for high-temperature PEH (up to 500°C) [21]. This makes LN and BFO two key materials, particularly attractive for the PEHs, since the elevated working temperature is possible (in engine oil, exhaust pipe, where, the temperature can reach up to 600°C), whereas PZT and similarly popular materials lose their piezoelectric properties at these temperatures. One of the highest notable power densities ($300\text{ }\mu\text{W}/\text{cm}^2/\text{g}^2$) achieved among the wide bandwidth ($\sim\text{Hz}$)

micro-PEHs was achieved by EH based on lead-free Sodium Potassium Niobate (KNN) films [22]. However, these materials are relatively new compared to the industrial standard PZT and the application of these materials in PEHs is still poorly investigated. Therefore, more efforts must be done towards their integration of novel lead-free piezoelectric materials into the conventional processing of MEMS structures. This thesis will address the issue of realizing high performing lead-free piezoelectric energy harvesters for scavenging vibrational energy, for the application in energy autonomous wireless sensors.

1 On the interest of ambient energy harvesting

This chapter discusses the current state-of-the-art energy harvesting devices at microscale such as piezoelectric, electrostatic, and electromagnetic energy harvesting with a focus on vibration energy harvesting. Strategies and outlooks towards a lead-free piezoelectric energy harvester are laid out.

1.1 Energy Harvesting at Microscale

Throughout the history of technological advancements during human evolution, there have been attempts to obtain energy from the ambient atmosphere and surroundings. The cavemen used friction to create sparks and fire producing electric charge; the waterwheel was a main source of energy during the medieval periods and windmills were widely used to grind grains. As technology developed the devices became more efficient and smaller and their energy consumption also reduced proportionally. The recent developments in micro and nanoelectronics have resulted in the miniaturization of devices that have power requirements in the order of several microwatts. IoT is one of the recent technologies with a direct and evident influence on several domains such as industry, healthcare, agriculture, automobile and smart homes. In IoT, WSNs, consisting of microcontrollers, memory chips and frequency transmitters, play a key part that collecting and transmitting data and MEMS relays that consume power in the order of several microwatts [23], [24]. Therefore, along with the Internet of Things (IoT), and equally with the developments in artificial intelligence, the need of the day is to develop self-powered sensors and circuits that consume infinitesimal power and, also, that these devices and sensors are powered from ambient energy sources [2], [11]. It is equally important that these WSNs are independently powered and disconnected physically from the master nodes to ensure full autonomy of the IoT. In addition, the availability of sensors that use a minimum number of cables to interconnect the electrical architecture of the vehicle could prove to be a significant advantage for the automotive industry, as this could lead to saving of the carbon footprint is a key criterion in the future vehicle design. Therefore, the energy devices that can generate power from ambient energy sources and that can

be integrated into the sensor systems, offer great scope for further development of autonomous sensor networks.

1.2 Power requirement of WSNs

Autonomous WSN is depicted in terms of four general functional boxes namely: (i) sensor section (ii) microcontroller section (iii) transmission section and finally the (iv) harvester section as shown in Figure 1.1. An IoT node will run through several operational cycles, which typically, involve several tasks such as sensing, actuation, processing, transmission, and consume similar amounts of energy at every operation sequence. Various types of sensors are used in condition monitoring such as accelerometers, thermal sensors, and bio-sensors for health monitoring, etc. [1], [2], [5] The power requirements for active sensing are generally on the micro-watt level [25]. However, the main power consumption of the system is from the microcontroller unit and the transmitter section. Therefore, to reduce the overall power consumption of the WSN, it is important to ensure that the microcontroller and the transmitter consume minimum power.

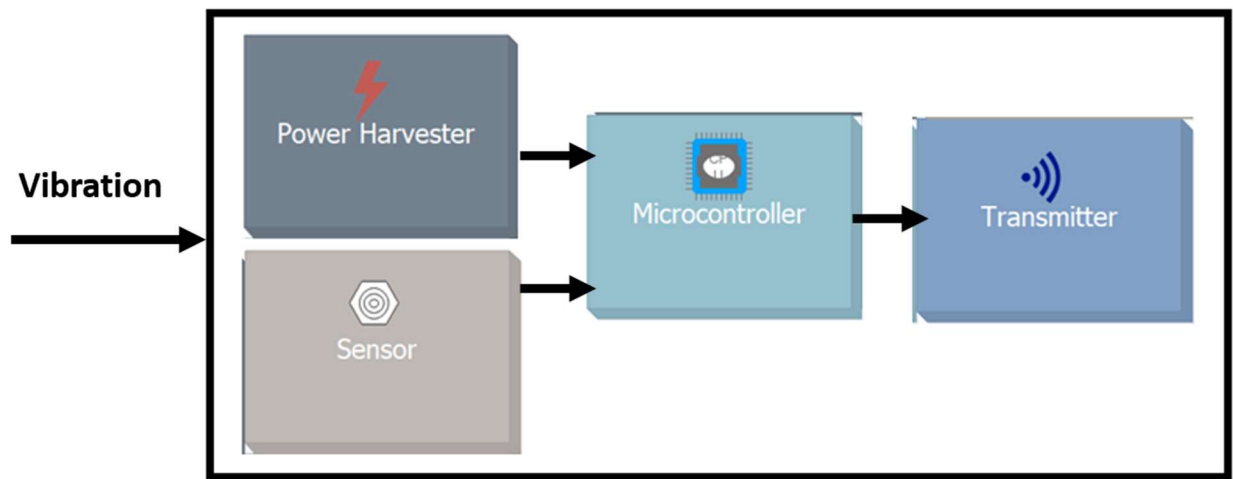


Figure 1.1: Block diagram of an Autonomous wireless sensor (WSN)

There has been a significant advancement in ultra-low power microcontrollers & RF Radio in recent years from the manufacturers. Some of the most popular microcontroller for low power applications are STM32L0-STMicroelectronics [12], PIC12LF1571-Microchip [26], MSP432P401-Texas Instruments [27] etc. For example, the STM32L0 series [12] microcontrollers from ST Microelectronics consume a quiescent current of only a fraction of microamperes while working in an operating voltage range of 1.8 V-3.6 V in the standby mode drawing power of few

microwatts. STM32L0 is based on a 32-bit Arm Cortex processor designed for a broad range of embedded applications which work in three operation modes: main/active, low power and power down/standby mode. In standby mode the current consumption is less than 1 μA , corresponding to a power consumption of $\sim 3 \mu\text{W}$. The active mode power consumption of these microcontrollers can be in the order of 50 μW -500 μW depending upon the processing needs and the duty cycle of operation. The total energy consumed by the processor is in the range of 50-500 μJ per transmission event and is controlled by the duration of active mode operation, which could last several milliseconds.

Regarding the transmission section, the most common wireless communication technologies are Bluetooth, ZigBee, and Near-Field Communication (NFC) as shown in Table 1.1.

Table 1.1: Wireless transmission protocols and specifications

Transmission Protocol	Power	Data rate	Distance
Wi-Fi	>500 mW	>100 Mb/s	10 m
LoRa	100 mW	1 kb/s	500 m
ZigBee	50 mW	250 kb/s	25 m
Bluetooth	10 mW	1 Mb/s	10 m

The total amount of energy required for the processing and the wireless transmission of the WSNs are typically in the order of 40-500 μJ that could change depending upon the RF protocol used for transmission. Bluetooth® Low Energy (BLE) consumes significantly less power during a transmission event compared to Wi-fi, LoRa and ZigBee. So, BLE is most suitable for applications requiring a transmission range less than 10 m, which is sufficient for IoT systems. For example, BLUENRG-2:Bluetooth® Low Energy wireless System-on-Chip (SoC) from ST Microelectronics [28], which is used in our work has an average advertising current consumption of about 15 μA during the transmitting phase while working at 2 V supply consuming power of 30 μW , at 8 dBm transmission power.

The total power consumption of all the components together (sensor, transmitter and microcontroller units) in a WSN during one duty cycle could be in the order of 100 μW to 1 mW

[1] depending on the duty cycle of operation. The power consumption of WSNs in comparison with various typical low-power devices are given in Table 1.2.

Table 1.2: A comparison of power consumption in various low-power electronic modules

Electronic module	Power range	ON-Time
Watch	1 μ W	continuous
RFID tag	10 μ W	< 10 ms
Remote	100 μ W	1-5 ms
WSNs	1 mW	< 5 ms
Bluetooth Device	10 mW	Continuous
GPS	100 mW	Continuous or intermittent

The total power consumed by an IoT device P_{WSN} in each cycle can be characterized by the power consumed by its components and their processes and expressed as:

$$P_{WSN} = P_{SB} + P_{MCU} + P_S + P_{TX} \quad 1.1$$

where P_{SB} is the standby power consumption, P_{MCU} is the power consumed by the processor unit P_S is the power consumed by the sensor, and P_{TX} is the power consumed by the transmission section. Although the microscale ambient energy harvesters may not be able to provide the power for continuous operation, it is sufficient to power these WSN nodes in an intermittent manner. For instance, the system goes to a standby mode when the energy from the harvester is stored in a capacitor and can be used to discharge as soon as enough energy is stored for the operational mode. For an IoT sensor device in a standby state, its power drawn can be extremely low (few microwatts). Therefore, the WSN can be designed smartly with low power consumption while awake, and negligible power consumption during sleep mode.

1.3 Ambient power sources for Energy harvesting

The ambient energy available in the environment can be broadly classified into mechanical sources (vibrations, stress), radiant sources (solar, infrared, and RF) and thermal sources (temperature gradients or fluctuations). The range of available power densities expressed in (μ W/cm²) of these sources is shown in Figure 1.2.

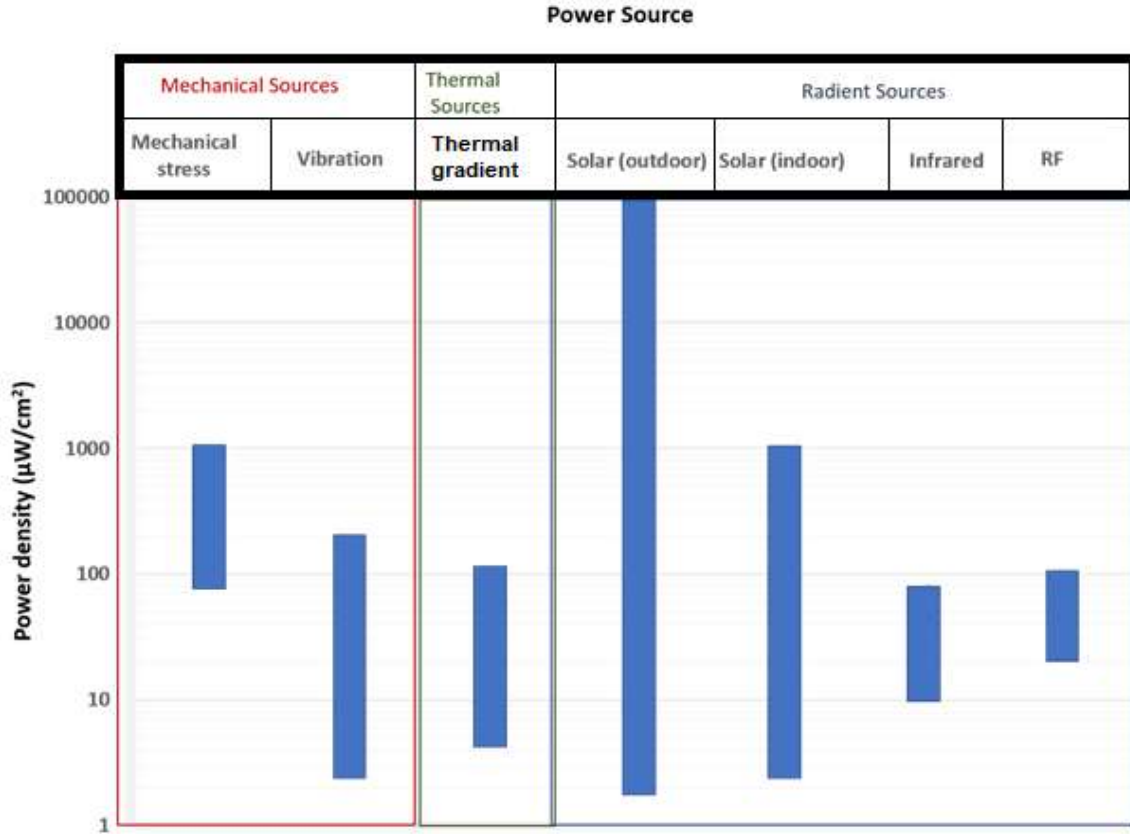


Figure 1.2: Range of available power densities of ambient energy sources

Although the power density of solar energy is high, harvesting is not possible in practical sensor application areas such as inside the machine, where the solar radiations cannot reach. Likewise, it is also difficult to harvest energy from thermal gradients where there is an absence of temperature gradient. However, for instance, automobile exhaust pipes can reach up to 700°C and can be used for harvesting thermal energy. Similarly, RF energy harvesting has also some limitations in the implementation in the machinery due to the strong absorption of RF energy by the metals, thus limiting the available power density. Therefore, the ambient energy harvesting is strictly application-specific, depending on the availability of the power source within the location of the installation target. Therefore, to power such sensor networks, that is to be installed especially in indoor applications, automotive and mechanical structures, the ambient mechanical energy can be a perfect choice. A comparison of the advantages and disadvantages of various microscale energy harvesting technologies are outlined in Table 1.3.

Table 1.3: Comparison of micro scale energy harvesting technologies

Technologies	Advantages	Disadvantages
Photovoltaic	<ul style="list-style-type: none"> ✓ Green, ✓ Renewable 	<ul style="list-style-type: none"> ❑ Affected by weather ❑ low output inside.
Piezoelectric	<ul style="list-style-type: none"> ✓ High power density ✓ MEMS, CMOS compatible ✓ Compact size 	<ul style="list-style-type: none"> ❑ Ceramics prone to break ❑ Narrow operating frequency
Electromagnetic	<ul style="list-style-type: none"> ✓ High output current ✓ Easy to scale up 	<ul style="list-style-type: none"> ❑ Not MEMS compatible ❑ Interference issues
Electrostatic	<ul style="list-style-type: none"> ✓ High output voltage ✓ Compatible with MEMS 	<ul style="list-style-type: none"> ❑ Electret need external source ❑ Small power output
RF	<ul style="list-style-type: none"> ✓ Long distance transfer ✓ Prolonged lifetime ✓ Easy integration 	<ul style="list-style-type: none"> ❑ Ultra-low output power ❑ Output power varies
Thermoelectric	<ul style="list-style-type: none"> ✓ High durability ✓ Small volume 	<ul style="list-style-type: none"> ❑ Not MEMS compatible ❑ Low output

1.3.1 Vibration Energy Harvesting (ViEH)

Vibration Energy Harvesting is the technique to convert vibrations into usable electrical power by a two steps conversion. Initially, the vibration is transformed into a relative motion between two elements, with the aid of an equivalent mass-spring system as shown in Figure 1.3. The relative motion is then converted to electric power by a mechanical-to-electrical conversion mechanism (mainly piezoelectric, electromagnetic or electrostatic). The equivalent spring-mass system creates a phenomenon of resonance, amplifying the relative spring displacement $z(t)$ compared to the input vibrations amplitude $y(t)$, leading to an increasing harvested power at resonance [29].

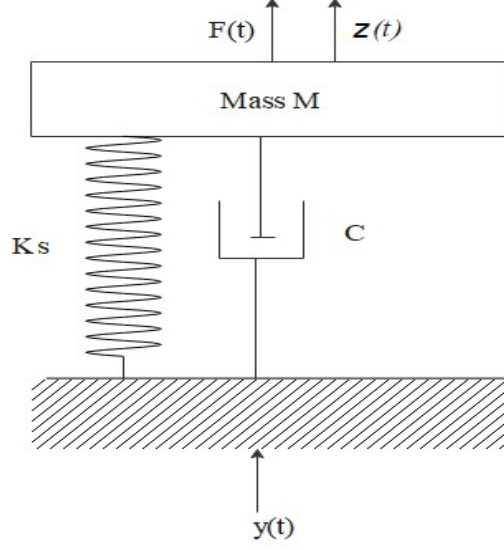


Figure 1.3: Representation of the electromechanical model of a ViEH

In the equivalent mechanical model, a mass (M) is suspended in a frame by a spring (stiffness k_s) and damped by dashpot C with an effective damping coefficient of $d_m + d_e$, where d_m is the mechanical and d_e is the electrical contribution to the damping respectively. The differential equation of the system can be described as [7]:

$$M\ddot{z}(t) + (d_m + d_e)\dot{z}(t) + k_s z(t) = -M\ddot{y}(t) \quad 1.2$$

The energy that can be extracted from the above system, attains a maximum when the excitation frequency ω of the is equal to the natural resonant frequency ω_r of the spring-mass system, that is given by:

$$\omega_r = \sqrt{\frac{k_s}{M}} \quad 1.3$$

The power converted by a vibration energy harvester to the electricity is equal to the power absorbed by the electrical induced damping d_e component of the dashpot C , given by:

$$P_{out} = \frac{M\zeta_e Y_0^2 \left(\frac{\omega}{\omega_r}\right)^3 \omega^3}{\left[1 - \left(\frac{\omega}{\omega_r}\right)^2\right]^2 + \left[2\zeta_T \left(\frac{\omega}{\omega_r}\right)\right]^2} \quad 1.4$$

where ζ_T is the total damping ratio, $\zeta_T = (\zeta_m + \zeta_e) = (d_m + d_e)/2M\omega$

Y_0 is the amplitude of vibration, ζ_m is the mechanical and ζ_e is the electrical damping of the system respectively. The maximum electrical power that can be extracted at the resonant frequency ($\omega=\omega_r$) can therefore, be given as:

$$P_{max} = \frac{m\zeta_e Y_0^2 \omega_r^3}{4\zeta_T^2} \quad 1.5$$

The several vibrating structures available in the environment present rich sources of usable energy for low power applications. Base accelerations of such structures vary from 0.01 to 10 g, with frequencies ranging between 1 and several kHz as shown in Table 2.3 [9].

Table 1.4: Available vibration level in various ambient sources

Vibration source	Available acceleration (g)	Available frequency range (Hz)	Reference
Aircraft	Up to 10	1-1000	[30]
Car Engine	1-1.5	200-500	[13]
Refrigerator	0.1	240	[9]
Microwave	0.2-0.3	100-200	[31]
Machines (heavy)	Up to 10	200	[32]
Bridge	0.01-3.71	1-50	[33]
Human movement	5-10	20	[34]

The ambient mechanical energy can be transduced to electrical energy by main mechanisms namely piezoelectric, electrostatic, electromagnetic, and triboelectric energy harvesters. For example, the typing in keyboard can generate power of the order of few milliwatts, energy generation by the motion of upper limbs is about 10 mW. Walking can generate as much as 10 W. The microscale Electro-Magnetic Energy Harvesters (EMEHs) tend to produce very low AC voltages in the order of millivolts. Furthermore, the output voltage reduces as the size is reduced.

While comparing the output power of all the vibrational energy harvesting technologies, Electrostatic Energy Harvesters (EEHs) have a limitation of implementation that the device vibrates with a magnitude of several hundreds of microns while maintaining a minimum capacitive air gap of 0.5 mm to produce similar performance [32]. For both piezoelectric and electrostatic

generators, the output current will reduce with size due to the reduction of the capacitance of the device which decreases with decreasing size. Furthermore, piezoelectric generators have the advantage that it produces high voltages. Out of all these microscale vibration energy harvesting, PEHs, therefore, have an upper edge due to higher output voltage, relatively high output power density, and simplicity in design over their counterparts such as EMEHs and EEHs. Moreover, the piezoelectric transduction mechanism does not need any moving parts and, thus, is easy to maintain.

1.3.1.1 Electromagnetic Energy Harvesters (EMEHs)

EMEHs can be used to convert the vibration energy available in the ambient environment to electrical energy using the principle of Faraday's law of electromagnetic induction. When a conductor move in a magnetic field (Figure 1.4), a voltage is induced across it. The conductor may be in the shape of a coil that is planar or wound. Generally, the magnet that is used to provide the field could be permanent magnets such as neodymium (NdFeB) [35] or Alnico (AlNiCo) [36].

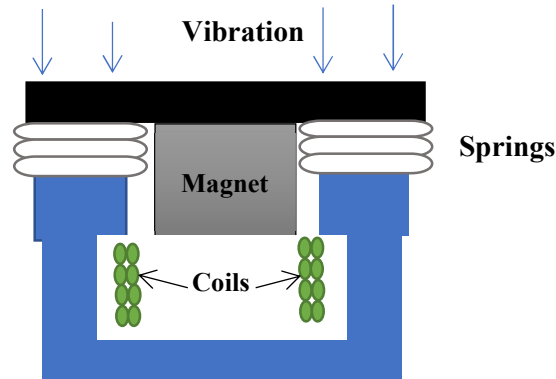


Figure 1.4: Illustration of an Electromagnetic Energy Harvester

The amount of induced voltage V_{EM} (peak to peak) in the electromagnetic coil can be computed by:

$$V_{EM} = -N \frac{d\phi}{dt} \quad 1.6$$

where, N is the number of turns, and ϕ is the total flux linkage between the magnet and the coil. The power generated by the EMEH is extracted by connecting a load resistance across the two ends of the coil. The energy harvested by the EMEH is influenced by the damping offered by the coil to the input vibrations. Also, EMEHs produce maximum power when the relative motion between the magnet and coil is maximum.

From an interesting application point of view as depicted in Figure 1.5a,b Gao et al. in 2017, proposed a novel Rail-Borne Energy Harvester for powering wireless sensor networks in the railway industry [37]. The authors proposed a magnetic levitation harvester that offers broadband harvesting at a low-frequency (3–7 Hz) for a given rail displacement of 0.6 to 1.2 mm. The harvester provided an output power of 119 mW and the output peak-peak voltage of 2.32 V is achieved with the rail displacement of 1.2 mm. Beeby et al. [35] reported a micro-EMEH of a cantilever type structure, with four magnets made from NdFeB bonded to the free end (Figure 1.5c). The coil is positioned between the two magnets, with the beam and magnets able to move relative to each other. The magnets move vertically relative to the coil that is adhesively bonded to the plastic base. The authors claimed to harvest output power of 46 μ W at a relatively low acceleration of 0.06 g which is a large value compared to other EMEH reported so far. Also, the aeroelastic EMEH has received widespread attention in recent years with the advancement of MEMS technologies [14].

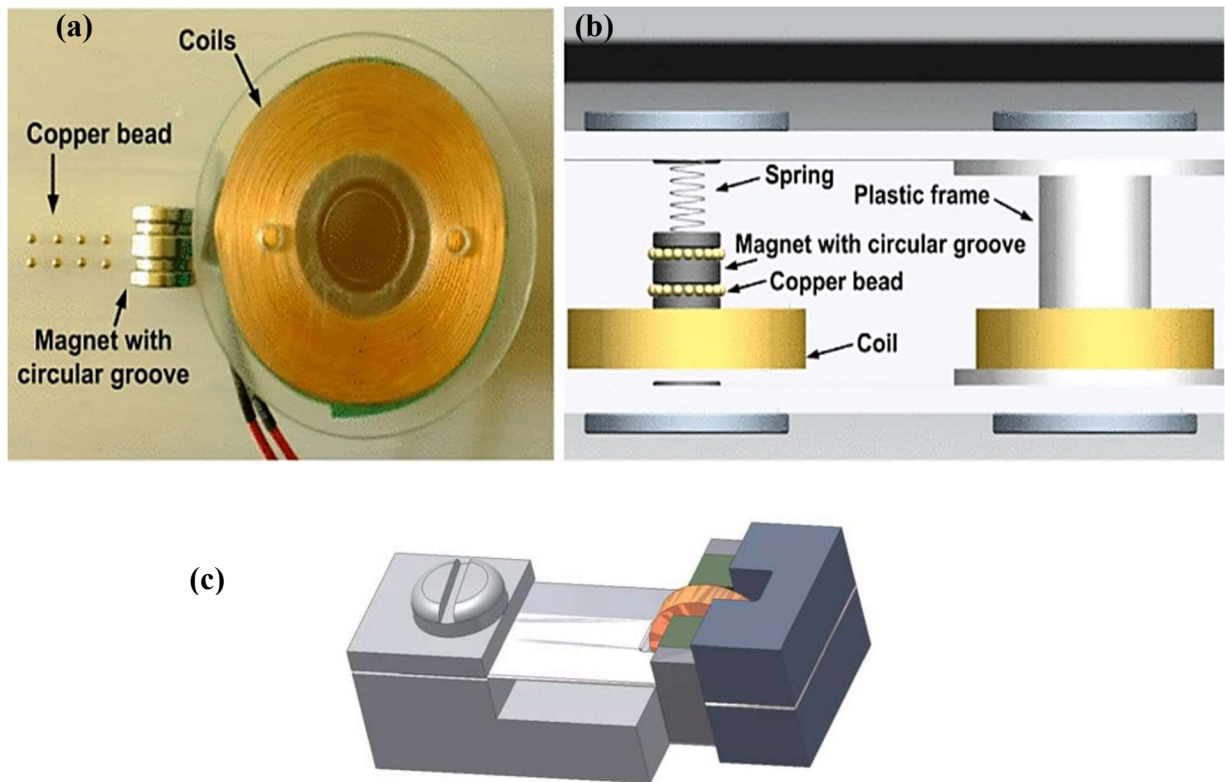


Figure 1.5: (a) Top view and (b) side view of the Rail-Borne Energy Harvester proposed by Gao et al. [37](c) 3D view of the EMEH proposed by Beeby et al.[35].

The disadvantage with an EM harvester is that its power production capacity reduces sharply with a decrease in its size [6]. But at the micro-scale, the materials used for the magnets are not CMOS compatible, and it is difficult to manufacture metallic coils with a large number of turns.

1.3.1.2 Electrostatic energy harvesters (EEHs)

EEHs uses the principle that a variable capacitor electrode induces the charge on the electrode plates when there is a relative motion between two plates that are separated by a dielectric or air [7]. Generally, a variable capacitor consists of a movable and a fixed electrode that is separated by a dielectric layer of permittivity ϵ with a spacing d . The micro scale capacitive transducers are usually represented by two parallel plate or comb drive electrodes as shown in Figure 1.6.

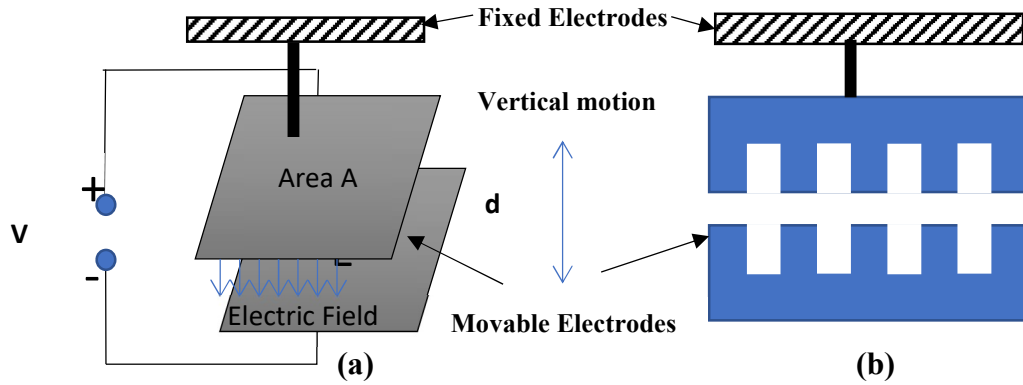


Figure 1.6: Illustration of electrostatic energy harvesting principle with different electrode configurations: (a) parallel plate electrode (b) comb-drive configuration

In order to have a variation of charges, the capacitance C_{ES} has to change. The capacitance of the parallel plate configuration of the EEH can be given as:

$$C_{ES} = \epsilon \frac{A}{d} \quad 1.7$$

$$E_{ES} = \frac{1}{2} QV = \frac{1}{2} CV^2 \quad 1.8$$

where ϵ is the permittivity, A is the area, and d , are the spacing between the electrodes of the capacitor. If the charge is held constant, the voltage can be increased by reducing the capacitance, and if the voltage is held constant, the charge can be increased with the capacitance. In both cases, the energy stored E_{ES} on the capacitor increases accordingly.

The main ways to alter the capacitance are:

- a) Change the gap d between the electrodes
- b) Change the facing area A
- c) Change the permittivity ϵ

The EEHs can be classified into two groups:

- (1) Electret-free EEHs: These are EEHs whose performance is dependent on an external voltage that is supplied to one of its electrodes: To achieve a maximum efficiency of the EEH, a high voltage polarization ($>100\text{V}$) is necessary that need to be supplied from an external voltage source such as battery or capacitor.
- (2) Electret-based EEHs: Electrets are pre-charged dielectric materials that can store the surface charge inside the structure for several years similar to the permanent magnets in the electromagnetic EHs. The word electret was coined by O. Heaviside in 1885 and is inspired from the term “electricity magnet”. The most commonly used electrets in electret-based EEHs are Teflon [38], SiO_2 [39] and CYTOP [40]. The electret-based generators have the advantage over the electret-free EEHs that they can convert the ambient mechanical vibration to electricity without any external supply.

R. Salem et al. [41] designed a micro-scale EH having a switchable dielectric constant capacitor to enhance the power output. It is observed from their study that a thousand times more power is generated in this configuration than the conventional EH. Models of different EEH designs were developed by S. Roundy [42] and showed that the optimal structure for EEHs was in the plane movement of the interdigitated comb drive structure with a variable air gap between the fingers. It was also shown in the same study that the EEH would be able to harvest up to $100 \mu\text{W}/\text{cm}^3$ at an acceleration of 2.25 m/s^2 at an operating frequency of 120 Hz. In 2005, Despesse et al. developed a macroscopic device able to work on low vibration frequencies and able to harvest a high power of 1 mW at a vibration acceleration amplitude of 0.2 g at a low frequency of 50 Hz [7]. Basset et al. [43] in 2014 developed a MEMS harvester (Figure 1.7) that can work at low frequency (150 Hz) and can generate $2.2 \mu\text{W}$ at an acceleration of 1 g.

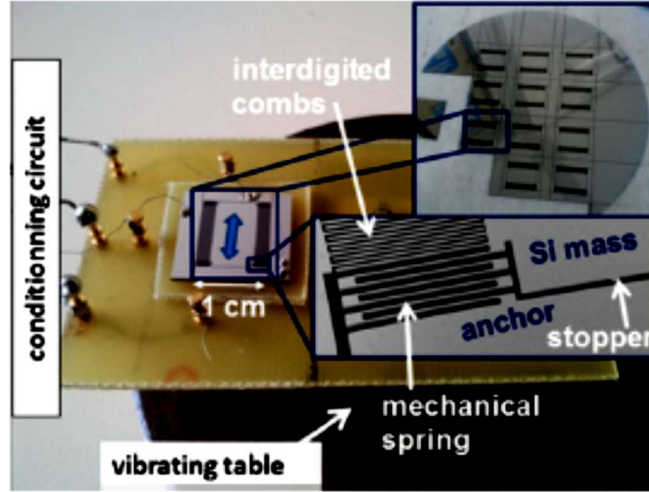


Figure 1.7: Electrostatic energy harvester (with SEM in inset) realized by Basset et al. [43].

The key advantage of electrostatic converters is their compatibility for integration with microelectronics. At the same time, the main disadvantages of EEHs are that the design, such as comb drive structure, imposes a mechanical limit during fabrication. Further, the gaps could be too close and gradually could come into contact and short the circuit due to electrostatic forces.

1.3.2 Piezoelectric Energy Harvesting (PEH)

Among various transduction mechanisms, piezoelectric transduction has drawn considerable attention because of its simplicity in structure, high energy density and good compatibility with micro/nano fabrication techniques [44]. The direct piezoelectric effect, discovered by Pierre and Jacques Curie in 1880, is the ability of certain crystalline materials to produce an electrical charge proportional to an externally applied force. With their knowledge of crystallography pyroelectricity, they postulated and demonstrated the ability of various materials such as quartz, to generate electrical charges under the application of pressure. The piezoelectric effect is reversible in materials, i.e., by the converse piezoelectric effect, the generation of a mechanical strain results from an applied electrical field. Until 1916, when P. Langevin developed the first notable application of the piezoelectric effect in the submarine detectors, piezoelectricity was considered as a laboratory curiosity. In the following years, the crystal microphone was introduced which again created interest in piezoelectric research and this resulted in major development of several kinds of piezoelectric devices. Quartz for instance, because of its high mechanical and thermal stability, is still being used widely in watches, oscillators, and so on. Additionally, piezoelectric ceramics are widely used in ultrasonic devices [45], precision instruments such as

Atomic Force Microscopy (AFM) [46], non-destructive testing, piezoelectric transformer [47] etc. Piezo sensors convert mechanical energy into electrical energy and therefore are often also referred to as "generators".

1.3.3 Piezoelectric Vibration Energy Harvesters

The global market value of piezoelectric devices was estimated to be ~20 billion Euros in 2019 and is expected to continue to increase at an annual growth rate of ~6.2% over the next five years [19]. The energy harvesting based on piezoelectricity become very popular for vibration energy harvesting in recent years due to its relatively higher power density over its counterparts such as electrostatics and electromagnetic energy harvesting. Broadly speaking PEHs can be treated as resonant PEHs or non-resonant PEHs based on their mode of operation.

1.3.3.1 Modes in cantilever beam piezoelectric harvester

Based on the relationship between the applied stress and polarization direction of the piezoelectric material, the PEHs can be classified into d_{31} , d_{33} , and d_{15} operational modes. The electrode configurations and poling direction of the d_{31} devices and the d_{33} devices are, respectively, shown in Figure 1.8.

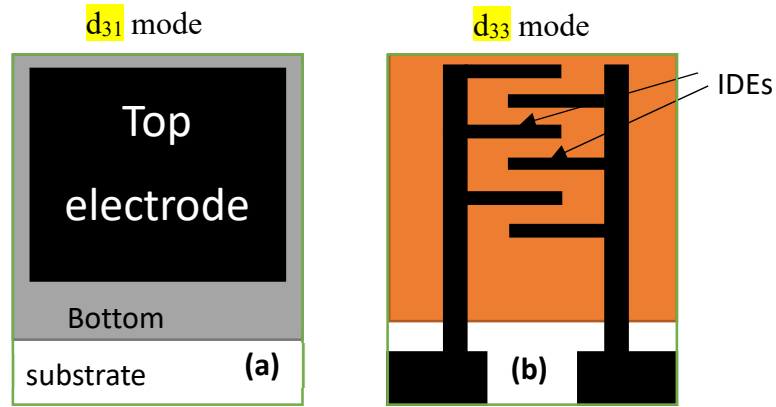


Figure 1.8: schematic top view of various electrode configurations (a) d_{31} mode (b) d_{33} mode

In d_{31} and d_{33} modes, the piezoelectric material is subjected to bending stress whereas in the d_{15} mode it is the shear stress that comes to play. The PEHs possess parallel plate electrodes in d_{31} mode with the direction of polarization perpendicular to the direction of applied stress. A d_{33} mode PEH consists of interdigital electrodes as the polarization direction is parallel to the direction of applied stress. The d_{31} mode is more commonly implemented than the d_{33} mode owing to its simplicity of fabrication [48]. However, d_{33} is normally larger than d_{31} coefficient in piezoelectric materials. So, the d_{33} mode generates higher output voltage; but the d_{31} mode PEHs have the

advantage of generating a larger electric current [48]. This is because, typically, the piezoelectric material in the PEH is thin, which leads to a smaller distance between electrodes of the d_{31} mode device compared to that of the d_{33} mode device.

1.3.3.2 Resonant mode PEH

In resonant PEHs, the most employed mechanism is a cantilever-type with one or two piezoelectric layers placed on a substrate. Among cantilever beam type PEH, the widely used harvester design is the single-clamped cantilever with a proof mass at the free end. It is because it is relatively easy to fabricate such designs using the standard silicon-based technology and the frequency is tunable by optimizing the weight of the proof mass. In resonant mode PEH, unimorph or bimorph cantilevers systems are mostly used because they provide large stress on the PM, therefore, reducing the size of the devices. In unimorph configuration, a piezoelectric layer is deposited onto an elastic material (metal, silicon or oxide layer) as shown in Figure 1.9 a. In bimorph, an elastic layer is sandwiched between two piezoelectric layers, and two piezoelectric layers act as two generators in series as in Figure 1.9 b. The fixed end is mounted onto a vibrating body. It is relatively easy to fabricate using the standard CMOS processes and the resonance frequency is tunable by adjusting the weight of the proof mass.

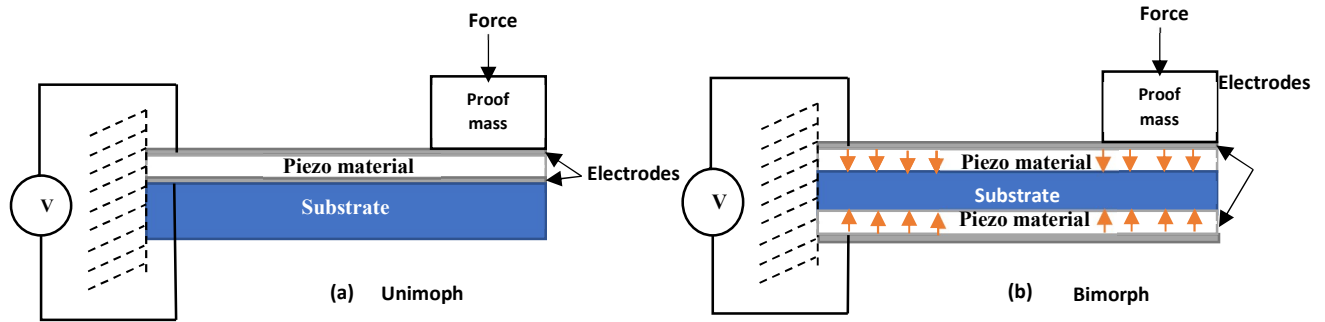


Figure 1.9: Schematic of (a) Unimorph and (b) bimorph PEHs

The difficulties in designing and optimizing the transducer resonance frequency, vibration modes, and the electromechanical coupling factor (K), is due to various factors like the uneven transducer topology and material properties. The PEH structure can be modeled as an SDOF system, that is comprised of a seismic mass ($M = m + 0.23m_c$) where ' m ' is the mass of proof mass and m_c the mass of cantilever, a spring with constant k_s , a dashpot with damping coefficient C and a vibrating base.

Therefore, the resonance frequency (f_r) of the cantilever can be tuned by varying the proof mass (m):[49]

$$f_r = \frac{1}{2\pi} \sqrt{\frac{k_s}{(m + 0.23m_c)}} \quad 1.9$$

$$k_s = \frac{Ywt^3}{4l^3} \quad 1.10$$

where, in Equations (2.13) and (2.14) ' k_s ' is the stiffness constant of the beam of width ' w ', thickness ' t ' and length ' l ', and ' Y ' being Young's modulus of the beam respectively. According to Equation (2.12), it is possible to alter the resonance frequency by reducing the spring stiffness coefficient k_s or by increasing the proof mass. Increasing the thickness of the cantilever will also increase the frequency, while increasing its length will decrease it. However, the length of the cantilever beam is limited in MEMS devices. In some particular cases, it is therefore impossible to reduce the resonant frequency of the PEHs by such means. Therefore, in recent years, several frequency up-conversion techniques have been proposed to match the frequency between the external excitation and the energy harvester fundamental resonance frequency [50]. Liu et al [50] developed MEMS-based, broadband frequency band PEHs that can convert low-frequency vibrations to high-frequency by frequency up-conversion method. In the first design, the lower resonant frequency cantilever (LRF) was quenched to broaden its bandwidth to 22 Hz under 0.8 g input acceleration, with the high-frequency resonant beam (HRF) made to vibrate at 618 Hz.

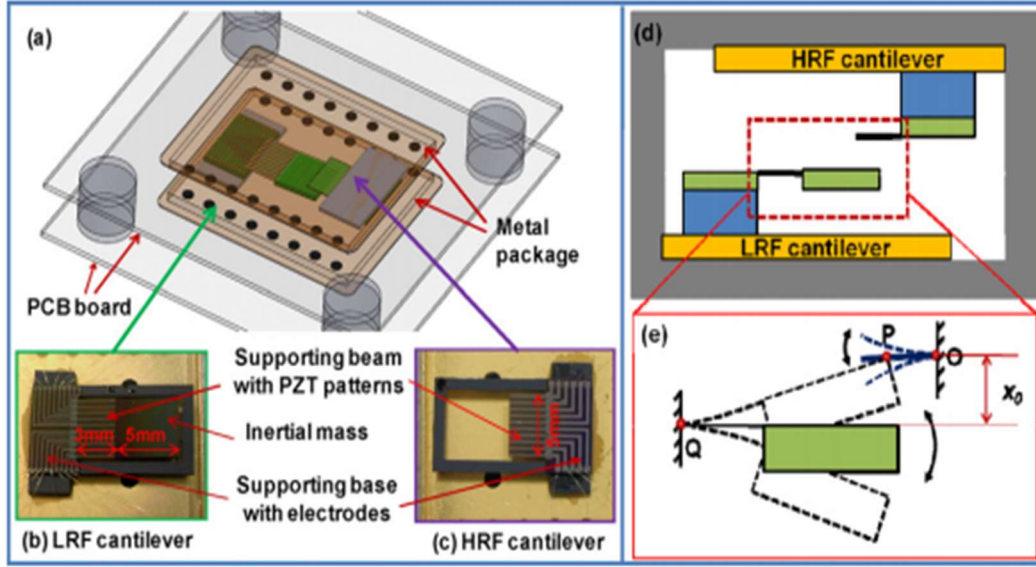


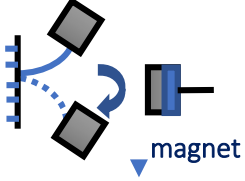
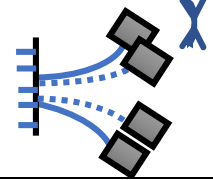
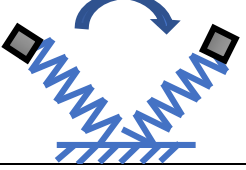
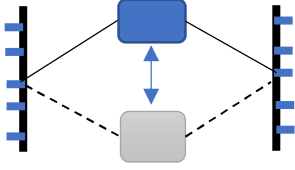
Figure 1.10: (a) Schematic drawing of EH-I system; (b) fabricated LRF cantilever; (c) fabricated HRF cantilever; (d) arrangement and (e) vibration behavior illustration of EH-I system [46]

The frequency of the second design was shifted from 22 to 26 Hz to achieve resonance with a lower frequency. They obtained power densities of 61.5 and 159.4 $\mu\text{W}/\text{cm}^3$ at operating frequencies of 20 and 25 Hz, respectively, at an acceleration of 0.8 g acceleration.

Another main challenge faced by resonant PEHs, is the narrow bandwidth of operating frequency as the output voltage and power reduce drastically from moving away from the resonant frequency [51]. This mismatch can also occur when the resonant frequency of PEH vary due to the aging or temperature variations of the environment. The PEH produces AC output voltage in phase with the applied frequency of the mechanical force and voltage needs to be rectified before it can be stored for practical applications [52]. Thus, if the voltage generated is under the diode threshold drop of the rectifier, the power is not utilized. Since the frequency of typical ambient environmental vibration sources is low (less than 300 Hz) and susceptible to variation to a certain extent, PEHs with low resonant frequencies and broadband operation capabilities are necessary for reliable performance [8]. Several methods have been proposed to achieve broadband energy harvesting in piezoelectric harvesters. Although nonlinear or bistable mechanical harvesters are effective in overcoming the narrow bandwidth limitation of classical resonator-based vibration energy harvesters, they are dependent on the input amplitude and multi-degree of freedom

harvesters suffer from low power densities. A comparison of various piezoelectric broadband energy harvesting techniques is given in Table 1.5.

Table 1.5: Various commonly used piezoelectric broadband energy harvesting techniques

Broadband mechanism	Schematic	Bandwidth	Reference
Force induced resonance tuning with a magnet		60 Hz	[53]
Multi-modal frequency tuning		7 Hz	[54]
Multi-modal degrees of freedom using spring-mass		16-28 Hz	[55]
Induced non-linearity		4-12 Hz	[56]

There are several reports of piezoelectric microgenerators with various complex configurations such as membrane structure [57], multiple stacked piezoelectric layers, etc. [51], [58] for forcing non-linearity in the system and to push towards a broader frequency regime. Recently, electrical techniques using impedance matching, to tune the resonant frequency of piezoelectric harvesters, have been proposed as a solution for broadband harvesting and opens new perspectives. Compared to the non-linear and bi-stable technique of broadband energy harvesting, electrical technique is less complex in fabrication and operation. However, this approach requires energy harvesters with very strong global electromechanical coupling coefficients K^2 , whose design remains a challenge today. Strongly coupled energy harvesters are considered as a solution to further extend the frequency bandwidth, due to resonance splitting. However, “green PEHs” with high coupling K

and simple configuration working at low ambient frequencies with a broadband operational capability are rarely reported. Therefore, this thesis aims to achieve a highly coupled lead-free piezoelectric energy harvesting, for broadband energy harvesting.

There have been numerous studies on the optimization of output power of resonant energy harvesting transducers at resonance. Some of them include the study of the effect of the cantilever topology on energy harvesting efficiency [59]. Some studies conclude that triangular beams are better than rectangular beams for the same maximum amplitude and output power [60]. There are also studies on the effect of size and shape of the piezoelectric transducer on the performance of harvesters [49], [61]. Adhikari et al. studied the impact of geometry of the piezoelectric layer on the output power where the width was changed along the beam length during the optimization which showed transducer shape to be affected by the capacitance and coupling factor [62]. Another similar work reported a better performance for a cantilever beam with a wide free tip has than the simple rectangular or the tapered cantilever [63]. A cantilever with a proof mass at the free end exhibited higher conversion efficiency and a wider bandwidth compared to a standalone bimorph [64].

1.3.3.3 Non-resonant PEH

There are several advantages for the non-resonant mode sensor especially in the case of energy transducers as it can utilize random loads effectively compared to the resonant mode that requires a near resonance condition i.e., a force with a frequency near to the resonance frequency of the cantilever structure. The non-resonant piezoelectric transducers utilize the direct piezoelectric effect along with certain conditioning circuits that can be used for dynamic measurement or random force power generation as it is not suitable for static operation as there can be leakage on the material [38]. The resonant mode is based on electromechanical response analysis in time or the frequency domain which can work in approximate proximity of their resonance frequency.

Nanoscience has enabled the fabrication of novel next-generation nanogenerators for piezoelectric energy harvesting [65]. Semiconductor nanowires (NWs), due to their size and surface-to-volume ratio offer a wider range of very attractive physical properties [66]. A simple nanogenerator consists of a nanowire array of semiconductors like GaN [67] or ZnO [68] deposited over an electrode immersed in an insulating layer such as PMMA that protects it from the electrical leakages and short circuits onto which an electrode is deposited. Nanoscale devices have several advantages over the bulk such as:

(1) Enhanced Piezoelectric Effect [69]: The nanowires exhibit an enhanced piezoelectric effect compared to bulk which is of several orders of higher magnitudes and also offers more robustness.

(2) Superior Young's Modulus(Y) [70]: Nanowires can withstand larger strains resulting in higher flexibility in bending more compared to the bulk. Young's modulus increases with an increase in NW's diameter with values ranging from 118 to 183 GPa.

The major work in this area leading to its popularity was conducted by Z. L Wang at Georgia-tech by the experiments in measuring the voltage output from zinc oxide (ZnO) nanowire by AFM tip [71]. This is supposed to be due to the Schottky junction between the platinum tip and n-type ZnO nanowire. The Schottky junction conducts electrons only when the ZnO is negatively charged along the compressed side of the wire. When a piezoelectric nanowire is strained, a potential is originated along the sides because of the lattice distortion. Nanogenerators have been implemented with several piezoelectric semiconductor materials such as ZnO, indium nitride (InN) [30] gallium nitride (GaN) [72], Cadmium Sulphide (CdS), and piezoelectric ferroelectric materials, such as PZT [65], and organic piezoelectric materials like PVDF [73], [74], have received extensive attention as nanomaterials for transduction.

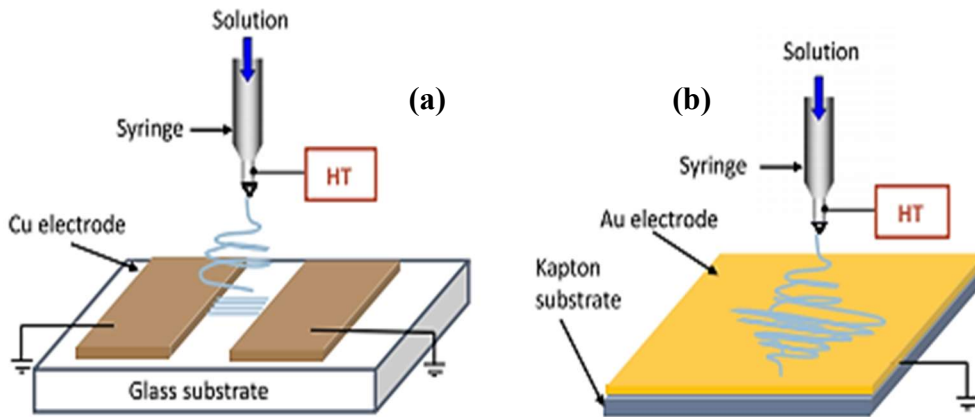


Figure 1.11: Schematic of nanogenerator fabrication by electrospinning process: (a) to obtain the aligned fibers; (b) to obtain the random fiber [65].

Nanogenerators offer excellent flexibility, making them an ideal low-cost option over their other counterparts. Several types of research into innovative designs have been performed for improving the performance and efficiency of the nanogenerators. Choi et al. [75] have demonstrated the working of a flexible hybrid cell, that can absorb both solar energy piezoelectric power consisting of ZnO nanostructures, serving as both piezoelectric material, and absorbing material for a solar

cell. Further, there is a piezoelectric nanogenerator based on lead-free electrically poled ferroelectric single-crystalline KNbO_3 nanorod of $1\ \mu\text{m}$ mixed with polydimethylsiloxane (PDMS) that has a large piezoelectric constant (d_{33} of $55\ \text{pmV}^{-1}$). When the applied strain of 0.38%, the composite device has an open-circuit voltage of 3.2 V and a closed-circuit current of 67.5 nA with a current density of $9.3\ \text{nA cm}^{-2}$, which could be enough to power an LCD.

1.4 Power Management circuits for PEH

PEH generates an AC voltage at the output. Therefore, a Power-Management Circuit (PMC) is needed to rectify, store, and regulate the AC output before it can be used to power WSNs. Since the microgenerators produce power in the order of microwatts, that is just enough to power the IoT nodes, such devices need to be efficient for low-power applications. PMC with the Integrated Circuit (IC) solutions on-chip obtain a better performance than implementations with off-the-shelf discrete components [76]. PMC acts as an interface between the Piezoelectric energy harvester (PEH) and the connected load. Figure 1.12 shows a general block diagram of power conversion circuits for piezoelectric energy harvesting applications.

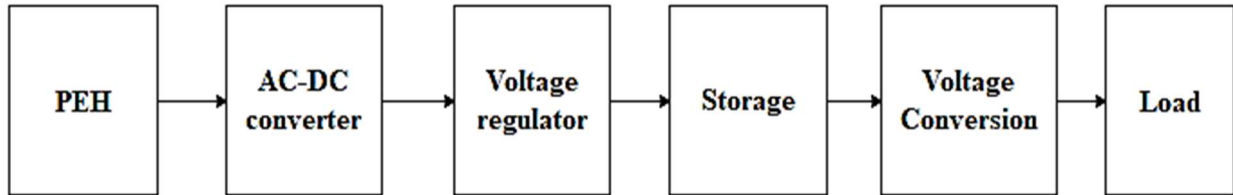


Figure 1.12: General block diagram of piezoelectric energy harvesting with power conversion circuits

Further, WSN circuits usually work at voltages different from the open-circuit voltage of the PEH which could fluctuate depending on conditions such as input acceleration and frequency. Hence, the PMC has to ensure a smooth operation of the WSNs irrespective of changing input conditions. PMC primarily consists of AC–DC converters to convert the AC output of the PEH to a usable DC output followed by a DC–DC converter to convert the stored voltage into required DC levels. In addition, a storage device such as a supercapacitor or battery is also required. Finally, a power management block such as a Maximum power point tracking (MPPT) is employed to ensure that the power is delivered at the optimal load. To maximize the harvested energy, the electronic interface must appropriately match the output reactance of the piezoelectric element. The reactance of the PEH is generally capacitive and therefore to obtain perfect impedance matching, the load

reactance should be an inductor. However, in practical cases, a resistor is used as the load due to the impracticality of obtaining a high value of the inductor. The optimal load resistance (R) can be obtained by [77]:

$$R_{opt} = \frac{1}{\omega C_p} \quad 1.11$$

The efficiency in the storage of piezoelectric energy harvesting devices can be enhanced through efficient interfacing circuit design. When the piezoelectric materials connect to the electrical load, the electrical load will absorb the energy from the piezoelectric and it will increase the damping factor for the piezoelectric system. The interface circuit has a greater role in regulating the AC into DC and indirectly affects the efficiency of the energy harvester.

With regard to Standard Energy Transfer rectifier circuits (SET) in PEH, the main schemes that are discussed in the literature, are 1) Full-Bridge Rectifiers (FBR) [78] and 2) voltage doubler [79] including those using a) MOSFET and other active switches (e.g., CMOS diode) [80] and b) diode-only passive schemes. However, in MOSFET-based circuits, a gate voltage is required for switching operations, which consumes additional power. In addition, since the power generated by vibration is low (in microwatts), and typically in an FBR the efficiency is only close to 80%, excessive consumption in the rectification circuits should be minimized. In addition to the standard rectifier circuit mentioned above, resonant PEH rectifiers are one of the several harvesting interfaces that have been suggested to maximize power extraction [81], [82]. Such resonant techniques exploit a resonance effect to efficiently rectify the piezoelectric voltage and the PEH is intermittently disconnected to the resonant electronic interface for a small interval of time.

The main criteria adopted to evaluate the performance of an energy harvesting circuitry can be described as follows [78]:

1. The power loss (P_{loss}) in harvesting circuit should be minimal compared to input power (P_{in}).
2. Low circuit complexity: minimum components should be employed in such circuits since input power is approximately $< 50 \mu W$, otherwise this could prove insufficient to power up complex electronic control schemes. Further, the interconnection with wires should be avoided to reduce resistive losses.

3. Adaptability: These schemes need to adapt to the variations in input frequency and the amplitude of the input conditions of the PEH during real-time operation, which might change with time.
4. Minimum forward operating voltage V_p of the conditioning circuit: ensures the output voltage V_{out} is greater than the threshold voltage V_{th} of the passive components such as diodes.

1.5 Summary

The state-of-the-art of micro-scale energy harvesting for powering autonomous WSNs has been detailed, with a focus on vibration-based energy harvesting. It is to be noted that the choice of the energy harvesting solution largely depends on the working conditions and available power density at the target location of installation of these WSNs. Therefore, the choice of ambient energy harvesters is largely application-specific and should be dealt with case by case. The vibration energy can be harnessed by various transduction mechanisms such as electrostatic, electromagnetic, and piezoelectric transductions. Among these various mechanical vibration-based energy harvesting options, piezoelectric energy harvesting is the most common and feasible option due to its high-power density, high output voltage, and relatively better compatibility with MEMS-based fabrication process. Piezoelectric energy harvesters (PEHs) are widely studied in the literature. The two approaches for the piezoelectric energy harvesting namely the resonant and non-resonant modes have been detailed. Several prototypes with different approaches to improving the harvested power and operating frequency range, which has been proposed in the literature, have been detailed. However, since most of the previous research in this area is focused on lead-based materials such as PZT, there is an urgent need for exploring new environment-friendly materials as active materials in piezoelectric energy harvesters. Further, some of the disadvantages of the piezoelectric energy harvesting technique such as low operating bandwidth need to be addressed, to meet the criteria in real time application. In real time applications such as powering IoT wireless sensor nodes using ambient vibrations, broadband harvesting capabilities are essential. Compared to the existing non-linear and bi-stable techniques to achieve broadband energy harvesting, strongly coupled PEHs are more promising solution to extend the frequency bandwidth, due to their simplicity. However, “green PEHs” with high global electromechanical coupling K , simple configuration, working at low ambient frequencies, and with a broadband operational capability are rarely reported. Therefore, this thesis aims to achieve highly coupled lead-free PEHs, for broadband energy harvesting. The next chapter will explore the

electromechanical properties and energy harvesting FoM of promising new lead-free piezoelectric materials such as Sodium Potassium Niobate (KNN), Lithium Tantalate and Lithium Niobate that are studied in the context of the EU ITN-ENHANCE project.

2 Electromechanical characterization of piezoelectric materials

In this chapter, the extraction of electromechanical properties of a few lead-free piezoelectric materials at the microscale, to develop vibrational energy harvesting devices are discussed. The techniques that have been used to characterize the piezoelectric properties, morphologies such as Atomic Force Microscopy (AFM) are detailed. Also, a brief discussion on the processing, deposition of these piezoelectric materials, and the list of extracted parameters such as the Figure of Merit (FoM) devices is presented.

2.1 Piezoelectric Materials

The piezoelectric effect being an anisotropic phenomenon is exhibited by materials with no centre of symmetry in their crystal structure. Out of the 32 crystallographic groups, 21 groups are non-centrosymmetric out of which 20 groups are piezoelectric. Those 20 piezoelectric point groups can be again classified into 10 polar and 10 nonpolar groups. The polar group exhibit a property known as spontaneous polarization and are also pyroelectric. For centro-symmetric crystal, the polarization remains zero, even under stress. Materials in which the centers of positive and negative charges do not coincide even without the application of an electric field are said to have spontaneous polarization, P_s . The spontaneous polarization is displayed by materials that have a unique polar axis [5], which are a subset of non-centro-symmetric point groups as shown in Figure 2.1b. On the application of mechanical stress on a non-centro-symmetric crystal, an asymmetric displacement of the ions is created resulting in the modification of the internal dipoles. An example of the perovskite unit cell structure of ABO_3 type is shown in Figure 2.1a with two positive ions on the A-site (in Green) and negative oxygen ions O_2 (in Yellow)- forming an octahedron around the B-site (in Blue).

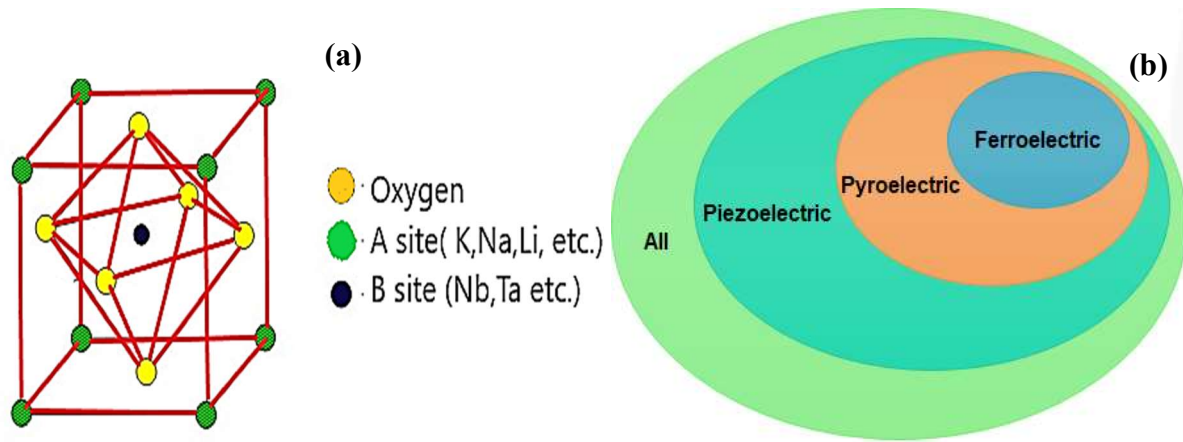


Figure 2.1: (a) Perovskite unit cell (b) Classification of families of dielectric materials [5]

The negative oxygen octahedron can be moved in the opposite direction relative to the positively charged A-ions along the (vertical) c-axis, thereby creating a spontaneous electric polarization. When the equilibrium spontaneous polarization of dielectric material can be reorientated by an electrical field of sufficient strength at temperatures below a characteristic temperature T_c , it is called a ferroelectric. The compression or expansion of the cell along the polar axis will shift the positive and negative charges accordingly resulting in a charge on the surfaces of the ferroelectric polarization direction. Also, the compression or expansion of the unit cell along the polar axis, can therefore distort the positive and negative charges in different directions resulting in an electric field in a normal direction as well. The polar axis also allows them to be pyroelectric, i.e., they can generate polarization of charges on the application of a temperature gradient across the material polarization direction. In a nutshell, all pyroelectric materials are piezoelectric, whereas only those piezoelectric materials whose symmetry belongs to these 10 polar groups are pyroelectric as shown in Figure 2.1

b. Since piezoelectric materials show anisotropy, their physical parameters such as elasticity, permittivity etc. are tensor and are associated with both directions of stress, electric field, etc. The Figure 2.2 presents convention used in the IEEE Standards for the piezoelectric axis: the axis 1, 2, and 3 indicate the translations, and 4, 5, 6 indicate the shear. By convention, the material polarization is taken along the 3-axis.

2.2 Piezoelectric constituent equations

The constituent equations of a piezoelectric crystal are the complex relations between the mechanical stress T_i , the strain S_k , and the charge density displacement D_i (electric charge per unit area), and the electric field E_i as given below:

$$S_k = S_{kl}^E T_l + d_{ij} E_i \quad 2.1$$

$$D_i = d_{ik} T_k + \epsilon_{ij}^T E_j \quad 2.2$$

where, d_{ij} is the piezoelectric charge coefficient (C/N or m/V), S_{kl} the elastic compliance matrix, ϵ_0 the absolute permittivity, and ϵ_{ij} the relative permittivity matrix of the material. The indices k and l through 1 to 6 (reduced index notation) and the index i and j from 1 to 3 as shown in Figure 2.2. The upper index T indicates constant stresses. The direct piezoelectric relates the electrical charge to the applied mechanical stress T . The inverse effect gives the relationship between the applied electric field and the generated strain.

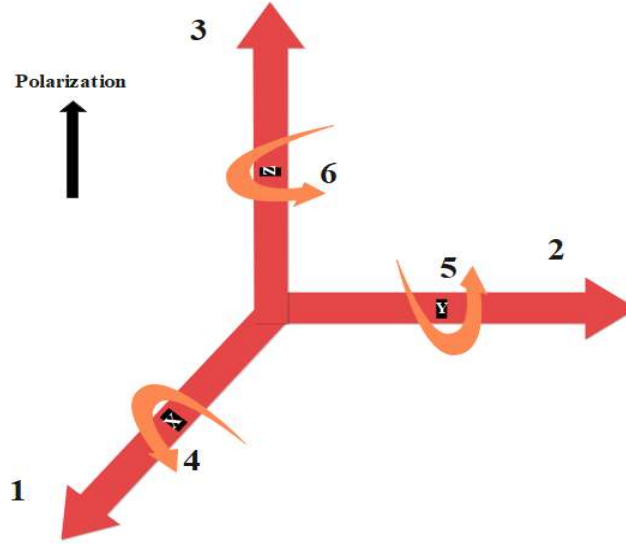


Figure 2.2: Axis numbering of piezoelectric tensors

2.3 Classification of Piezoelectric Materials:

The Piezoelectric Materials (PM) can be broadly classified as crystalline, ceramic, and polymeric piezoelectric materials. In contrast to the naturally occurring piezoelectric crystals like quartz, piezoelectric ceramics are of “polycrystalline” structures [83]. The most commonly produced piezoelectric ceramics are lead zirconate titanate (PZT) [84], [85], barium titanate [86] and lead

titanate. Recently widespread interest has been generated in semiconducting PM like Gallium Nitride [87], and Zinc Oxide [66], which can also be regarded as a ceramic due to their relatively wide bandgap. The semiconducting PM possesses unique advantages such as compatibility with the integrated circuits and semiconductor devices [68]. Also, it was shown that the transverse piezoelectric coefficient d_{31} and the FoM of the well-known piezoelectric thin film material AlN (001) increase considerably by substituting Al partially by Sc18. Further, inorganic ceramic PM has several advantages over single crystal, such as the ease of fabrication into a variety of shapes and sizes as single crystals require cutting along the crystallographic directions, thus minimizing the possibilities of cutting into different shapes [3,10]. The next class of PM namely organic polymer such as PVDF has low Young's modulus compared to the inorganic PM [73]. Piezoelectric polymers (PVDF, 240 mV-m/N) possess higher piezoelectric voltage constants (g_{33}), an important parameter in sensors, even comparable with ceramics. Also, piezoelectric polymeric sensors and actuators with their processing flexibility and their lightweight can be readily manufactured into large areas, and cut into a variety of shapes. In addition, polymers also exhibit high strength, high impact resistance, low dielectric constant, low elastic stiffness, and low density, thereby a high voltage sensitivity which is a desirable sensor characteristic along with low acoustic and mechanical impedance useful for medical and underwater applications. However, they have relatively low d_{33} which limits their application.

Among the ceramics, PZT ceramics are very popular as they have a high sensitivity, a high g_{33} value [88]. However, they have some important limitations such as: 1.) hard to process as they are brittle, and thereby fracture prone. 2.) the output signal they produced for a load depends on the temperature 3.) Thirdly, the difficulty in integration of ceramic disks into industrial appliances molded from plastic. This results in the development of PZT-polymer composites [89], [90] and it is, therefore, feasible to integrate functional PM composites in the product by simple thermal welding or by conforming processes.

2.4 Poling of Piezoelectric Materials

In contrast to the naturally occurring piezoelectric crystals like quartz, ferroelectric ceramics are of “polycrystalline” structures with the electric dipoles randomly orientated.

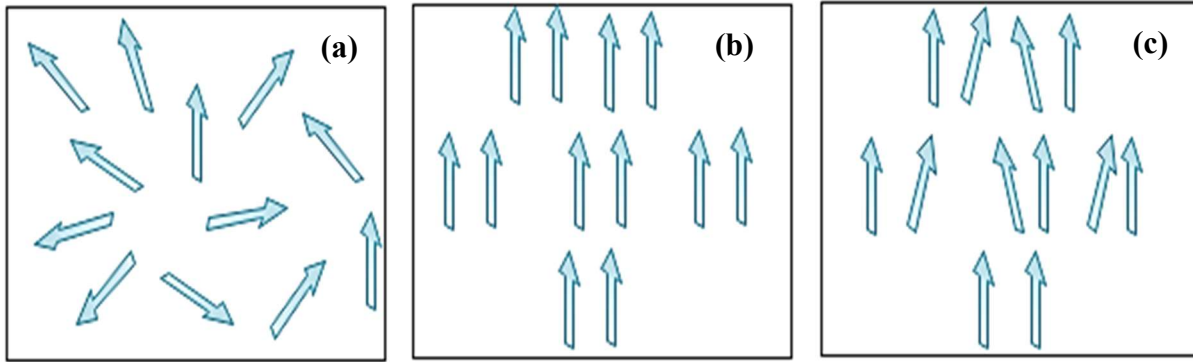


Figure 2.3: Domain orientation in ferroelectric ceramics (a) before poling (b) during Poling (c) after the poling electric field is removed

Regions of the material with uniformly oriented spontaneous polarization are called ferroelectric domains. Therefore, the domains in each grain are randomly arranged in polycrystalline ceramics and thus result in a zero net polarization as shown in Figure 2.3a. However, during the application of a very high electrical field (typically 1-10 kV/mm) at a higher temperature (known as poling), the polarization of domains aligns in the direction of the applied Electric field as shown in Figure 2.3b. Once the electric field is removed, the domains tend to retain their orientation as shown in Figure 2.3c, given the condition that the temperature is above a particular value, which is known as the Curie temperature T_c of the material. The poling can be performed only on ferroelectric materials where it is possible to switch the crystal polarization.

2.5 Ferroelectric Hysteresis Loop and Butterfly Loop

2.5.1 Ferroelectric Hysteresis Loop

The ferroelectric hysteresis loop (Figure 2.4a) is a unique property of ferroelectric materials. An applied alternating, large electric field (surpassing the coercive field) will modify the polarization of the material and provoke a polarization switching in every half-cycle.

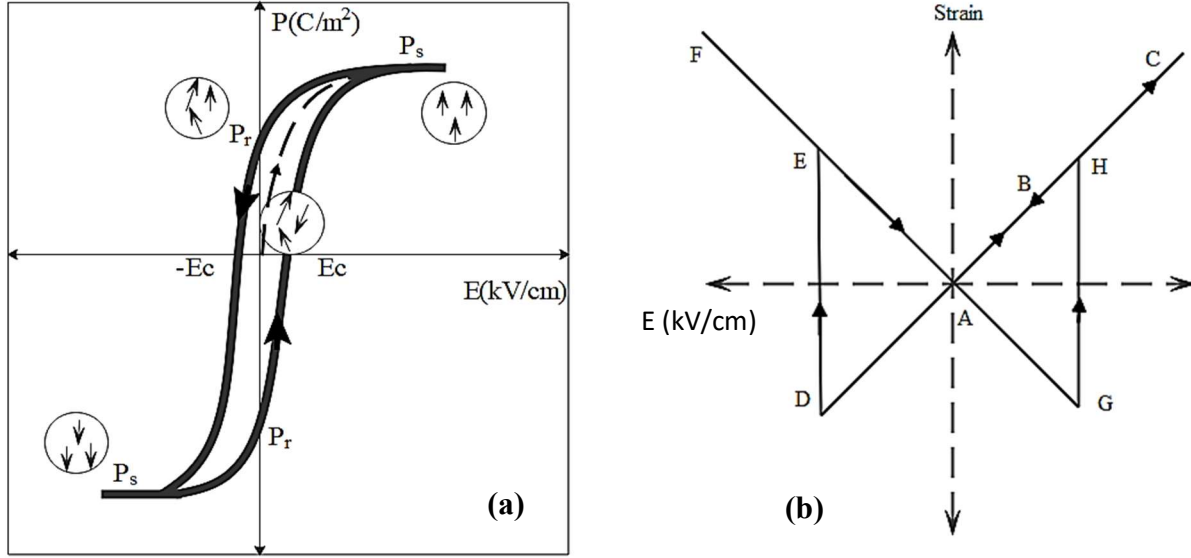


Figure 2.4: Typical (a) Hysteresis (b) Butterfly curves of ferroelectric ceramics

Polarization switching is an important characteristic of a ferroelectric material during the application of an external electric field resulting in the exhibition of the ferroelectric hysteresis loop. At small values of the AC field, the polarization increases linearly. This is because the initially unpolarized domains become more aligned with the applied field direction. However, as the field exceeds a certain value, there is no further increase in polarization since the dipoles are fully aligned with the electric field direction. The value of the field is known as its saturation polarization P_s . As the field is then reversed to zero, the domains become less aligned, although they do not completely return to their original alignment state as they remain in the favorable state which is closer to the applied field. However, since most domains are in the direction of the applied field, the net polarization does not return to zero but to a lower value than the saturation polarization P_s which is known as the remanent polarization P_r . The area inside the hysteresis loop corresponds to the energy loss per cycle per unit volume.

2.5.2 Butterfly loop

Initially, at zero field (point A in Figure 2.4b), the ferroelectric material experiences no strain. When the electric field is then applied in the polarization direction, the domains expand due to the strain developed by the piezoelectric effect, as depicted by the points A–B–C. The domains extend linearly until the maximum field (point C). When the field is reduced to the initial value from point C to A the field starts to the strain is again zero. The field then changes its direction, becoming antiparallel to P_s . As the electric field increases in the opposite direction, the ferroelectric domains

contract compared to point A. At point D the direction of polarization is switched. After switching, the polarization becomes parallel to the field, and the strain becomes positive again at point E. During further increase of the field in the opposite direction, strain increases to point F, and then return to point A. The strain–field curve is linear, indicating that the strain is purely piezoelectric except at the switching points D and G.

2.6 Key Properties of Piezoelectric Materials

2.6.1 Piezoelectric coefficients

Piezoelectric coefficients with double subscripts link electrical and mechanical properties in piezoelectric material. The " d_{ij} " coefficients are most used in transducers, which associates the mechanical strain due to an applied electric field and, therefore, are also known as the strain constants (meters per volt). Other types of coefficients are related to other variables namely: h_{ij} coefficient (relating strain and charge), e_{ij} coefficient (relating strain and electric field), g_{ij} coefficient (relating stress and charge). The first subscript gives the direction of the electric field associated with the voltage applied, or the charge produced. The second subscript gives the direction of the mechanical stress or strain. The four piezoelectric coefficients are used to describe different elements of the piezoelectric conversion. For example, the coefficient d_{ij} gives the displacement of the material during the application of a voltage. Similarly, the coefficient e_{ij} is the electrical charge generated due to the straining of the piezoelectric material. The piezoelectric voltage constant, g_{ij} , is the electric field generated by a piezoelectric material due to the application of mechanical stress applied. h_{ij} coefficient indicates the voltage produced per unit strain when displacement is constant.

2.6.2 Youngs Modulus

The mechanical stiffness properties of the piezoelectric ceramics are described by the Young's Modulus (N/m^2 or Pa). Young's Modulus is the ratio of stress (force per unit area) to strain (change in length per unit length). The stiffness of the piezoelectric material plays an important part in determining resonant frequency. The poling process of piezoelectric ceramic can also induce a strain that can be proportional to the polarization field. When an external electric field is applied to ferroelectric ceramics (poling), the dimensional change/strain developed depends on the stiffness of the ceramic material. For larger stress, the non-linearity should also be taken into account. Due to the converse piezoelectric effect, if the generated electric charge is not transported quickly, it may accumulate and therefore, leads to an opposing force in the reverse direction of the

applied stress due to which the open-circuited electrodes get stiffer than that of shorted electrodes. So, the effective Young's Modulus of a piezoelectric material under a short circuit is lower than with the electrodes open-circuited due to the electrical response that counteracts the resultant strain. Furthermore, the stiffness is anisotropic in all 3 directions from that in the 1 or 2 directions. Therefore, while representing them, both direction and boundary conditions need to be specified. YE_{33} gives the relationship between stress and strain in the 3 directions at constant electric field E with electrodes shorted. YD_{33} gives a similar relationship with the electrodes open-circuited.

2.6.3 Dielectric Permittivity

The permittivity, or dielectric constant, ϵ_{ij} , for a piezoelectric ceramic material, is the dielectric displacement per unit electric field. The first subscript i refer to the direction of the dielectric displacement and the second subscript j is the direction of the electric field. A lower dielectric permittivity is preferred for a piezoelectric material for energy harvesting application.

2.6.4 The electromechanical coupling factor, K_{ij}

The efficiency of mechanical to electrical energy conversion is a key factor for the improvement and optimization of PEH devices. The K_{ij}^2 value is a measure of the effectiveness with which a piezoelectric material converts electrical energy into mechanical energy or the other way. The first subscript to K denotes the direction along which the output electrodes are placed and the second denotes the direction along which the mechanical force is applied or vice versa. The ratio of the energy stored (mechanical or electrical) to the input energy (electrical or mechanical) is defined as the K_{ij}^2 , square of the coupling coefficient.

$$K_{ij}^2 = \frac{\text{Energy converted or stored}}{\text{Input Energy}} \quad 2.3$$

Obtaining high power output from piezoelectric harvesters in many applications requires a high K_{ij}^2 . Mostly, the PEH is operating at its resonant frequency, where the important parameters for performance are the electromechanical coupling coefficient K_{ij}^2 , the quality factor Q_m . Richards et al. derived an exact efficiency formula for cantilever based PEH based on a simplified Single degree of Freedom(SDOF) model [91]:

$$\eta_{PEH} = \frac{\frac{1}{2} \left(\frac{k^2}{1-k^2} \right)}{\left(\frac{1}{Q_m} + \frac{1}{2} \frac{k^2}{1-k^2} \right)}$$

The efficiency η_{PEH} depends only upon the quality factor Q_m and the electromechanical coupling coefficient K_{ij}^2 of the whole system working at resonance. The theoretical study estimated that the efficiency value can be over 90% with the assumed weak damping and strong coupling effects.

2.7 Towards Lead free Piezoelectric ceramics

For several decades, lead-based piezoelectric ceramics such as PZT, have been regarded as the most used piezoelectric materials due to their higher piezoelectric constants [92], high Curie temperature T_c [85], and relatively matured processing steps. The existence of a morphotropic phase boundary (MPB) between two ferroelectric phases helps in their effective poling, resulting in improved electromechanical properties.

However, the adverse issues that arise due to excessive use of lead-based piezoelectric ceramics in commercial applications have resulted in an increased interest in the scientific community to investigate more novel lead-free piezoelectric materials. For instance, lead and its derivatives, like lead oxide (PbO), have been reported to show toxicity and are therefore regarded as hazardous material [93]. Also, recently there have been increasing regulations in the electronic industry to use green materials that are eco-friendly in nature [2]. Recently, the European Union has also implemented the Restriction of Hazardous Substances legislation (RoHS), which has set a strict standard restricting the use of lead-based piezoelectric materials in future electronic devices. Hence, there have been several approaches towards lead-free ceramic PM in recent years, such as piezoelectric single crystals [86], and ferroelectric ceramics with a perovskite structure and Bismuth Layer-Structured Ferroelectrics (BLSF) [94] have been extensively researched. Also, several ferroelectrics with perovskite-structure BaTiO_3 [BT] [86], $(\text{Bi}_{1/2}\text{Na}_{1/2})\text{TiO}_3$ [BNT] [95], $(\text{Bi}_{1/2}\text{K}_{1/2})\text{TiO}_3$ [BKT] [96], KNbO_3 [KN] [97], $(\text{K,Na})\text{NbO}_3$ [KNN] [98] have been probed extensively. The materials used for the measurement purpose in actuators should possess desirable properties like stability, high output, insensitivity to extreme temperature and humidity, and ability to be formed or machined into any shape. But none of the materials exhibiting the piezoelectric effect possesses all the properties. Quartz, which is a natural crystal, is highly stable but the output obtained from it is very small due to low d_{33} . It also offers the advantage of measuring very slowly varying parameters as they have very low leakage when they are used with high input impedance

amplifiers. Obtaining high power output from piezoelectric harvesters requires a high K^2 . Ferroelectric material, such as LiNbO_3 (LN) presents FoM similar to that of PZT20 [99]. Moreover, LN is compatible with high-temperature applications of transducers (up to 1000°C) and energy harvesters (EHs) (up to 500°C , further experiments are needed to find the temperature limit) [20]. BFO is also a potential candidate for high-temperature Vibrational (Vi)-EH (up to 500°C) [21]. This makes LN and BFO particularly attractive for the EHs applications where the working temperature is elevated (in oil, exhaust pipe, close to motor temperature can reach 600°C), as PZT, BTO, and KNN lose their piezoelectric properties at these temperatures. The comparable output power density to that of PZT films was reported for (100)-oriented BiFeO_3 (BFO) films [100]. One of the highest power density values among the wide bandwidth micro-piezoelectric EHs was achieved by EH based on lead-free Sodium Potassium Niobate (KNN) films [101]. Thus, these lead-free materials present the real potential for PEHs. However, the application of these materials in PEHs is still very little studied and considerable efforts have to be done towards their integration into the conventional processing of piezoelectric materials for MEMS applications.

Therefore, several lead-free piezoelectric materials especially alkaline Niobates and Tantalates, synthesized by sol-gel technique will be studied in this chapter. Lithium Tantalate, Sodium Potassium Niobate and Tantalum doped Sodium Potassium Niobate, of the morphology thin films and fibres are studied for their piezoelectric and energy harvesting Figure of Merit (FoM). The thin films are grown by a novel sol-gel route on steel substrate by spin coating. The protocol of deposition of the films on a stainless-steel substrate was developed by A. Verma, Ph.D. student of Prof. Sanjay Mathur group, UoC, under the collaboration within the ITN ENHANCE framework.

2.8 Piezoresponse Force Microcopy (PFM)

Advances in atomic force microscopy (AFM) techniques and their ability to probe matter with the nanometric lateral resolution have allowed the electromechanical phenomena at the nano-micro scale to be explored with precision. Piezoresponse Force Microscopy (PFM) has emerged as a powerful tool to study electromechanical properties, the switching mechanism of ferroelectric domains, and the piezoresponse in low-dimensional materials in recent years [46], [102]–[105]. The schematic of the PFM setup (Bruker, ICON 2018 [106]) is shown in Figure 2.5.

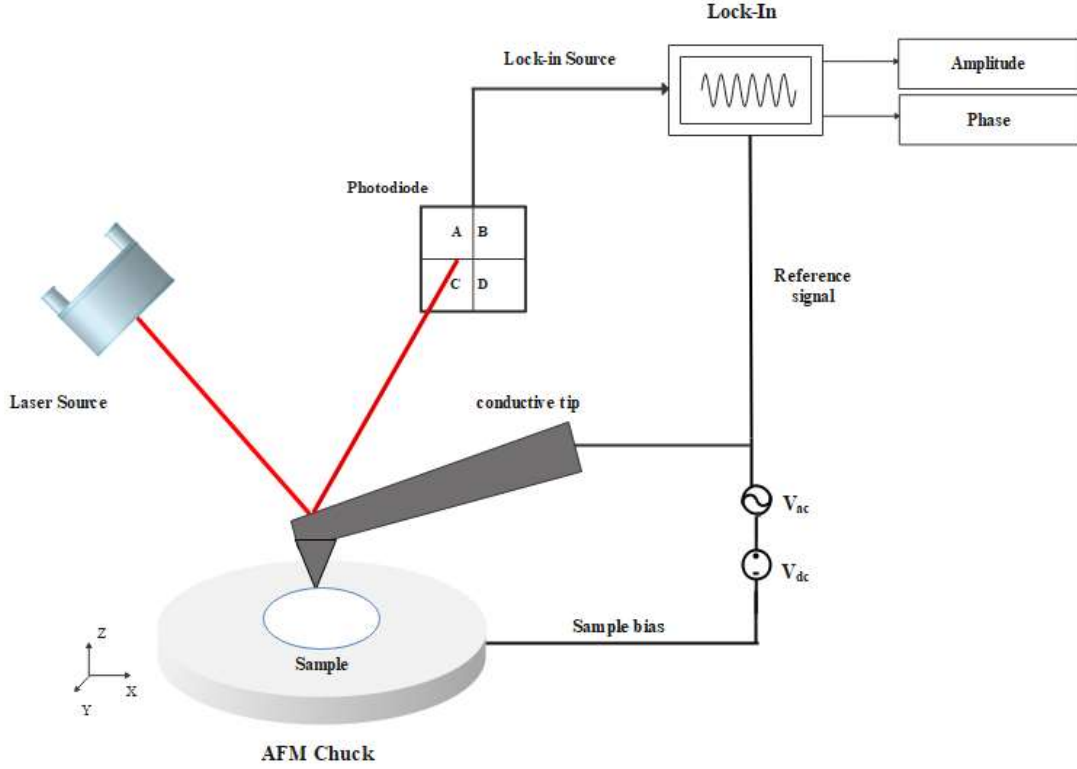


Figure 2.5: Schematic illustration of PFM setup

The PFM technique is based on the contact-mode Scanning Probe Microscopy (SPM), where the SPM is equipped with a function generator, a lock-in amplifier, and a cantilever that is conductive as shown in Figure 2.5. In the PFM technique, a conductive AFM tip act as a top electrode, while the other side of the sample is connected electrically to the conductive chuck that is grounded and acts as the bottom electrode. The piezoresponse of the sample is obtained by applying a voltage (AC) to the tip:

$$V_{tip}(t) = V_{dc} + V_{ac}\cos(\omega t) \quad 2.5$$

The applied voltage (V_{tip}) results in a displacement of the sample and thereby deflection of the cantilever d , under contact with the sample as given below:

$$d = d_0 + A_m \cos(\omega t + \Phi) \quad 2.6$$

Where, A_m is the amplitude of the piezoelectric response (in photodetector voltage V) and Φ defines the phase-shift, generated by the ferroelectric domain located under the tip. The ferroelectric domains under the tip could involve several domains in different directions (in-plane

or a-domains, out of plane or c- domains or both) contributing to the overall phase (Figure 2.6a). Lateral and vertical displacements are created by in-plane and the out of plane responses from the sample respectively. Amplitude and phase are therefore demodulated from the piezoresponse data by the Lock-in Amplifier (LiA). PFM can therefore measure both out-of-plane and in-plane components of the piezoresponse, often also referred to as Vertical PFM (VPFM) and Lateral PFM (LPFM). VPFM indicates the vertical movements of the laser position on the Position Sensitive Photodetector (PSD), associated with the out of plane movement of the sample (buckling of the cantilever) as shown in Figure 2.6 b, c, while LPFM indicates the in-plane motion of the sample (lateral deflections) of the laser, linked to the lateral shear of the cantilever.

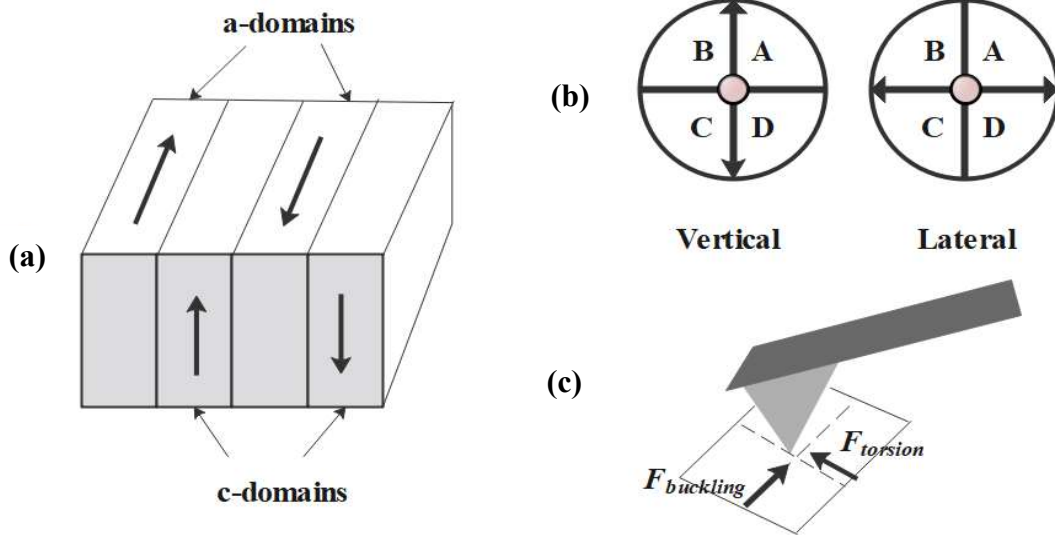


Figure 2.6: (a) schematic illustration of the a and c-domains in a ferroelectric (b) possible movement of the laser spot on the photodetector (c) possible movements of the cantilever due to a force developed by the interaction of various domains with the applied AC voltage resulting in the torsional and buckling forces

Therefore, a quantitative measure of the piezoelectric coefficient d_{33} is possible by calculating the PR amplitude A , out of cantilever resonance frequency, given the electric field produced by the applied voltage V_{tip} is homogeneous in the z-direction as given below [101]:

$$A = \alpha \cdot d_{33} \cdot V_{ac} \quad 2.7$$

Table 2.1 List of parameters and units

Parameter	Description	Units
A	Piezoresponse amplitude	V
V_{tip}	Applied tip voltage	V
α	Cantilever inverse deflection sensitivity	V/m
d_{33}	Piezoelectric coefficient	m/V
f_{CR}	Cantilever resonance frequency	Hz

where α is the calibration factor determined from the lock-in amplifier and the optical deflection sensitivity of the cantilever. The effective d_{33} coefficient is measured via VPFM, and d_{15} is measured by LPFM.

2.8.1 Choice of AFM tip and operating frequency

In PFM technique, a conductive AFM tip acts as a top electrode. A relatively high stiffness tip (>1 N/m) is chosen to reduce the effect of electrostatics interference between tip and sample [105]. In this thesis conductive platinum-coated Si tip (SCMPIT-V2 from Bruker) (Details in APPENDIX I) with a stiffness (~ 3 N/m) is chosen for the PFM experiments. The cantilever resonant frequency of SCMPIT-V2 is 75 kHz. In the standard PFM technique, the operation frequency f of the excitation voltage V_{ac} is typically in the 10–100 kHz range [105]. This ensures that f is away from the contact resonance frequency f_{CR} of the cantilever-sample system generally (>100 kHz). The piezoresponse is nearly independent of the applied AC frequency, which is confirmed by performing the measurements at different frequencies of 50 kHz and below, (in Appendix 4) on reference sample (PPLN, Bruker). An operating frequency of 50 kHz is chosen throughout this characterization work for this reason. An applied AC voltage (1 V peak) is used to scan the domains, wherever not specified.

2.8.2 Calibration of vertical deflection sensitivity

Quantitative determination of the vertical and lateral displacements in PFM is a continuing challenge due to the inherent complexity of the contact electromechanics of piezoelectric materials with an AFM tip. Therefore, the proper calibration of the sensitivity of the cantilever is important. The calibration parameter vertical deflection sensitivity α depends on the inverse Optical Lever Sensitivity (inv-OLS), and the LiA gain, G ($=1$ in this study case), as:

$$\alpha = inv - OLS. \frac{1}{G} \quad 2.8$$

The inv-OLS relates the photodetector voltage (in V) to the vertical deflection of the cantilever (in pm) and is determined from the contact mode force curve against a hard sapphire substrate (to ensure there is no deformation), a calibration sample from Bruker, before the measurement of d_{33} .

2.8.3 Measuring d_{ij} coefficients

The piezoelectric coefficient d_{33} is measured by measuring the slope of the VPFM piezoresponse amplitude A (in pm) as function of applied driving AC bias (V_{ac}) in contact mode as equation 2.7. The slope gives the value of d_{33} that is measured in picometre per volt.

$$d_{33} = \frac{A_m}{\alpha V_{ac}} \quad 2.9$$

Where $\frac{A_m}{\alpha}$ is piezoresponse in pm.

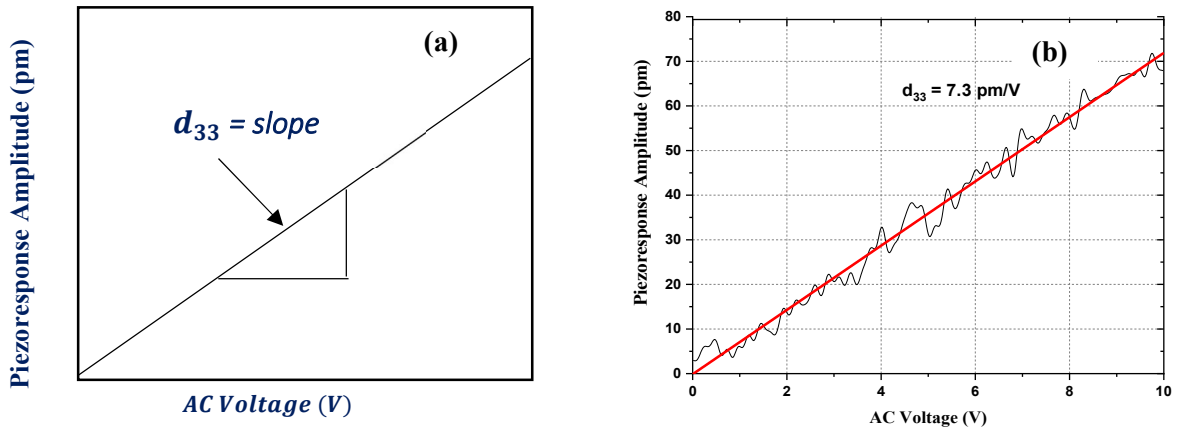


Figure 2.7: (a) Piezoresponse amplitude vs applied AC voltage (slope = d_{33}) (b) estimation of d_{33} in PPLN reference sample.

So, based on equations 2.8 and **Error! Reference source not found.**, the piezoelectric coefficient d_{33} can be extracted from this slope value if the vertical inverse deflection sensitivity α is known as shown in Figure 2.7b. Before each PR measurement, the d_{33} values are checked and calibrated against a known reference sample (Periodically Poled Lithium Niobate-PPLN, Bruker, $d_{33} = 7.3 \text{ pm/V}$) [107] as shown in Figure 2.7 (b).

2.9 PFM Characterization of Lithium Tantalate samples

In this chapter, the PFM characterization of Lithium Tantalate films grown by spin-coating of sol-gel with different thicknesses is discussed. This section of the chapter has been published in [108].

2.9.1 On the interest of Lithium Tantalate

Curie temperature T_c is one of the most critical parameters for piezoelectric materials as above T_c , material lose its ferroelectric property. Lithium tantalate (LiTaO_3)-(LT) is a perovskite with a high curie temperature (650 °C) that can be used at elevated temperature for electromechanical energy harvesting, for instance, in high-temperature acoustic transducer [109]. Given its wide transparency range (400-500 nm), LiTaO_3 has found its applications in photonic devices [110]. Further, single crystal LT is also widely used for the generation of surface acoustic waves and filters for RF applications. Despite its promising properties and lead-free composition, the use of LiTaO_3 remains elusive mainly due to its lower piezoelectric coefficient coefficients ($d_{33}=21$ pm/V, $d_{15}=26$ pm/V) [18], [111], when compared to other lead-free alternatives such as potassium sodium niobate (KNN) ($d_{33}=80$ pm/V) [112]. However, LiTaO_3 is a potential contender for lead-free PEHs for high temperature applications as they have high T_c compared to other lead-free alternatives such as KNN ($T_c = 400$ °C) [113]. LT-PEHs can be used to power low-powered devices such as watches, microphones, sensors and high temperature transducers. In this context, it is interesting to study the local electromechanical properties of LiTaO_3 grown by sol-gel techniques by PFM, for possible applications in PEHs.

2.9.2 LT samples and topography

The LiTaO_3 piezoelectric cantilevers are fabricated by sputtering of Ti (20 nm) and Au (100 nm) as electrical top contacts over the LiTaO_3 deposited by spin coating of the precursor sol using a shadow mask. The stainless-steel substrates serve also as the bottom electrodes. The specimen size of the piezoelectric cantilever was $16 \times 1.6 \text{ mm}^2$ area and the electrode area was $10 \times 1.5 \text{ mm}^2$. In this study the LT films of various thickness, deposited by sol-gel technique on steel substrate are studied for their d_{33} and energy harvesting Figure of Merit (FoM). The samples are named LT2, LT4, and LT6 to denote the increasing thickness of LiTaO_3 films with the numbers denoting the number of spin coating steps. The SEM images (top and cross-sectional views) of the LT2, LT4, and LT6 cantilevers are shown in Figure 2.8, indicating the thickness of the samples. From the

AFM topography Figure 2.9, their average roughness is measured to be 19, 21, 26 nm for LT (2, 4, and 6 respectively). Details are given in Table 3.1.

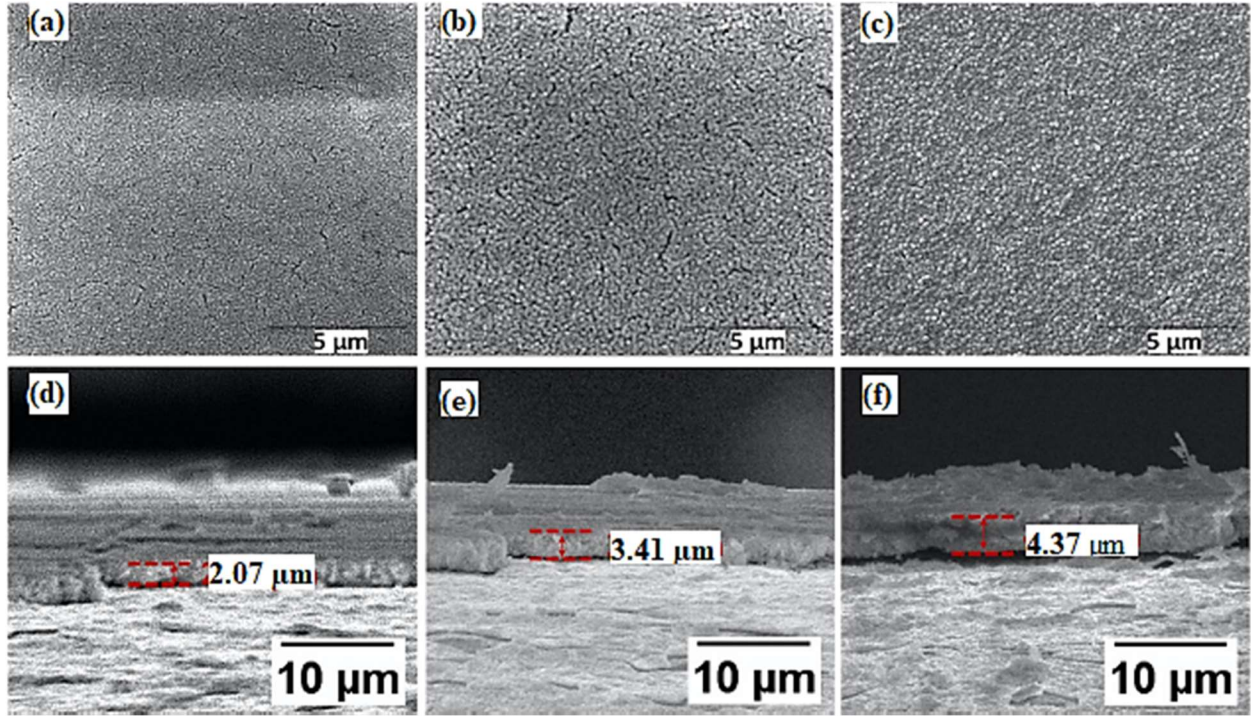


Figure 2.8: (a, b, c) scanning electron micrograph (SEM) top view of LiTaO_3 thick films (d, e, f) cross-sectional SEM confirming uniform deposition of thick films of the thickness [108].

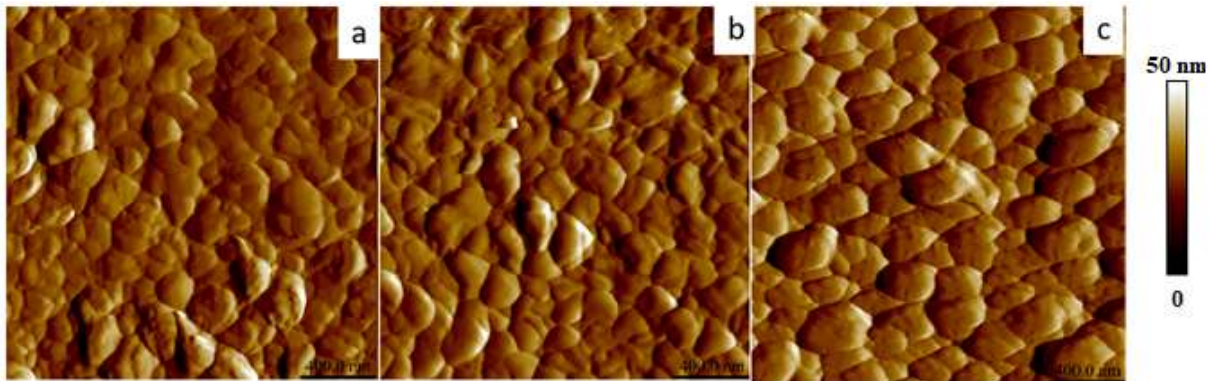


Figure 2.9: AFM contact mode topography image of (a) LT2, (b) LT4 and (c) LT6 (scan size: $2\ \mu\text{m} \times 2\ \mu\text{m}$)

2.9.3 Domain polarization of LT samples

The polycrystalline material has randomly oriented grains or crystallites and has no net domain polarization, however, after the application of high electric field or poling, the material gains a

polarizing effect as in Figure 2.10. Figure 2.10, presents a typical piezoresponse (PR) phase and amplitude change in the LiTaO_3 samples recorded with respect to the increase in film thickness by VPFM and LPFM on an area of $2 \times 2 \mu\text{m}^2$ before and after polarization at 20 V with AFM tip at a scan rate of 512 Hz. The PFM amplitude signal indicates the sample displacement, and the PFM phase signal provides information about the polarization vector of individual domains. The appearance of bright or dark regions in the phase image indicates a contrast in the direction of the polarization vector in the LT samples (Figure 2.10 b, d, f).

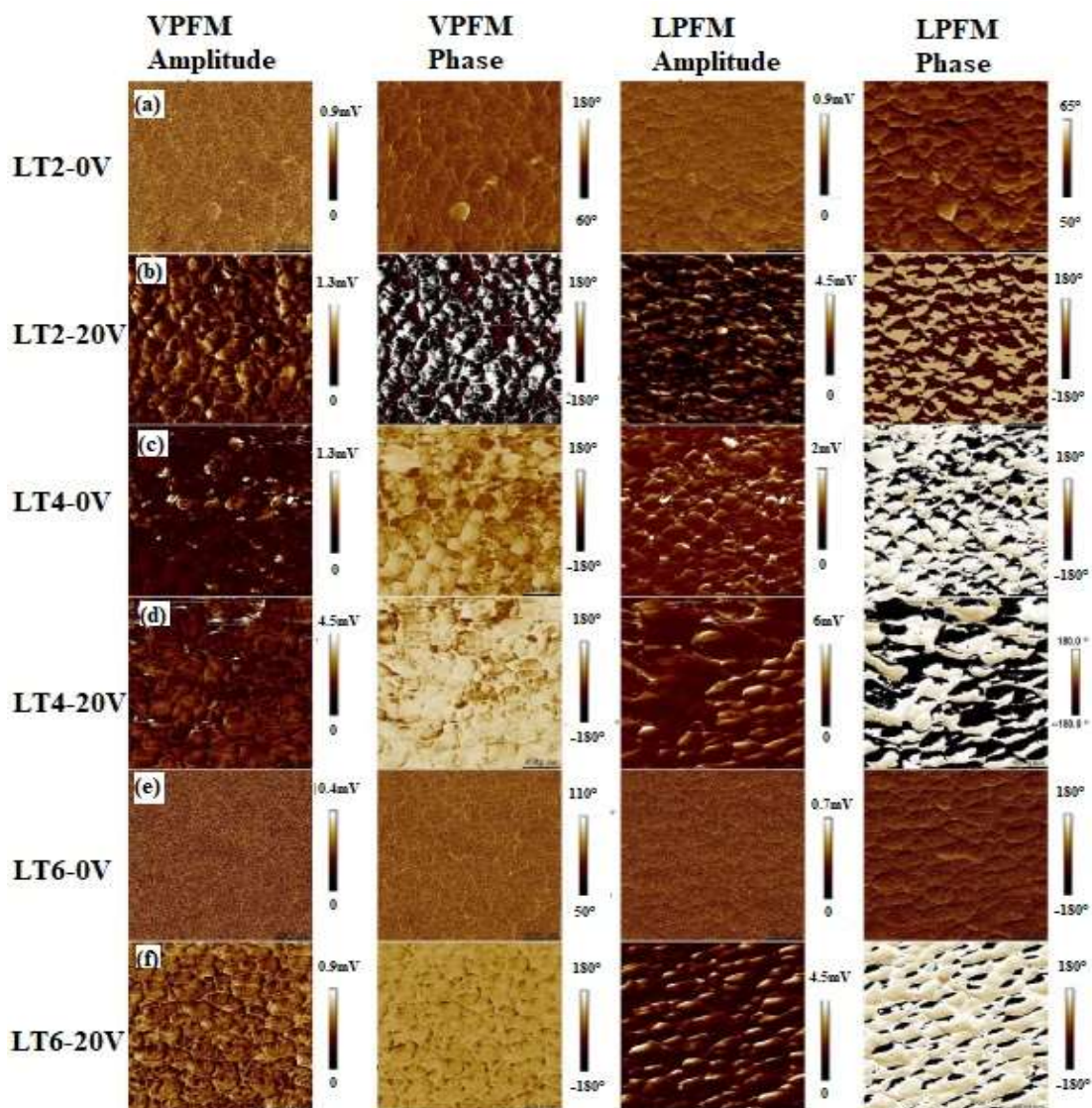


Figure 2.10: VPFM and LPFM phase and amplitude images of LiTaO_3 cantilever surface (lateral scale $2 \times 2 \mu\text{m}^2$) after different polarization voltages (a) LT-2 at 0 V; (b) LT-2 at $V_{\text{DC}}=20$ V; (c) LT4 at $V_{\text{DC}}=0$ V (d) LT4 at $V_{\text{DC}}=20$ V; (e) LT6 at $V_{\text{DC}}=0$ V, and (f) LT6 at $V_{\text{DC}}=20$ V

The applied voltage of 20 V corresponds to Electric field of 4 kV/mm, which is greater than the switching coercive field E_c . However, a voltage above E_c have to be maintained for a longer time to achieve complete poling of the material. Maintaining a high electric field across the AFM tip for longer time is having limitation since it could result in heating and thereby damage the conductive coating. There was no clear contrast present in the VPFM phase before polarization for the LT films as shown in Figure 2.10 a, c, e, which indicated that the out-of-plane domains in the film are largely homogeneous across the entire film possessing early similar domain orientation. The contrast observed at lateral phase mapping in Figure 2.10 c indicated an arbitrary in-plane domain distribution in the case of LT4 possibly due to an in-plane strain or the surface charge induced polarization. Further, the spontaneous polarization in the domains was observed by the application of constant DC-bias of 20 V across LT thin films by the AFM tip as shown in Figure 2.10 b, d, f, showing a clear modulation in phase between the adjacent domains as analyzed from the dark and bright regions in the LPFM and VPFM phase signals. The higher contrast in VPFM and LPFM images in the 20 V poled sample, compared to the unpoled samples is also due to the resulting internal stress that is generated in the sample due to poling. The local internal stress could induce additional internal fields inside the material [114]. It was observed that many domains consisted of several grains and some of the grains showed multi-domain structure as well. The piezoelectric properties are supposedly enhanced in the multidomain state in comparison with the single-domain state due to the strong orientation dependence as well as the extrinsic contribution from the domain wall motions that are absent in single-domain crystals [115]. The dynamic out-of-plane and in-plane piezo-responses due to the spontaneous polarization of the corresponding domains of the LT film upon 20 V bias, as presented in Figure 2.10 b, d, f, also showcase their good ferroelectric and piezoelectric performances. Remarkably, the analysis of LPFM and VPFM images at 20 V showed that the in-plane enhancement was higher when compared to the out-of-plane polarization indicating that the response was originated from the polarization of lateral domains aligned perpendicular to the applied electric field. The PFM results confirmed that the LT film possesses strong spontaneous polarization, and the polarization switching can be induced at a certain applied voltage. The variations of the PR amplitudes of unpoled LT films and 20 V poled LT films with the DC bias voltage ramped in two directions, exhibit typical “butterfly” loops that are observed in ferroelectric materials. This confirmed the remarkable local microscopic ferroelectric characteristic of the films as shown in Figure 2.11 a, c, e. Further, the ferroelectric

domain switching behavior in the LiTaO₃ cantilevers was observed from the well-saturated hysteresis loop (Figure 2.11 b, d, f) indicating a 180° phase-switching of local domains under the AFM tip. Figure 2.11, shows the hysteresis and butterfly curve of LiTaO₃ before and after 20 V poling for 20 minutes. Figure 2.11 a, c, and d, shows the phase vs electric field strength and Figure 2.11 b, d, and f represent the typical butterfly curve showing the amplitude under the AFM tip that is in contact (tip-on process) with the LiTaO₃ surface. It should be noted that due to the dissimilar switching mechanisms among the microscopic PFM and macroscopic P-E measurement, the observed coercive voltage E_c obtained from the PR hysteresis loop is generally smaller than that from the P-E loop as reported for the bulk phase [105].

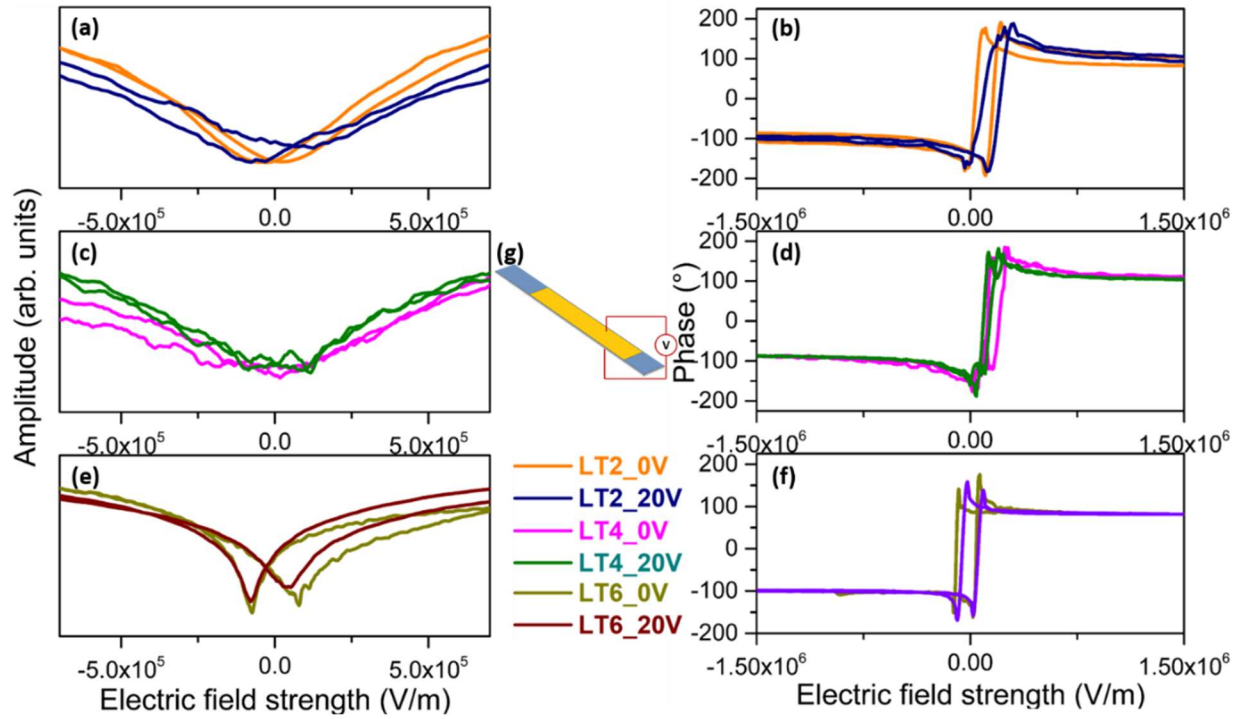


Figure 2.11: Local ferroelectric domain switching behavior in LiTaO₃ cantilevers: (a, c, e) Butterfly (strain vs field) curve, (b, d, and f) the local hysteresis loop showing 180° switching of domains at 0 and 20 V polarization for cantilevers LT 2, 4 and 6 respectively [108].

The converse piezoelectric coefficient (d_{33}) is recognized as an important figure of merit (FoM) for electromechanical applications, such as energy harvesters. The d_{33} coefficient was measured from the slope of PR amplitude (A) vs driving AC bias (V_{ac}) according to the equation as discussed in section 3.14:

Using equation **Error! Reference source not found.**, the piezoelectric coefficients d_{33} for the samples LT (2, 4, and 6) were estimated to be 23.23, 21.99, and 24.07 pm/V respectively, which were measured at 6 different points of the sample and averaged over an area of 18 x18 mm². These coefficient values match well with the values reported in the literature for polycrystalline LiTaO₃ films [109], [116] as shown in Table 3.1.

Table 2.1 summary of the electromechanical properties of the Lithium Tantalate samples

Samples	Sample name	Size	Extracted d_{33} (unpoled) (pm/V)	Reported d_{33} (pm/V)	Reference	Dielectric permittivity ϵ_{33}^T	FOM ($\frac{d_{33}^2}{\epsilon_{33}^T}$) ($10^{-18} \text{m}^2/\text{V}^2$)
S060-S062	LT2	2 μm	23	13	[111]	163	3.2
	LT4	3.4 μm	22		[112]	362	1.3
	LT6	4.3 μm	24			479	1.2

2.10 PFM study of Sodium Potassium Niobate (KNN) thin films

In this section the PFM study of single phase KNN films grown by a novel sol-gel route on steel substrate by spin coating (1680 rpm) is discussed. The samples have a thickness (7 μm) as deposited on a stainless-steel substrate.

2.10.1 Introduction

(Na-K)NbO₃ ceramics- KNN have recently received a lot of attention as suitable candidates for lead-free ferroelectrics materials due to the high d_{33} (>400 pm/V) and relatively Curie temperatures (> 400° C) [96], [101]. The Piezoelectric Thin Films (PTFs) of lead-free materials such as KNN are increasing in popularity due to their increasing applications in sensors and actuators [117], [118], energy, [119]–[121] etc. The PTFs are generally polycrystalline and have domains arranged in different orientations. Polycrystalline PTFs may be brought into a polar state by poling process, where a large electric field 10–100 kV/cm is applied across the film, usually three times the coercive field E_c of the material at elevated temperatures less than the Curie temperature T_c [122]. Poling will not orient grains but can reorient domains within individual grains in the direction of the applied electric field. However, localized piezoelectric characteristics local inhomogeneity, and non-linearities in nanoscale properties such as piezoelectric coefficient (d_{33}) of the KNN based PTFs are poorly understood. To fully understand the piezoelectric properties at the nano/micro-

scale, detailed nanoscale characterization of the structure and piezoelectric properties is needed, including probing of nanodomain switching and estimation of local piezoelectric coefficients after poling. Earlier studies on the nonlinearity of PZT suggested that the nonlinearity is an effect of domain wall motions, and their contribution to the piezoelectric property throws light on improvement for various applications of PTF [123]. PFM permits the mapping of the domains along with the piezoelectric properties of PTFs with a resolution of a few nanometers. Further, this allows the local poling and imaging of domains with the application of an external electric field which can be used to determine the ferroelectric properties of a sample. A proper understanding of the origin and the variation in determining the piezoelectric constant after poling is important. The effect of free surfaces and size on ferroelectricity has been the focus of several theoretical studies [124]. The profound and direct impact of these side effects of local domains and their response to the external fields helps to design and engineer the next generation of KNN-PTF based devices. In contradiction to the temperature-independent MPB in PZT systems, KNN-based ceramics is considered to have the drawback of the high sensitivity of the piezoresponse to temperature [125]. Nevertheless, only a few works reported the poling temperature-dependence of piezoelectric coefficient d_{33} of KNN-based ceramics [126]. Therefore, it is necessary to carefully evaluate the temperature-dependent localized effect of poling piezoelectricity of KNN-based ceramics.

2.10.2 KNN cantilever dimensions and topography

The KNN piezoelectric cantilevers are fabricated by sputtering of Ti (20 nm) and Au (100 nm) as electrical top contacts over the KNN films (grown by sol-gel technique) using a shadow mask, whereas stainless steel substrates (Fe/ Cr15/ Ni 7/Mo 2.25) served as the bottom electrodes. The specimen size of the piezoelectric cantilever was $16 \times 1.6 \text{ mm}^2$ area and the electrode area was $10 \times 1.5 \text{ mm}^2$. The bottom metal substrate was naturally used as a bottom electrode during the PFM study. The SEM and AFM topography images of the KNN films exhibited smooth and uniform morphology (Figure 2.12 a, b). Average surface roughness, was measured using the PFM topography image (Gwyddion Analysis [127]) and found to be 26 nm over a scanned length of 10 μm (Fig. 3.8d), showing the smooth surface of the film.

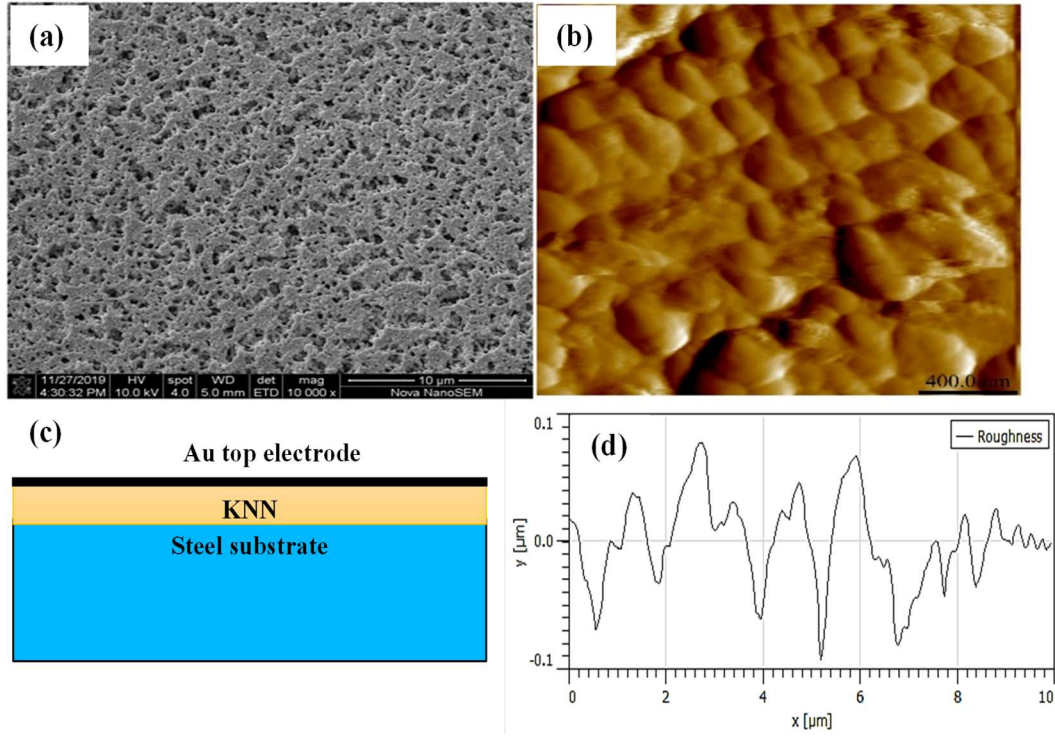


Figure 2.12: (a) SEM image of the KNN film (b) AFM topography image (c) cross-sectional schematic of the cantilever sample (d) roughness profile of the AFM topography.

2.10.3 Piezoresponse characterization of KNN films by PFM

The KNN films grown by the sol-gel techniques are polycrystalline with randomly oriented grains and domains have therefore do not possess net domain polarization. However, after the application of a high electric field or poling, the material gains a polarizing effect. Figure 2.13 a-d, presents piezoresponse (PR) phase and amplitude change in the KNN samples recorded before polarization by VPFM and LPFM on an area of $2 \times 2 \mu\text{m}^2$. Figure 2.13 e-h represents the VPFM and LPFM images of the KNN samples after polarization at 20 V by the AFM tip. The PFM amplitude signal indicates the sample displacement, and the PFM phase signal provides information about the polarization vector of individual domains.

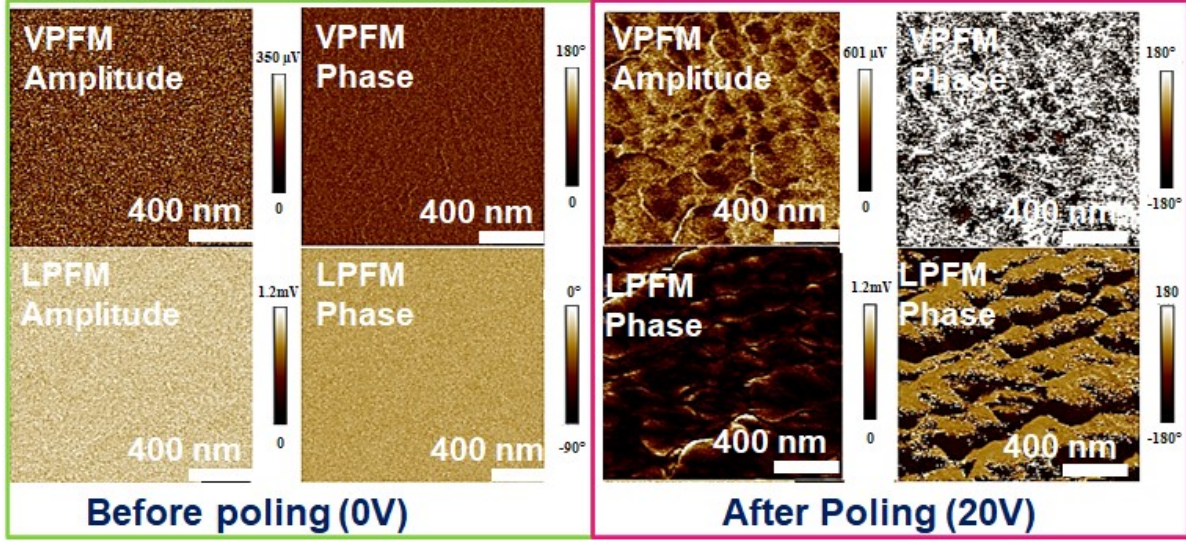


Figure 2.13: VPFM and LPFM phase and amplitude images of KNN cantilever surface (scale $2 \times 2 \mu\text{m}^2$) before and after poling at 20V.

There was no clear contrast present in the VPFM and LPFM phase before polarization for KNN film as shown in Figure 2.13 b, d which indicated that the in-plane and out-of-plane domains in the film are largely homogeneous across the entire film possessing early similar domain orientation. However, the spontaneous polarization in the domains was observed in LPFM and VPFM by the application of constant DC-bias of 20 V ($\sim 3 \text{ kV/mm}$) across KNN thin films by the AFM tip as shown in Figure 2.13 f, h showing a clear modulation in phase between the adjacent domains as analyzed from the dark and bright regions, suggest their ferroelectric switching properties. The LPFM and VPFM result indicate that the in-plane enhancement was higher when compared to the out-of-plane polarization indicating that the response was originated from the polarization of lateral domains aligned perpendicular to the applied electric field. The PFM results confirmed that the KNN film possesses strong spontaneous polarization, and the polarization switching can be induced at a certain applied voltage.

The variations of the PR amplitudes of unpoled KNN film and 20V poled KNN film with the DC bias voltage ramped in two directions, exhibit a well-saturated hysteresis loop (Figure 2.14 b) indicating a 180° phase-switching of local domains under the AFM tip. Figure 2.14 b, c, d, shows the hysteresis and butterfly curve of KNN before and after 20 V polarization by AFM for 20 minutes. Figure 2.14 c, d represents the typical butterfly curve showing the amplitude under the AFM tip that is in contact (Tip- on process) with the sample.

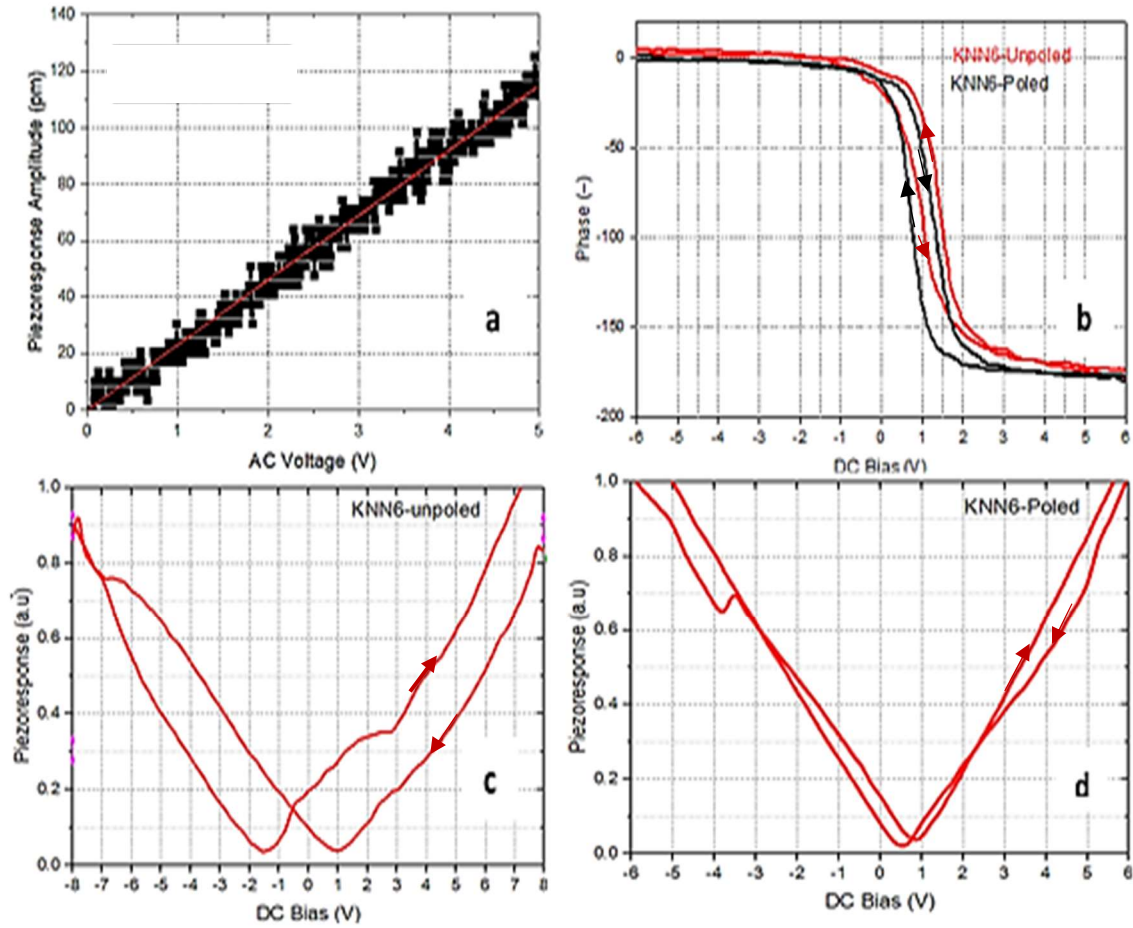


Figure 2.14: (a) PR Amplitude vs applied AC voltage (b) Hysteresis loop at 0V and 20 V (c) Butterfly-loop at 0V (d) Butterfly loop after 20 V polarization of KNN film (KNN6)

The d_{33} coefficient is measured from the slope of PR amplitude (A) vs driving AC bias (V_{tip}) according to the method as discussed in section 3.14. The piezoelectric coefficients for the KNN cantilever measured at 6 different points over an area of $18 \times 18 \text{ mm}^2$ of the sample were estimated to be 23-24 pm/V. There was no significant effect of poling by the AFM tip on the d_{33} values of these films.

Table 2.2 Piezoelectric properties of KNN thin film sample

Sample	Sample name	Thickness	Extracted d_{33} (pm/V)	Reported d_{33} (pm/V)	Reference	Dielectric permittivity ϵ_{33}^T	FOM ($\frac{d_{33}^2}{\epsilon_{33}}$) ($10^{-18} \text{ m}^2/\text{V}^2$)
KNN thin film	S049	7 μm	23	18,83(films)	[124],[126]	466	1.1

This could be due to the requirement of need for a higher poling field (7 kV/mm), compared to the applied field via the AFM tip which is limited to ~ 3 kV/mm (corresponding to 20 V DC tip voltage), to retain the polarization. [128] The d_{33} value is decent among lead-free materials for energy harvesting application. However, the d_{33} is lower than the state-of-the-art values reported in the literature for polycrystalline KNN films.

2.11 External Poling of KNN PTF

At present, irrespective of the fabrication technique, the reported piezoelectric strain coefficients (i.e., d_{33}) for various KNN-based PTFs fall in the range of 40–61 pm/V [129]. These values are significantly inferior compared to bulk KNN-based materials. PTFs exhibit much higher coercive fields (typically up to 3–10 kV mm⁻¹) and higher breakdown voltages (20–40 kVmm⁻¹) [130]. Wu et al. studied phase transitions and electrical behavior in 300-nm (K_{0.5}Na_{0.5})NbO₃ thin film deposited on the SrRuO₃-buffered (100) SrTiO₃ substrate by RF magnetron sputtering. The phase transition temperatures orthogonal to tetragonal (T-o-t = 120 °C) and Curie temperature ($T_c = 310^\circ$ C) in films were shown to be lower than those in the bulk ($T_c = 420^\circ$ C) [96]. It is therefore possible to drive thin film actuators with higher poling fields (E_p) to pole without breakdown. Depolarization occurs when the applied field (E_p) is greater than the coercive field (E_c) or when the temperature is above Curie temperature (T_c). Theoretically, a poled polycrystalline PTF has only monodomain grains with each grain pointing vertically to the PTF film plane. Practically, it is very difficult to achieve this because in polycrystalline PTFs the majority of grains possess an unfavorable crystallographic orientation, and, thus, the orientation of the domains after poling cannot strictly be normal to the substrate plane. The AFM tip-based poling of the PTFs has limitations due to the limitation with the applied voltage between tip and sample. Therefore, it is interesting to study the effect of poling by an external field on the localized piezoresponse of the KNN PTFs. The samples poled by an external field at elevated temperature are explained in the following section, and the local effects of poling are studied by PFM, which could help to improve the performance of KNN based devices.

2.11.1 Poling process:

The KNN sample of thickness 7 μ m is deposited on a steel substrate (bottom electrode). Au layer was sputtered as the top electrode. The sample is placed on the probe station with a hot plate with

adjustable temperature control as shown in Figure 2.15. A DC voltage source (Keithley 236 electrometer) is used between the two electrodes of the sample for poling.

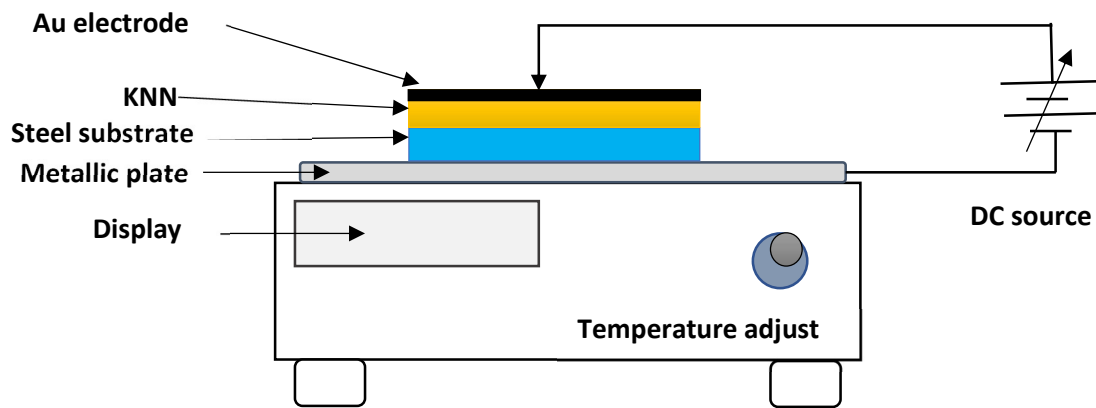


Figure 2.15: Illustration of poling setup of KNN film with probe station with hot plate.

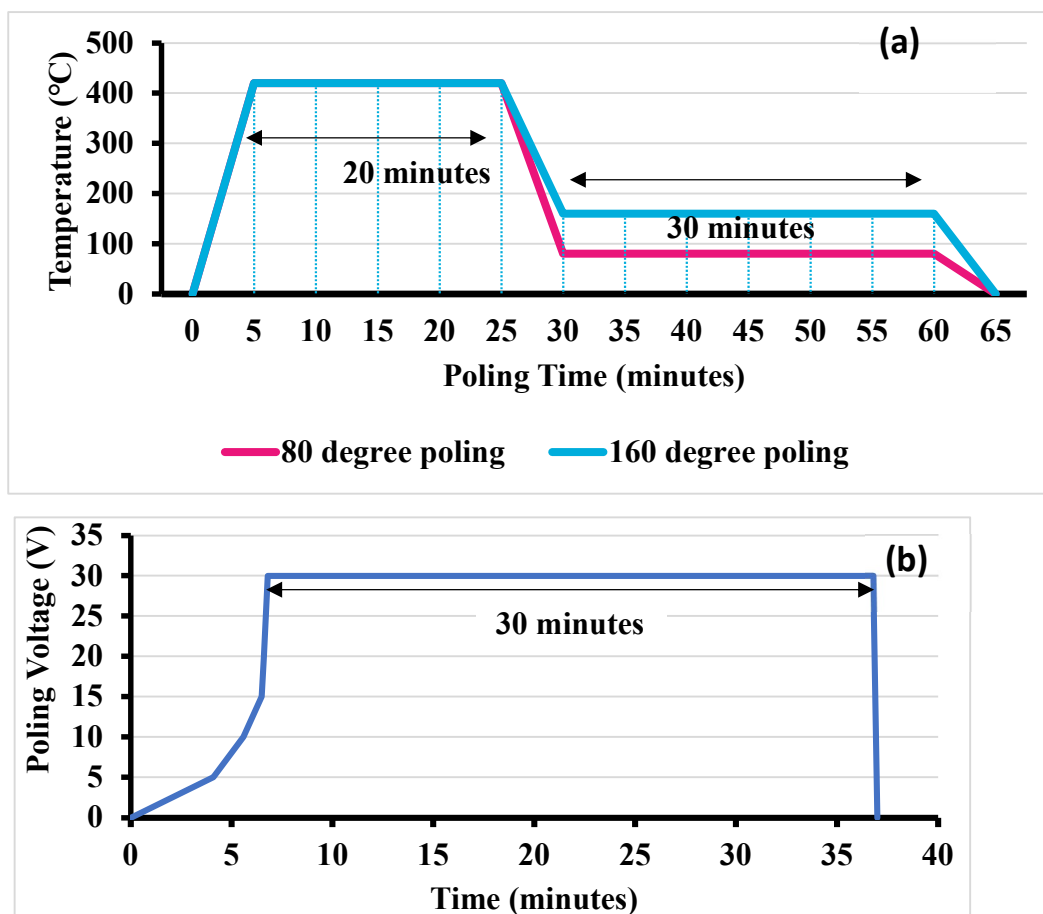


Figure 2.16: (a) Poling Temperature vs Time and (b) Poling Voltage (V) vs Time (minute)

Before each poling measurement, the KNN film sample is depolarized completely by heating at 420 °C for 20 minutes. The sample is cooled down to the required temperature and is maintained (80 °C or 160 °C) while applying the DC bias of 30 V (4.2 kV/mm). KNN-80P refers to the KNN sample poled at 80 °C and KNN-160P refers to the KNN sample poled at 160 °C. A Compliance of 1 mA is set to the voltage source to detect any breakdown of the sample and limit the applied bias in this case. The applied field was ramped slowly in steps. At the beginning at approx. rate of 20 mV/s till 5 V, 0.06 V/s till 5 V-10 V, 0.1 V/s till 10 V-15 V and then to 1 V/s for 15-30 V as shown in 2.16b. A voltage of 30 V is maintained for 30 minutes to complete the poling process as shown in 2.16 b.

2.11.2 PFM study of the poled KNN PTF

2.11.2.1 Topography studies

Two typical domain configurations and lamellae zig-zag structure in 90° domains (Figure 2.17) and a wavy herringbone in 180° domains (Figure 2.18) where the coupling is head-to-head (or tail to tail) was observed by the AFM 3D topography images as shown in Figure 2.18. 90° domains are aligned in the plane antiparallel direction with the applied field, whereas 180° domains are aligned out of plane in the direction of applied field. The grain size in lamellar 90° domains stripes is found to be close to 200 nm. Similar complex domain patterns consisting of typical lamellar ferroelectric, with small domain width with irregular shapes, even nanodomains domains are reported in the literature [131]. Such domain sites generally possess ultralow domain wall energy, which is expected at these small domain sites because the domain wall energy is proportional to the square of domain width. Nevertheless, a close look at the topography image shows the existence of a few zig-zag-shaped 90° domain walls [125] indicating a distance of 100 nm between two walls as shown in Figure 2.17. This result is also in agreement with a previous study of the 90° domains of orthorhombic (Li, K, Na)NbO₃ ceramics [132].

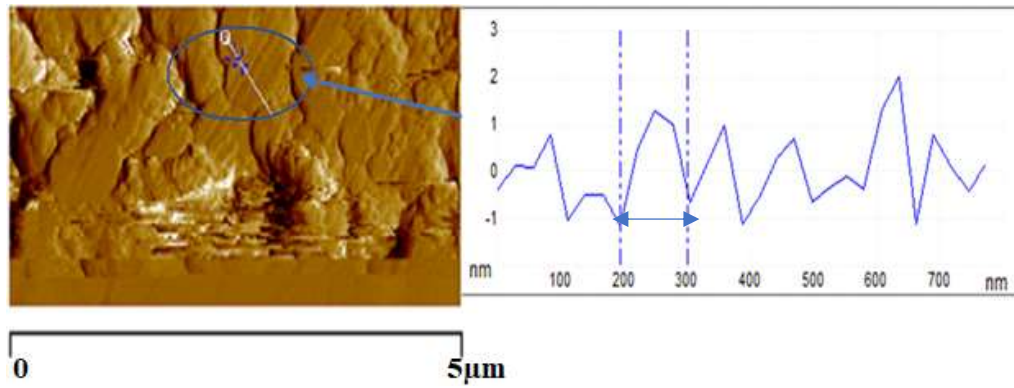


Figure 2.17: Domain patterns in KNN-80P films with cut line view of topography on the right

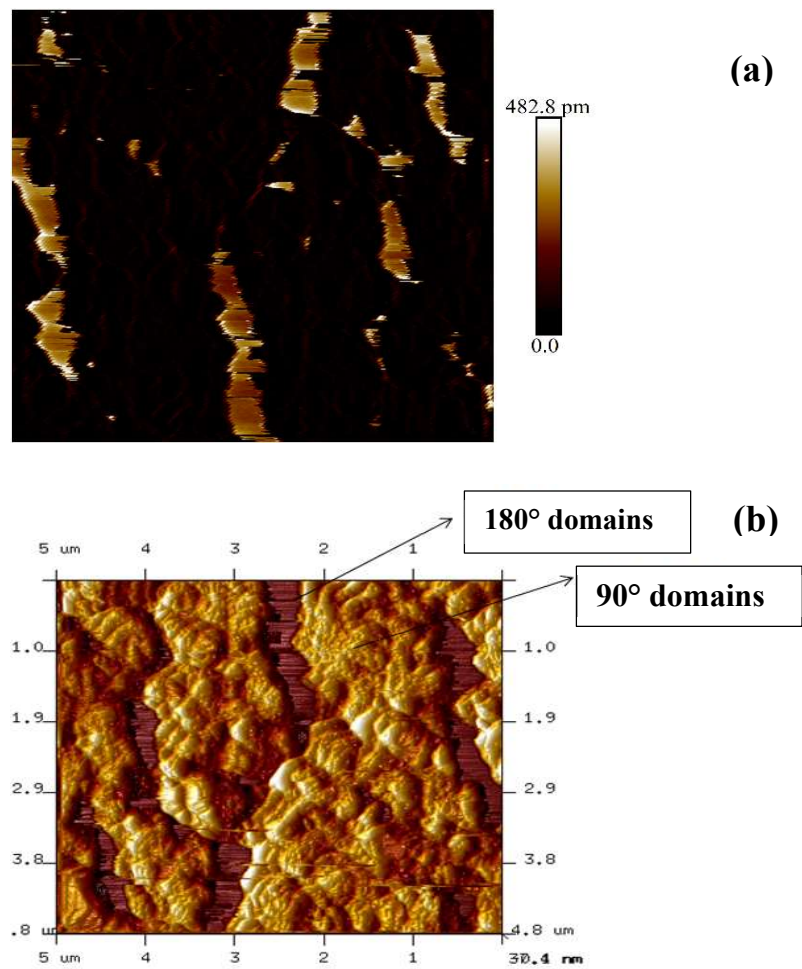


Figure 2.18: (a) PFM amplitude and (b) 3D topography of the $5\mu\text{m} \times 5\mu\text{m}$ scanned surface after poling at 160°C (KNN-160P)

2.11.2.2 PFM Analysis of domains after poling

The domain structure and switching phenomena in KNN-PTF were studied by the piezoresponse (PR) of the films as demonstrated in Figure 2.19. For PFM measurements, an AC electric field is applied with a 2 V peak at a frequency of 50 kHz. Figure 2.19 displays the PR image of the film which contains both the PR amplitude Figure 2.19 (a, c) and phase response Figure 2.19 (b, d) of the films on the probed area. The PR image of the film primarily consists of a matrix largely covered with a range of values, mostly corresponding to 180° or 90° domains with a polarization direction perpendicular to the electrode and left to right in the plane of the electrode respectively.

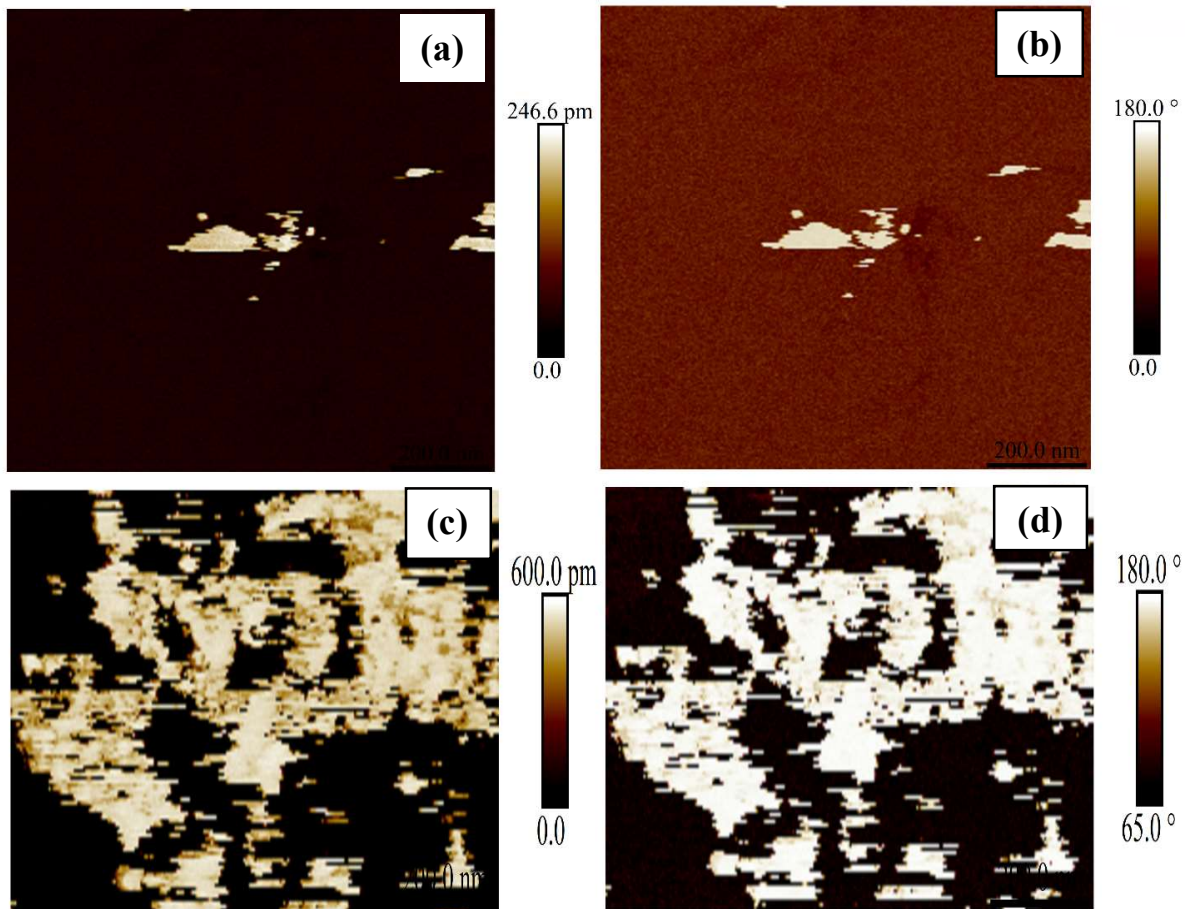


Figure 2.19: (a) PR amplitude (b) Phase of KNN PTF poled at 80°C (KNN-80P) (c) PR Amplitude (d) Phase of KNN poled at 160°C (KNN-160P) (scan size: $1\ \mu\text{m} \times 1\ \mu\text{m}$)

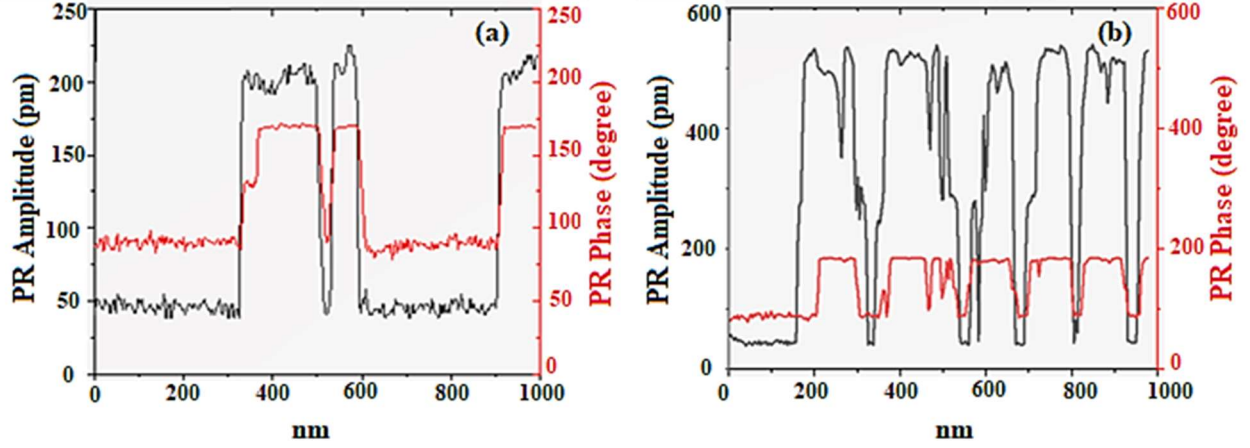


Figure 2.20: (a) The PR amplitude and Phase profile of the sample across $1\mu\text{m}$ width: KNN-80 P and (b) KNN-160 P respectively

Note that the phase angle (degree), which can be linked to the poling degree, reaches close to the highest ideal possible value of 90° and 180° that can be obtained on complete poling. This is supposed to be due to the poling process that induces switching which can induce the distortion of adjacent domains. The angles between two polarization vectors for KNN can be 90° and 180° as in a tetragonal system or 60° and 120° for orthorhombic crystals [125]. By poling, we increase the polarization degree. Thus, the domain switching creates lattice distortion and internal stress, impeding further domain switching and domains become balanced and the poling process reaches a saturation, although the phase angle is not accurately 90° or 180° [133]. The bright domains in the PR image indicates the 180° domains, and the dark region mostly correspond to the 90° domains respectively as shown in Figure 2.19. The cut line view of the PR shown in Figure 2.20 clearly shows simultaneously the PR amplitude and phase across the two domain regions with a phase difference of 90° across the two domains. The PR amplitude and therefore the d_{33} in KNN-80 P and KNN-160P shows significant variation across 90° and 180° domains. Note that the ratio of the PR Amplitude to the applied AC bias (2 V) should give the average d_{33} across the sample. It is observed that along the 90° domains the PR amplitude and the $d_{33} \sim 23 \text{ pm/V}$ remains relatively unchanged before and after the poling at both the poling temperatures (80°C and 160°C respectively).

However, it can be noted that along the 180° domain region the PR amplitude and therefore the d_{33} shows a significant enhancement with poling temperature. The enhancement can be attributed to the formation of smaller domains or nanodomains [134] of average size $\sim 100 \text{ nm}$ as in Figure

2.17, which is supposed to have improved d_{33} values compared to the larger domains. The domain morphology also plays an important role in determining the piezoelectric and ferroelectric responses. The reduction of domain dimensions (domain thickness d_t) in PZT material can be attributed to the decrease in the domain wall energy coefficient (W_d), following the classical theory [134], [135]:

$$d_t \propto W_d^{1/2} \quad 2.10$$

The reduced domain wall energy thus enables the enhanced PR amplitude of the 180° domains, which are relatively smaller in size (nano-domains) to external excitations, such as electrical or mechanical fields as discussed in the following section. The average d_{33} values across 180° domains show a significant enhancement in poling which can be estimated to be around 100 pm/V and ~260 pm/V at KNN-80P and KNN-160P respectively (Figure 2.19, Figure 2.20). The average d_{33} of 27 pm/V for KNN-80P and 106 pm/V for KNN-160 P was estimated for the $1 \mu\text{m} \times 1 \mu\text{m}$ scan area in the PTF. Thus, the formation of 180° domains after HT poling possibly leads to an increase in the overall average macroscopic d_{33} of the KNN PTF as shown in Figure 2.20.

Table 2.3 Poling conditions and piezoelectric coefficient (d_{33})

Sample	Poling Temperature	Poling Voltage	d ₃₃ - 90° domain		d ₃₃ -180° domain		Average d ₃₃
			d ₃₃	(%)	d ₃₃	%	
KNN	0 °C	30 V	23 pm/V	100	-	0	23 pm/V
thin film	80 °C	30 V	23 pm/ V	85	100 pm/V	15	27 pm/V
(S049)	160 °C	30 V	23 pm/V	22	260 pm/V	78	106 pm/V

The origin of the formation of mutual occurrence of 180° and 90° domains in the PTF after poling can be explained by the presence of nonstoichiometric defects in these crystals generated after poling process that led to anomalous local electromechanical properties across these domains. Further, as a result, a single domain state is unstable because of the high elastic energy that is associated with 90° domains leading to the formation of 180° domains. Wang et al [136] proposed a mechanism of aging and re-poling induced enhancement of piezoelectricity after re-poling in KNN ceramics which could explain the origin of the 180° and 90° domains after poling. Because of inevitable volatilization of the alkali species during heating A site (VA') and Oxygen vacancies inside KNN (ABO₃ perovskite structure) [137], are formed during high-temperature annealing,

leading to an aging-assisted switching of the tetragonal 90° domains. The aging process could be accelerated at elevated temperatures, especially above T_c . It should be noted that the T_c and phase transition temperatures of the KNN thin film, namely those from orthorhombic to tetragonal phase and then from tetragonal to cubic phase, are lower than those in the bulk ceramic counterpart. Domain switching does not change the crystalline structure of the ceramics, but it does have a striking influence on the macroscopic orientation of the local atom arrangement and vice versa and affect the rotation of domains [138]. The increase in d_{33} measurements as discussed before also offers solid evidence for this assumption, with an increasing d_{33} and decreased E_c for the same sample after the first and second poling, respectively.

2.11.2.3 Polarization switching and non-linearity in piezoresponse

The PR amplitude consists of both intrinsic and extrinsic contributions [139]. The intrinsic contribution, associated with the field-induced lattice distortion (linear effect), is linked with the change in the polarization of the unit cell by polarization extension or polarization rotation. Whereas the extrinsic contribution is largely associated with the domain wall motion (non-linear effect). Domain walls can be categorized as either 180° or non- 180° domain wall types based on the crystallinity of the PTF, such as the 90° domain walls found in tetragonal perovskite ferroelectrics in this case. The extrinsic contribution due to domain wall motion is supposed to be the key factor to the macroscopic piezoelectric properties at room temperature. The below methodology distinguishes between the intrinsic contribution, related to the field-induced lattice distortion, and the extrinsic contributions, related to domain wall motion. In order to determine the effect of varying AC fields on the sample and thereby variation in piezoresponse inside the 180° and 90° domains, the AC bias across the tip was ramped against the PR amplitude and Phase at 6 different locations in the sample as shown in Figure 2.21. Points 1, 2 and 6 corresponds to the 180° domains and the remaining corresponds to the 90° domains.

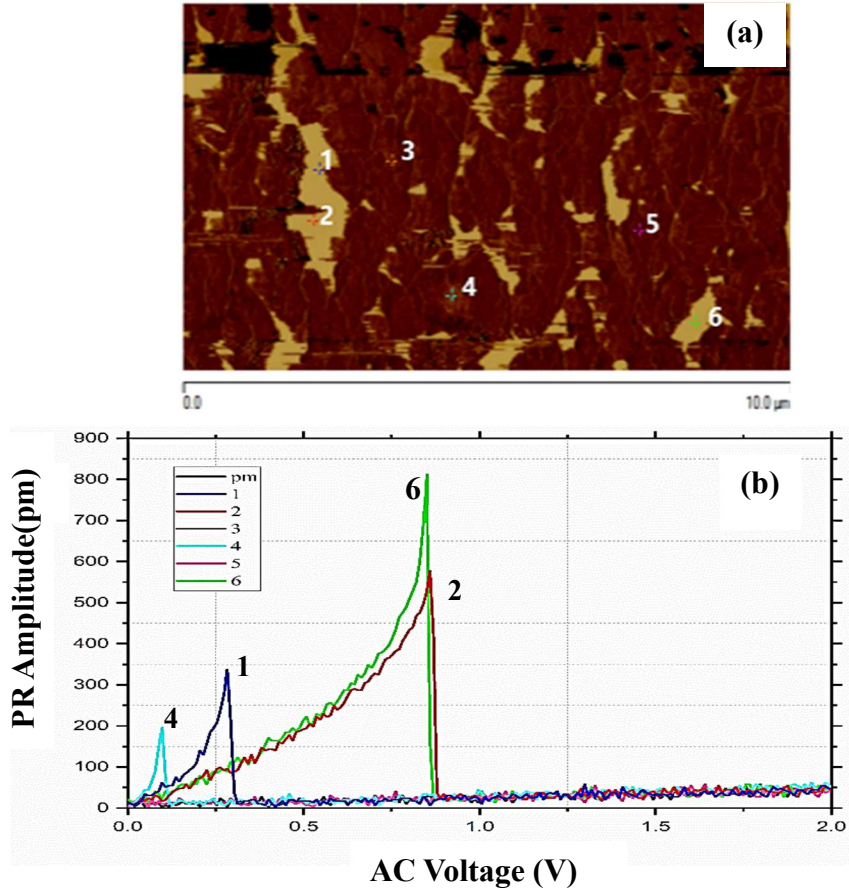


Figure 2.21 (a) Point and shoot locations at 180° domains (1,2,6) and 90° domains (3,4,5) on the KNN 160P sample (b) PR amplitude vs AC bias indicating high non-linearity and non-reversible switching at low E_c for KNN-160P.

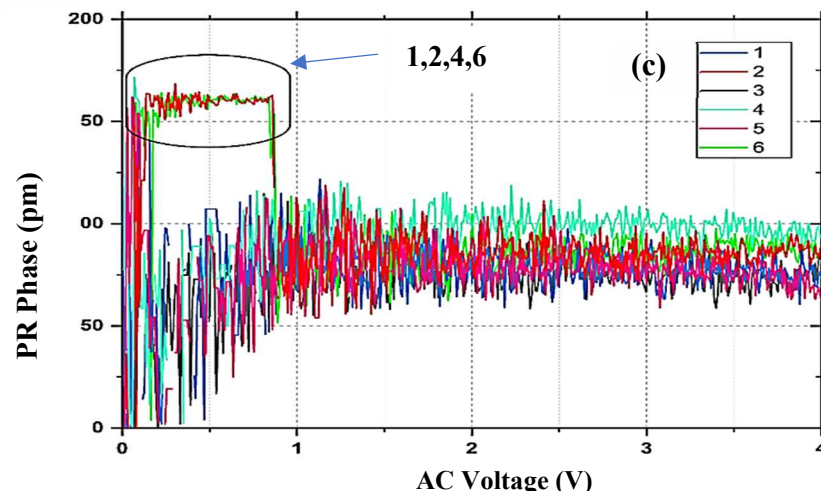


Figure 2.22: PR phase image vs AC bias indicating the switching of domains from 180° to 90° at low E_c for KNN-160P.

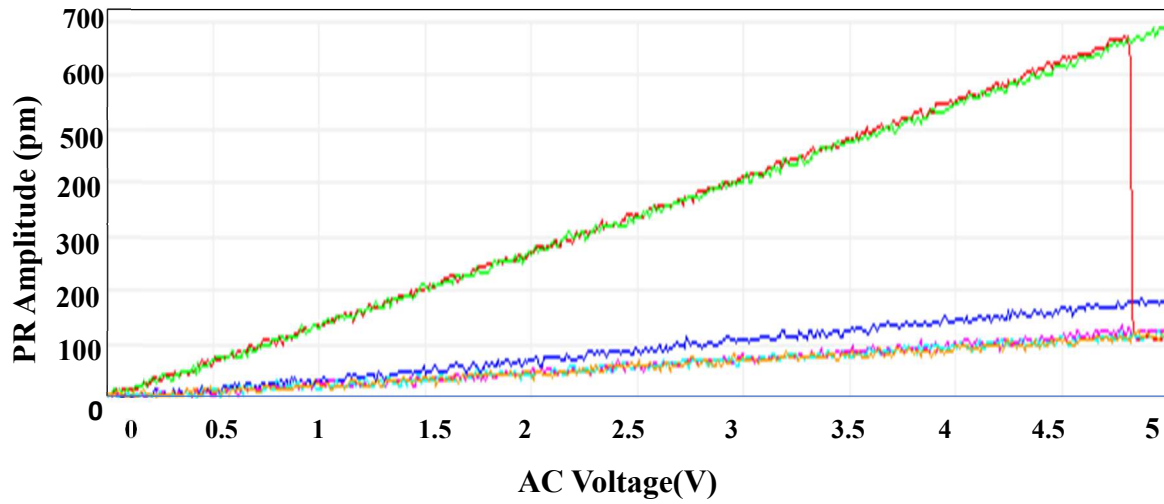


Figure 2.23: PR Amplitude vs Applied AC Voltage for KNN-80P

Figure 2.21 b clearly shows variation in the PR Amplitude and Figure 2.22 shows the variation in PR phase across the two domains (180° and 90°) for KNN-160P. The piezoelectric coefficient d_{33} can be estimated by taking the slope of the PR Amplitude vs Applied AC bias of the sample as in Figure 2.23. The 180° domains in KNN-160P have increased d_{33} on poling compared to the 90° domains (23 pm/V), that do not show any significant increase in d_{33} . KNN-160P show a localized increase in the d_{33} values as shown in Figure 2.21. It should be noted that the 180° domains in KNN-160P shows high non-linearity as shown in Figure 2.21. Nonlinearity in PR amplitude in a ferroelectric ceramic is generated by strain generated by domain wall motion (extrinsic contribution) [136]. Also, the non-reversible switching of 180° domains to 90° domains is observed from the phase image at a low AC coercive field of 0.1 kV/mm as shown in Figure 2.22 suggesting an electric field induced [140] phase transition. The result of this study and similar studies elsewhere suggests that domains can respond to such high frequency as 50 kHz, and their contributions of them are not negligible in the overall performance of a PTF device. The AC coercive switching field can be estimated as low as 0.1 kV/mm in this case. Many models define the polarization switching in piezoelectric materials. Hwang et al. [141][22] proposed the model that is simple and successful at predicting the homogeneous average response of piezoelectric materials. According to this model, the direction of a spontaneous polarization P_s of each grain can change by 90° or 180° by ferroelectric switching or by the nucleation and growth of new

antiparallel domains induced by a sufficiently large electric field (field-induced) that is generated under the tip.

Also, the ferroelastic switching from 180° to 90° might be induced by a sufficiently large stress field (stress-induced) that is pre-existing or generated inside the crystal lattice during the measurement [142]. The polarization switches when the combined electrical and mechanical work exceeds a critical value; that is:

$$\sigma_{ij}\Delta s_{ij} + E_i\Delta P_i \geq 2P_s E_c \quad 2.11$$

where E_c is a coercive electric field, E_i internal field, σ_{ij} is the stress tensor, and Δs_{ij} and ΔP_i are the changes in the spontaneous strain and spontaneous polarization during switching, respectively. It is to be noted that the strain part is very high in the case as seen from, which could result in the requirement of low switching fields for the switching from 180° to 90° to take place leading to low coercive fields (E_c) as observed in the case. Further, the size of the miniaturized domain is easily prone to switching under an applied electric field, and the low degree of polarization anisotropy energy in the multi-phase zone allows easy polarization rotation. The decrease in E_c with a decrease in the domain wall-size w_d can also be partially interpreted by observing the role of domain walls in the nucleation process of new inverse domains that are nucleated during the application of an applied bias, as reported elsewhere [132].

2.11.2.4 Conclusion

In summary, this study has shown that the internal stresses generated during high-temperature poling, due to the thermal gradient and structural transitions in KNN PTFs, influence large variations in properties of the ferroelectric domains, and thus the electromechanical properties such as d_{33} . The PR image of the PTF after the poling consists of 180° or 90° domains with different piezoelectric coefficients. Along with the 90° domains, the $d_{33} \sim 23$ pm/V remains relatively unchanged before and after the poling at both the poling temperatures (80°C and 160°C respectively). However, it can be noted that along the 180°-domain region the PR amplitude and therefore the d_{33} shows a significant enhancement with poling temperature with a final value of 100 pm/V in KNN-80P and ~ 260 pm/V for KNN 160P. There is strong nonlinearity associated with d_{33} in KNN-160P possibly due to domain wall motion. This study could be useful for the understanding and optimization of piezoelectric properties of PTFs for various applications and thereby to improve the performance of PTFs devices.

2.12 PFM study of Sodium Potassium Niobate (KNN) thin films doped with Tantalum

In this section, PFM study of single phase KNN film cantilever doped with 7% tantalum, by a novel sol-gel route on steel substrate by spin coating on stainless steel substrate, is discussed. The KNNT piezoelectric cantilevers are fabricated by sputtering of Ti (20 nm) and Au (100 nm) as electrical top contacts over the KNNT films (grown by sol-gel technique) using a shadow mask, whereas stainless steel substrates (Fe/ Cr15/ Ni 7/Mo 2.25) served as the bottom electrodes. The as deposited KNN samples have a thickness (7 μm) on a stainless-steel substrate.

2.12.1 Introduction

In the case of polycrystalline ceramics, the orientation of the grains is fixed and randomly distributed. Therefore, most grains do not have an available dipole orientation that is perfectly aligned with the applied electric field, and hence the piezoelectricity is limited. The construction of phase coexistence has become the most efficient method of improving piezoelectricity. In order to increase the piezoresponse of the material, the KNN phase transition from the orthorhombic (O) to the tetragonal (T) phase should be close to room temperature. The energy barrier between the two phases is minimum at the phase transition temperature, so the electric-field-induced local phase transition (polarization rotation) can enhance dipole alignment. This is essentially achieved by doping KNN (ABO_3) with the donor atoms at A-site as well as the acceptor on the B-site to influence the dielectric properties as well as figure of merit. Ta has a similar valance, ionic radius, and similar electro-negativity to niobium (Ta, 1.5; Nb, 1.6). These properties make Ta an ideal candidate to act as a B-site substituent in KNN. When Nb^{+5} is replaced in KNN with Ta^{+5} , the density and piezoelectric properties of the doped KNN-ceramic improve.[109], [143] This effect of Ta doping on KNN has been studied in the form of single crystals, ceramics, and thin films. Among these methods, chemical modification is the most frequently used approach to achieve high piezoelectric coefficients. Moreover, Ta-doped KNN material has been tested for different dopant concentrations to obtain superior piezoelectric properties at the Ta-doping concentration of 6-8 %, which is ascribed to a phase transition from monoclinic phase to tetragonal phases at $x > 6$ mol % [144]. However, studies on the comparison of Figures of Merit (FoM) of KNN and Ta-doped KNN for energy harvesting applications remain elusive. The cross-sectional schematic and the SEM image of the KNNT sample are given in Figure 2.24. The average surface roughness of the KNNT films was determined to be 250 nm, indicating the surface being rougher than the KNN films of similar thickness. The increased surface roughness is associated with homogeneously distributed

minor cracks possibly formed due to fast shrinkage and the mismatch of thermal coefficient between the steel substrates and deposited film.

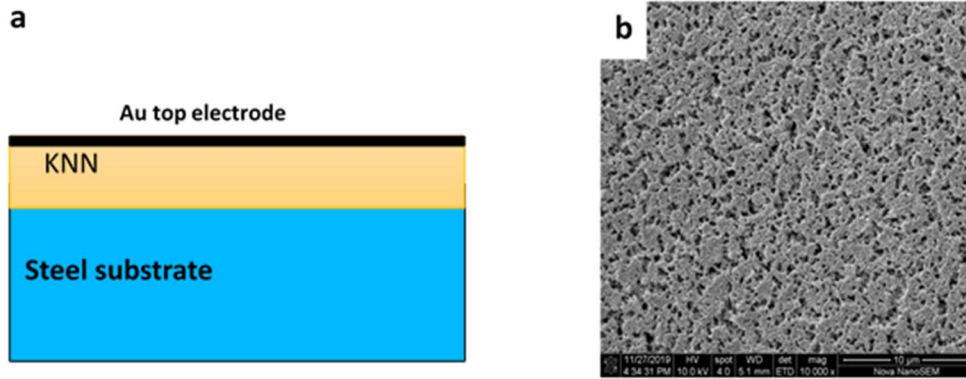


Figure 2.24: (a) cross-sectional schematic (b) SEM image of KNNT before Au deposition.

2.12.2 Piezoresponse characterization of KNNT film by PFM

Figure 2.25a-d presents piezoresponse (PR) phase and amplitude change in the KNN samples recorded before polarization by VPFM and LPFM on an area of $2 \times 2 \mu\text{m}^2$. Figure 2.25 e-h represents the VPFM and LPFM images of the KNNT samples after polarization at 20 V by the AFM tip. The PFM amplitude signal indicates the sample displacement, and the PFM phase signal provides information about the polarization vector of individual domains.

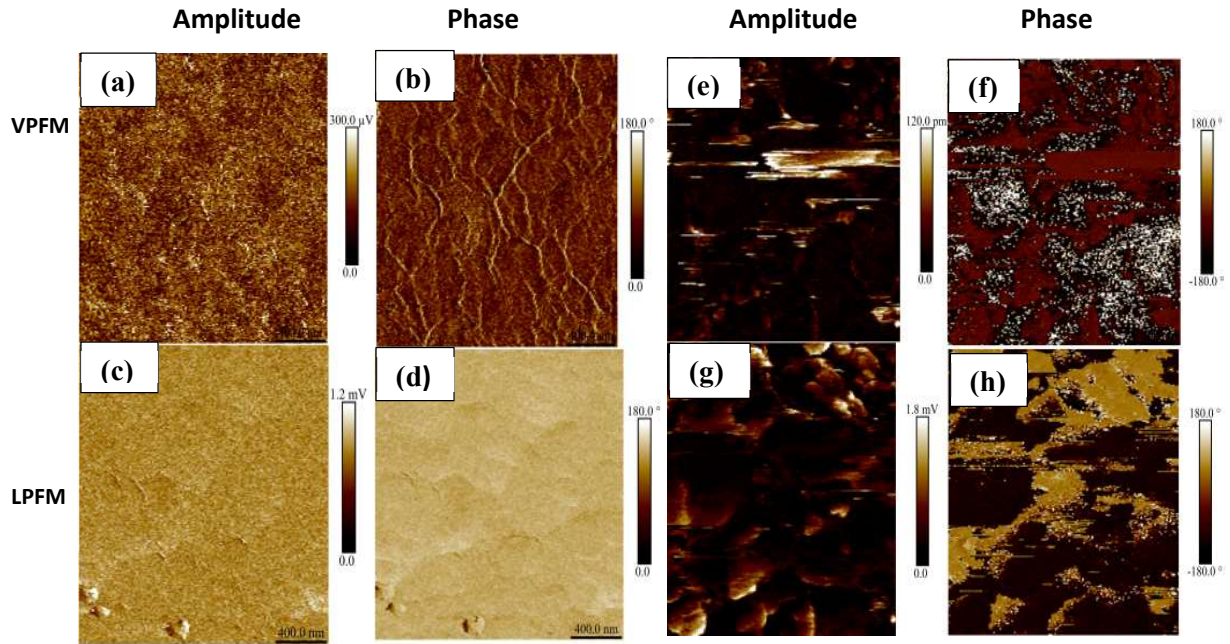


Figure 2.25: Figure 2.20 VPFM and LPFM phase and amplitude images of KNNT cantilever surface (lateral scale $2 \times 2 \mu\text{m}^2$) after different poling voltages: KNNT-VPFM Amplitude at (a) $V_p = 0$ V; (e) at $V_p = 20$ V (b): KNN-VPFM Phase at $V_p = 0$ V, (f) $V_p = 20$ V; LPFM Amplitude at (c) $V_p = 0$ V, (g) $V_p = 20$ V (d) LPFM Phase at $V_p = 0$ V, (h) $V_p = 20$ V

There is no clear contrast present in the VPFM and LPFM phase before polarization for KNNT film as shown in Figure 2.25 which indicates that the in-plane and out-of-plane domains in the film is largely homogeneous across the entire film possessing early similar domain orientation. However, the spontaneous polarization in the domains was observed in LPFM and VPFM after the application of constant DC-bias of 20 V across KNNT thin films by the AFM tip as shown in Figure 2.25 f, h showing a clear modulation in phase between the adjacent domains as analyzed from the dark and bright regions, suggest their ferroelectric switching properties. The LPFM and VPFM results indicate that the in-plane enhancement was higher when compared to the out-of-plane polarization indicating that the response was originated from the polarization of lateral domains aligned perpendicular to the applied electric field. The PFM results confirmed that the KNN film possesses strong spontaneous polarization, and the polarization switching can be induced at a certain applied voltage. The variations of the PR amplitudes of unpoled KNNT film and 20 V poled LT film with the DC bias voltage ramped (-5 V to +5 V) in two directions, exhibit a well-saturated hysteresis loop (Figure 2.26 a, b) with a 180° phase-switching of local domains under the AFM tip. Figure 2.26 c, d represents the typical butterfly curve showing the amplitude under the AFM tip that is in contact (Tip-on process) with the sample.

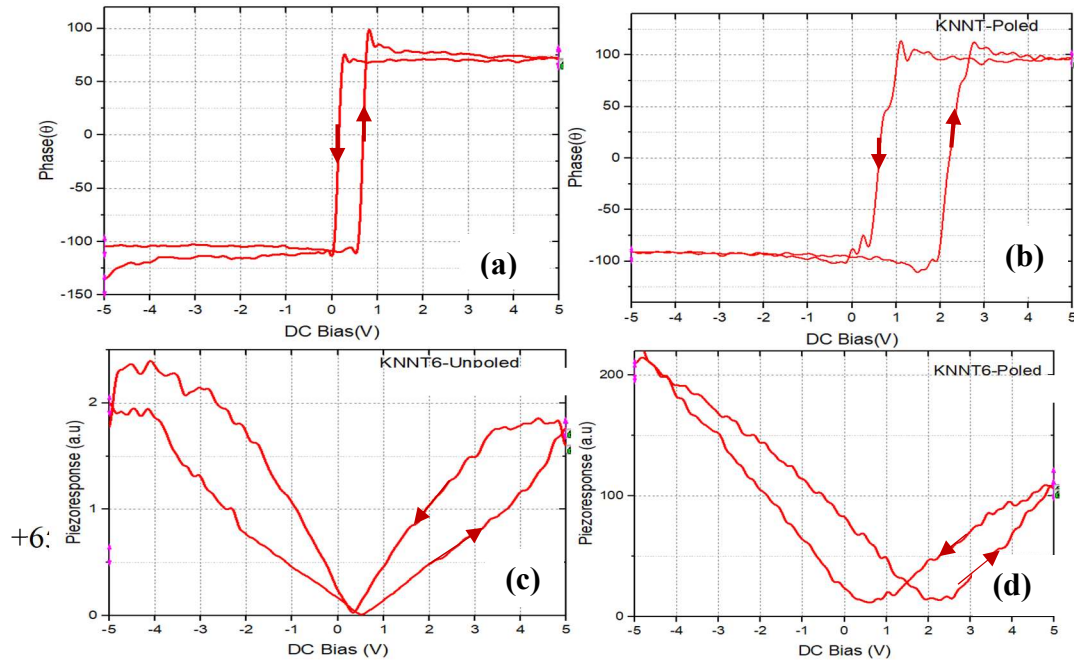


Figure 2.26: Hysteresis loop obtained by ramping DC bias vs PR Phase: at (a) before and (b) after 20 V polarization (c) Butterfly loop (c): before (0 V) (d) after 20 V polarization

The unpoled sample generally possesses smaller domains that may be exposed to several nucleation sites upon the application of the electric field through the tip, providing the possibility for rapid nucleation, thus resulting in a reduction of the overall coercive field. Thus, as a result, when the domain size (W_d) decreases, the shapes of the hysteresis loops tend to be slim and E_c decreases significantly. The wider hysteresis loop ($V_c > 1$ V) of the 20 V poled KNNT compared to the unpoled sample ($V_c < 1$ V) could therefore be an indication of increased domain size after poling. Asymmetric butterfly curves are observed for poled samples in the domains having different shapes and degrees of asymmetry as seen in Figure 2.26 d.

The d_{33} coefficient was measured from the slope of PR amplitude (A_m) vs driving AC bias (V_{up}). The piezoelectric coefficients for the KNNT cantilever were estimated to be 46 pm/V and 221 pm/V before and after polarization at 20 V respectively, which were measured at 6 different points of the sample and averaged over an area of $18 \times 18 \text{ mm}^2$.

Table 2.4 Extracted piezoelectric properties of KNNT film

Sample	Sample name	Size	Extracted d_{33} (pm/V) (virgin/unpoled)	Reported d_{33} (pm/V)	Reference	Dielectric permittivity ϵ_{33}^T	FOM ($\frac{d_{33}^2}{\epsilon_{33}}$) ($10^{-18} \text{ m}^2/\text{V}^2$)
KNNT Films	S054	7 μm	48	60	[145]	397	5.9

These coefficient values match well with the values reported in the literature for polycrystalline KNNT films. The FoM of KNN has improved 3 folds upon the doping with Ta. The spin coating is an industrially scalable method of deposition of thin films. The KNNT films on steel are therefore promising candidate for the fabrication of high-performance lead-free energy harvesting devices at low cost.

2.12.3 Conclusion

In summary, the effect of Tantalum doping on the piezoelectric properties of KNN films was studied. 7% Ta doped KNNT films showed improved the d_{33} of 48 pm/V compared to 23 pm/V in pure undoped KNN films. In addition, the poling of KNNT films at 20 V enhanced the d_{33} significantly from 48 pm/V to 221 pm/V. The KNNT devices outperformed KNN devices due to lower permittivity in the range of 17 %. Furthermore, KNNT devices showed a four-fold higher Figure of Merit (FOM) compared to KNN films, making them a better candidate for PEHs.

2.13 PFM study of Sodium Potassium Niobate (KNN) and KNN-Ta doped (KNNT) fibres

A collaborative effort within the ENHANCE project with Arun Ichangi, Ph.D. student of Prof. Sanjay Mathur Group, University of Cologne; whose individual contributions are as follows:

KNN and KNNT fibre samples are provided by Arun Ichangi, who developed the protocols for depositing single-phase KNN fibers and KNN fibers doped with 10% Ta (referred to as KNNT hereafter) by electrospinning process on a Pt/Si substrate.

2.13.1 Introduction

Potassium sodium niobite (KNN) is an environmentally-friendly bio-compatible piezoelectric ceramic with a piezoelectric coefficient (d_{33}) comparable to lead zirconate titanate (PZT) in transducer [101], [146]. The concept of smart composite materials with integrated fibers for sensing and actuation leads to the increasing interest in the study of piezoelectric ceramic fibers [65]. The doping of the KNN (with Ta) [147] leads to the enhancement of the dielectric and piezoelectric properties [144]. This is due to Ta acting as an ideal candidate for B-site substituent in KNN due to the closeness to valance, ionic radius, and similar electro-negativity to niobium (Ta, 1.5; Nb, 1.6) [144]. The fibers are a promising material for sensing due to higher electromechanical coupling coefficient K_p , and higher flexibility compared to ceramic counterparts [88], [148]. The so-called 1-3 composites can be used for sonar, hydrophones, energy harvesting systems or medical diagnostic applications [121]. The piezoelectric transformer (PT) technology [47] is a viable alternative to magnetic transformers in various applications, e.g., power supplies that employ PT rather than the classical magnetic transformers, resulting in smaller-sized power supplies with better self-cooling. A significant enhancement in the piezoelectric response of KNN ceramics through phase boundary engineering was reported by incorporating Li, Ta and Sb to form solid-solutions [147]. However, efforts to enhance the piezoelectric response by doping at B-site in the perovskite unit cell structure, which is widely explored in bulk ceramics and thin films, remain unexplored in case of fibres.

In this study, KNN and KNN-Ta doped (KNNT) nanofibers prepared through electrospinning technique, of high aspect ratio, with a diameter between 300 nm and 500 nm, were evaluated. Their electromechanical properties, such as piezoelectric coefficient (d_{33}), polarization evolution (P-E) loop and strain evolution (S-E) loop are also extracted.

2.13.2 Experimental setup and procedure

The schematic illustrating the study of the electromechanical properties of the KNN and KNT fiber is shown in Figure 2.27 a. An AC voltage at 50 kHz (or also DC voltage during poling) is applied radially to the fiber between the AFM tip and the bottom Pt/Si electrode that is electrically connected to the AFM chuck with silver based glue.

2.13.3 Topography of KNN fibers

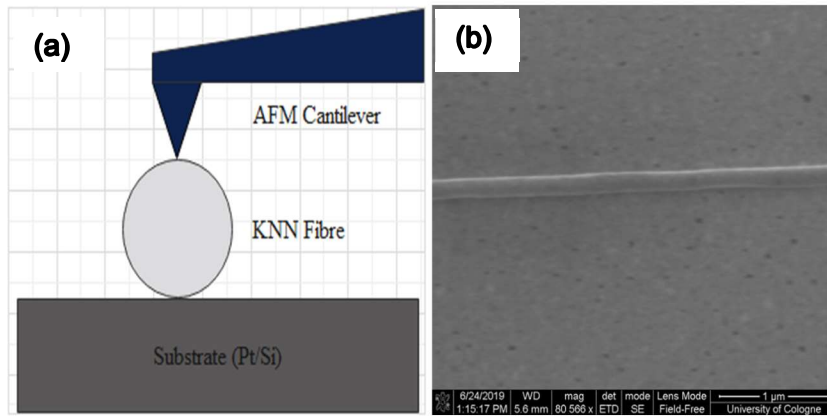


Figure 2.27: (a) Schematic view of the PFM experiment of fibre (b) SEM topography image of KNN micro-fibre.

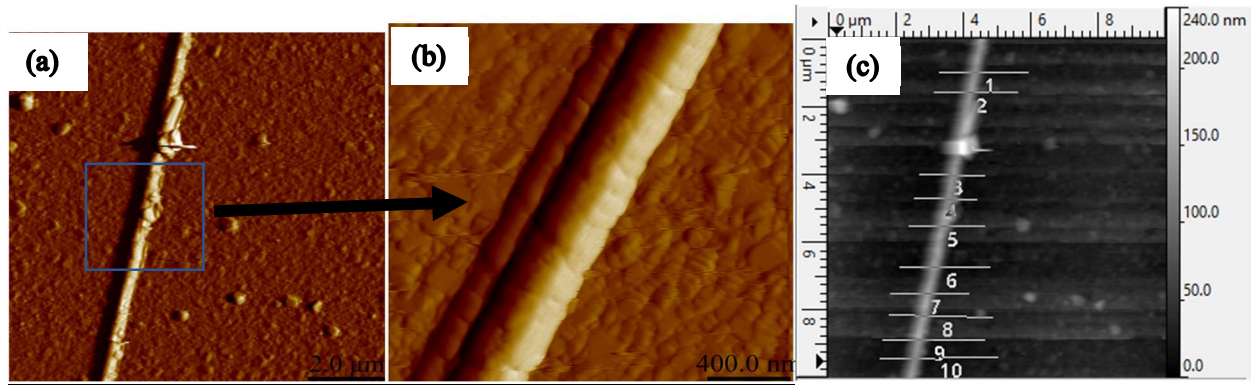


Figure 2.28: (a) AFM contact mode topographic image (10 µm X 10 µm) (b) Zoomed image (2 µm x 2 µm) (c) Cut-Line profile for diameter extraction (Tip details: see Annex 2)

From AFM and SEM topography images the diameter of the nearly cylindrical fibre is roughly estimated to be 600 nm. The diameter was obtained by the averages of the profiles of 10 horizontal cut-lines as shown in Figure 2.28 c.

2.13.4 PFM study of the KNN fibres before poling

In order to understand the domains from a microstructure point of view for the piezoelectric performance, the domain structure measurement was performed by PFM. PFM can be used to visualize the in-plane and out of plane response of ferroelectric domains to the applied AC bias in the lateral direction (LPFM) and vertical direction (VPFM) since the piezoelectric response depends on the polarization magnitude and direction. An AC drive voltage of 1 V peak at 50 kHz frequency was applied to the tip (SCM-PIT V2) at a scan rate of 1 Hz and the sample was grounded to obtain the amplitude and phase response from the domains

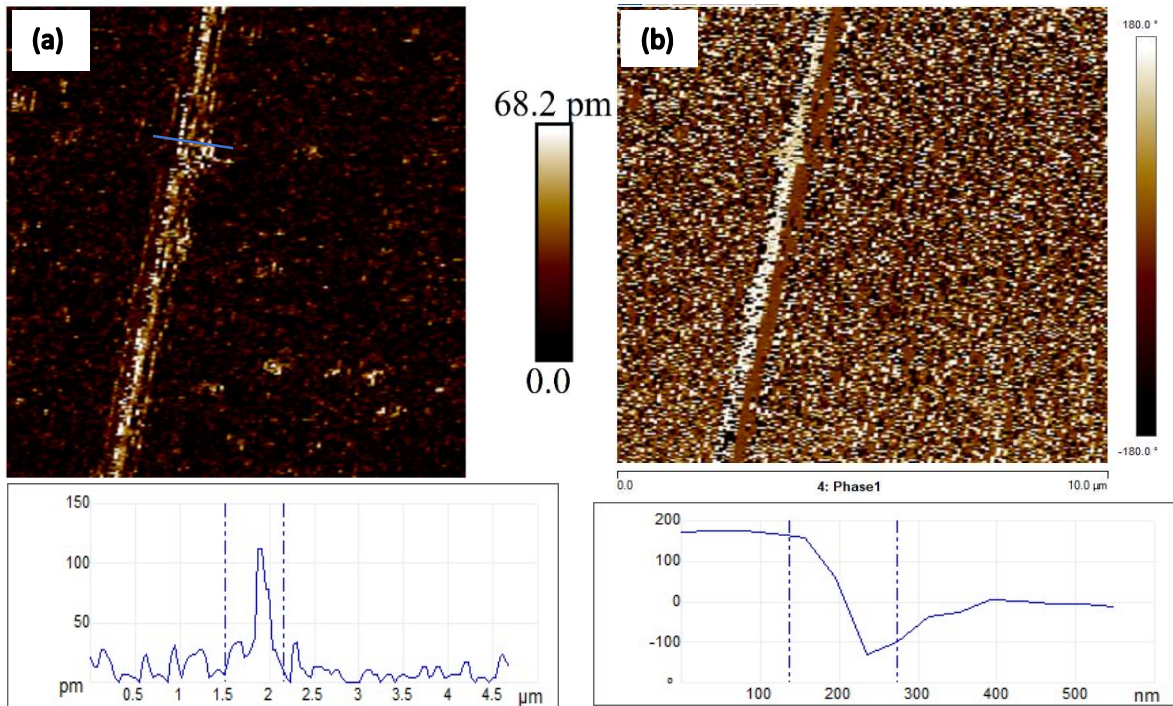


Figure 2.29: comparison of (a) piezoresponse amplitude and (b) Phase responses of KNN fibers.

PFM images (amplitude and phase) of the KNN fibres are shown in Figure 2.29 (a) and (b), where two regular domains are observed in the fibre along the radius as seen from the phase response. A high piezoresponse is observed in the middle of the fibre as evident from the cut-line view in the amplitude image. A 180° phase contrast between the domains (cut-line view) indicates the directions of the out-of-plane (OP) polarization components for the middle and side domains are opposite. The local ferroelectric switching responses give a comprehensive analysis of collective domain switching behavior.

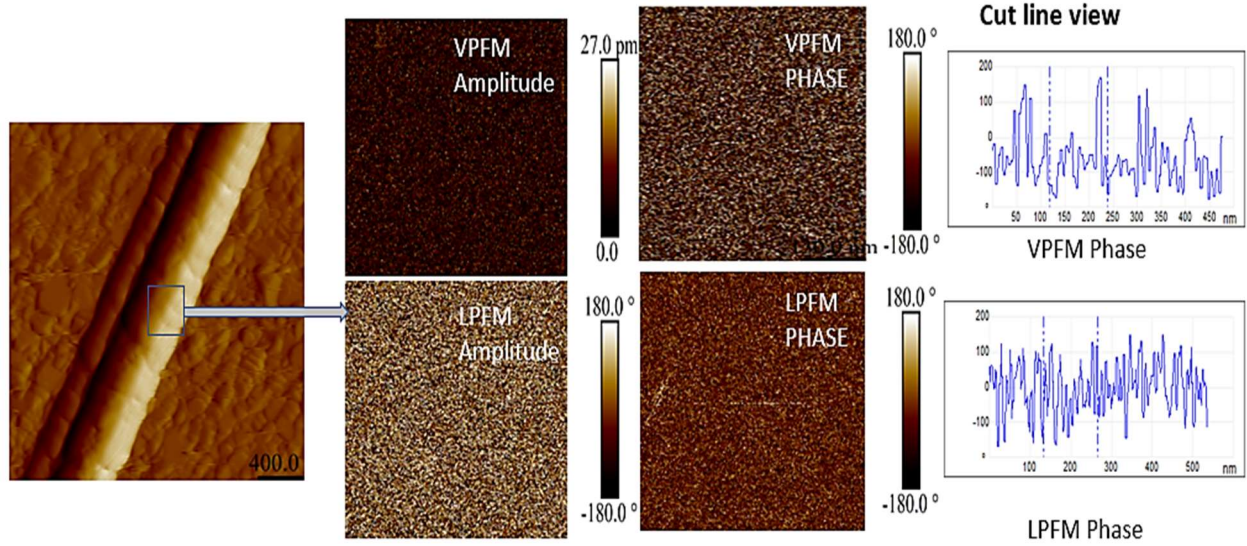


Figure 2.30: VPFM and LPFM Amplitude and phase image of the KNN fiber before poling

To investigate the po within the fiber an area of $400 \times 400 \text{ nm}^2$ was scanned at a rate of 0.5 Hz by the tip at 1 V AC, 50 kHz before and after poling with 5 V DC tip bias. It can be noted that the domains are distributed randomly between $+90^\circ$ and -90° as seen from the VPFM phase before poling.

2.13.5 Radial Poling of KNN fibres

In the study of the polarization switching behavior, poling processes with DC biases (+5 V) are applied between the tip and the sample. The DC poling process was achieved by applying a positive bias to the conductive tip, and the bottom Pt electrode of the sample was grounded. By applying a 5 V DC bias between the tip and sample, it is possible to switch the polarization inside the region under the tip and thereby observe the bright contrast in the LPFM and VPFM phase between the local domains as shown in Figure 2.31. After the poling, the fiber is imaged by scanning at 1 V AC, at a scan rate of 1 Hz. After applying a poling tip bias of 5 V DC, the phase image clearly shows that most domains are aligned in the upward direction of the applied field with a 180° phase difference with the unpolarized domains (refer cut line view Figure 2.31). Further, there is increased piezoresponse in the PR amplitude image upon poling, and almost all polarizations under the scanning area are rotated to the upward direction.

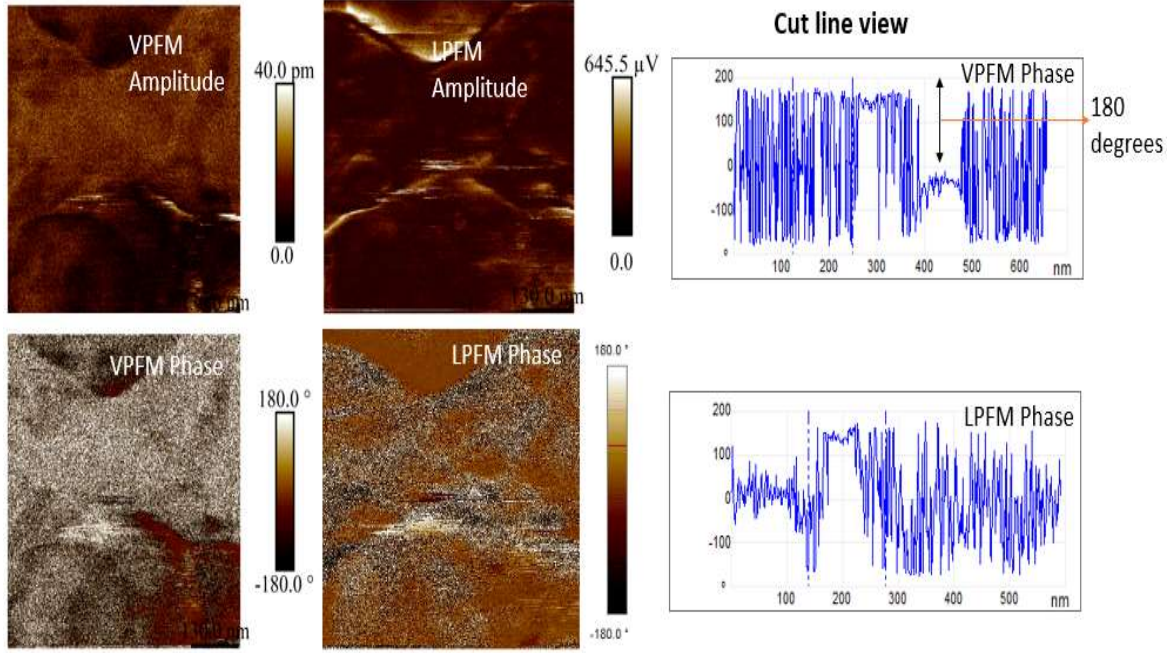


Figure 2.31: VPFM and LPFM Amplitude and phase image of the KNN fiber after poling at 5 V.

2.13.5.1 Polarization Switching curves of KNN fibres

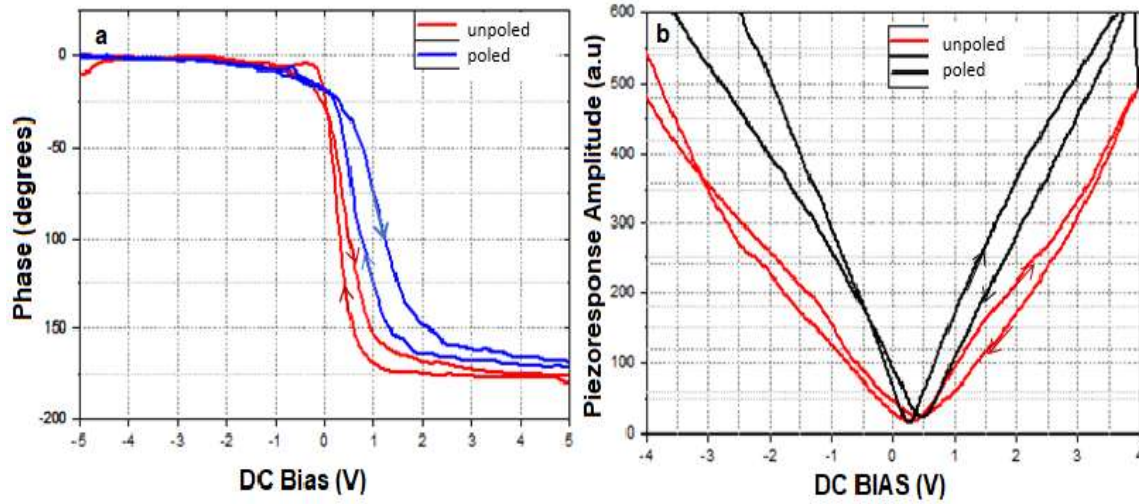


Figure 2.32: comparison of KNN fiber (a) Hysteresis and (b) strain evolution (S-E) butterfly loops as a function of the applied DC Voltage (at 1 Hz) showing before (0 V) and after poling at 5 V

The voltage necessary to induce a polarization switching, known as the ‘coercive voltage’ V_c , should be defined as $(V_c^+ - V_c^-)/2$, where V_c^+ and V_c^- are the right- and left quadrant coercive voltages in the hysteresis loop, respectively [149]. The value of V_c before and after poling is

estimated to be nearly 1 V for poled fiber and 0.7 V for the unpoled respectively from the hysteresis loop. The unpoled sample possessing several tiny domains may be exposed to several nucleation sites due to the increase in the domain wall density, providing the possibility for rapid nucleation, thus resulting in a reduction of the overall coercive field E_c . Thus, when the domain wall width (W_d) decreases, the shapes of the hysteresis loops tend to be narrow and V_c decreases significantly. The wider hysteresis loop (larger V_c) of the 5 V poled KNN fiber compared to the unpoled is an indication of increased domain size after poling [150]. Asymmetric butterfly curves are observed for both the poled and unpoled samples in the domains having different shapes and degrees of asymmetry as seen in Figure 2.32 b. The maximum PR amplitudes are lower for the unpoled when compared with poled samples. The hysteresis loop in Figure 2.32 shows a tilt present after poling, which is attributed to the probability that KNN ceramics may transform from a normal ferroelectric to a relaxor ferroelectric, exhibiting a slim and tilted loop. There is a shift in the loop along the positive voltage axis possibly due to unintentional and intentional defects, which can be present in the system. Such defects are stabilized in preferred lattice sites, creating an internal bias within, that constrains the switching of the polarization along specific directions.

2.13.5.2 Estimation of piezoelectric coefficients (d_{33})

The d_{33} is estimated at 5 locations inside the fiber within a scan size of 300 nm by measuring the slope of the PR amplitude ramping against the AC voltage as shown in Figure 2.33.

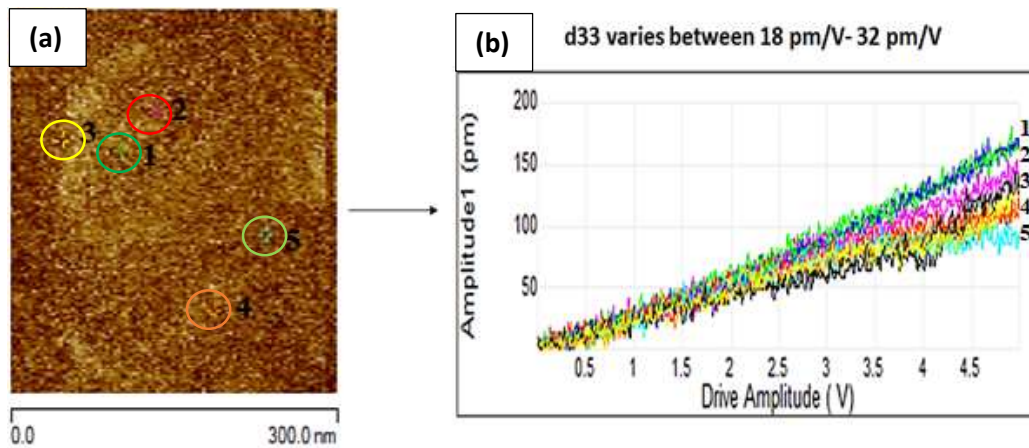


Figure 2.33: (a) Point and shoot of KNN fibers at 5 locations (b) PR amplitude vs AC bias.

The d_{33} is determined at 5 locations vary between 18-33 pm/V with an average of 25 pm/V.

2.13.6 PFM study of KNNT (KNN doped with 10% Ta) Fibers

2.13.6.1 Topography of KNNT fibers

The topography of the KNNT fiber is shown in Figure 2.34 diameter of the KNNT fibers can be roughly estimated to be between 500 - 600 nm with the roughness of 5 nm from the AFM images. The image shows one fiber overlapping over another one.

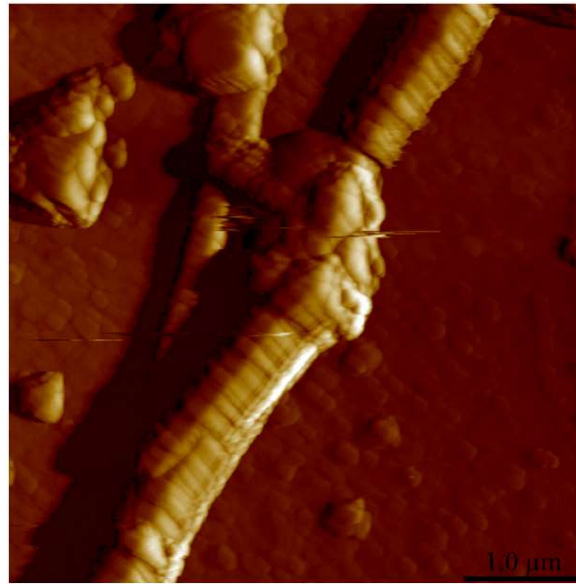


Figure 2.34: AFM image (topography) of the KNNT fiber

2.13.6.2 Analysis of phase and amplitude of KNNT fiber before and after poling process

PFM imaging (Amplitude and phase) of the KNNT fibers before poling are shown in Figure 2.35. Two regular domains are observed in the fiber along the radius (0 and 180 degrees polarized) as seen from the phase image. However, the domains are small and not well oriented as seen from the spikes. A high piezoresponse is observed for the left side of fiber as seen in the PR amplitude image which is in phase with the applied field as seen in Figure 2.35.

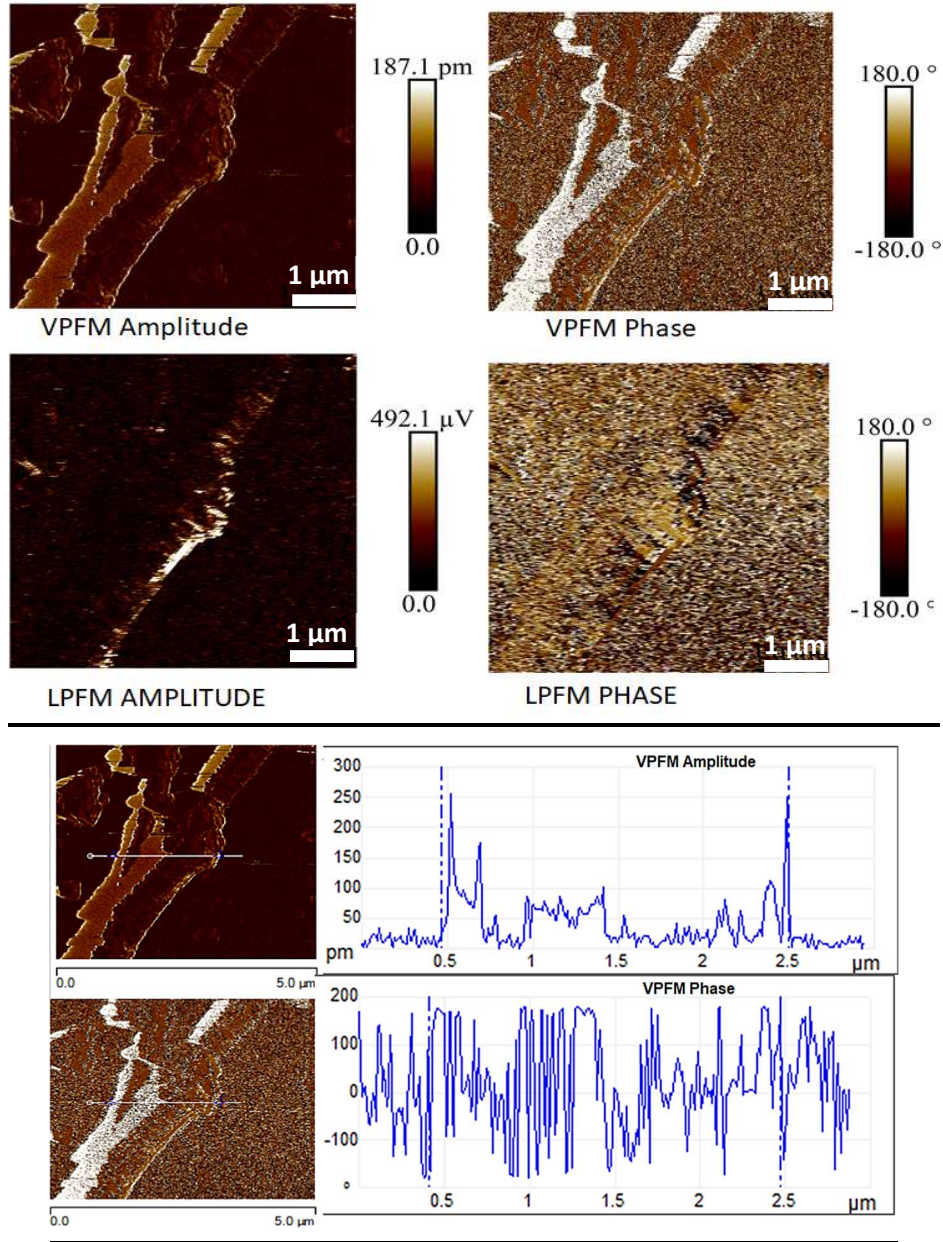


Figure 2.35: VPFM and LPFM Amplitude and phase image of the KNN fiber before poling

PFM imaging (Amplitude and phase) of the KNNT fibers after poling are shown in Figure 2.36 and where two regular domains are observed in the fiber along the radius (0 and 180 degrees polarized) as seen from the phase image. A higher piezoresponse is observed for the poled KNNT fiber compared to the unpoled as seen in the amplitude image in Figure 2.36.

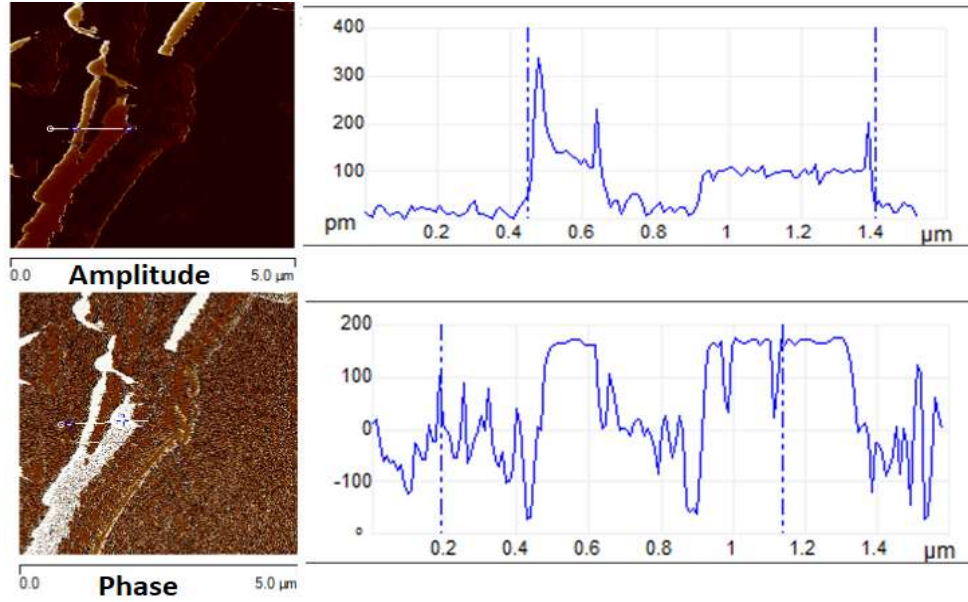
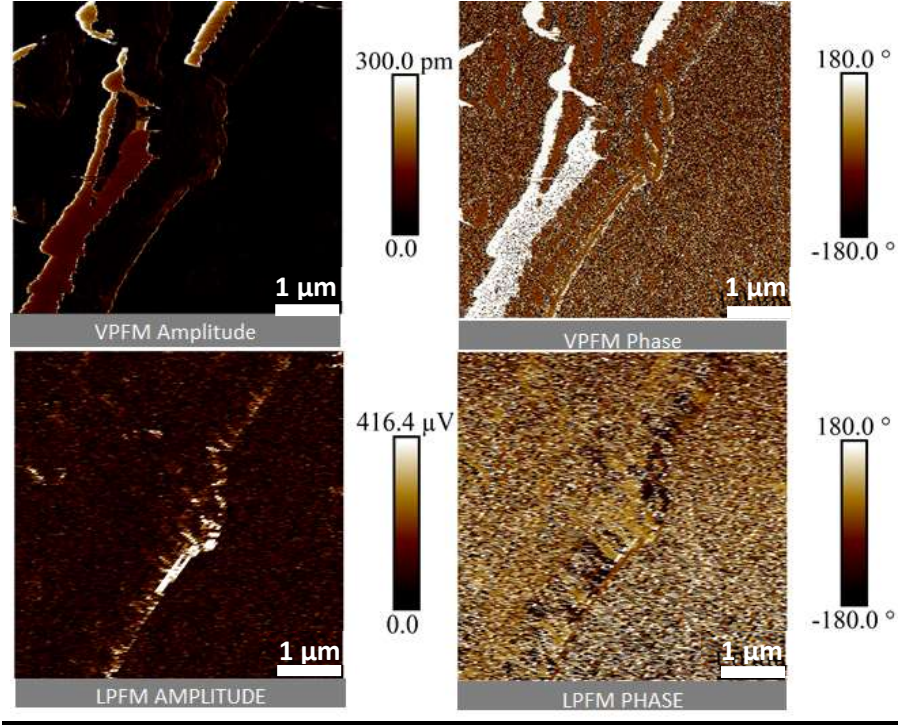


Figure 2.36: VPFM and LPFM Amplitude and phase image of KNNT fiber after poling at 5 V.

A clear 180° phase contrast between the two domains indicates the directions of the out-of-plane polarization components domains are opposite. The local ferroelectric switching responses are collected for the analysis of collective domain switching behavior. To understand the various domain polarization of KNNT inside the scanned area, the polarization switching and the

corresponding measurement of variations of the PR amplitude are performed at 5 points inside the scanned area as shown in Figure 2.37. The d_{33} , PFM phase, hysteresis, and amplitude butterfly loops are directly associated with the polarization switching of the local regions of 1, 2, 3, 4, and 5, where the characterizations were done. Figure 2.37c shows that the phase changes for the phase are about 180° , which further indicates unambiguous ferroelectric switching for regions under an applied AC bias.

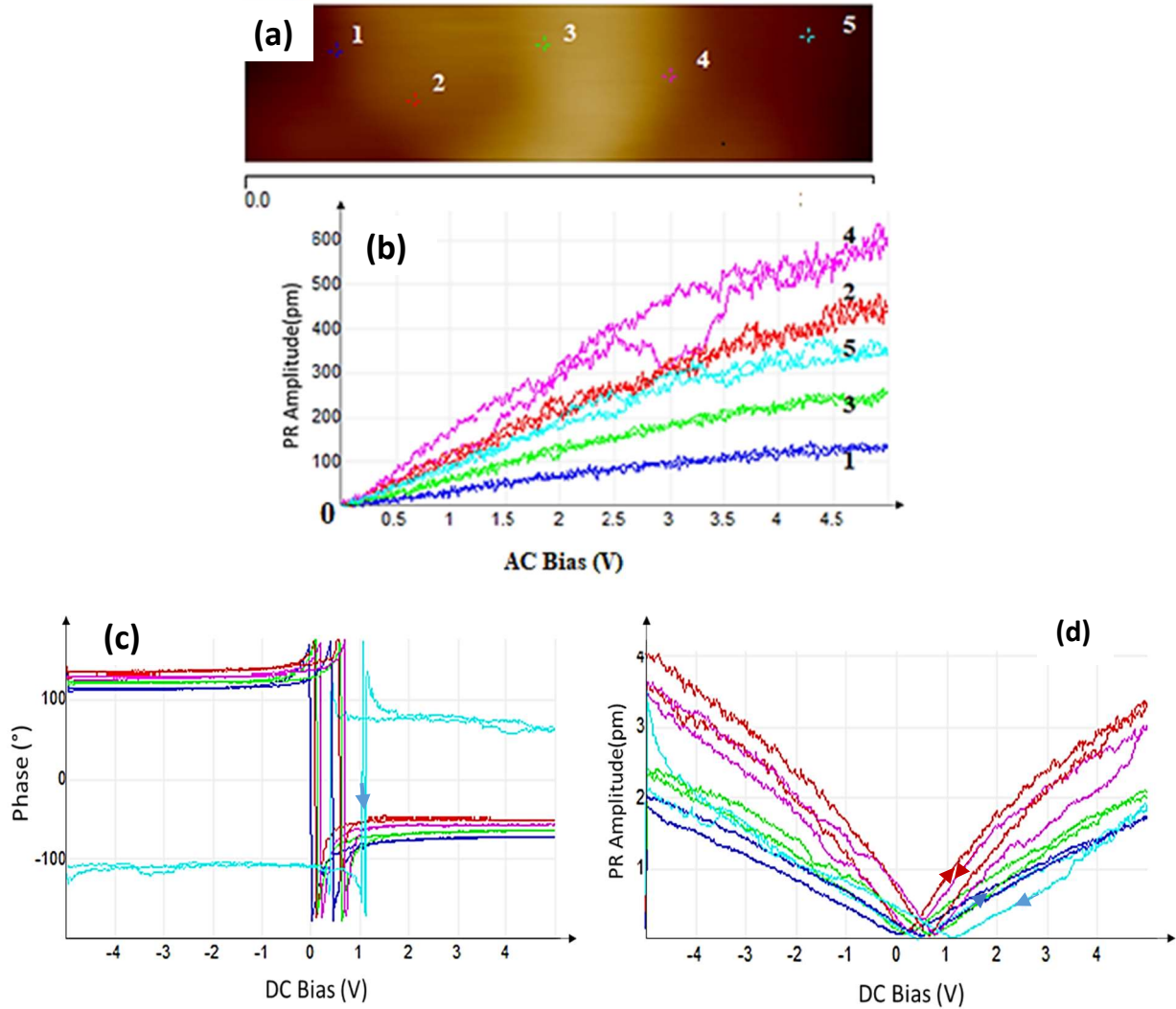


Figure 2.37: (a) Point and shoot locations at 5 different points (b) PR Amplitude vs AC bias, (c) hysteresis (phase vs DC bias), and (d) S-E butterfly curves (PR Amplitude vs DC bias) at 5 different points in the fiber

This trend describes the variation in the point of polarization switching point within the scanned area (Figure 2.37a) at different regions of 1, 2, 3, 4 and 5 in the sample, indicating an influence of

the domain size on polarization switching voltage that is larger domains are more difficult to switch. The coercive voltage is roughly $V_c = 1$ V for both poled and unpoled samples. The decrease in switching voltage with a decrease in the domain radius (W_d) can be partially attributed to the role of domain walls in the nucleation process, where novel spots of inverse domains are generated under an applied bias [151]. PR amplitude in Figure 2.37b increases linearly with an increase in the lower applied bias regime till a point (~ 2 V in this case) and then abruptly changes in magnitude. The non-linearity at a larger voltage (3 V) corresponds to the quick growth of the nucleated domains through sidewise domain wall motion until it spreads to the specimen, where it is well saturated [152]. Thus, the unpoled sample possessing several tiny (in nm) domains may be exposed to several nucleation sites due to the increase in the domain wall density, providing the possibility for rapid nucleation, thus resulting in a lower coercive field (below 1 V).

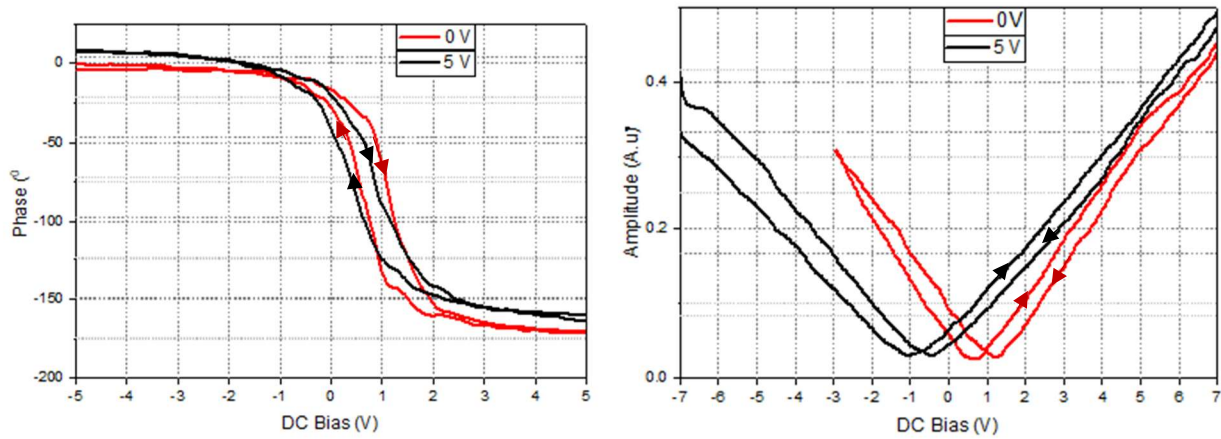


Figure 2.38: Hysteresis and butterfly curves of KNNT fibers before (red) and after poling at 5 V (Black) by PFM.

The microscopic hysteresis loops (Figure 2.38a) are observed when the applied electric field nucleates new domains by the voltage between the tip and surfaces and strongly depends on the number of nucleation sites, termed as ‘soft spots’ located around the domain walls [153]. The shape modifications of unsymmetric hysteresis loops before poling (0 V) are represented by pinched loops (constricted P-E loops in the region $E \approx 0$), asymmetric loops (shift of the P-E “hysteresis” loops along with the E- and P-axis, Figure 2.38a, suppression of left or right wing of the S-E “butterfly” loop, Figure 2.38b) which have been found in different ferroelectric systems in both polycrystalline ceramics and single crystal generated by aging and fatigue [154].

2.13.6.3 Estimation of d_{33}

The d_{33} is estimated in a similar way as mentioned in the case of KNN fibres obtaining the slope of the piezoresponse amplitude with the AC bias voltage. KNNT fibers showed significant improvement in d_{33} upon poling. The average d_{33} at 5 different points can be estimated to be nearly 75 pm/V for unpoled fibers and 130 pm/V for the 5 V poled samples as shown in Figure 2.39.

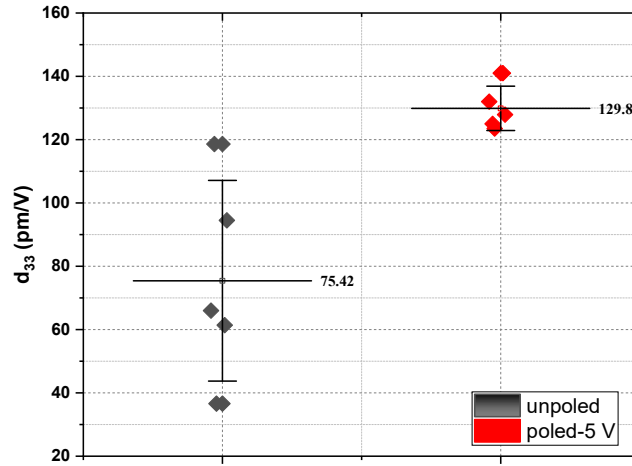


Figure 2.39: Dispersion of d_{33} values of KNNT fibers

2.13.7 Conclusion

In summary, the piezoelectric and ferroelectric properties of the KNN and KNNT fibers have been studied by the AFM method. The piezoelectric coefficient (d_{33}) has been determined for the KNN and KNNT fiber samples before and after poling are given in table 3.5. The KNN fibres have a d_{33} of 25 pm/V and do not show significant improvement upon poling. However, Ta doping of KNN fibers lead to a nearly 3-fold enhancement in the d_{33} compared to pure undoped KNN films. Further, the poled KNNT films showed a piezoelectric coefficient (~130 pm/V) compared to the undoped KNNT fibers (75 pm/V).

Table 2.5 Piezoelectric properties of KNN and KNNT fibers

Material	Morphology	Size	Reported d_{33} (pm/V)	Reference	Extracted d_{33} (pm/V)	
					(unpoled)	Poled (5 V)
KNN	fiber	500 nm	26 (nanowire)	[155]	25	28
KNNT	fiber	600 nm	87 (fiber)	[147]	75	130

The excellent piezoelectric properties of the KNN/KNNT fibers suggest that the fibers could be excellent candidate for fabricating novel flexible PEH devices, and nanogenerators.

2.14 Comparison of the Figure of Merit of the cantilevers.

There is significant interest in the application of ferroelectric materials in energy harvesting and therefore several definitions of Figure of Merit (FoM) have been devised to compare their performances [156]. A variety of FoMs has been postulated for piezoelectric materials for energy harvesting applications [157]–[159]. The efficiency of a piezoelectric energy-harvesting device is generally related to both its piezoelectric and elastic responses and generally expressed in terms of FoM_{ij}^S [156], [160].

$$FoM_{ij}^S = \frac{d_{ij}^2}{\varepsilon_{33}^T S_{jj}^E} \quad 2.12$$

However, when the thickness of the piezo layer is small compared to the substrate layer, the elastic compliance part S_{jj}^E is neglected [156], [160]. When a piezoelectric is subjected to mechanical vibrations at low frequencies away from the electromechanical resonance, the relevant FoM is [156], [161], [162]:

$$FOM_{ij} = \frac{d_{ij}^2}{\varepsilon_{33}^T} \quad 2.13$$

This FoM depends on the square of the piezoelectric coefficient (d_{ij}) and ε_{33}^T , which is the permittivity at constant stress. T , and subscripts i and j follow conventional piezoelectric matrix notation. Therefore, the piezoelectric materials showing high piezoelectric constants and low dielectric constant can provide higher power output for MEMS energy harvesters. To determine FoM of the LT, KNN and KNNT thin-film cantilevers, the dielectric permittivity was measured from the capacitance of the parallel plate configuration of the cantilever at room temperature away from its resonant frequency at 1 kHz [163], [164] using an Agilent E4980A precision LCR meter. The dielectric permittivity was measured to be 366, 466 and 397 for LT (4.3 μm), KNN (7 μm) and KNNT (7 μm) cantilevers respectively at 1 kHz applying a signal of 2 V (DC). The FoM of these sol-gel processed, lead-free piezoelectric materials are compared with a commercially available Lithium Niobate (LN) single crystal wafer (YXlt)/128°/90° cut (from Roditi) [165]. There are several advantages as well as disadvantages of the ceramic materials grown by the sol-

gel process and the particular material choice is governed by the application requirements. The comparison of FoM, would, therefore, permit us to compare the usefulness of these materials from an energy harvesting application point of view. A higher FoM indicate a higher energy conversion efficiency. The summary of the extracted electromechanical properties and the figure of merits of the various samples (KNN film, KNNT film, KNN fiber, KNNT fiber, LN) are given in Table 2.6.

Table 2.6: summary of the electromechanical properties of the lead-free piezoelectric materials

Material	Morphology	Size	Extracted d_{33} (pm/V) (unpoled)	Reported d_{33} (pm/V)	Reference	Dielectric permittivity ϵ_{33}^T	FOM ($\frac{d_{33}^2}{\epsilon_{33}^T}$) ($10^{-18} \text{m}^2/\text{V}^2$)
Lithium Tantalate	Films	2 μm	23	13- 28	[111], [112]	163	3.2
		3.4 μm	22			362	1.3
		4.3 μm	24			479	1.2
KNN	Films	7 μm	23	18 (films)	[164], [167], [168]	466	1.1
KNNT	Films	7 μm	48	60	[145]	397	5.9
KNN	Fiber	500 nm	28	26 (nanowire)	[155]	-	-
KNNT	Fiber	600 nm	75	87 (fiber)	[147]	-	-
Lithium Niobate	Single crystal	27 μm	-	27	[165]	50.5	14.8

A lower value of dielectric constant is desired for a higher energy harvesting FoM. The KNN films have the lowest FoM among the sol-gel processed lead-free piezoelectric materials, which is essentially due to the higher dielectric permittivity compared with LT and KNNT films. Pure KNN films have 17% higher dielectric permittivity compared to KNNT due to its lower density, along with a slight deficiency of alkali metal, when compared to dense KNNT [169]. Further, the KNNT film also has nearly two-fold higher d_{33} , compared to KNN samples. Therefore, a five-fold increase in FoM is observed in Tantalum doped KNN films. The Lithium Tantalate FoM decreased with an increase in thickness due to the increase in the dielectric permittivity with the thickness. This is because the polarization in the piezoceramic films decrease with increasing film thickness due to

relaxation of strain [170]. Further, with the increasing film thickness, the grain boundary volume also increases, which consequently decreases the net electron mobility in the system due to intergranular charge trapping [171]. In comparison, the FoM of Lithium Niobate single crystal is superior to sol-gel processed KNN and KNNT films, and nearly three-fold of KNNT film, thanks to lower dielectric permittivity of LN.

2.15 Summary

In summary, the electromechanical properties and polarization switching of lead-free ferroelectric materials namely Lithium tantalate (thin films), Sodium Potassium Niobate (KNN), and KNN doped with Ta (films and fiber) have been studied using PFM. The energy harvesting FoM of these materials are compared with the Lithium Niobate crystal, for potential fabrication of highly coupled PEHs. Although the KNN films did not show any improvement in d_{33} by poling by AFM tip at 3 kV/mm (20 V V_{tip}), the poling at elevated temperatures at 4 kV/mm was found to increase the piezoelectric coefficient (d_{33}) from 23 pm/V to 100 pm/V. Although the d_{33} values of the unpoled samples are lower than the state-of-the-art values that have been reported so far (detailed in Table 2.6), the increase in d_{33} upon poling is a promising sign of the use of these materials in energy harvesting applications. Further, the study of KNNT films shows that the B site substitution by Ta can lead to a significant increase in the d_{33} compared to pure KNN samples. The d_{33} of the unpoled KNNT cantilever was found to be 48 pm/V, which increased to 221 pm/V upon poling at 3 kV/mm. These values are close to the d_{33} values of KNNT films reported so far and therefore can be exploited to be used in energy harvesting applications in the future. This study of the piezoresponse of these films could be useful for the understanding and optimization of piezoelectric properties of PTFs for various applications and thereby the performance of PTFs devices. Additionally, the ferroelectric properties and polarization switching (hysteresis and butterfly curves) of the KNN and KNNT fibers have been studied before and after poling by AFM. The KNNT fibers showed piezoelectric coefficient d_{33} (~130 pm/V) compared to the undoped KNN fibers (28 pm/V). The good piezoelectric properties of the KNN/KNNT fibers suggest that they could be used for fabricating novel flexible PEH devices working in non-resonant mode. It was observed that the FoM of the Lithium Tantalate cantilevers increases with the thickness, which is due to the increase in the dielectric permittivity. Among all the sol-gel processed films, KNNT film shows higher FoM due to its higher d_{33} and lower dielectric permittivity values. Finally, the FoM of the sol-gel processed lead-free films was determined for the possible evaluation as a

candidate for energy harvesting applications. The FoMs of these sol-gel processed films on steel are compared with commercially available lead-free Lithium Niobate single crystal. In comparison, the energy harvesting FoM of Lithium Niobate single crystal is superior to sol-gel processed KNN and KNNT films, thanks to their lower dielectric permittivity. This makes Lithium Niobate crystals as the favorite candidate material for the fabrication of highly coupled lead-free PEHs. Also, even though the sol-gel processed piezoelectric films on steel have advantages such as lower resonance frequency and low cost in comparison with single crystals, they may not be compatible with CMOS and MEMS technologies. In addition, sol-gel processed materials are polycrystalline and anisotropic and therefore their electromechanical properties depend usually much more on the temperature than it is for single-crystals. Sol-gel processed polycrystalline materials are therefore not the best choice in the high temperature applications such as car engines. Further, in real-time applications as harvesters, the sol-gel process has some limitations such as hygroscopic nature of the precursors and volatilization of K and Na elements during high temperature sintering. These issues with sol-gel processed lead-free piezoelectric materials needed to be addressed before it can be made industrially viable. Single crystals on other hand, are less prone to such issues. Although Lithium Niobate crystals are widely utilized for optical and RF applications, their application in vibration energy harvesting is seldom studied. For this reason, a lead-free piezoelectric energy harvester based on Lithium Niobate single crystal on a silicon substrate will be explored in the next chapter.

3 Piezoelectric Microgenerator based on lead-free Lithium Niobate single crystal

In this chapter, the fabrication and characterization of a lead-free microgenerator based on lead-free Lithium Niobate single crystal on Si is discussed. Further, we develop an electromechanical equivalent circuit model of the piezoelectric energy harvester and, in addition, the voltage conditioning and device interfacing for controlled and stable DC output is discussed. An efficient architecture to maximize the power transferred to the load with a Maximum Power Point Tracking (MPPT) is also investigated, with a specific focus on low power circuits.

3.1 Introduction

Keen interest has been generated in recent years to harvest power from ambient vibrations to power low power sensors or actuators that are used in the “Internet of things” (IoT) networks to replace traditional batteries [172], [173]. Piezoelectric Energy Harvesters (PEHs) that produce the voltage on the application of strain across the electrodes have gained a lot of attention in this regard due to their high power density and conversion efficiency at the microscale as well as its simple design. Currently, most of the high performing PEHs are based on lead-based materials such as PZT [10], [148], [174] and there has been little effort towards the development of next-generation “green PEHs” with high K despite the growing consensus in the electronics industry for the use of environment-friendly materials such as Lithium Niobate (LN) that is used in our present work. Indeed, innovative, lead-free materials and structures represent a tremendous challenge and opportunity to enable energy harvesters or self-powered sensors. Concerning piezoelectric LiNbO_3 (lithium niobate - LN), it was demonstrated that the electro-mechanical properties of LN single crystals highly depend on the orientation, and is comparable to PZT ceramics [175]. LN (YXI)/128 has been scarcely investigated in the energy harvesting field, even though it presents a much lower dielectric constant than the PZT family ($\epsilon_{33} = 50.5$) and a higher piezoelectric coefficient compared to other Pb-free materials ($d_{23} = 27 \text{ pC/N}$) [176]. Another main challenge faced by PEHs is the narrow bandwidth of operating frequency as the output voltage and power reduce drastically from

moving away from the resonant frequency [177]. The PEH produces AC output voltage in phase with the applied frequency of the mechanical force and voltage needs to be rectified before it can be stored for practical applications [52]. Thus, if the voltage generated is under the diode threshold drop of the rectifier, the power is not utilized. Since the frequency of typical ambient environmental vibration sources is low (less than 300 Hz) and susceptible to variation to a certain extent, PEHs with low resonant frequencies and broadband operation capabilities are necessary for reliable performance [8]. There are several reports of piezoelectric microgenerators with various complex configurations such as membrane structure [57], multiple stacked piezoelectric layers, etc.[58], [177] for forcing non-linearity in the system and to push towards a broader frequency regime. However, such multi-degree freedom approaches generally have limitations like reduced power density due to low-quality factor Q . Recently, a new interest emerged with the tuning of the operating frequency of PEHs by exploiting the high electromechanical coupling effect [178]. Strongly coupled PEHs is therefore considered as a solution to enhance the frequency bandwidth of PEHs. For PEHs with large K^2 , resonance splitting gives two well-separated output power peaks between thereby extending the harvesting BW [178], [179]. Badel and Lefeuvre [180] showed that it is possible to largely tune the resonant frequency of highly coupled piezoelectric energy harvesters to achieve broadband energy harvesting with the aid of interface circuits. Such promising perspectives for broadband vibration energy harvesting can only be achieved through the design and the fabrication of PEHs with a strong global electromechanical coupling coefficient K . However, most of the highly coupled PEHs reported so far are based on lead-based materials such as PZT and PMN-PT. Lead-free “green PEHs” with simple configuration, working at low ambient frequencies with high coupling K , exhibiting a broadband operational capability are rarely reported.

Hence, this chapter address the study of a microgenerator green PEH with Lithium Niobate as active piezoelectric material that operates at low resonant frequency (~ 200 Hz) has a broadband operation frequency range. The design aspect and considerations such as geometry, choice of open circuit voltage and power of the harvester from an application point of view of an Energy Autonomous Wireless Vibration Sensor (EAWVS), will be detailed in chapter 5. The characterization of the device performances such as output voltage, power at optimal load at various accelerations is presented along with the extraction of internal parameters such as electromechanical coupling K and mechanical quality factor Q_m . Further, the overall Masons

electromechanical model of the device is derived from the impedance analysis and the results are compared with the LT-Spice simulations. Finally, an appropriate rectification circuit output is chosen to convert the AC voltage to DC based on extracted device parameters (K^2Q_m).

3.2 Microgenerator geometry and Fabrication process

The Lithium Niobate single crystal samples on Silicon wafer were obtained from Giacomo Clementi, Ph.D. student, workgroup of Prof Auserine Bartsyte, Femto-ST Besancon under the collaborative framework of ITN- ENHANCE project.

A standard 4-inch Si substrate $525 \pm 25 \mu\text{m}$ thick was Au-Au bonded to $350 \mu\text{m}$ thick LiNbO₃ (YXl)/128° crystal using an EVG bonding machine. A 200 nm thick Au layers with Cr adhesive layers, were deposited on one side of the LiNbO₃ wafer and on one side of a 500 mm thick Si wafer. This is to facilitate the mechanical compression of Au layers by Au-Au bonding using an EVG wafer bonder. The standard 4-inch wafer ($525 \pm 25 \mu\text{m}$ thick) is chosen as substrate for bonding, due to the compatibility with the available photolithography process. The piezoelectric LiNbO₃ layer is thinned down by lapping and then micro-polishing steps until the thickness reaches $27 \pm 2 \mu\text{m}$. The top electrodes (200 nm thick Cr/Au), deposited by electron-beam evaporation, are patterned by UV lithography, and finally lift-off. The Cr/Au layer used for wafer bonding was also acting as bottom electrode of the device. The wafer is diced to form a cantilever (dimensions in Table 4.1) is finally glued to the clamping side and made free to vibrate. The cantilever device is wire bonded to obtain a device as shown in Figure 3.1. The Lithium Niobate layer is carefully scratched from the top using a diamond tip to obtain the bottom electrode. The top and bottom electrodes are then wire-bonded to the designed PCB, to obtain the final PEH device. A Tungsten proof mass cube 0.125 cm^3 (2.3 grams) is added to the free side end of the cantilever. When an input vibration is applied to the cantilever beam structure, the effective mass transforms the input acceleration into force. The strain generated along the beam due to applied force is converted to the electrical voltage across the electrodes through the transverse mode (d_{31}) piezoelectric effect.

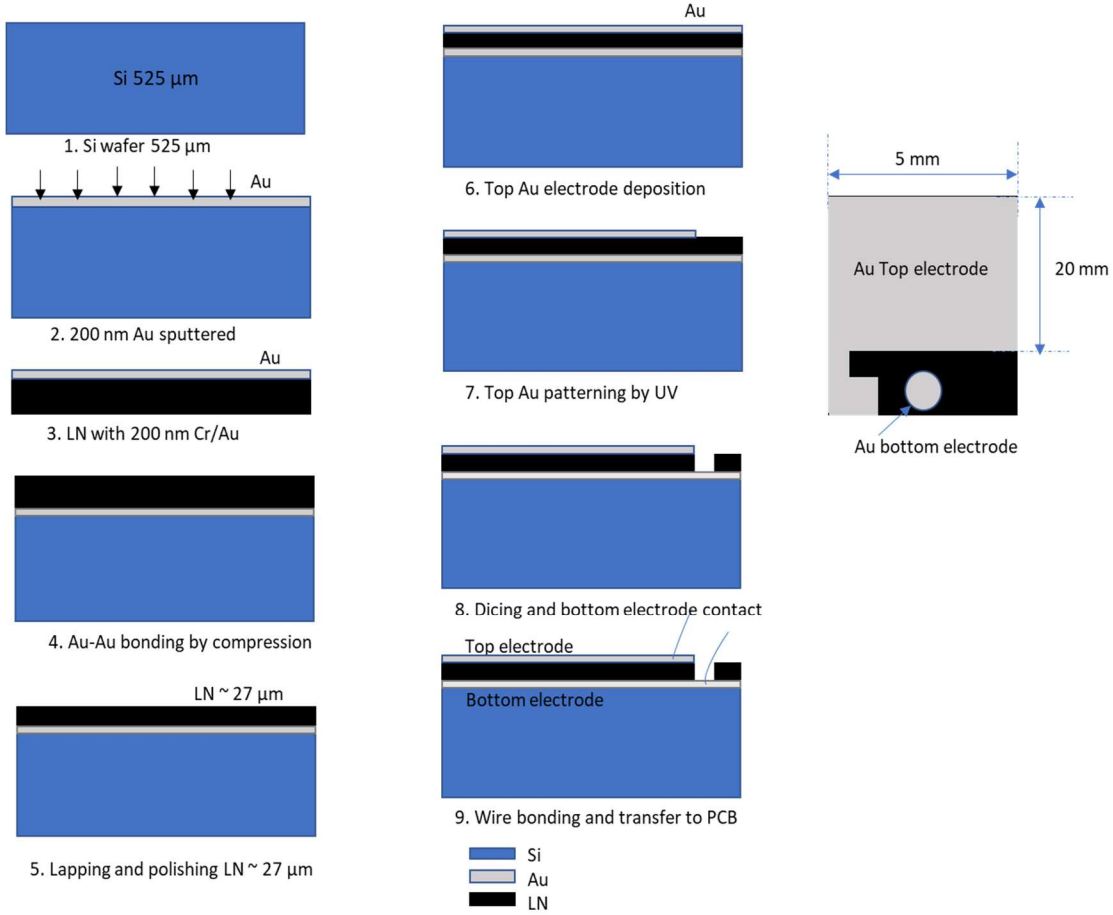


Figure 3.1: Process flow of fabrication steps of the microgenerator

Table 3.1 Cantilever and electrodes geometrical details of the microgenerator

<i>cantilever</i>		<i>electrodes</i>		<i>Si</i>	<i>LN</i>	<i>Proof mass</i>
<i>Length(mm)</i>	<i>Width(mm)</i>	<i>Length(mm)</i>	<i>Width(mm)</i>	<i>Thickness(μm)</i>	<i>Thickness(μm)</i>	<i>weight(g)</i>
22	5	22	4.9	525 ± 25	27 ± 2	2.3

A photograph of the final diced cantilever 22 mm long and 5 mm wide, wire bonded and soldered onto the PCB is presented in Figure 3.2.a, and Fig. 4.2 b shows a cross sectional schematic of the harvester with proof mass.

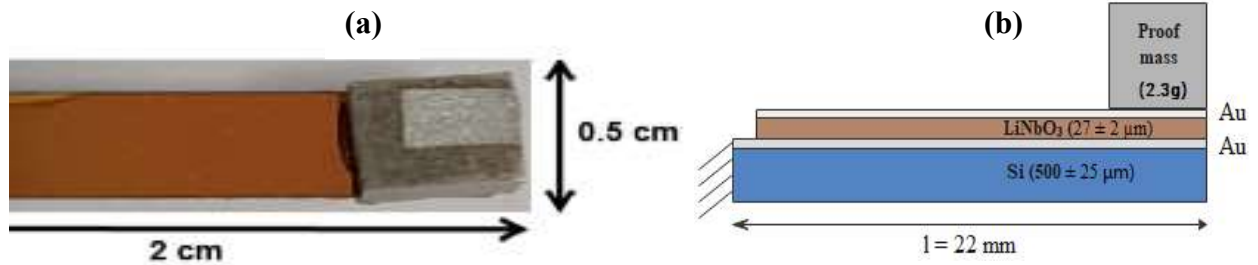


Figure 3.2: (a) Photograph top view of the PEH (b) cross sectional schematic of the microgenerator with a proof mass

3.3 Dynamic Electrical Characterization

This part of the work was carried out at Federation of Micro Nano Technology (FMNT), in the lab of Prof. Skandar Basrour, Grenoble. In this part, the electro-mechanical response of the device such as the behavior at high frequencies, and the resonance frequencies of the given geometry is identified using the impedance analyzer. The impedance analyzer measures the electrical response of the device when an AC voltage signal is applied to the sample. The voltage across the electrodes and the current flowing through it are measured, from which the modulus and the phase of the impedance can be estimated. The impedance analyzer can therefore be used to measure the electrical impedance of the device and analyze the electro-mechanical resonance frequencies. The impedance of the device was measured with a HIOKI -IM3570 impedance analyzer as shown in the schematic in Figure 3.3.

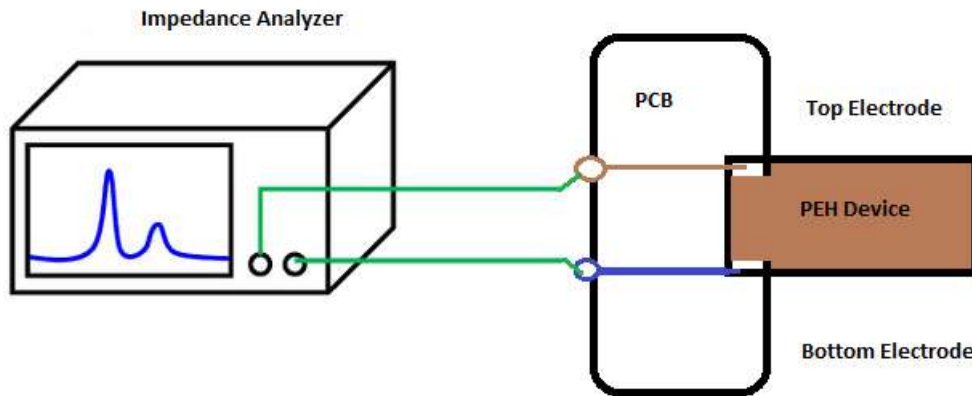


Figure 3.3 Schematic of the measurement with an impedance analyzer

The resonance occurs when the frequency of the applied voltage is identical to the natural mechanical resonance frequency of the piezoelectric device which is determined by the geometry

and stiffness of the cantilever beam. A sinusoidal signal with low AC amplitude (1 V) is applied on the device and the voltage and current on the electrodes are measured to deduce the impedance. In piezoelectric materials, there exists resonance and anti-resonance as shown in Figure 3.4, which can be taken as electrical short circuit condition and open circuit condition respectively. The impedance modulus and phase of the cantilever are shown in Figure 3.4 showing clearly the antiresonance and resonance peaks for the device.

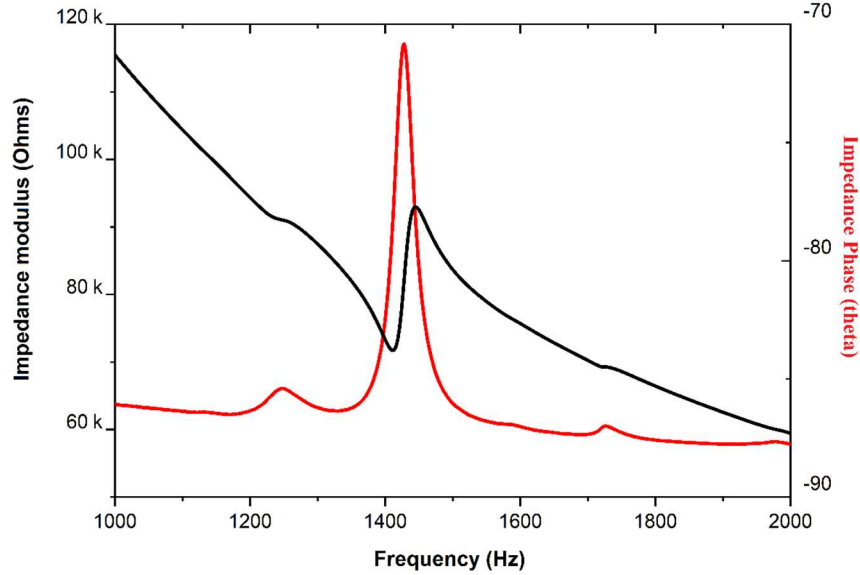


Figure 3.4 Impedance modulus and phase of the PEH without proof mass

3.4 Estimation of Mechanical Quality Factor (Q_m) based on impedance curve

Loss in piezoelectric materials can be described in terms of electrical and mechanical dissipation factors [181]. ‘Hard’ ceramics are characterized by small displacement at off-resonance, low dielectric loss, and high mechanical quality factor (Q_m). On the contrary, ‘soft’ ceramics present a large mechanical strain at off-resonance or have a broad peak, high dielectric loss, and a low mechanical quality factor [182]. Therefore, the Q_m value is used as a figure of merit for the losses in piezoelectric materials. Quality factor (Q_m) is a measure of the time constant for the decay of a resonating system’s amplitude to its resonance period. It is generally defined as [183]:

$$Q_m = \frac{\text{Average energy dissipated per cycle}}{\text{Energy stored}} \quad 3.1$$

At resonance in PEH, the mechanical losses are the significant among other losses and it has been shown that the mechanical quality factor Q_m , is inversely proportional to the mechanical loss factor, ' $\tan\phi$ ' [184]. The Q_m can be obtained from the resonator measurements by determining the electrical impedance as a function of frequency. Resonance frequency (f_r) and anti-resonance frequency (f_r'), the capacitance, and the dissipation factor in the desired frequency range are required to determine the material constants.

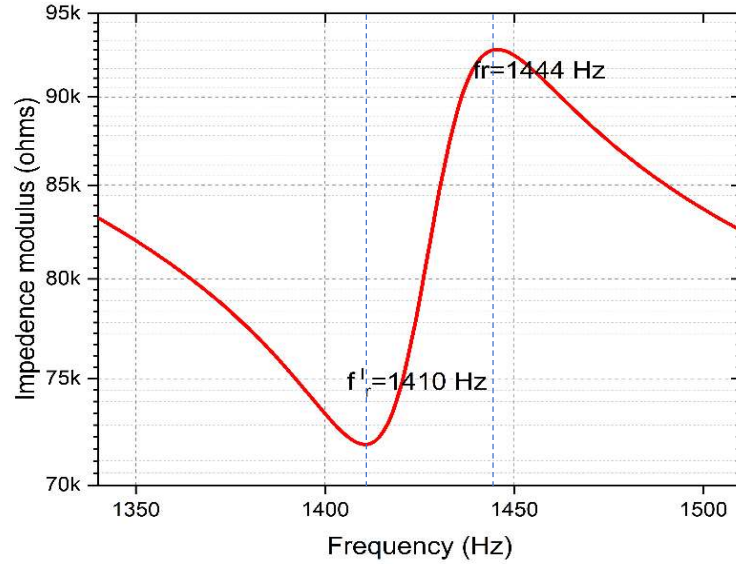


Figure 3.5: Resonant frequency $f_r = 1440$ Hz at $Z_{max} = 92.75$ k Ω and antiresonant frequency $f_r' = 1410$ Hz at $Z_{min} = 71.8$ k Ω respectively after subtracting the baseline.

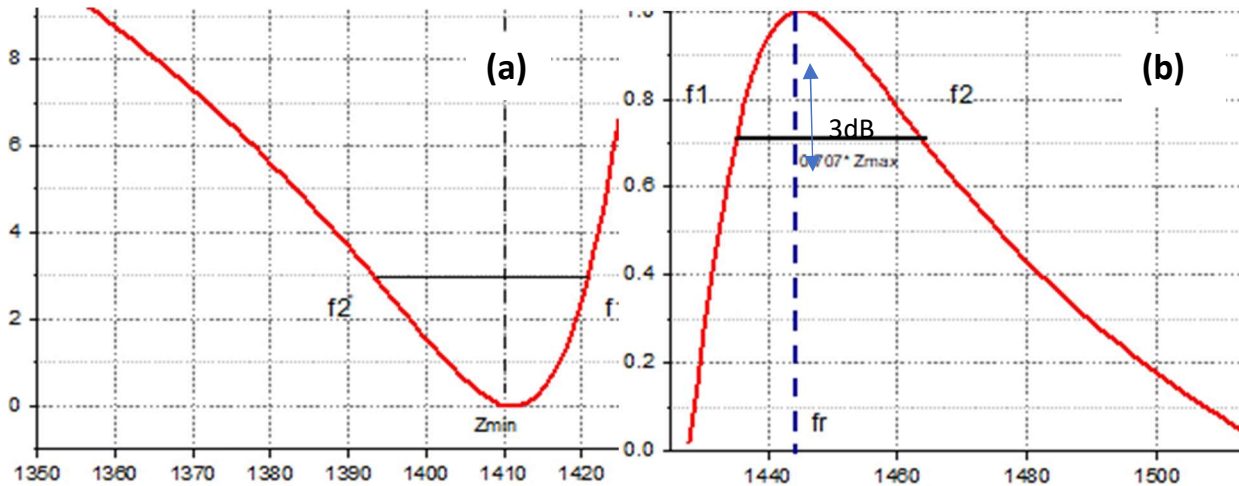


Figure 3.6: Impedance (a) anti-resonance and (b) resonance in the PEH with no proof mass after fitting the baseline.

Taking a narrow frequency range close to the resonance and anti-resonance, we can define the resonance quality factor (Q_R) and the anti-resonance quality factor (Q_{AR}) as shown in equation (4.2 and 4.3) [185]. Here the difference between two quality factors, Q_R and Q_{AR} calculated at resonance (f_r) and antiresonance (f_r') respectively were investigated [186], [187].

$$Q_R = \frac{f_1 - f_2}{f_r} \quad 3.2$$

$$Q_{AR} = \frac{f_1' - f_2'}{f_r'} \quad 3.3$$

where, $(f_1 - f_2)$ or $(f_1' - f_2')$, is the 3 dB bandwidth of the impedance or admittance curve of resonance and anti-resonance respectively.

$$Q_R = 50$$

$$Q_{AR} = 49$$

A higher-quality factor indicates broadband harvesting capabilities of the harvester, ensuring efficient harvesting over a broad frequency range.

3.5 Electromechanical coupling coefficient (k_{33} and k_{31})

If there is no load resistance on the output of the transducer, then the square of the coupling coefficient is simply the energy stored at the output port divided by the total energy put into the system. The electromechanical coupling factors k_{31} and k_{33} were obtained using the following equations defined in the IEEE standards [182], [187]:

$$K_{31}^2 = \frac{\frac{\pi f_r}{2 f_r'}}{\frac{\pi f_r}{2 f_r'} - \tan\left(\frac{\pi f_r}{2 f_r'}\right)} \quad 3.4$$

$$K_{33}^2 = \frac{\pi f_r}{2 f_r'} \cot\left(\frac{\pi f_r}{2 f_r'}\right) \quad 3.5$$

$$K_{31} = 0.22$$

$$K_{33} = 0.23$$

3.6 Design of Proof mass

Since most ambient mechanical vibrations available in the environment are less than 300 Hz, it is advantageous to set the operating frequency of the PEH in this regime.

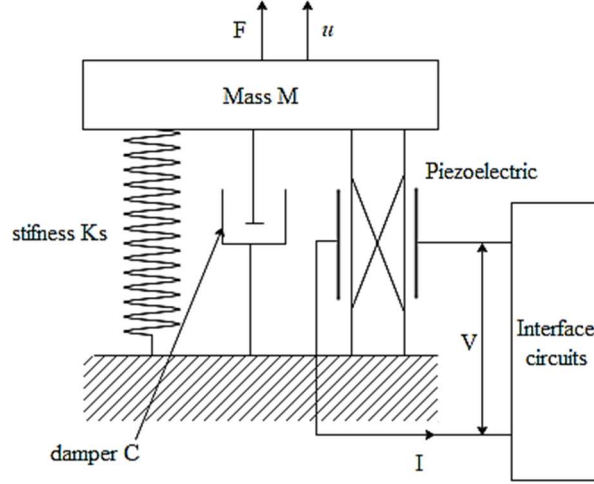


Figure 3.7: SDOF model of the electrotechnical equivalent for PEH

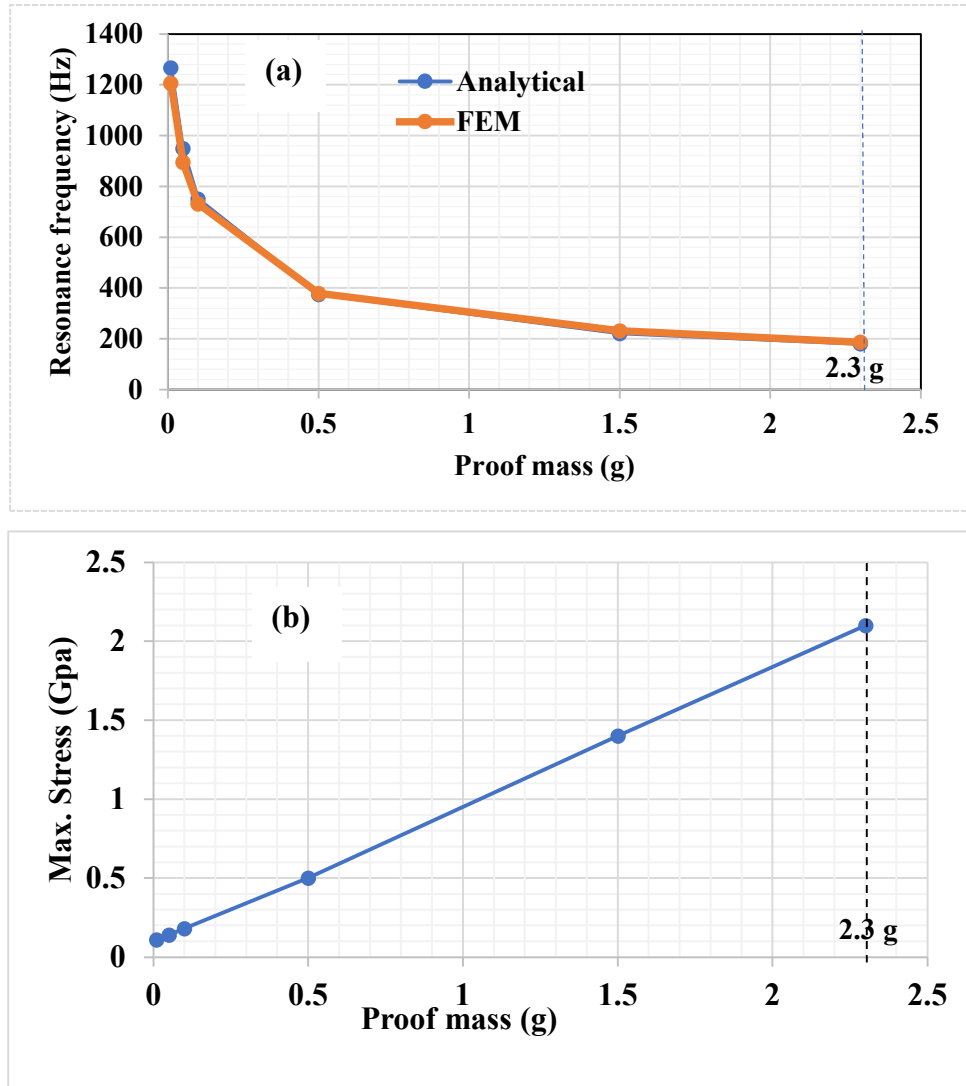
The piezoelectric harvester considered here is a seismic resonant electromechanical device converting mechanical energy into electrical energy. Therefore, a lumped-parameter modeling method is suitable for system behavior analysis [172]. The PEH structure was modeled as a Single Degree of Freedom (SDOF) system Figure 3.7, which comprises a seismic mass ($M = m + 0.23m_c$) where ‘ m ’ the mass of proof mass and m_c is the mass of cantilever, a spring with constant K_s , a dashpot with damping coefficient C and a vibrating base. Therefore the resonance frequency (f_r) of the cantilever can be tuned by varying the mass of the added proof mass (m):[49]

$$f_r = \frac{1}{2\pi} \sqrt{\frac{k_s}{(m + 0.23m_c)}} \quad 3.6$$

$$k_s = \frac{Ywt^3}{4l^3} \quad 3.7$$

where, in Equations (4.6) and (4.7) ‘ k_s ’ is stiffness constant of the beam of width ‘ w ’, thickness ‘ t ’ and length ‘ l ’, and ‘ Y ’ being Young’s modulus of the beam respectively. Eigen-frequency analysis was performed with the Finite Element Analysis (FEM) to obtain the resonance frequencies and the stress distribution for various proof mass weights. The variation of the resonance frequency f_r of the PEH with the proof mass weight determined by analytical equation is in good agreement with the FEM as shown in Figure 3.8a. The resonance frequency f_r decreases sharply from 1.26 kHz to 187 Hz when the mass of the proof mass increases from 0.01 g to 2.3 g. Thus, by selecting

a proof mass of 2.3 g, the resonance frequency of the piezoelectric energy harvester is significantly lowered to a value close to 200 Hz. It is equally important to ensure that the stress developed inside the cantilever beam is within the breaking stress of the substrate material (Si). The maximum stress distribution inside the cantilever beam for various proof mass weights at 1g ($g = 9.81 \text{ m.s}^{-2}$) acceleration as determined by FEM is given in Figure 3.8b. The maximum stress $\sim 2 \text{ GPa}$ developed at the bottom corner of the Si cantilever as shown in Figure 3.8c which is within the limit of breaking stress in Si plates ($>3 \text{ GPa}$) [188], [189].



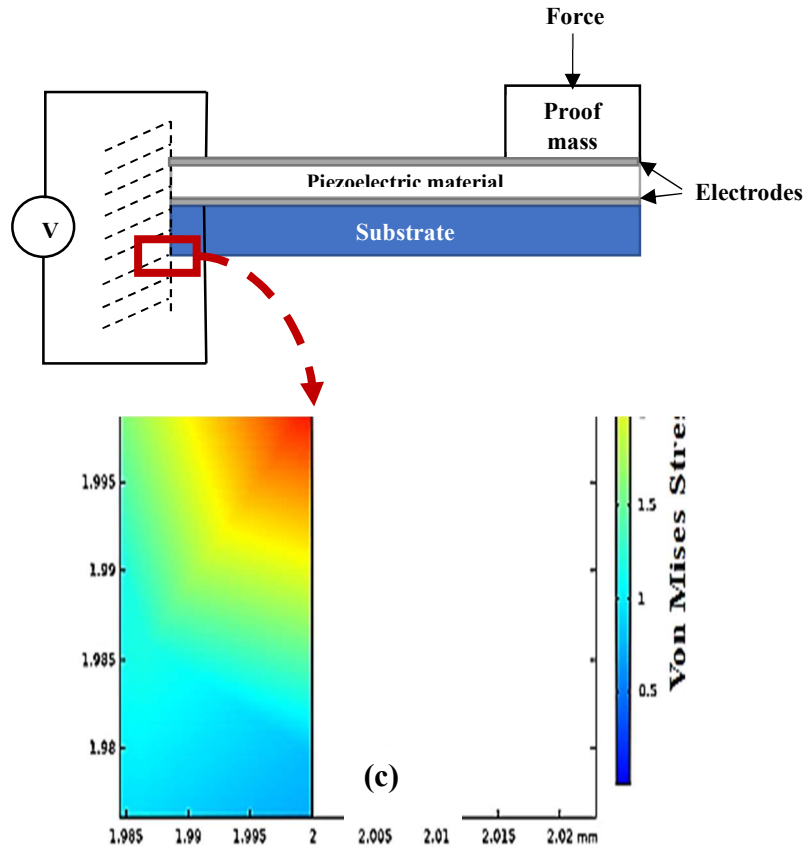


Figure 3.8: (a) Resonance frequency (f_r) vs proof mass weight (b) Max. stress developed vs proof mass (c) stress distribution inside the Si cantilever beam obtained from FEM at $1g$ acceleration.

3.7 Equivalent Circuit model of Piezoelectric Energy Harvester (PEH)

This part of the work was done at INSA Lyon under the supervision of Prof. Michael Lallart, during the secondments under the collaborative framework of ITN-ENHANCE.

A piezoelectric energy harvester (PEH) converts the mechanical vibration energy into AC electrical power. Since the storage devices such as supercapacitors and rechargeable batteries generally need a DC power supply. A rectification and power conditioning circuitry are necessary to rectify the AC power to stable DC power [47]. The overall performance of the piezoelectric devices can be evaluated by the global parameters represented in the form of an electromechanical equivalent circuit [190]. This work aims to model the PEH by a one-dimensional electromechanical circuit inspired by Mason's model [177]. The first part is devoted to the derivation of global parameters of the PEH experimentally from the impedance analysis using an impedance analyzer. The analogies between electrical and mechanical systems are used to obtain

the full Masons piezoelectric electromechanical equivalent circuit model which can precisely describe the global performance of the device. The model is validated by comparing the experimental results with the LT-Spice simulation. Then, the optimal load resistance for the maximum power harvest is obtained through experimental methods and is compared with the simulation using the electromechanical equivalent circuit. Finally, the voltage doubler rectifier is implemented, and the results are compared with the LT Spice model under given base excitation and operating frequency for a given load. The equivalent circuit models with an overall impedance Z_{in} can be used for the analysis and design of piezoelectric systems. The equivalent circuit model is based on an analogy between mechanical and electrical state variables. The first model of the piezoelectric transducer was proposed by W.G. Cady (1922) [191] which was later expanded by Van Dyke (1925), that introduced mechanical losses indicated by a resistor R suggesting an RLC-series network in parallel to the capacitor of the electrical system as shown in Figure 3.9 [190]:

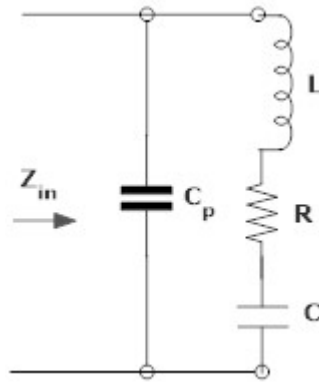


Figure 3.9: Van Dyke model for the electrical part of the piezoelectric element [192]

C_p is the capacitance of the PEH. Generally, the leakage resistance R_p is large and several orders of magnitude higher than capacitive impedance and is neglected. The parameters used in models (C_p , L , R , C) are extracted using impedance analysis and are represented in the form of Mason's equivalent circuit. The “global” state variables of the system are force F , displacement x , charge flow Q , and voltage V . The quasi-static electro-mechanical behavior of a piezoelectric system can, on a global scale, be described by [190]:

$$F = K_s x - \alpha V \quad 3.8$$

$$Q = \alpha x + CV \quad 3.9$$

where K_s is the mechanical stiffness of the system with short-circuited electrodes. The electro-mechanical coupling is expressed by the coupling factor α which has the dimension N/V or As/m. Using mechanical (or electrical) standard elements, Equations (4.8 and 4.9) can be displayed as a system of electrical components and transformers as shown in Figure 3.10. Considering the analogies between the electrical and the mechanical domains, the mechanical force is considered to be analog to the electric voltage and the velocity is equivalent to the electric current. The parameters describing the electrical properties are the shunted capacitance C_p and resistor R_p , which represents dielectric losses. Mason (1935) introduced an ideal transformer (N turns ratio) [190]. In the mechanical circuit that can be represented by an ideal lever with a coupling factor α of dimension [N/V] as shown in Figure 3.10. This model decouples the mechanical and electrical sides of the harvester and, thus, it is made possible to predict the electrical output with various load resistance conditions and to optimize the power harvested and conditioning circuit.

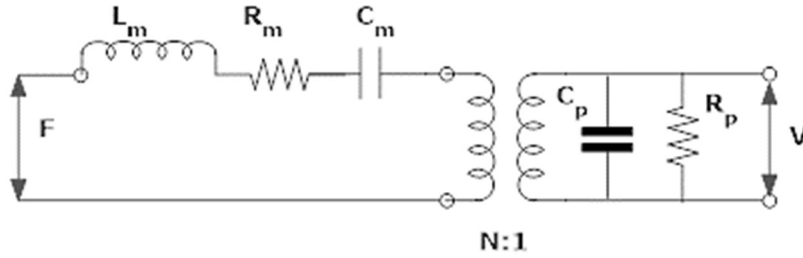


Figure 3.10: Mason's model with both electrical and mechanical side of the PEH coupled by a transformer [193]

On the mechanical side, a voltage generator ($F = m a$) represents the effective force induced by the base vibration acceleration a where m is the effective mass term. The equivalent inductance L_m indicates the modal mass (m) of the first mode. The resistance R_m and the capacitance C_m represent the mechanical damping (dm) and stiffness ($1/c_m$) of the beam respectively. The electromechanical coupling is represented as a transformer with the turn-ratio N representing the piezoelectric coupling coefficient α .

3.7.1 Experimental Parameter Identification

As a first step, the amplitude and phase of the impedance of the device are estimated using the impedance analyzer. For the electrical side, the electrical circuit parameters of the PEH in the Van Dyke model (Figure 3.9) are estimated using the impedance measurements as shown in Figure 3.11.

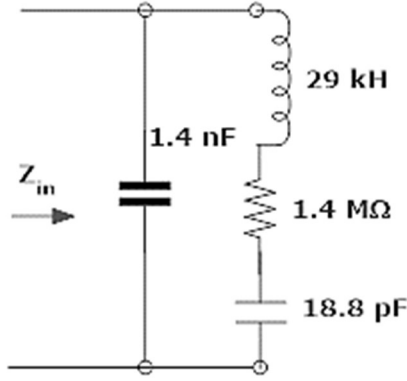


Figure 3.11: Van Dyke model of the electrical side determined from the impedance analysis

Here, the mechanical branch has been converted to the electrical side resulting in the Butterworth–Van Dyke topology. For the mechanical side, to obtain the mechanical parameters (m , d and $1/cm$) in electrical equivalent form (L_m , R_m , $1/C_m$) the conversion factor α is used [193]:

$$R_m = \alpha^2 R \quad 3.10$$

$$1/C_m = C\alpha/\alpha^2$$

$$L_m = \alpha^2 L \quad 3.11$$

To determine the parameter α the PEH is fed by a sinusoidal voltage with peak amplitude V in open circuit condition, ($V=11.4$ V). The vibration amplitude peak (x) is measured using a Laser setup, ($x=31$ μ m). The system is mechanically unloaded, i.e., $F=0$. The capacitance C is determined from the impedance analyzer, ($C=1.4$ nF).

From the equation (8):

$$\frac{dQ}{dt} = \alpha \frac{dx}{dt} + C \frac{dV}{dt} \quad 3.12$$

In open circuit $I_p = 0$,

$$\alpha \frac{dx}{dt} = C \frac{dV}{dt} \quad 3.13$$

$$\alpha = \frac{CV}{x} = 4.9 \times 10^{-4} \quad 3.14$$

Table 3.2: Extracted parameters

Parameters	C_0	C	C_m	R	R_m	L	L_m	α
	1.4 nF	18.8 pF	78 uF	9 M Ω	300 m Ω	29 kH	7 mH	4.9×10^{-4}

The final equivalent circuit is given in Figure 3.12:

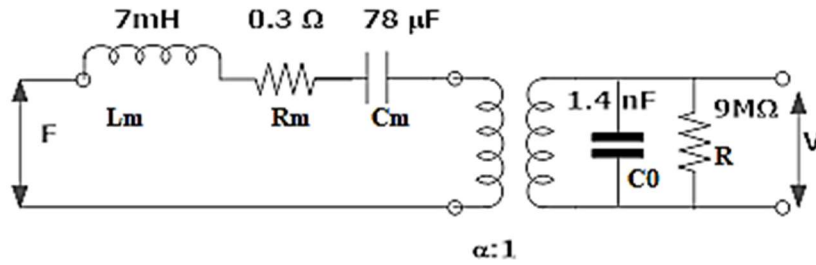


Figure 3.12: Mason's equivalent for the PEH

3.7.2 Analysis of the impedance of the equivalent circuit in SPICE

The validity of the extracted equivalent circuit of the device is ascertained by performing the impedance analysis in LT-Spice (XVII) (Figure 3.13) using model parameters extracted from the experiment are listed in Table 3.2 and comparing it with the experimental impedance analysis results obtained using an impedance analyzer for the given frequency range of 100-300 Hz.

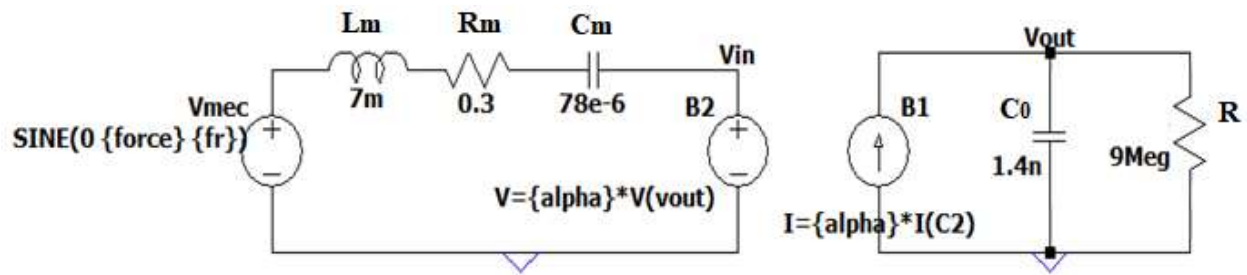


Figure 3.13: Spice model for the electromechanical equivalent circuit (transformer is replaced by an alternate current-controlled voltage source).

The Spice simulation of the full Mason's model closely agrees with the theoretical impedance of the reduced circuit as well as the experimental results obtained from the impedance analyzer as shown in Figure 3.14.

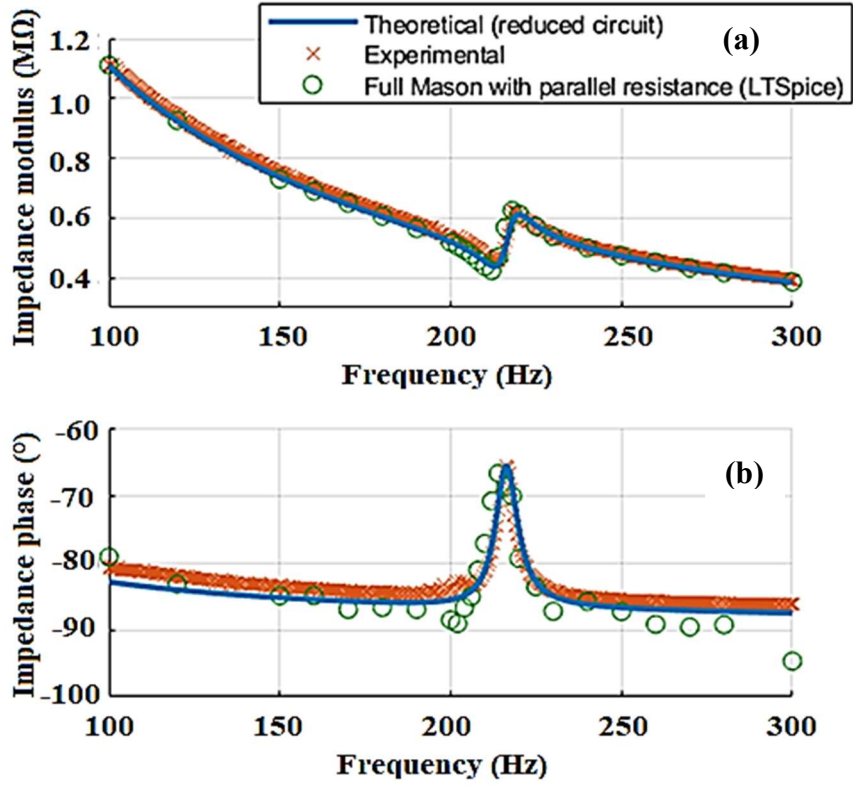


Figure 3.14: Comparison of the (a) impedance modulus and (b) phase from theoretical (reduced circuit), experimental, and full Mason's model in Spice.

3.8 Estimation of the mechanical quality factor (Q_m) and coupling coefficient K with proof mass

At resonance in PEH, mechanical losses are the most significant. The mechanical quality factor Q_m , therefore, is used as a figure of merit for losses in piezoelectric materials.

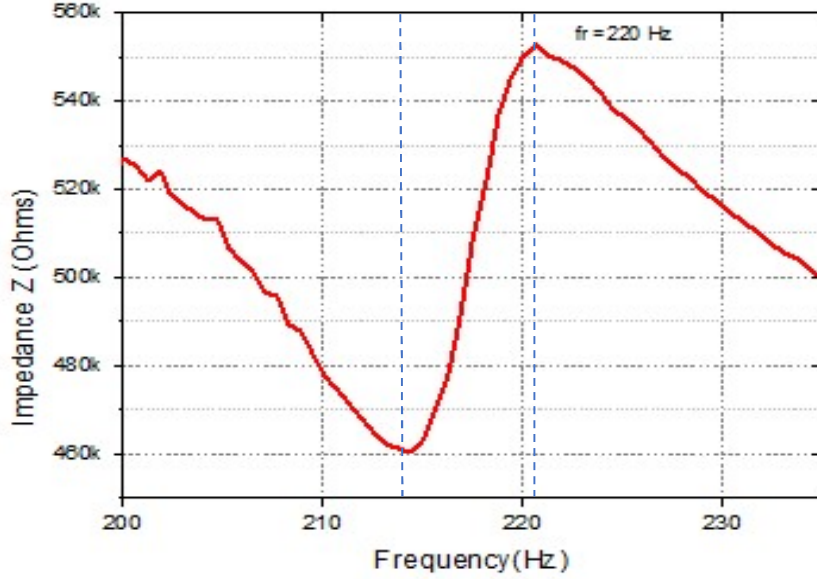


Figure 3.15: (a) Resonant frequency $f_r = 220$ Hz at $Z_{max} = 540$ k Ω and (b) antiresonant frequency $f_r' = 214$ Hz at $Z_{min} = 460$ k Ω respectively.

Taking a narrow frequency range close to the resonance (f_r) in Figure 3.15, the resonance quality factor (Q_R) is determined to be 44 [185]. The electromechanical coupling factor $k_{31} = 0.26$ is obtained using the following equations defined in the IEEE standards [182], [187]:

3.9 Optimal load resistance for maximum output power

One of the most important characteristics of an energy harvesting circuit is the maximum power output P_{out} . The harvested power can be maximized, when the input impedance of the harvesting circuit matches the output impedance of the PEH. Since a piezoelectric generator exhibits a large capacitive reactance, a complex conjugate matching requires a large inductance for the load to cancel the capacitive term. An alternative solution to complex conjugate matching is to adopt resistive matching. The optimal load resistance R_{opt} at which maximum power P_{max} is delivered is determined theoretically and is compared with experimental simulations.

3.9.1 Theoretical prediction

The voltage on the piezoelectric element can be expressed in the frequency domain as a function of the displacement, where ω is the angular frequency [194]:

$$V = \frac{\alpha R}{1 + jRC\omega} (j\omega u) \quad 3.15$$

where α is the electromechanical conversion coefficient, C is the parallel capacitance, and u is the amplitude of the displacement of the beam. The theoretical harvested power P is given by:

$$P = \frac{V^2}{2R} = \frac{R\alpha^2\omega^2u^2}{2(1+(RC\omega)^2)} \quad 3.16$$

it is possible to give a general expression of the harvested average power P as a function of the external force amplitude F , the load R , and the various model parameters

$$P = \frac{F^2}{2} \frac{R\alpha^2}{1+(RC\omega)^2} \frac{1}{\left(C + \frac{R\alpha^2}{1+(RC\omega)^2}\right)^2} \quad 3.17$$

In this case $\alpha = 4.9 \times 10^{-4}$ (table 4.2).

So, $\frac{R\alpha^2}{1+(RC\omega)^2}$ term can be neglected, which leads to a simplified expression of the theoretical harvested power P reaching a maximum P_{max} for an optimal load R_{opt} :

$$P = \frac{R\alpha^2F^2}{2C^2(1+(RC\omega)^2)} \quad 3.18$$

$$R_{opt} = \frac{1}{C\omega} \quad 3.19$$

3.9.2 Experimental determination of optimal load

The PEH was excited by an arbitrary acceleration and the optimal load was determined by varying the load resistance R_{load} and obtaining the output power P_{RMS} for different load resistances as shown in Figure 3.16. The terminal output voltage (V) was measured for different load resistances (R_{load}) and RMS power (P_{RMS}) was determined from:

$$P_{RMS} = \frac{V^2}{2R_{load}} \quad 3.20$$

3.9.3 Optimal load by LT-SPICE

The optimal load at resonant frequency was simulated by the transient analysis of the full Masons equivalent circuit (Figure 3.13) by LT Spice at different load resistances (R_{load}) at the resonant frequency. The optimal load was also determined experimentally. The PEH is excited by an

arbitrary acceleration and the terminal output voltage (V), and RMS power (P_{RMS}) dissipated in the load was determined as shown in Figure 3.16.

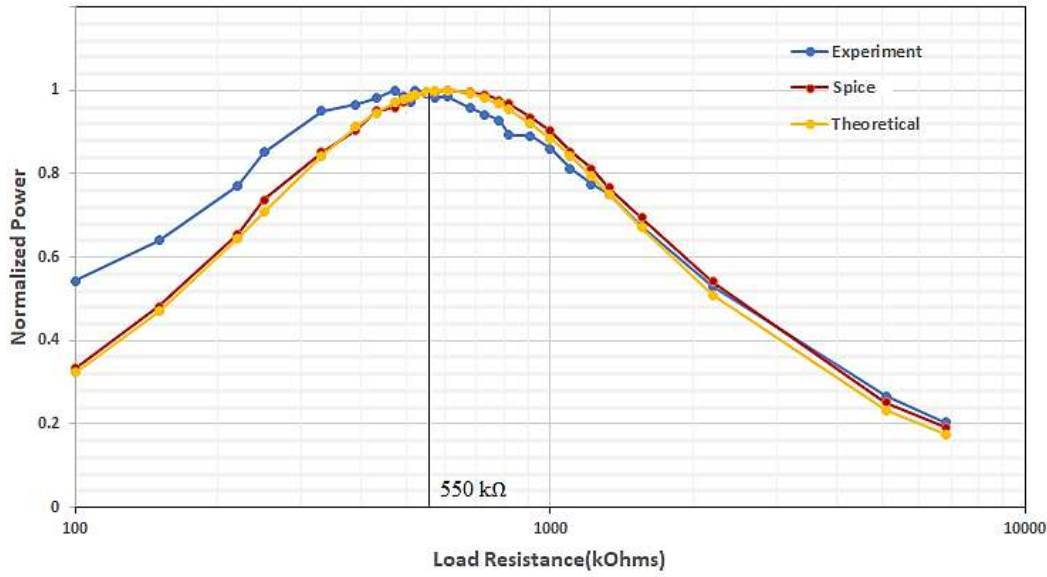


Figure 3.16: Normalized harvested power vs load resistances for different models

The optimal load vs normalized power for the simulation, experimental and theoretical results are shown in Figure 3.16. The spice simulations, experimental results closely agree with the theoretical model of the harvester indicating the optimal load $R_{opt} \sim 550 \text{ k}\Omega$.

3.10 Output Voltage and RMS power of the harvester

The open circuit voltage V_{oc} response and power (P_{PEH}) are determined by the shaker system, TIMA Lab, FMNT. It consists of a vibration exciter (electrodynamic shaker, Signalforce DataPhysics), an accelerometer with a charge amplifier (PCB Piezotronics 355B04), a 100 W power amplifier (PA100, DataPhysics), an oscilloscope a signal generator (Agilent 335095B), and along with the data acquisition software to display the output in the computer. The schematic and photo of the experimental setup are shown in Figure 3.17. An accelerometer is fixed on the vibration exciter together with the PEH device for the acceleration measurement. The signal from the signal generator is amplified by the power amplifier and set the vibration amplitude and frequency of the shaker. The output voltage signal from the PEH corresponds to the input signal from the signal generator which is recorded to the oscilloscope and acquired by the software.

Simultaneously, acceleration will also be amplified by the charge amplifier and then shown on the monitor of the computer.

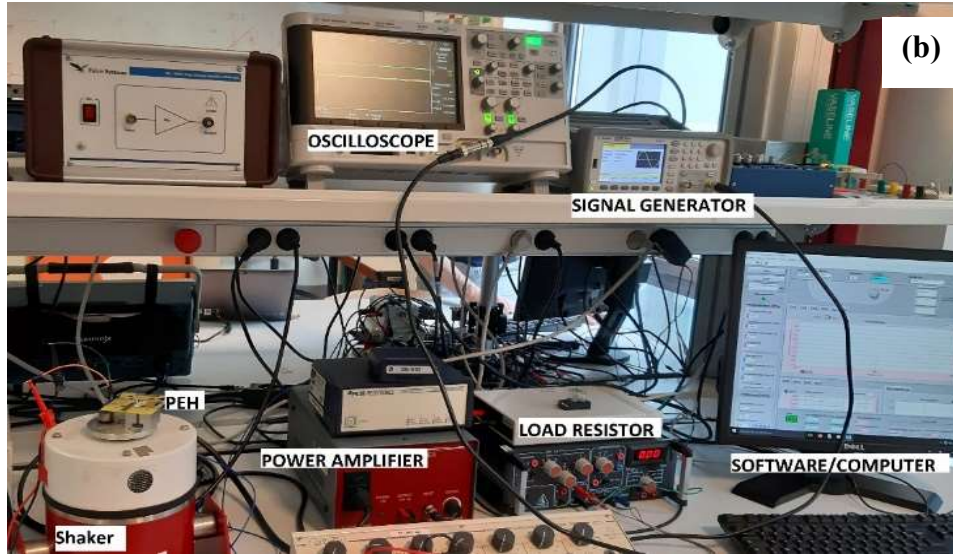
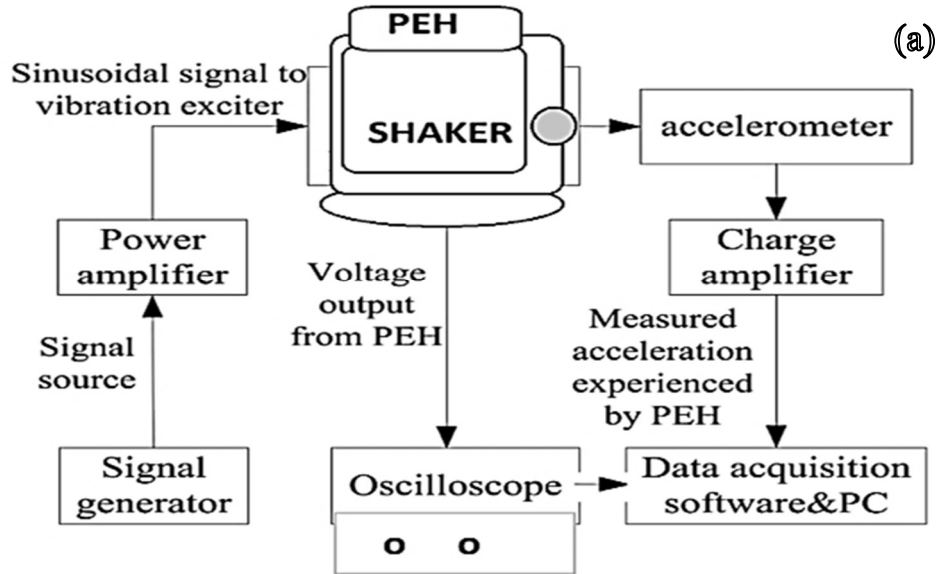


Figure 3.17: (a) Schematic and (b) photo of the shaker experimental setup.

3.11 Test Results and Analysis

The peak output voltage V and RMS power P_{RMS} at various accelerations from 0.2 g to 1 g at the optimal load $R_{opt} = 550 \text{ k}\Omega$ are presented in Figure 3.18. For the resonant peak at the optimal load, the peak voltage V and RMS power (P_{RMS}) at 1 g are found to be close to 6 V and 35 μW respectively.

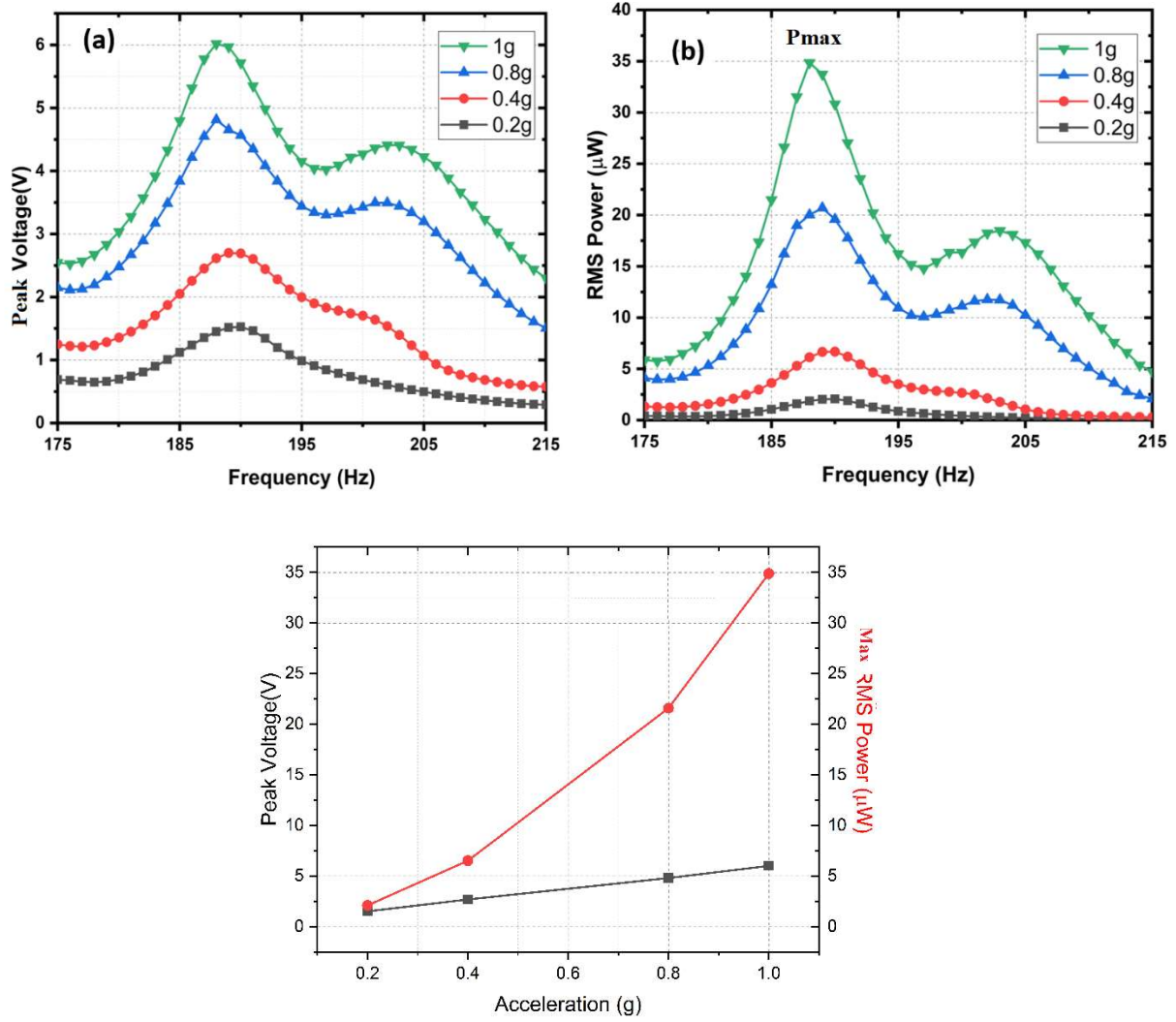


Figure 3.18: Experimental results: (a) RMS power and (b) voltage at optimal load for the frequency range 175 Hz to 215 Hz (c) Peak Voltage and maximum RMS Power for various input accelerations from 0.2g to 1g.

In several application scenarios, the input vibration spectrum of the PEH fluctuates. For instance, the vibration frequency range of a water pump in a combined heat and power plant varies in the range of 210 Hz to 219 Hz (~5%) as the speed of the pump changes [195]. Therefore, the power bandwidth BW, an important parameter to determine the operating frequency range is defined by the half-power cut-off frequencies f_{B1} and f_{B2} (for which $P_{PEH} = 0.5 P_{PEH_max}$) as [196]:

$$BW = \frac{f_{B1} - f_{B2}}{f_0} \quad 3.21$$

where, f_0 is the corresponding frequency at maximum power P_{PEH_max} . The device has a full width half maximum bandwidth of 10.8% at resonance. This is a clear advantage as it can be used to extract energy from a broader spectrum of the input frequency. The overall power density of the PEH-PM can be estimated to be $36 \mu\text{W}/\text{cm}^2/\text{g}^2$.

Table 3.3 Performances of the fabricated prototype and comparison to the highly coupled state-of-the-art PEHs in terms of operating frequency, power and bandwidth.

Piezoelectric Material	Power (μW)	Acceleration (g)	F_r (Hz)	Q_m	K^2_{31}	Bandwidth
PZT[197]	670	5.6	253	50	15.4%	7.5%
PZT[198]	90	0.4	152	95	6.7%	10.5%
PMN-PT[178]	0.58	0.019	29	130	16%	10.1%
PZN-PT[199]	1.3	0.017	32	91	16.4%	11.3%
PMN-PT[199]	32.7	0.1	31	58	17.6%	8.4%
LN(This work)	35	1g	187	44	7.2%	10.8%

3.12 Power harvesting circuit for Piezoelectric Energy Harvester

The load requires a stabilized DC voltage and the output of the PEH is AC, the desired output needs to be rectified, filtered, and regulated to ensure the usable power output for various applications. Several types of electronic interfaces have been proposed in literature such as standard model, series and parallel Synchronized Switch Harvesting on Inductor (SSHI), Hybrid SSHI, Double Synchronized Switch Harvesting (DSSH) etc.[200]–[202] for collecting the DC output, based on the coupling (K^2Q_m) of the device [203]. The concept of nonlinear circuits or synchronized switch harvesting on inductor (SSHI) has shown significant improvement in power extracted from the PEH for relatively low coupled systems with $K^2Q_m < 2$. In comparison to the standard rectifier circuit, the parallel SSHI circuit provides higher output voltage. The optimal load resistance is also higher in parallel-SSHI, than with the standard rectifier circuit. This voltage

amplification property may be used to get high voltages, or to reduce the energy losses related to the voltage drop of the diodes in the rectifier bridge. This is particularly interesting in the case of low-voltage PEH microsystems, whose open-circuit voltage is typically lower than 1 V. In series SSHI, the output voltage and the optimal load resistance are smaller than those of the standard rectifier circuit. The DSSH circuit implementation is complicated than both the SSHI and standard circuits. The performances of DSSH is better than that of the standard and SSHI techniques in the case of PVEH with small K^2Q_m . In our case, the K^2Q_m is determined to be nearly equal to 3, therefore, we have chosen the standard rectification scheme employing a full bridge as shown in Figure 3.19, since the standard rectification circuit is more efficient when the $K^2Q_m > 2$ [82]. To maximize the efficiency of rectification, the forward conduction voltage of the voltage rectifier diode V_f must be as low as possible. However, since the current harvested by the PEH is low in the order of microamperes, the diode reverse current I_r should be as low as possible. Therefore, there is a compromise between the forward voltage and reverse current performance of the diode and for this reason, an ultra-low leakage diode (FJH1100) with a maximum reverse current of 10-30 pA, and a forward voltage V_f of 0.6 V with a forward current of 10 μ A is chosen. The charging profile across a 220 μ F capacitor at 1 g acceleration is shown in Figure 3.20. The PEH could charge the capacitor to nearly 6 V in 500 s.

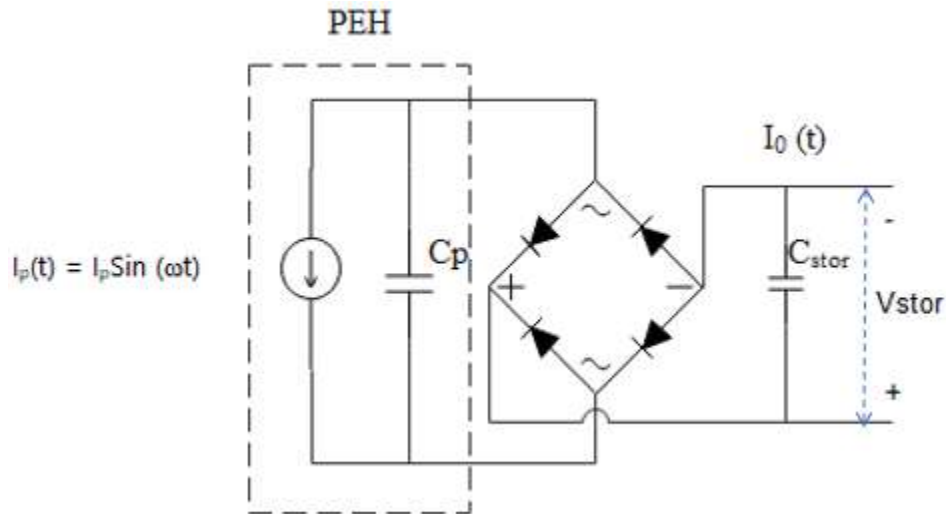


Figure 3.19: Standard rectification scheme with a full bridge rectifier

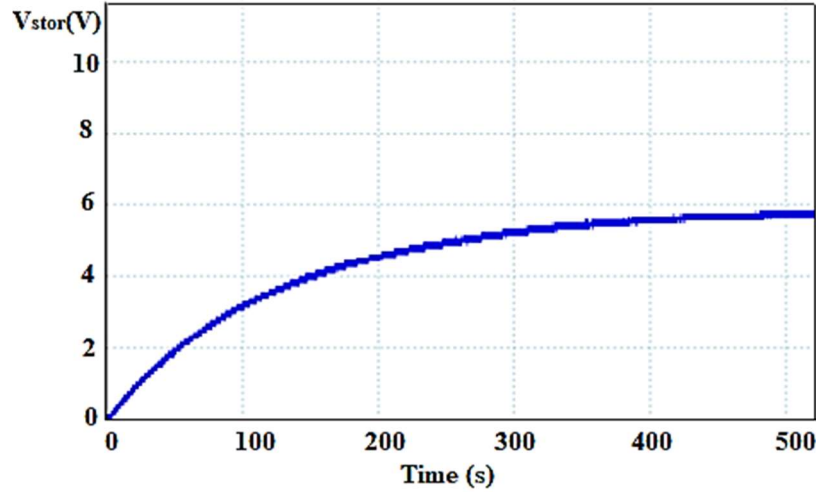


Figure 3.20: Charging voltage profile across a 220 μ F capacitor after rectification at 1 g acceleration.

3.13 A novel three-terminal harvester concept with Maximum Power Point Tracking (MPPT) for ultra-low power applications

3.13.1 Introduction

The amount of power generated from a PEH system mainly depends on the factors, such as input frequency and amplitude of the input vibration. The variations in input vibrations change the optimal operating point or the Maximum Power Point Tracking (MPPT) of a PEH significantly with time [52], [78], [204]. Since the microgenerators produce power in the order of microwatts that is just enough to power the IoT nodes, its operation at the MPP irrespective of the input conditions such as frequency, acceleration, or load variations must be ensured. Several MPPT techniques have been investigated in literature for PEH systems to have automatic control of the optimal power delivery to the load [78], [205]–[209].

MPPT ensures that the voltage at the output of the converter (V_{load}) is properly regulated. The commonly used power conditioning architecture is based on the use of a bridge rectifier followed by a DC/DC converter whose duty cycle is determined by the MPPT as shown in Figure 3.21 [77], [210].

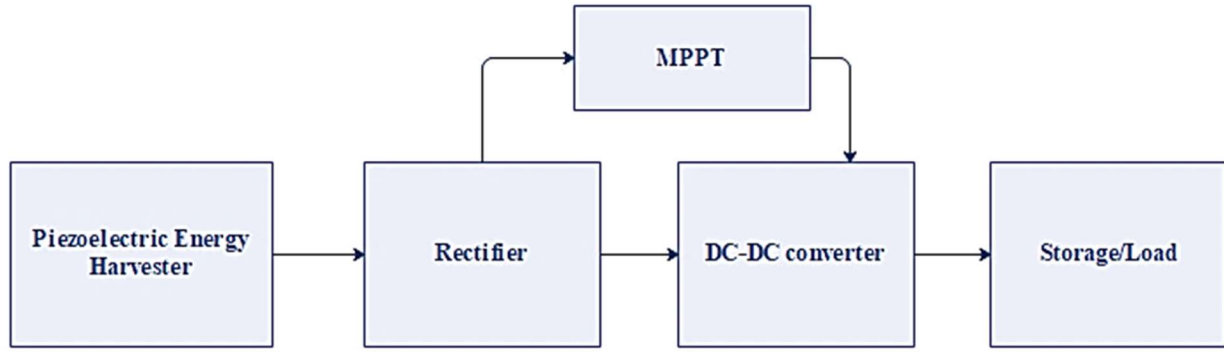


Figure 3.21: Functional block diagram of the piezoelectric Energy harvesting solution with an MPPT

Among various techniques for MPPT algorithms in energy harvesting, the hill-climbing method or perturb and observe method [209], [211] and the Fractional Open-Circuit (FOC) method [205], [206], [212] have been commonly used. In the hill-climbing method, the instantaneous output power is usually computed using a microcontroller by sampling the values of the current and voltage in real-time. Since V_{oc} is difficult to be measured when the PEH is connected to a load, the current flowing through the load is usually measured and used as the feedback signal to the controller. This necessitates the use of the complicated sampling circuit as well as the need for momentary breaking of the circuit, making this approach unsuitable for micro-scale energy harvesting. The FOC method is relatively simple and is based on the concept that the MPP voltage of PEH (V_{MPP}) is a fraction of its open circuit voltage (V_{oc}). The rectifier, that is used to convert the AC voltage from the PEH to DC, has an optimal output voltage (V_{MPP}) that is a fraction of the open circuit voltage (V_{oc}), that corresponds to the maximum harvested electrical power (P_{max}). In this method, the Maximum Power Point (MPP) voltage is computed by sensing its open circuit voltage (V_{oc}) in real-time.

Ottman et al. proposed MPPT schemes by using DC-DC converters and complex signal processing and intensive control algorithms to adaptively adjust the duty cycle of the DC-DC converters to match the load [212]. To reduce the power dissipation, the signal processor is replaced with discrete components and the step-down converter running at a fixed duty ratio. Chao et al. presented an MPPT scheme based on a time-multiplexing mechanism that adaptively senses the vibration status and directly generates an optimal output reference voltage of the AC-DC rectifier for maximum power harvesting [210]. Kong et al. [213] applied a dynamic resistive matching to

achieve MPP that employs a microcontroller unit, where the switch ON-time is sampled, and the required input resistance R_{in} is evaluated by software. But the system only evaluates R_{in} without precisely detecting the PEH output voltage. Similarly, Hu et al. [214] proposed a double-sampling technique, in which the V_{oc} is predicted based on the point-slope formula. With the increase in complexity of the circuit, MPPT tracking speed also varies. There is a trade-off between the complexity of the control circuitry that is used to determine the MPP and power consumption by this circuitry. Complex MPPT algorithms such as perturb and observe algorithms could increase the overall conversion efficiency of the system if the harvested power is relatively high (mW range). If a PEH (microgenerator) provides low input power levels (\sim tens of μ W), custom IC designs of simplified MPPT control schemes such as FOC might be a good option [215]. In ultra-low power applications, such as battery-free sensor nodes based on vibration energy harvesting, the level of power to be transferred is often so low that makes it quite difficult for the design of a typical MPPT circuitry efficient enough to consider its implementation worthwhile [216]. Therefore, it is necessary to design a viable energy efficient energy harvester circuit, minimizing the non-scalable losses in the circuitry, especially for low-power applications. Therefore, it should be noted that to use piezoelectric conversion with micropower applications, it is vital to develop a novel MPPT method that is simple and low-cost in approach and has an ultra-low power consumption. To make MPPT worthwhile in ultra-low power energy harvesting applications, a negligible portion of the harvested power has to be accounted for in the implementation of this function. Since this may represent a tough challenge for the IC designers, we mean to propose a novel three-terminal piezoelectric energy harvester with one of the terminals exclusively dedicated to sensing the open circuit voltage (V_{oc}). Thus, we explore a novel approach to the FOC method to determine the open circuit voltage (V_{oc}) in real-time using a third additional terminal that acts as a V_{oc} sensor. This approach can be advantageous as long as the V_{oc} sensing cell is designed with area occupancy smaller or even negligible compared to the main harvester so that the area being used for measurement purposes, rather than for energy production is insignificant. According to this designed harvester design, the loss in the produced power by the harvester, due to the presence of the sensing cell is less than 1%. From the system point of view, this loss in power and the presence of an extra pin may be compensated by various advantages, including the simplification of the circuit architecture associated with MPPT functions (such as pre-regulation, sampling, series switch and logic), and the relative reduction of the power

absorption. With this new concept of the harvester, the power management IC can be greatly simplified to a simple, ultra-low power comparator, used to compare the voltage provided by the main harvester with the voltage provided by the sensing cell used as a reference.

3.13.2 Theory and working principle

A vibrating piezoelectric element is electrically considered as a capacitive ac source which must be rectified at a desired DC voltage level before it is stored for powering an electronic device as shown in Figure 3.22. The maximum power that can be extracted by a PEH, in given vibration frequency f_r , closely depends on the value of the open circuit voltage V_{oc} and therefore there exist an optimal value of the load voltage $V_{MP} (= X*V_{oc})$ for harvesting the maximum power from the PEH, where X is a fraction. Based on load conditions or the input vibration conditions deviate, the VMPP changes and, therefore, it needs to be tracked by V_{oc} .

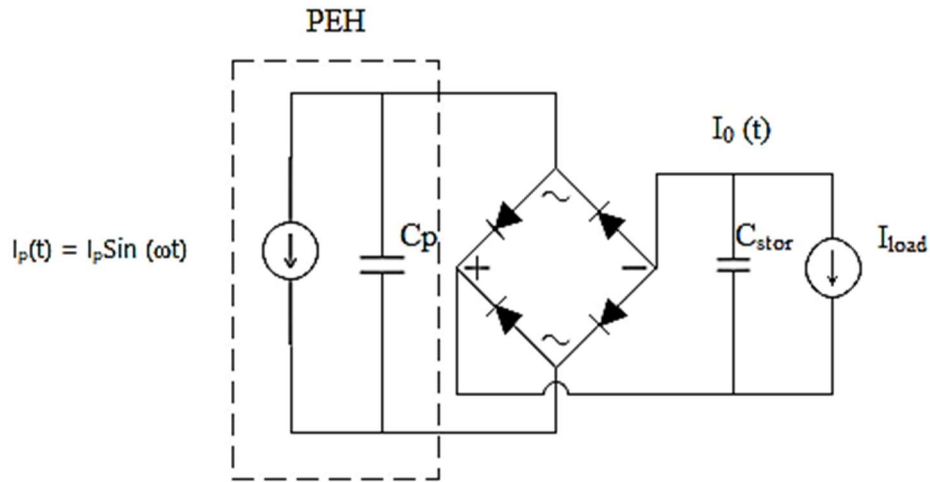


Figure 3.22: Simplified electrical equivalent circuit of a PEH with a rectifier

The system architecture of this harvester consists of two different sections, namely the main harvester, with larger area occupancy which contributes to the output power, and a sensing cell exclusively dedicated to sensing the open circuit voltage V_{oc} of the main harvester. Since the power transferred by the piezoelectric transducer is sensitive to the electrical load, the operating frequency and the applied mechanical power to be transduced, an effective MPPT is used to deliver power with the maximum efficiency to the external load (R_{load}) regardless of the variation of those parameters. The PEH converts the mechanical vibration energy into electrical energy corresponding to a sinusoidal mechanical excitation that is equivalent to an AC source $i(t)=I_p \sin$

$(2\pi ft)$ (Figure 3.22), connected in parallel with the internal capacitance C_p of the harvester where I_p is the peak current and $f=\omega/2\pi$ is vibration frequency of the harvester.

$$I_p(t) = I_p \sin(\omega t) \quad 3.22$$

A full-bridge rectifier then converts the AC output voltage of the PEH to a DC voltage the diodes are assumed to exhibit ideal behavior. A full bridge rectifier results in a forward voltage drop of 1.4 V. A fast switching diode with a minimum leakage current should be chosen. In the case of a 1N4148, the reverse leakage current is guaranteed to be less than 25 nA, making it an apt choice. Assuming that the capacitance of the rectifier is large compared to the internal parasitic capacitance C_p , $C_r \gg C_p$, most of the current I_p will be delivered. If $I_p(DC)$ is the DC component of I_p , and $I_r(DC)$ is the DC component of I_r , the net DC component of output $I_{out}(t)$ is given in terms as:

$$I_{out}(t) = I_p(DC) - I_r(DC) \quad 3.23$$

$$I_{out}(t) = \frac{2I_p}{\pi} - \frac{2V_r\omega C_p}{\pi} \quad 3.24$$

The output power (P_{out}) varies with the output voltage of the rectifier (V_r) as:

$$P_{out} = V_r * I_{out}(t) \quad 3.25$$

$$P_{out} = \frac{2V_r(I_p - 2V_r\omega C_p)}{(\pi)} \quad 3.26$$

where C_p is the internal parasitic capacitance of the PEH.

From 3.26, it follows that the peak output power occurs when:

$$V_r = \frac{I_p}{(2\omega C_p)} \quad 3.27$$

This is one-half the peak open-circuit voltage of the PEH. We utilize this concept that the maximum power transfer of a piezoelectric transducer to the load takes place at half the open circuit voltage (V_{oc}) of the harvester[216]–[218]. A DC-DC converter is introduced between the rectifier output and the storage that will enable the rectifier output voltage (V_r) held at its optimal value, which is one-half the open-circuit voltage of the PEH to achieve MPPT.

3.13.3 Design considerations

To implement the three-terminal PEH with this novel MPPT concept, we require two different sections namely:

- 1) the main harvester, with larger area occupancy that contributes to the output power along with
- 2) a smaller area sensing cell that is exclusively dedicated to sensing the V_{oc} .

Apart from the above requirements, we need to cater to certain design rules to implement the proposed idea. Firstly, the sensor cell and the main harvester should be working at the same resonance frequency, so that they work in phase synchronization and produce similar V_{oc} under the given mechanical excitation. One of the most important design parameters in designing a vibration energy harvesting device is the resonant frequency. The output voltage attains a peak value if the excitation frequency matches the resonant frequency of the cantilever. This reduces drastically when it changes from the resonant frequency of the device. Secondly, from the system engineering point of view, the area efficiency (loss of power due to the area consumed by the sensor cell) needs to be low. To satisfy the above design constraints, we have considered a harvester design with two top electrodes in the same harvester with the same length and thickness but with different widths, with the sensor cell occupying the minimum possible width.

3.13.4 The feasibility study of 3 terminal harvester

The feasibility of the 3 terminal MPPT Model was first analyzed by lumped parameter approach and verified by Finite element analysis in COMSOL Multiphysics. When a Piezoelectric material is mechanically deformed, an electrical charge is produced in it. The piezoelectric constitutive equations in IEEE standard in the strain-charge form are as follows [219]:

$$S = S^E T + dE \quad 3.28$$

$$D = dT + \epsilon^T E \quad 3.29$$

S : Mechanical strain.

S^E : Elastic compliance tensor (1/stiffness- N/m),

T : Mechanical stress vector (Nm⁻²)

E : Electric field vector (Vm⁻¹)

D : Electrical Displacement (Cm^{-2})

ϵ^T : Dielectric permittivity tensor (Fm^{-1})

d : Electro-mechanical coupling factor (CN^{-1})

A cantilever beam can have many different modes of vibration, each with a different resonant frequency. The first mode of vibration has the lowest resonant frequency, and typically provides the most deflection and therefore the most electric energy.

3.13.5 Bending-Mode Resonance Frequency

The bending-mode vibration of the unimorph obeys the following differential equation [220]:

$$D\Delta^2 h = \frac{-m_a \partial^2}{\partial t^2} \quad 3.30$$

The resonant frequency of this system (f_r) can be calculated by following equation:

$$f_r = \frac{1}{(2\pi L^2)} \sqrt{\frac{D_p}{m_a}} \quad 3.31$$

where, L is the length, m_a is the mass per unit area which depends on thicknesses and densities,

$$m_a = \rho_p t_p + \rho_s t_s \quad 3.32$$

ρ_p and ρ_s are the densities of the piezoelectric and substrate, material respectively. The bending modulus (D_p) is a function of Young's modulus (E) and thickness and is expressed by [220], [221]:

$$D = \frac{(E_p^2 t_p^4 + E_s^2 t_s^4 + 2E_p E_s t_p t_s (2t_p^2 + 2t_s^2 + 3t_p t_s))}{12(E_p t_p + E_s t_s)} \quad 3.33$$

where E_p and E_s are Young's modulus of piezoelectric and substrate materials and t_p and t_s their thicknesses.

$$f_r \propto \frac{\sqrt{t_p t_s}}{L^2} \quad 3.34$$

This relation shows that the resonant frequency is independent of the width of the unimorph cantilever and depends only on the length and thickness. Also the V_{oc} can be written as [222]:

$$V_{oc} = \frac{d_{ij}\sigma_{ij}g_e}{\epsilon_r\epsilon_0} \quad 3.35$$

Assuming that the same acceleration is experienced throughout the mass, which is homogeneous, the stress on the piezoelectric element can be given as the force experienced by unit area:

$$\sigma_{ij} = \rho g t_p \quad 3.36$$

g is the input acceleration, ρ the density and t_p the thickness of the piezoelectric layer. From equation (4.36), the open circuit voltage V_{oc} is independent of the width of the beam and proportional to the applied stress σ_{ij} , the piezoelectric coefficient d_{ij} , and the gap distance between electrodes g_e . ϵ_r and ϵ_0 are the relative dielectric constant and the permittivity of vacuum, respectively. The most important aspect of the MEMS piezoelectric generator is its capability to deliver an electric current because of the stress it is subject to. Because of the direct piezoelectric effect, the electric displacement inside the material caused by the mechanical stress is given by:

$$D = d_{31}\sigma_1 \quad 3.37$$

σ_1 is the stress in the beam. This relationship holds for an infinitesimal element of the film. To find the total electric charge generated because of the strain, it is necessary to integrate over all the film along the 3-direction and use Hooke's law as follows:

$$Q = \int D_3 dA_3 \quad 3.38$$

Since the amount of current delivered by the PEH, $I_p \propto Q$, the current scale linearly with the width. This shows that a cantilever beam can be designed to serve this purpose in such a way that along with a main cell that harvest the power, a reference cell with a smaller width can be employed to serve the purpose of sensing of V_{oc} . This will mean that we can sense the open circuit voltage in real time without the need for disconnecting the load as the sensor electrode is disconnected from the load all the time.

3.13.6 Finite element Analysis

The above model was verified by Finite Element Method (FEM) [223]. The variation of the open circuit voltage with various widths of the cantilever beam was simulated. The design under study was a unimorph cantilever structure with piezoelectric material Lithium Niobate, placed on a

silicon (Si) cantilever based on an SOI wafer on a 350 μm handle layer and 1 μm oxide layer as shown in Figure 3.23.

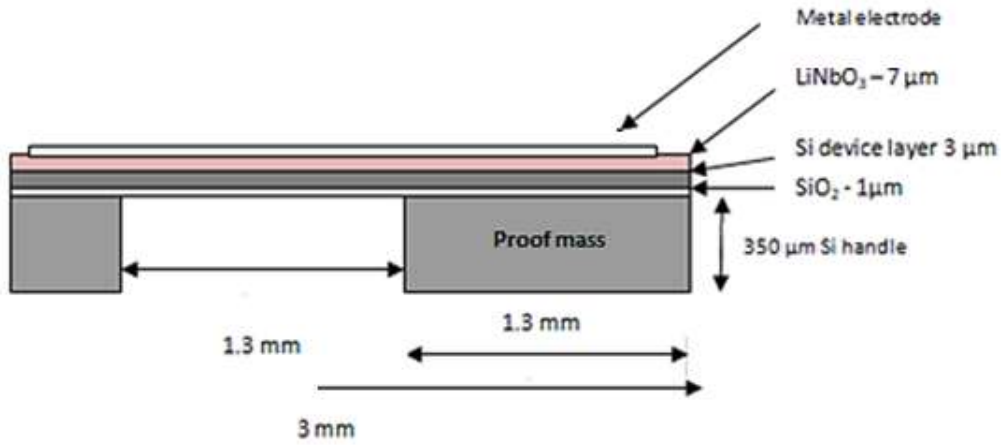


Figure 3.23: schematic of the PEH device simulation

3.13.7 Boundary Conditions

The device is modeled such that one end of the unimorph cantilever is fixed when the other is free to vibrate. The substrate is assumed to be linear elastic material that bends according to the stress produced. The fixed constraint condition is applied to the bottom face of the fixed handle layer, while all other faces are free to move. The d_{31} mode is selected by applying floating potential for the upper face and grounding the lower face of the piezoelectric layer while all other faces of the piezoelectric layer are kept at zero charge constraint. The body load is given an acceleration of 1g to the device to generate a strain.

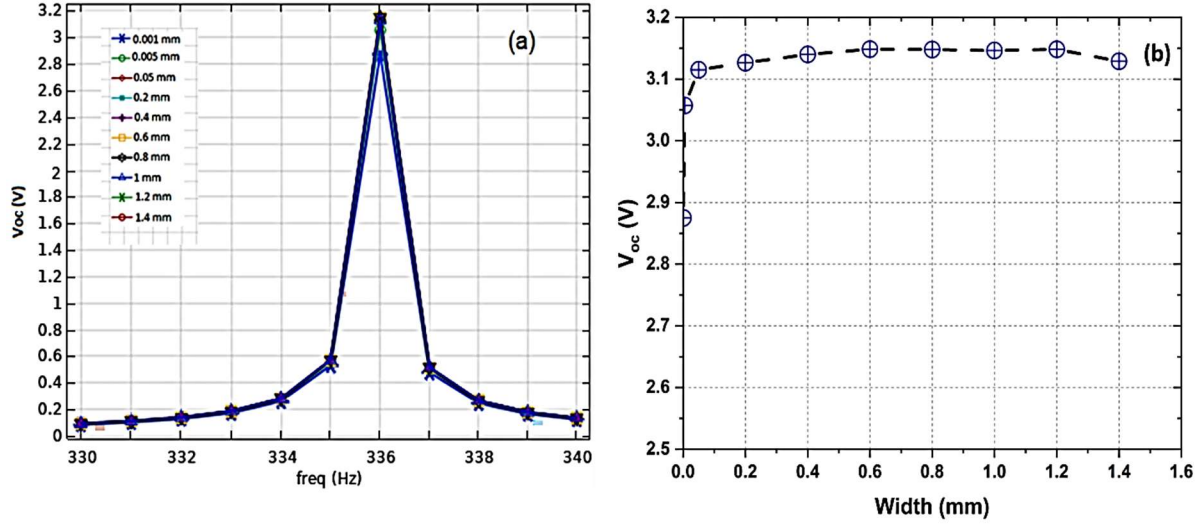


Figure 3.24: (a) open circuit voltage V_{oc} at various frequency ranges (b) open circuit voltage V_{oc} vs width of cantilever [52]

A sinusoidal mechanical force is applied as the input to the energy harvester. The open circuit Voltage (V_{oc}) and the output power are then evaluated as a function of frequency. The frequency response analysis was performed at 1g acceleration to determine the resonant frequency and the output voltage for different cantilever width at open circuit condition as shown in Figure 3.24. The output voltage was determined as a function of frequency and the results clearly indicate that the resonant frequency f_r and V_{oc} is independent of the width at open circuit condition ($R \sim \infty$). This implies that since V_{oc} and resonant frequency of a PEH is independent of the width of the cantilever beam, an electrode of minimum possible width and the same geometry harvester (thickness and length) of the main can be implemented as a sensor cell in order to supply the reference voltage to the low power comparator as shown in Figure 3.25.

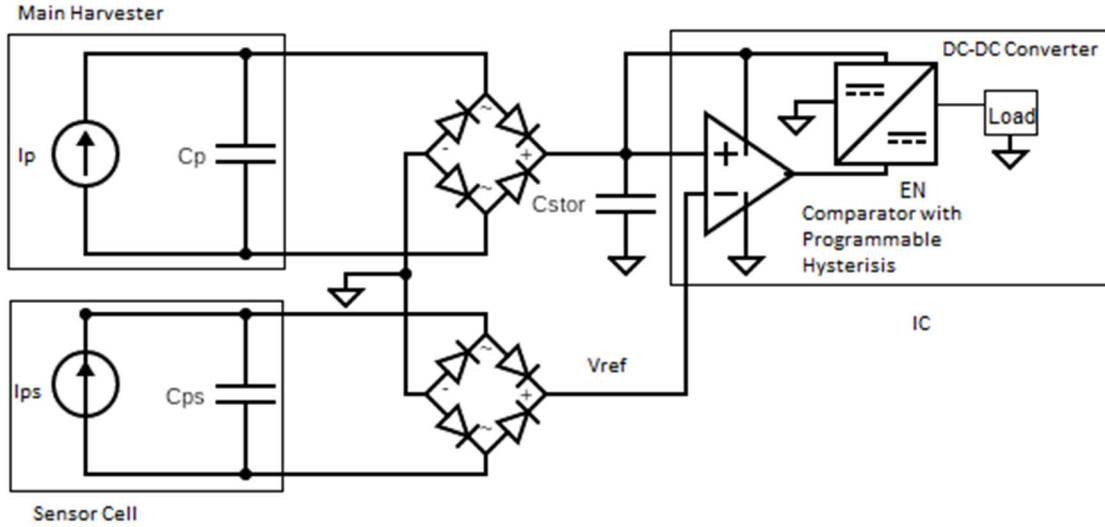


Figure 3.25: Proposed electrical schematic of the 3 terminal PEH with MPPT

However, due to the presence of the extra sensor cell that does not contribute to the overall power output of the system, there is a reduction in the system efficiency. Therefore, the additional loss due to the area consumed by the sensor cell and the gap between the main harvester and sensor cell was expressed in terms of area efficiency that is defined as follows:

$$\text{Area Efficiency} = \frac{A_{mh}}{A_{(W_s+W_{mh}+W_g)}} \quad 3.39$$

where, A_{mh} is the area main harvester and $A_{(W_s+W_{mh}+W_g)}$ is the overall area of a harvester without the reference electrode that takes into account of area of the sensor cell and the gap. The evaluated area efficiency was found to be 98% with a sensor cell of 50 μm and a main harvester cell of 4.9 mm in width.

3.13.8 Experimental results

A three-terminal harvester was designed and fabricated to test the theoretical model discussed in earlier section, considering a practical area efficiency of 98%. The harvester consists of Lithium Niobate (27 μm) as the active piezoelectric layer on Si substrate (525 μm) and gold top electrode. The dimensions of the harvester fabricated for testing are different from the simulated device, due to the intrinsic limitation in thinning down the LN below 27 μm . The LN is carefully scratched from the top using a diamond tip to obtain the bottom electrode. A Tungsten proof mass cube 0.125

cm³ (2.3 grams) is added to the free side end of the cantilever. The fabrication steps are detailed in section 4.2.

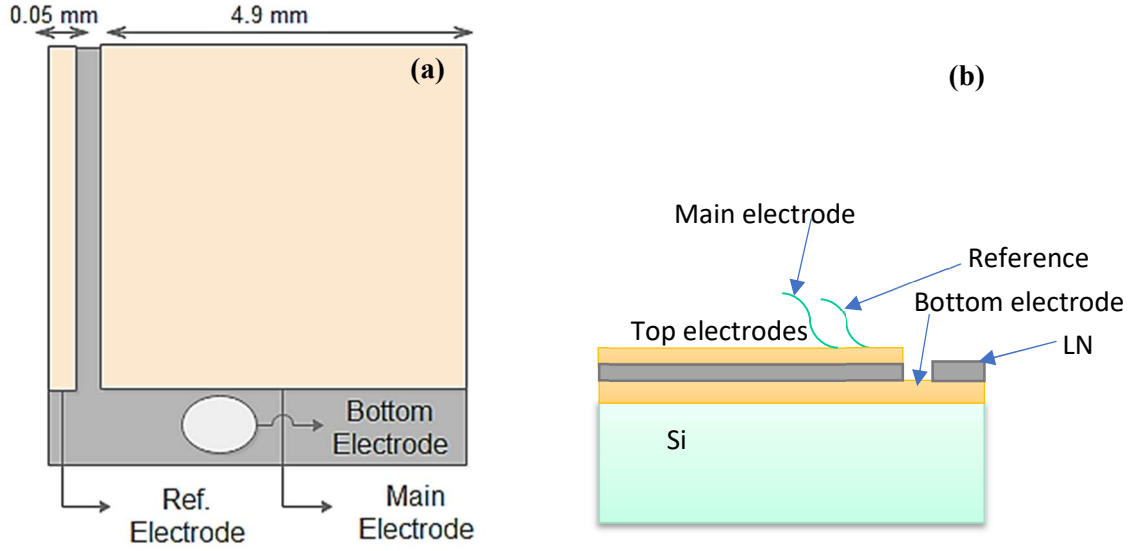


Figure 3.26: Illustration of the (a) top view (b) cross sectional view of the three terminal PEH

Table 3.4 Geometry of the 3 terminal PEH

Length cantilever (mm)	Width cantilever (mm)	Length electrodes (mm)	Width electrodes (mm)	Thickness Si (μm)	Thickness LN (μm)	Proof mass weight(g)
22	5	22	4.9 & 0.05	525	27	2.3

3.13.9 Measurement of Open circuit voltage

The measurement of open circuit voltage from the reference cell has some challenges due to its very high impedance due to its low surface area. The impedance of the reference (Z_{ref}) cell can be given as:

$$Z_{ref} = \frac{1}{\omega C_{ref}} \quad 3.40$$

$$C_{ref} = \epsilon \frac{A_{ref}}{d} \quad 3.41$$

where, ϵ is the permittivity, A_{ref} the reference electrode area and d the thickness of the piezoelectric material. Since the area of the reference electrode is nearly 1% of the main electrode, the impedance of the harvester is nearly 40 M Ω . The measurements with standard oscilloscopes (input resistance 1-10 M Ω) thus leads to a lower estimation of the voltage than actual measurements. Therefore, a buffer amplifier was implemented using an operational amplifier TL081 to isolate the measurement circuit from loading the device under test as shown in Figure 3.27.

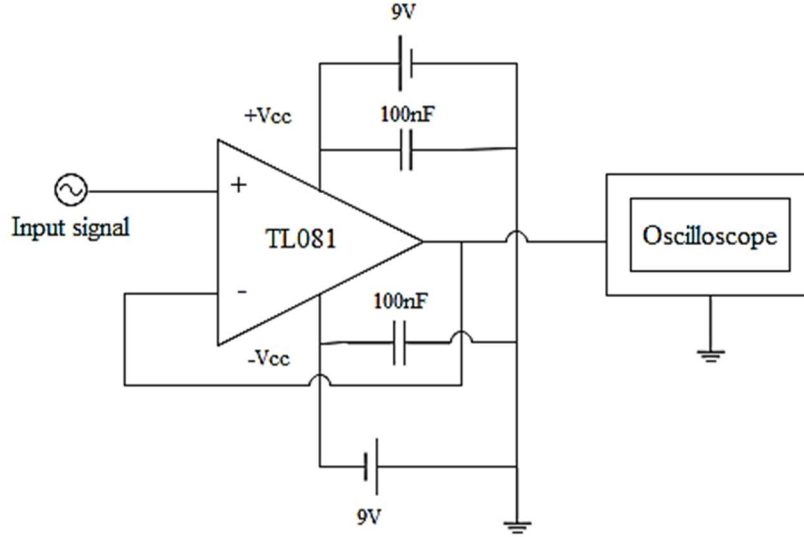


Figure 3.27: Circuit diagram of the measurement circuit with buffer amplifier with TL081 opamp

The open circuit voltage of the main and the reference electrode (with buffer circuit) was measured simultaneously using an oscilloscope by vibrating the harvester with a shaker setup at various accelerations. It can be observed that the peak open circuit voltage of the reference (V_{ref}) electrode is less than the open circuit voltage of main (V_{main}). The ratio of the open circuit voltage of the reference and the main electrodes for various accelerations from 0.1 g to 1 g is given in Figure 3.28. The ratio was found to be close to 0.8 for the given range of accelerations.

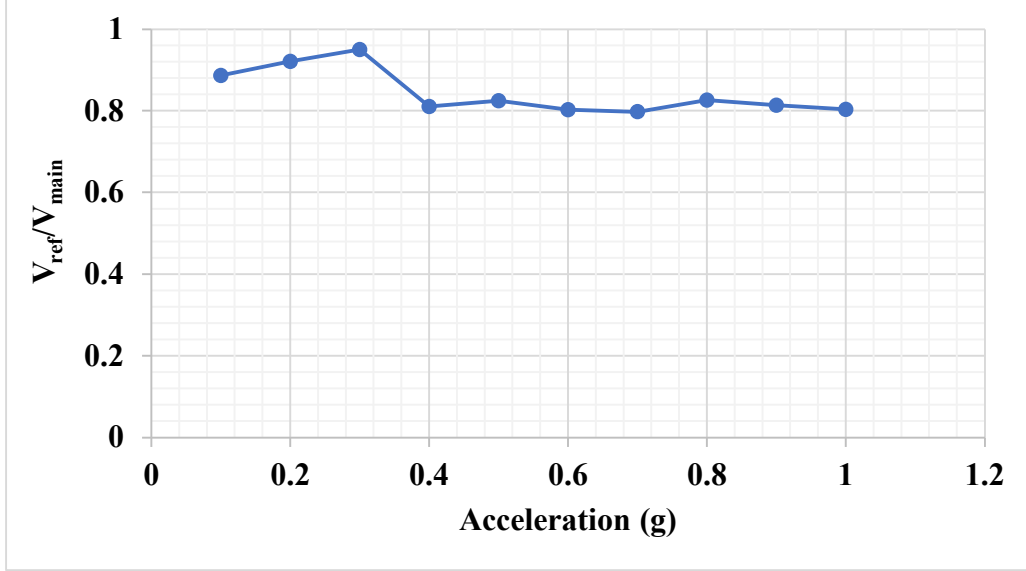


Figure 3.28: Ratio of the open circuit voltage from reference and main electrode for various accelerations from 0.1 g to 1g.

This proves that with the addition of the reference electrode, we achieve real-time tracking of the V_{oc} without unloading the main electrode without the need for disconnecting the circuit momentarily. The reference voltage can therefore be used to track V_{MPP} ($= 0.5 V_{oc}$) in real time without loading the main harvester, without the need for complicated sampling circuits and algorithms.

3.13.10 Conclusion

In summary, we have proposed a three terminal PEH that consists of a novel MPPT architecture whose primary purpose is to render MPPT worthwhile in sub microwatt power systems. With the proposed architecture Power Management IC (PMIC), the power harvesting circuit can be simplified to a minimal ultra-low power comparator without any oscillators, sensing or pre-regulation circuits. It leads to a considerable simplification of the PMIC circuitry at the expense of a small complication in the harvester structure. The feasibility of this new PEH was proven theoretically and verified by using finite element simulations and experimental results of the open circuit voltages. The resonant frequency f_r and the open circuit voltage V_{oc} are nearly independent of the width w of the cantilever beam provided the geometry parameters such as length L and thickness t remain the same. A PEH with a minimum process width can therefore be implemented as a V_{oc} sensor cell, to be used as a reference voltage for the MPPT circuitry of the PMIC, which in relation to the main harvester can contribute to a negligible power loss of less than 1%. Since

the ultralow power circuits is efficient only when implemented in ASIC rather than implemented with discrete components, the fabrication of a three terminal PEH based on the proposed design with the new MPPT architecture is being carried out, and in future, the performance will be compared with the existing MPPT architectures.

3.14 Summary

In summary, A unimorph single clamped cantilever based piezoelectric energy harvester based on a lead-free Lithium Niobate crystal has been designed and conceived and its performance was evaluated. By taking advantage of the addition of proof mass, the device operational frequency was tuned to be in the range of available ambient vibrations (~ 200 Hz). The harvester has a quality factor $Q=50$, and a high coupling $K^2Q_m=3$, giving an output voltage of 6V and an overall power density of the PEH was estimated to be $36 \mu\text{W}/\text{cm}^2/\text{g}^2$ at an optimal load of $\sim 550 \text{ k}\Omega$, at resonance. The device has a full width half maximum bandwidth of 10.8% at resonance. This is a clear advantage as it can be used to extract energy from a broader spectrum of the input frequencies.

The electromechanical Mason's equivalent circuit model was developed for the harvester from the impedance analysis and was simulated in SPICE. The validity of the model was confirmed with theoretical and experimental analysis. In addition, the optimal load for the harvester to deliver the maximum power was derived experimentally to be $\sim 550 \text{ k}\Omega$ and was compared with the theoretical and SPICE models. Furthermore, a comprehensive comparison between the proposed MEMS harvester and the recently published vibration energy harvesters from the literature shows that our conceived harvester is well comparable with the state of the art, to offer a promising vibration energy harvesting system for being deployed in the real environment from a lead-free aspect.

Further, a three terminal PEH has been proposed that consists of a novel MPPT architecture whose primary purpose is to render MPPT worthwhile. With the MPPT architecture, the Power Management IC (PMIC) and the power harvesting circuit can be simplified to a minimal ultra-low power comparator without any oscillators, sensing or pre-regulation circuits. The resonant frequency f_r and the open circuit voltage V_{oc} are found to be nearly independent of the width w of the cantilever beam provided the geometry parameters such as length L and thickness t remain the same. It is shown that a PEH with a minimum process width can therefore be implemented as a V_{oc} sensor cell, to be used as a reference voltage for the MPPT circuitry of the PMIC, which in relation to the main harvester can contribute to a negligible power loss of less than 1%. The

feasibility of this new PEH has been proven theoretically and verified by using finite element simulations and experimental results of the open circuit voltages at various accelerations.

In the next chapter, the Lithium Niobate based lead-free vibration energy harvester will be demonstrated to be used in a real-time application, in terms of an Energy Autonomous Wireless Vibration Sensor (EAWVS).

4 Energy Autonomous Wireless Vibration Sensor based on Piezoelectric Microgenerator

In this chapter, the harvester is demonstrated to power a battery free IOT-WSN based on Bluetooth Low Energy-(BLE) connectivity with ambient vibration is demonstrated. Also, the operating principle and system implementation of the Energy Autonomous Wireless Sensor (EAWVS) based on STM32 [12] microcontroller is detailed. The ability of the harvester in sensing input acceleration is demonstrated. Finally, the application scenario of the EAWVS is laid out.

4.1 Introduction

Autonomous Wireless sensors (WSNs) are the key part of an IoT system that collects and exchanges data remotely with the master node for ensuring smarter and faster wireless data transfer[15], [23]. IoT infrastructure makes wide use of WSNs that can perform simultaneously as sensors, communication and information process. However, currently, WSNs are mostly based on bulky, expensive batteries for powering that have limited charge/discharge cycles. This hinders the IoT devices to be used for their continuous and uninterrupted operation [224]. Further, in the case of heavy machinery, such nodes are often placed in locations that are difficult to reach, which require human interventions with specialized tools thus contributing to increasing costs. For powering such WSNs without the use of batteries, energy harvesting from ambient sources such as solar, vibration, thermal, and radiofrequency waves has been investigated in recent years [16], [225], [226]. Therefore, where possible energy-autonomous and battery-free WSN should be considered a suitable choice for a sustainable and autonomous IoT. In industries employing heavy machinery and automobiles, the failure of the components such as shaft may result in serious damage during operation [227]. Such faults can often be identified in real-time by monitoring the vibration pattern of the selected parts.

These vibration monitoring systems based on a non-contact technique employing WSNs could prove to be of great advantage over conventional contact methods that require a direct connection between a sensor and the control system. The non-contact techniques employed so far are based

on magnetostrictive sensors [227], [228], optical sensors [229], [230]. However, most of such non-contact sensors have limitations due to the requirement of an external battery source apart from the difficulties in operating in a harsh environment.

The use of a battery could be eliminated by introducing an energy harvester that harnesses energy from the location where the WSN is mounted. The harvester selection usually depends on the energy density of the available ambient energy source such as mechanical vibration, solar, electromagnetic, RF, etc. [8], [52], [231]. A piezoelectric transducer is one of the most convenient ways to convert the ambient mechanical energy of such structures into electrical energy. PEH can be a simple cantilever beam with a piezoelectric material and a substrate that can be used as a self-powered sensor that can monitor vibration and power the data transmission circuits simultaneously [232], [233]. In this chapter, we explore a battery-free system - Energy Autonomous Wireless Vibration Sensor (EAWVS) for monitoring the vibrations and faults which consists of a PEH, and a radio transmission system based on a Bluetooth Low Energy (BLE) scheme which is self-starting and fully autonomous. Since defective parts have a more pronounced acceleration profile than non-defective parts, this work introduces a failure detection methodology based on measuring acceleration and its deviation from nominal values of non-defective parts. The EAWVS consists of only a PEH for power supply and a Bluetooth Low Energy (BLE) radio for connectivity. The sensor node can be connected wirelessly to a Base Station (BS) that performs data processing and continuous data transfer to the cloud. BLE is used as the communication standard because of its low power consumption and the compatibility and ease of BLE use in portable devices to communicate with the WSNs. The sensor node is designed to transmit beacons intermittently, and thus the radio is shut down after every transmission to minimize the overall energy consumption. The peculiarity of this system is that the PEH plays the dual role of energy transducer and vibrational sensor. The fabrication and characterization of the PEH based on Lithium Niobate is discussed in chapter 4. The monitoring of the input vibration is realized by measuring the time between successive beacons, also known as advertising time (t_{adv}), emitted by the EAWVS radio to the BS as shown in Figure 4.1.

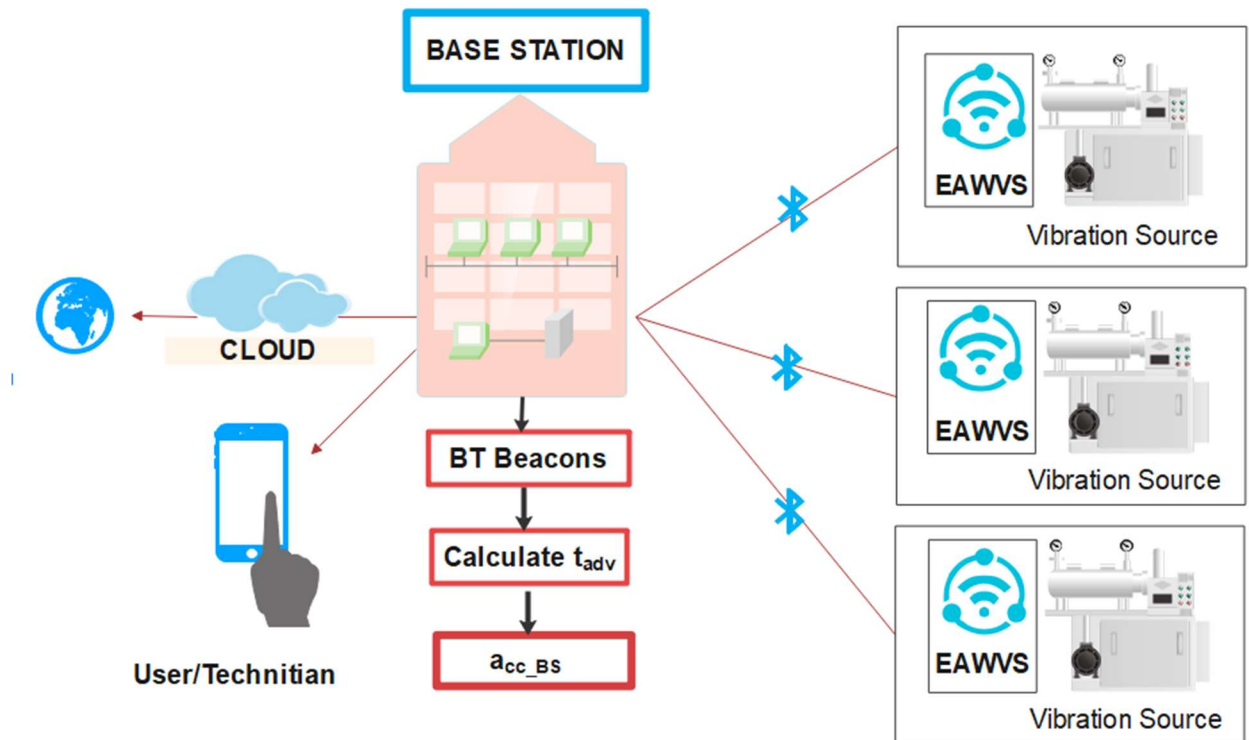


Figure 4.1: Application Scenario with BS and several EAWVSs

This method avoids the use of a specific sensor for vibration monitoring. The main advantage is to reduce power consumption and consequently also reduce the energy to be stored. Furthermore, it has the advantage of using fewer components and no need for a battery or supercapacitors with a consequent reduction in costs, dimensions, and weight. The EAWVS has a limit of detection (LOD) as low as 0.6 g and can successfully monitor the acceleration within an error limit of 15%. The fault detection can be performed by monitoring the rate of increase of the input acceleration is sensed by the EAWVS as the vibration characteristic of the parts under fault would experience a sudden surge in the amplitude of vibration. The chapter is organized as follows. Firstly, system description is given in terms of circuit implementation and functionality. Then, the design aspects of the PEH are discussed whose fabrication and characterization is described in chapter 4. It is followed by the techniques and the method based on energy to time conversion used to measure vibrations. Then finally, sensor calibration is discussed followed by the experimental results and conclusion.

4.2 System description

Figure 4.2 shows the block diagram of the system which includes the energy-autonomous wireless vibration sensor (EAWVS) and the receiving/base station (BS).

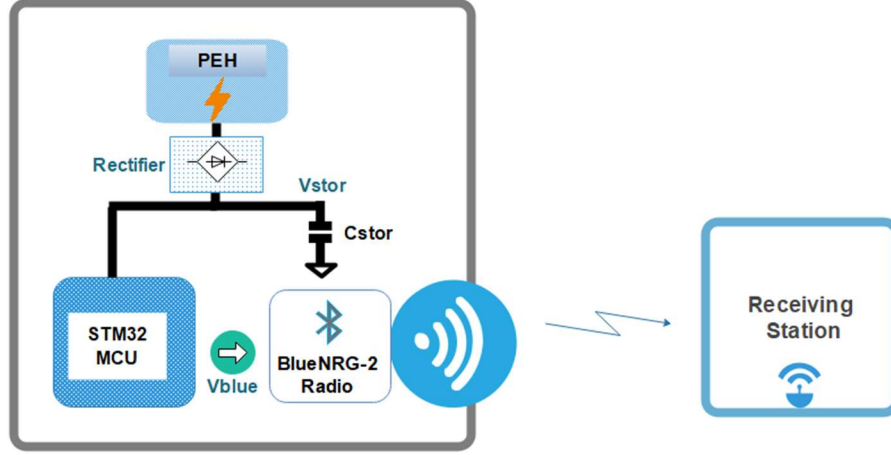


Figure 4.2: schematic of the EAWVS

The EAWVS consists of a piezoelectric energy harvester (PEH) that is used to convert the ambient vibration and kinetic energy into electrical energy. The harvested AC voltage is rectified using a bridge rectifier and is used to charge a capacitor, C_{stor} . The energy stored in the capacitor is used to power the Bluetooth Low Energy (BLE) radio system to transmit data from the EAWVS. The Bluetooth radio is implemented with the low-energy SoC BLUENRG-2 (provided by STMicroelectronics) as it consumes low power at low cost and provides easy connection and human interfacing via smartphone. The system implements a Programmable Voltage Detector (PVD) with the STM32L0 ultra-low-power microcontroller (STMicroelectronics). This circuit detects the voltage V_{stor} across the storage capacitor C_{stor} .

The BS is powered by a stable power source, such as a battery located remotely from the application target. Its function is to process the data received wirelessly by one or more EAWVSs and process the subsequent implementation phases to control the machinery, including sending data to the cloud.

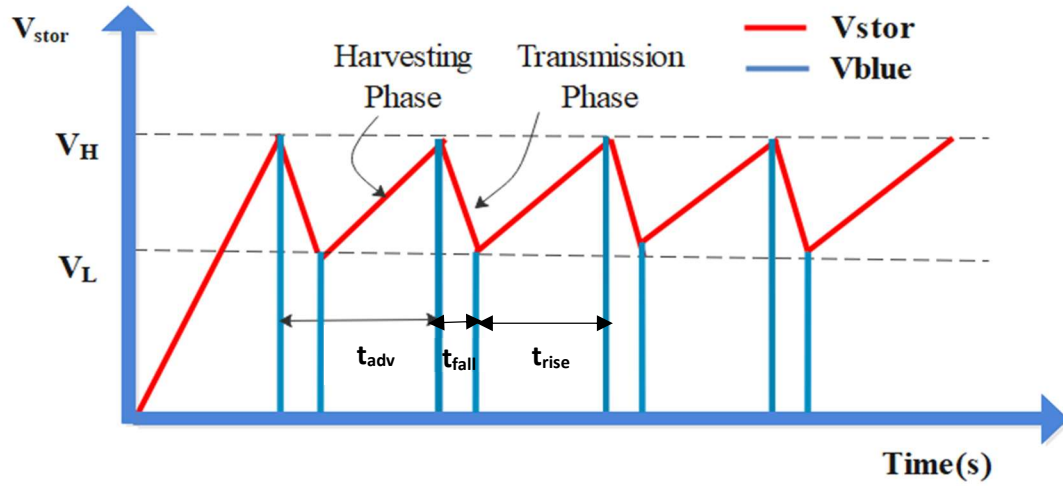


Figure 4.3: Charging and discharging voltage profile across the storage capacitor

As Figure 4.3 reveals, as soon as the voltage V_{stor} reaches the highest value $V_H = 3.0\text{ V}$, the system turns to the transmission phase where the microcontroller supplies the BLE through one of its General-Purpose Input/Output (GPIO) pins. Soon after the transmission phase, when the voltage drops to the lowest values $V_L = 2.0\text{ V}$, the microcontroller shuts down the BLE radio, turns in sleep mode and the whole system returns to the energy harvesting phase. The sensor works on the principle that the time delay between two successive beacons depends on the input acceleration of the PEH. The values of V_L and V_H are chosen such that the voltage never exceeds or is lower than the rated maximum(3.6 V) and a minimum supply voltage (1.6 V) of the microcontroller respectively. Since the minimum energy requirement $E_{harvested}$ of the EAWVS is $\sim 100\text{ }\mu\text{J}$ per beacon, the minimum value of the storage capacitor C_{stor} can be determined by:

$$C_{stor (min)} = \frac{E_{harvested}}{V_H^2 - V_L^2} = 40\text{ }\mu\text{F} \quad 4.1$$

To allow some margin and extra energy capability to optionally activate other embedded sensors and thereby render the system performance less sensitive to the inevitable parametric variations of the various components involved, the chosen value for the C_{stor} capacitor is $200\text{ }\mu\text{F}$. In addition to meeting the extra leakage losses in capacitor, larger storage capacity will also ensure that, in future, additions sensors can be added to the system. Additional sensors require more data bytes to be sent and therefore more power is consumed by the transmitter.

4.3 Piezoelectric Energy Harvester Design

To sense the input vibrations, the input mechanical energy is converted to the electrical domain using a piezoelectric harvester. The PEH was designed to meet the typical vibration levels of most transportation and industrial environments (cars, trains, heavy machinery, and the like), that typically show frequency peaks between 100 Hz and 300 Hz, and with an acceleration of 0.1 g up to 2 g. Besides, the harvester should also ensure that the minimum current delivered should overcome that consumed by the voltage monitoring section in the microcontroller, that consumes a continuous current in the order (~ 100 nA). The harvester is designed in such a way that it works in a lower frequency regime (200 Hz) that is available in the ambient environment and produces enough voltage (V_{oc}) required to charge the storage capacitor after considering the rectification drop of 1.4 V in the diodes. Further, the PEH must produce a minimum power P_{PEH_min} to supply the EAWVS during the energy harvesting phase under the minimum vibrational acceleration a_{cc_min} which could define the Limit of Detection (LoD) of the system in its function as a vibration sensor. To ensure that the capacitor C_{stor} effectively gets charged from V_L to V_H , the harvester generated power P_{PEH} must be greater than the quiescent power P_q consumed by the voltage monitoring circuit ($P_{PEH} > P_q$). During the harvesting phase, the only current consumption is due to the voltage detection unit of the STM32L0 microcontroller, which is programmed to operate in sleep mode and has a quiescent current consumption $I_q \approx 1$ μ A. The voltage V_{stor} varies between the values V_H and V_L providing the average voltage V_{stor_avg} given by:

$$V_{stor_avg} = \frac{V_H - V_L}{2} = 2.5 \text{ V} \quad 4.2$$

The quiescent power consumption P_q of the EAWSN during the harvesting phase is given by:

$$P_q = V_{stor_avg} \cdot I_q = 2.5 \text{ } \mu\text{W} \quad 4.3$$

Therefore, the minimum power P_{PEH_min} that the PEH must generate at the minimum acceleration a_{cc_min} is given by:

$$P_{PEH_min} > \frac{P_q}{\eta_{rectifier}} \quad 4.4$$

$\eta_{rectifier}$ is the power conversion efficiency of the full-bridge voltage rectifier at the PEH resonance frequency and under minimum acceleration a_{cc_min} , whose theoretical maximum value is equal to $8/\pi^2$ given by:

$$\eta_{rectifier} = \frac{P_q}{P_{PEH}} = 0.81 \frac{V_{stor_avg}}{2V_f + V_{stor_avg}} \quad 4.5$$

The factor 0.81 is added because the maximum theoretical efficiency of a full bridge diode rectifier is 81%. Equation 4.5 suggests that to maximize $\eta_{rectifier}$, the forward conduction voltage of the voltage rectifier diode V_f must be as low as possible. This choice, however, contrasts with the other requirement that the diodes have a reverse current I_r as low as possible (i.e., $I_r \ll I_q$) and requires a compromise between the forward voltage and reverse current performance of the diode. These considerations led to the choice of an ultra-low leakage diode (FJH1100) with a maximum reverse current of 10-30 pA, and a forward voltage V_f of 0.6 V with a forward current of 10 μ A. With this choice, from equation 4.5 arises the theoretical power conversion efficiency of the voltage rectifier of ≈ 81 %. Equation 4.4 shows that the specification for the minimum power that PEH must generate when stressed by vibrations with minimum acceleration a_{cc_min} is given by:

$$P_{PEH_min} = \frac{P_q}{8} \pi^2 \sim 3 \mu W \quad 4.6$$

Another electrical parameter to specify for the PEH design is the PEH V_{oc} open-circuit voltage. The specification of the value of V_{oc} is defined both to be greater than the minimum supply voltage of the voltage detector circuit ($V_{dd_min} = 1.8$ V) and to ensure the maximum power transfer between the PEH and the rest of the EAWVS system, at the minimum acceleration a_{cc_min} . The maximum power transfer of a PEH is at half the open circuit voltage as described in chapter 3. So effectively, maximum efficiency of the system is when the half open circuit voltage across the PEH equals sum of forward drop in diode (V_f) and the average voltage across the microcontroller $((V_H + V_L)/2)$ given by:

$$\frac{(V_{oc} - 2V_f)}{2} = V_{stor_avg} \quad 4.7$$

Equation 4.8 defines the condition of V_{oc} to achieve maximum power transfer:

$$V_{oc} = 2V_f + V_H + V_L = 6.2 \text{ V} \quad 4.8$$

The maximum detectable acceleration a_{cc_max} by the EAWVS is related to the highest stress level that the PEH substrate material can withstand (Si 3-6 GPa)[234]. The maximum limit of the input acceleration was determined to be 2 g from the Finite Element Method (FEM) simulations as discussed in chapter 4. However, in this work, the device testing has been limited to 1.2 g, which is 60% of the theoretical maximum acceleration of 2 g to ensure some safety margin in not exceeding the material stress reliability limits. In chapter 3, the characterization of the PEH with regard to the output power P_{PEH} and V_{oc} measurements as the function of the input acceleration a_{cc} has been detailed. At resonance condition and at the minimum acceleration a_{cc_min} of 0.5 g, the PEH provides an open circuit voltage V_{oc} of 6 V and can supply the minimum power P_{PEH_min} of 12 μ W enough to compensate for the quiescent power consumption P_q and successfully charge the storage capacitor C_{stor} . The open circuit output voltage V_{oc} and power P_{PEH} for various acceleration levels in the log scale are shown in Figure 4.4 and Figure 4.5 respectively, to indicate the power law as indicated by the slope. Output voltage V_{oc} of the harvester increases linearly and power P_{PEH} is shown to vary quadratically.

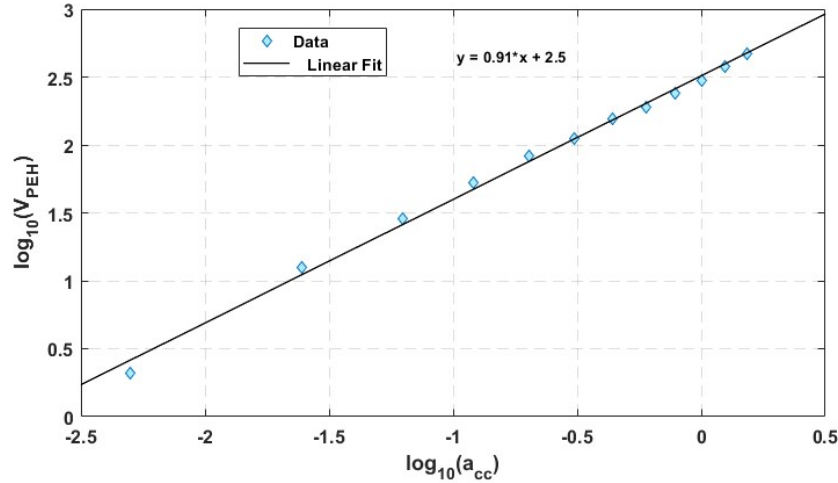


Figure 4.4: Open circuit voltage V_{oc} of the PEH vs input acceleration a_{cc} in g in log scale

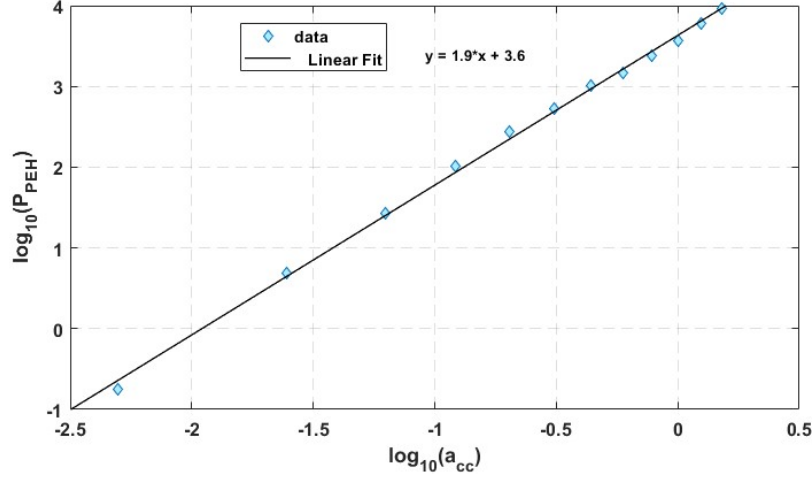


Figure 4.5: Generated power P_{PEH} in μW vs acceleration a_{cc} in g in log scale

4.4 Energy Autonomous Wireless Vibration Sensor Working Principle

The PEH generates an electrical field/voltage across its electrodes during the application of mechanical stress according to the direct piezoelectric effect:

$$S = s^D T + d_{ij}^T D \quad 4.9$$

$$E = -g_{ij} T + \varepsilon_{ij}^T D \quad 4.10$$

Where D is electric displacement, E the electric field, T mechanical stress and S mechanical strain and $-g_{ij} = d_{ij}/\varepsilon_{ij}$ is the piezoelectric voltage coefficient. Under open circuit conditions, the dielectric displacement D is zero. Therefore from equation 5.9, the open-circuit voltage V_{PEH} (V), or electric field E ($V\ m^{-1}$), from a piezoelectric device in d_{31} mode that results from the applied mechanical stress and is defined as [235]:

$$V_{PEH} = E \times t = \frac{F \cdot d_{31}}{A\varepsilon} l_p \quad 4.11$$

where, $F = \text{equivalent mass } (m) \times \text{acceleration } (a)$, l_p the length of piezo with a resistive external impedance load Z_{load} (Ω), the generated power P_{PEH} is given as [236]:

$$P_{PEH} = \frac{V_{PEH}^2}{2Z_{load}} \quad 4.12$$

$$P_{PEH} = \frac{(md_{33}l_p)^2}{2A^2\epsilon^2Z_{load}}a_{cc}^2 \quad 4.13$$

- d_{33} is the piezoelectric coefficient of Lithium Niobate (27 pm/V).
- m is the effective mass of the proof mass-cantilever system (2.3 g).
- a_{cc} is the input acceleration
- A is the area of the electrode (1 cm²)
- ϵ is the dielectric permittivity of Lithium Niobate (50.5)
- t_p is the thickness of piezoelectric transducer (30 mm).

During the harvesting phase, the load Z_{load} is constant, hence P_{PEH} varies proportionally with the power of two of the acceleration a_{cc} as given by:

$$P_{PEH} = K_{acc}a_{cc}^2 \quad 4.14$$

Where K_{acc} is a constant of proportionality given by:

$$K_{acc} = \frac{1}{2 \cdot Z_{load}} \cdot \left(\frac{m \cdot d_{33} \cdot l_p}{A \cdot \epsilon} \right)^2 \quad 4.15$$

The power harvested after each beacon in the C_{stor} capacitor is given by:

$$P_{harvested} = \eta_p P_{PEH} \quad 4.16$$

where η_p is the power efficiency conversion of the EAWVS system when converting the power P_{PEH} into the power $P_{harvested}$ harvested in the storage capacitor C_{stor} . By combining equations 4.14 and 4.17, the power $P_{harvested}$ can be related to the acceleration a_{cc} :

$$P_{harvested} = \eta_p \cdot K_{acc} \cdot a_{cc}^2 \quad 4.17$$

Equation 4.18 relates $P_{harvested}$, $E_{harvested}$ and the time t_{rise} that it takes to charge the C_{stor} capacitor from the voltage value V_L to the voltage value V_H during the energy harvesting phase.

$$P_{harvested} = \frac{E_{harvested}}{t_{rise}} \quad 4.18$$

The communication between the EAWSN and the base station is made through Bluetooth wireless beacons. The time distance between two successive beacons is called the advertising time t_{adv} .

The time t_{adv} is remotely measured by the BS while receiving the beacons and is used to measure indirectly the acceleration a_{cc} induced on the PEH. The time t_{rise} is related to the advertising time t_{adv} as:

$$t_{rise} = t_{adv} - t_{fall} \quad 4.19$$

The fall time t_{fall} is related to the parameters of the system, V_H , V_L , $C_{storage}$ and I_{ble} as:

$$t_{fall} = \frac{C_{stor.}(V_H - V_L)}{I_{ble}} \quad 4.20$$

The parameter I_{ble} represents the average current consumption of the BLE radio during the transmission phase and has a constant value of ~ 9 mA with the BLE radio configured in non-connectable advertising mode to transmit an out power of 8 dBm and a data length of 20 bytes. Therefore, t_{fall} is also constant, and in this implementation is 45 ms. By combining equations, 4.1, 4.16, 4.17, 4.18 and 4.19, the acceleration a_{cc} can be indirectly derived from the measurement of the time t_{adv} as:

$$a_{cc}^2 = \frac{C_{stor.}(V_H^2 - V_L^2)}{K_{acc} \cdot \eta_p \cdot (t_{adv} - t_{fall})} \quad 4.21$$

The parameter η_p is specific to the EAWVS system and is experimentally derived from its post-production characterization. Figure 4.6 shows the experimental characterization of the parameter η_p while varying the acceleration a_{cc} . The high initial variation of η_p at low acceleration levels between 0.5 g, and 0.6 g affects the linearity of the EAWVS in its sensor function. Therefore, even though the EAWVS is self-powered starting from an input acceleration of 0.5 g, the system efficiency is so low and variable that the use of the EAWSN as a sensor is greatly compromised. Therefore, the LoD of the EAWVS is at the higher level of 0.6 g where the η_p is higher and remains almost constant (max variation $< 15\%$) in the range. Figure 4.6 reveals that η_p remains nearly constant within the acceleration range [0.6 g - 1.2 g].

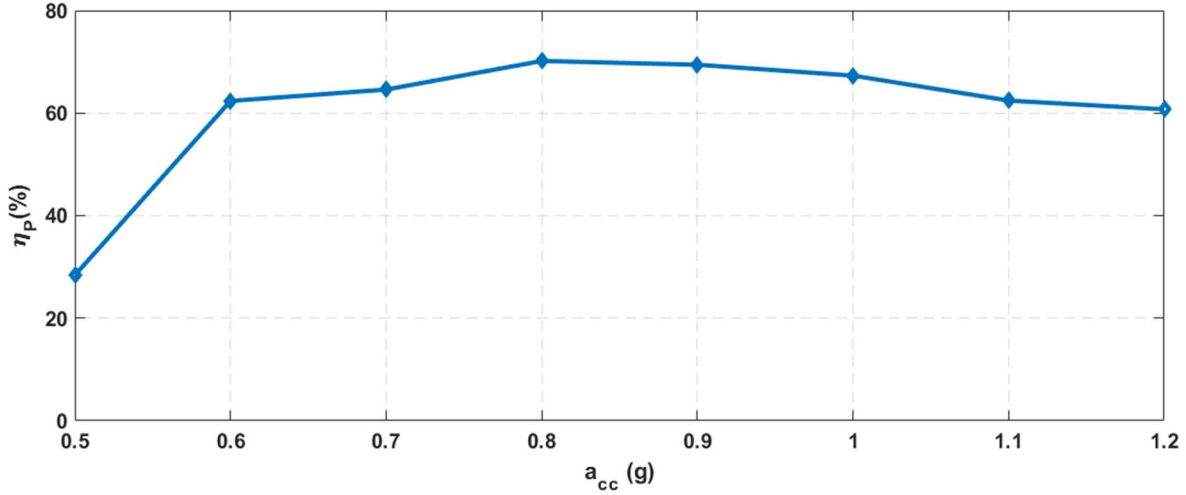


Figure 4.6: EAWVS Power conversion efficiency η_p vs acceleration acc . (Inset: η_p vs acc nearly constant starting from 0.6 g).

Therefore equation 4.21 can be rewritten as:

$$a_{cc} = \frac{S_v}{\sqrt{(t_{adv} - t_{fall})}} \quad 4.22$$

where S_v , is the sensitivity of the EAWVS given by:

$$S_v = \sqrt{\frac{C_{stor} \cdot (V_H^2 - V_L^2)}{K_{acc} \cdot \eta_p}} \quad 4.23$$

Furthermore, the high imbalance between the current produced by the PEH during the harvesting phase (mA) and that consumed by the EAWVS during the transmission phase (mA) results in a big difference between the time t_{adv} (seconds) and t_{fall} (msec). Hence, it is possible to assume that in a real application scenario $t_{adv} > t_{fall}$ implying that, with negligible error, it is possible the approximation $t_{adv} - t_{fall} \sim t_{adv}$ so that Equation 4.22 can be simplified as:

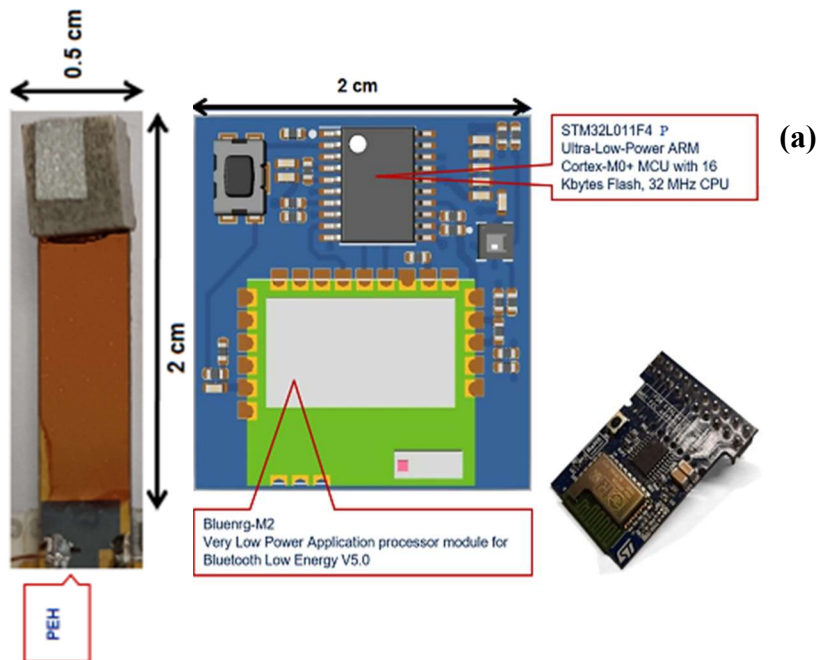
$$a_{cc} \approx \frac{S_v}{\sqrt{t_{adv}}} \quad 4.24$$

Equation 4.24 can be implemented in the embedded firmware of the BS so that the acceleration a_{cc_BS} can be remotely and indirectly measured at the BS that can measure the time t_{adv} from the received beacons. It is worth highlighting that, since the EAWVS exploits measurements in the time domain, the data reading interface is inherently digital. This feature is very convenient

because it gives less complicated electronics for data reading than analog architectures, and above all, lower energy consumption, which is a fundamental characteristic of energy-autonomous and battery-free systems [43]. Since the BS can measure the time t_{adv} , the only unknown parameter to calculate the acceleration a_{cc_BS} via equation 4.24 is S_v , that will be derived experimentally through the characterization of the EAWVS in section 5.5.

4.5 Experimental Results

Figure 4.7 a show the System on Chip (SoC) with PEH and Figure 4.7 b shows the block diagram of the experimental setup.



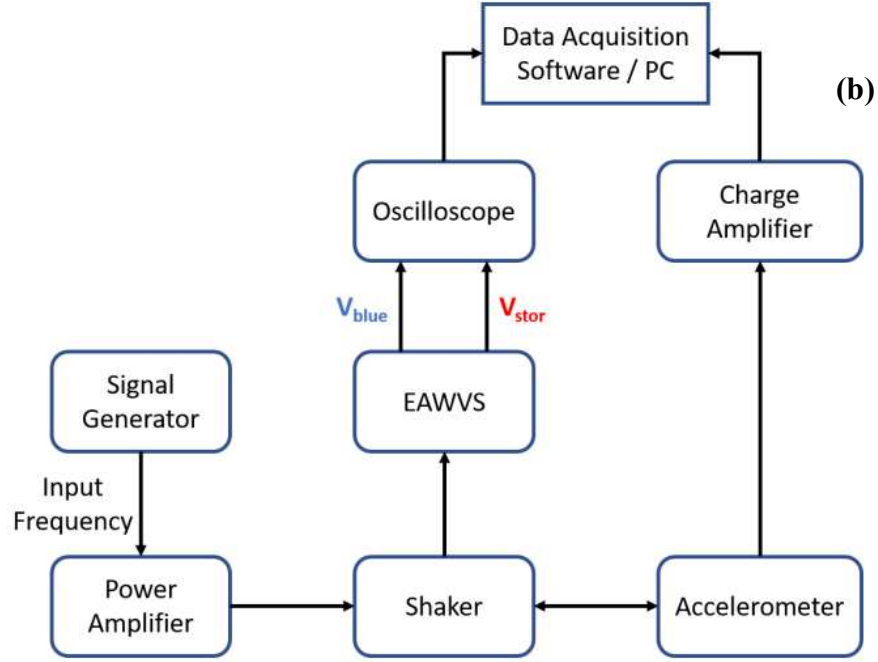


Figure 4.7: (a) Image of the system on Chip (SoC) with the PEH (b) Block diagram of the experimental setup with shaker

The EAWVS characterization in terms of LoD and sensitivity in response to the vibrational acceleration has been carried out at room temperature in the air ambient. The EAWVS, positioned on the shaker, has been subjected to various vibration levels with the acceleration a_{cc_in} varying in the range [0.5 g - 1.2 g]. Several measurements have been performed as shown in Figure 4.8 by probing the output voltage V_{blue} and measuring the time t_{adv} with an oscilloscope. Figure 4.8 reveals how the time t_{adv} decreases with the increase of the acceleration a_{cc} in agreement with Equation 4.24.

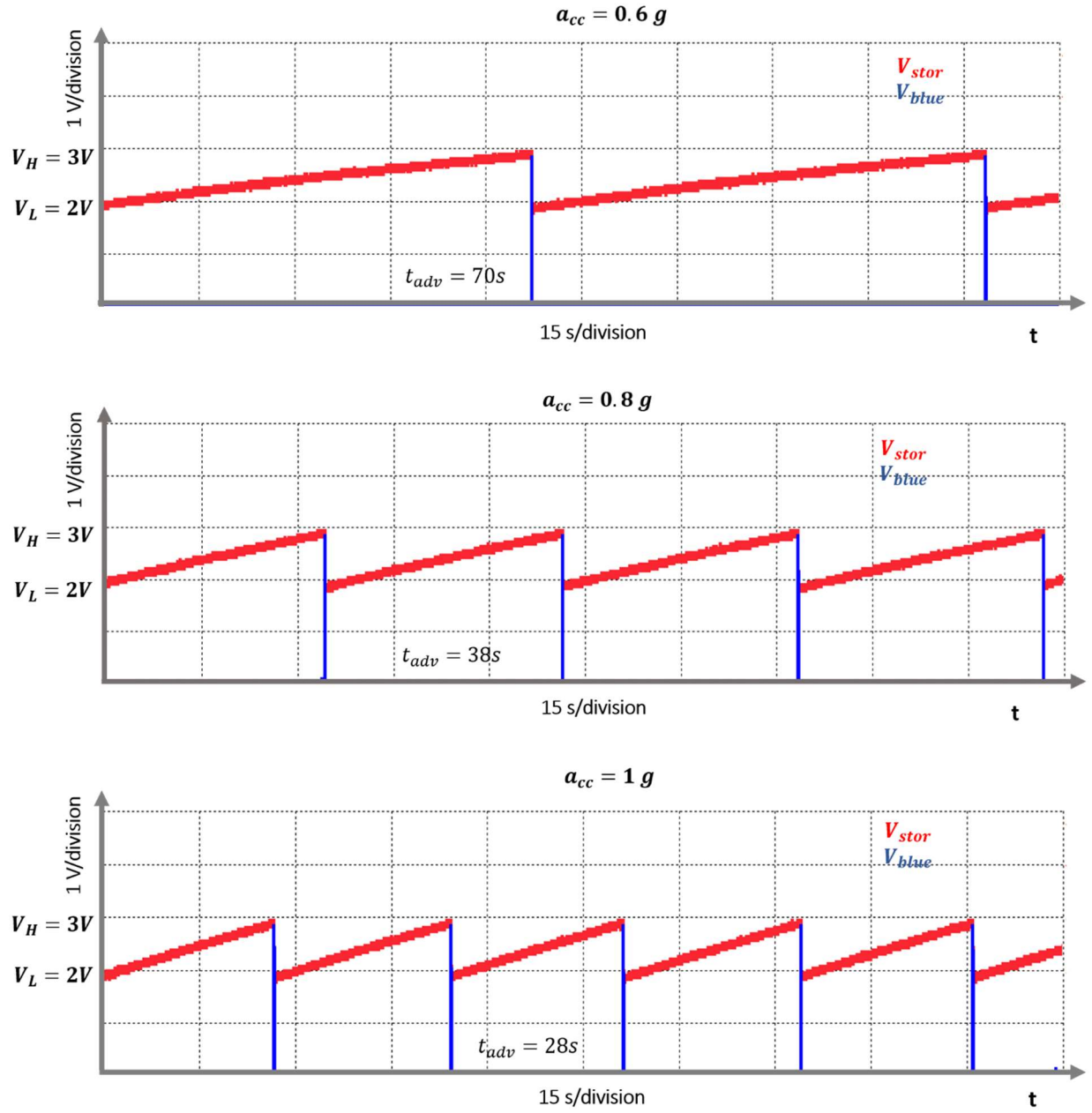


Figure 4.8: Experimental results of V_{stor} and V_{blue} vs time at three different accelerations $0.6g$, $0.8g$ and $1g$ respectively.

Figure 4.9 reports the calibration of the EAWVS from the measured data. The solid line reveals the linear fit of the experimental data.

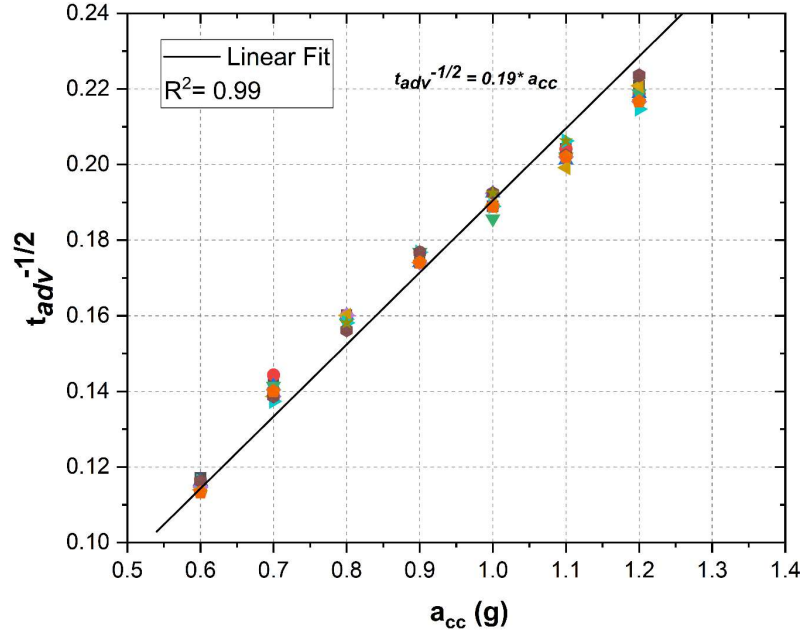


Figure 4.9: Linear Fit of the experimental measurement data

The EAWVS sensitivity S_v is the inverse of the fitting line slope reported in Figure 4.9. Hence, from the EAWVS characterization $S_v = 5.27 \text{ g.s}^{1/2}$, therefore, the acceleration at the BS can be indirectly measured by the knowledge of S_v and the measurement of the time t_{adv} by:

$$a_{cc_bs} \approx \frac{5.27}{\sqrt{t_{adv}}} \quad 4.25$$

The intrinsic error that is committed with the proposed measurement technique is indicated with $Error_a$ and calculated through equation 4.26, representing the acceleration measurement error, between the acceleration a_{cc_BS} , indirectly measured at the BS and the forced acceleration a_{cc_in} at the EAWVS.

$$Error_a = 100 \frac{(a_{cc_in} - a_{cc_BS})}{a_{cc_in}} \quad 4.26$$

Figure 4.10 shows the variation of a_{cc_in} and a_{cc_BS} with respect to the advertising time t_{adv} .

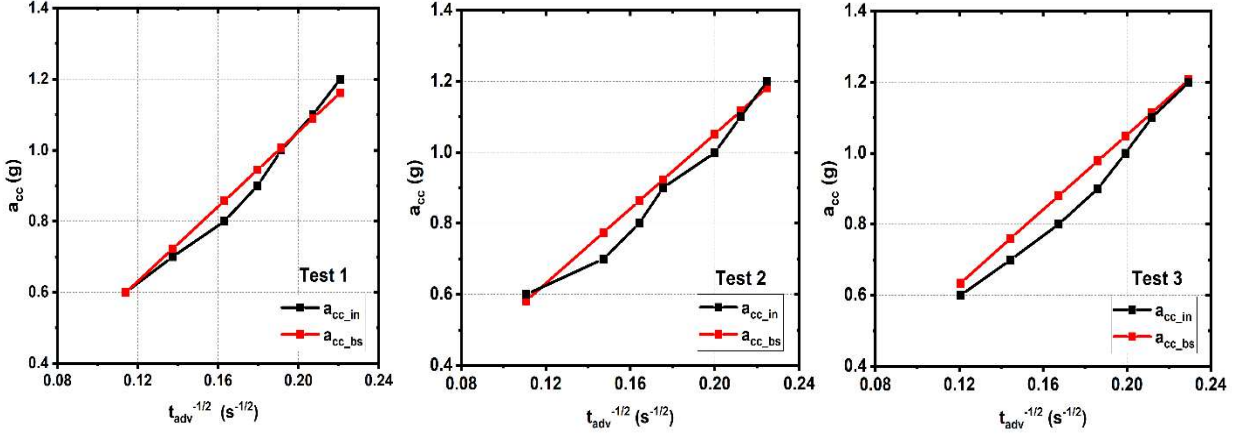


Figure 4.10: variation of a_{cc_in} and a_{cc_BS} vs t_{adv} for three different tests

Figure 4.11 shows the variation of the error $Error_a$ as the input acceleration a_{in} varies in the range [0.6 g - 1.2 g].

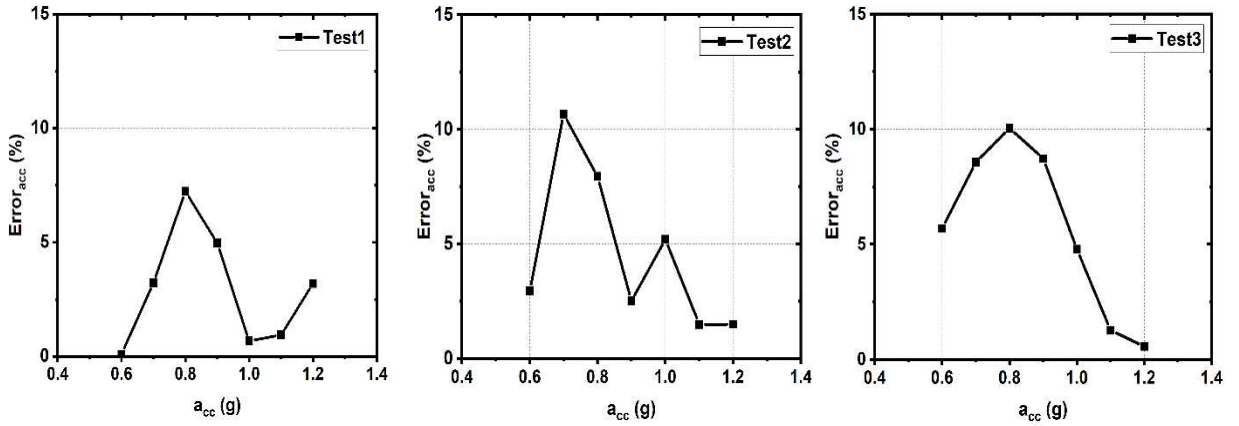


Figure 4.11: $Error_a$ in measurement vs input acceleration a_{cc} for three different tests

The test measurements unveil that it is possible to measure remotely and wirelessly at the BS the acceleration forced onto the EAWVS. The measurement results are repeatable with an error consistently below 11%. The BS can therefore receive beacons from one or more EAWSNs, placed on the vibrating parts of machines under test, and exercise predictive maintenance or fault detection by simply measuring the advertising time t_{adv} of the received beacons as shown in Figure 4.1. For long-term predictive diagnosis of machines, the EAWVS can be embedded in specific mechanical parts that require regular maintenance as bearings, gears, conveyors, turbines, shafts, valves, and the like. In case of a mechanical fault, there is a sudden increase in the rate of change in the acceleration. The rate can be monitored by the base station measuring the vibration accelerations at two successive time intervals.

$$\text{Rate } (K_t) = \frac{a_{cc}(t_2) - a_{cc}(t_1)}{(t_2 - t_1)}$$

4.27

The base station upon sensing can sent interrupt or standby signals to the machine control and also alarm signals to the user if the measured rate K_t is above a critical threshold K_c as shown in Figure 4.12.

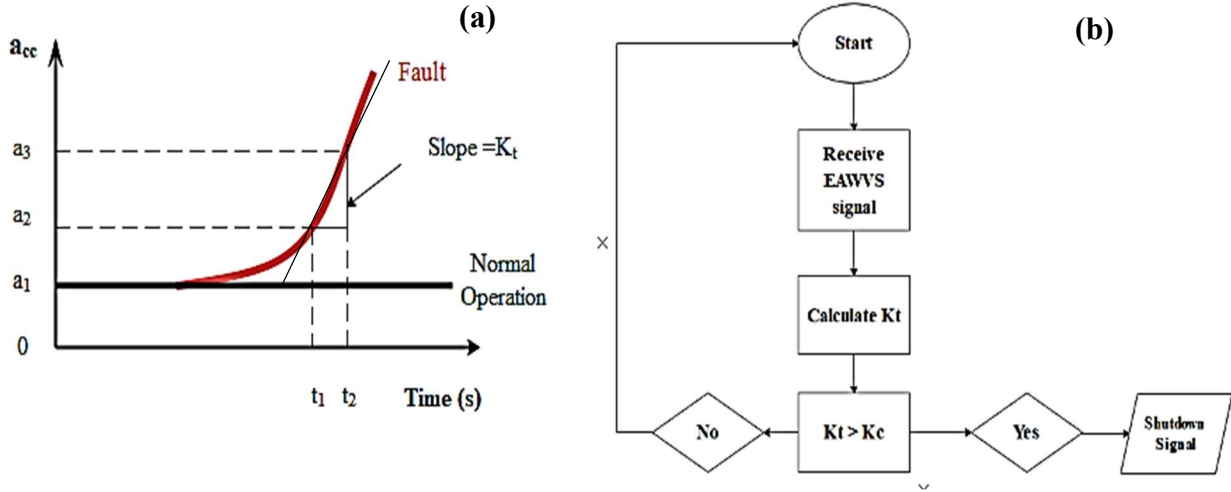


Figure 4.12 Application scenario of the predictive maintenance with EAWVS (a) a_{cc} vs time (b) application algorithm

4.6 Conclusions

In summary, a novel self-powered and battery-free device for vibration sensing method based on vibration energy to time conversion was explored, that have potential application in automotive and heavy industries. The working principle of the sensor has been explained with theoretical and analytical equations. The EAWVS provides the added flexibility, that allows the measurement readout remotely and wirelessly by exploiting the BLE communication and transmitting beacons at a remote BS with the sensor reading based on the easy-to-implement time-domain readout by measuring the advertising time T_{adv} . The PEH performs the dual function of energy harvester and vibrational sensor and as shown by the experimental results, it can perform vibrational sensing in the acceleration range [0.5 g - 1.2 g] with LoD of 0.6 g. Further, experimental tests have shown that the system, based on the EAWVS and the BS, can perform repeatable and accurate sensing capabilities within an error limit of 11%. It has been shown how the simplicity of the EAWVS architecture translates into several advantages such as eco-friendliness, size, cost, and above all the feature to be used as a maintenance-free install-and-forget device in practically every

application where vibration energy is available. Finally, all experimental measurements were performed on a 2 cm x 2 cm PCB with a thickness of 0.45 cm, implemented, except for PEH, with standard components only to demonstrate the feasibility of a proof of concept whose operational performance could be further improved by upcoming advances that the research of both materials and electronic components will bring in the future.

Conclusion and Perspectives

The work presented in this manuscript focuses on the exploitation of ambient vibration to harvest power at microwatt level using lead free piezoelectric energy harvesters in order to power standalone WSNs. First, a comprehensive survey on recent state of the art and principles of vibration-based energy harvesting devices was carried out. In addition, the need for a lead-free approach in future energy harvesting devices and the challenges faced are outlined. The piezoelectric-based energy harvesting technique, thanks to the compatibility of material deposition with the existing micromachining process and relatively higher output voltage, has received more attention compared to its counterparts for implementation in vibration energy harvesting applications.

Further, the piezoelectric and electromechanical properties of various lead-free ferroelectric materials such as alkaline Niobates and Tantalates (Lithium Tantalate, KNN, KNNT, LN) have been studied. The microscale electromechanical properties such as piezoelectric coefficient(d_{33}) and Figure of Merit of various morphologies such as fiber and thin films of these materials has been studied using Piezoresponse Force Microscopy (PFM). In addition, the effect of poling of these structures on localized piezoelectric properties has been investigated. It has been shown that the piezoelectric properties such as d_{33} of these polycrystalline films grown by sol-gel techniques, can be improved by poling. KNN films was found to have d_{33} of 23 pm/V before poling. By poling externally at elevated temperatures at 4 kV/mm was found to increase the piezoelectric coefficient (d_{33}) of KNN films from 23 pm/V to 100 pm/V. Further, the study of KNNT films shows that the B site substitution of KNN by Ta can lead to a significant increase in the d_{33} compared to pure KNN samples. The d_{33} of the unpoled KNNT cantilever was found to be 48 pm/V, which increased to 221 pm/V upon poling at 3 kV/mm by AFM tip. Further, ferroelectric nature of these materials is investigated by ferroelectric hysteresis and butterfly loops, verified by 180-degree polarization switching. The enhanced piezoelectric properties (d_{33}) of these materials are comparable with lead-based materials such as PZT thin films. Also, the ferroelectric properties and piezoresponse of KNN and KNNT electro-spun fibres were investigated. The KNNT fibers showed enhanced

piezoelectric coefficient d_{33} (~ 130 pm/V) compared to the undoped KNN fibers (28 pm/V). The good piezoelectric properties of the KNN/KNNT fibers suggest that they could be used for fabricating novel flexible PEH devices. These coefficients and FoMs values can be valuable information for the optimization of properties and also a tool for selection of lead-free materials for future devices and energy harvesting applications. The FoMs of various sol-gel processed alkaline Niobates and Tantalates on steel substrate namely KNN, KNNT and LT was compared with a commercially available Lithium Niobate single crystal. The LT single crystal showed superior FoM, compared to the sol-gel processed films. A higher FoM requires a lower permittivity and higher d_{33} . This lower FoM in sol-gel processed films are essentially due to the higher dielectric permittivity. This indicates that the sol-gel processed films need further optimization before it can be used for real-time industrial applications.

Therefore, to obtain a realistic harvester from an application point of view, a unimorph single clamped cantilever based piezoelectric energy harvester based on a lead-free Lithium Niobate crystal has been designed and conceived and its performance was evaluated. Finite element and SDOF analytical models are used to identify the appropriate proof mass weight and the maximum stress developed in the beam, to tune the harvester operating resonant frequency. Thus, by taking advantage of the addition of proof mass, the device operational frequency was tuned to be in the range of available ambient vibrations (~ 200 Hz) in car engines or industrial motors. We have realized a harvester possesses a quality factor $Q=50$, and a high coupling $K^2 Q_m=3$, which indicates the higher electromechanical conversion efficiency of the harvester. The harvester is found to be capable to oscillate in the multiple modes with a strong nonlinear behavior. These two factors, ie, the coupling and non-linearity, aid the broadband energy harvesting capabilities of the harvester. The PEH gives an output voltage of 6V and an overall power density of the PEH was estimated to be $36 \mu\text{W}/\text{cm}^2/\text{g}^2$ at an optimal load of $\sim 550 \text{ k}\Omega$, at resonance. The device has a full width half maximum bandwidth of 10.8% at resonance. This is a clear advantage as it can be used to extract energy from a broader spectrum of input frequency.

An electric modelling circuit such as Mason equivalent circuit is very practical to represent physically the harvester and its impedance. Hence, the electromechanical Mason's equivalent circuit model was developed for the harvester from the impedance analysis and was simulated in SPICE. The validity of the model was confirmed with theoretical and experimental analysis. In addition, the optimal load for the harvester to deliver the maximum power was derived

experimentally to be $\sim 550 \text{ k}\Omega$ and was compared with the theoretical and SPICE models. Furthermore, a comprehensive comparison between the proposed MEMS harvester and the recently published vibration energy harvesters from the literature shows that our conceived harvester is well comparable with the state of the art, to offer a promising vibration energy harvesting system for being deployed in the real environment from a lead-free aspect. A standard rectification circuit with a full bridge rectifier was developed based on the K^2Q_m value to convert the AC output of the harvester to DC power that is eventually stored in a $220 \text{ }\mu\text{F}$ capacitor.

To ensure a maximum conversion efficiency in sub microwatt power systems, a three terminal PEH has been proposed that consists of a novel MPPT architecture whose primary purpose is to render MPPT worthwhile. With the MPPT architecture, the Power Management IC (PMIC) and the power harvesting circuit can be simplified to a minimal ultra-low power comparator without any oscillators, sensing or pre-regulation circuits. It leads to a considerable simplification of the PMIC circuitry at the expense of a small complication in the harvester structure. The resonant frequency f_r and the open circuit voltage V_{oc} are found to be nearly independent of the width w of the cantilever beam provided the geometry parameters such as length L and thickness t remain the same. A PEH with a minimum process width can therefore be implemented as a V_{oc} sensor cell, to be used as a reference voltage for the MPPT circuitry of the PMIC, which in relation to the main harvester can contribute to a negligible power loss of less than 1%. The feasibility of this new PEH has been proven theoretically and verified by using finite element simulations and experimental results of the open circuit voltages at various accelerations.

Finally, the harvester is used to power a novel self-powered and battery-free wireless sensor for vibration monitoring. It can perform vibrational sensing in the acceleration range $[0.6 \text{ g} - 1.2 \text{ g}]$. The working principle of the novel sensing method based on vibration energy to time conversion was explained with theoretical and analytical equations. The conceived Energy Autonomous Wireless Vibration Sensor is shown to provide flexibility of measurement of vibration via remote wireless readout, by exploiting the BLE communication. The sensor reading based on the easy-to-implement time-domain readout by measuring the advertising time T_{adv} , has an LoD of 0.6 g . Moreover, the experimental tests indicate the repeatability of measurements and accurate sensing capabilities within an error limit of 11%. The EAWVS is therefore ideal for condition monitoring

and predictive maintenance industrial applications due to its the eco-friendly, compact, and maintenance-free install-and-forget capabilities.

The present work offers several perspectives. First of all, the possibilities of improving the piezoelectric energy harvester performance by better design and possible miniaturization of the harvester needs to be explored. This could be achieved by exploring new fabrication processes steps compatible with the MEMS/microelectronics industry. The main difficulty with Lithium Niobate crystals are the limitations with the thinning down of the LN wafer below 27 μm . This makes it difficult to achieve LN thin films and thereby optimize the stress distribution beyond a certain level. New process like dry and wet etching may be investigated in the future to obtain and pattern LN films on silicon. The enhancement in harvester output can thereby improve the LoD of the EAWS. In addition, the performance of other harvesters based on sol-gel processed lead-free materials such as KNN and Lithium Tantalate need to be explored from an application point of view of a sensor. The drawback of the current sol-gel processed devices are the low output voltage and power due to the lower FoM. Although ways such as Ta doping improved the FoM of sol-gel processed thin films to several fold, it is still not comparable with single crystals like Lithium Niobate. The low FoM is essentially due to the higher dielectric permittivity of these sol-gel processed materials, and ways to optimize them needed to be explored to make it practically applicable to industrial scenario. Another key prospect is to explore the possible ways of physical implementation of the three terminal harvesters based on novel MPPT architecture, whose proof of concept has been detailed in this thesis. It is unworthy to implement the interface circuits with discrete electronic components in the case of microelectronic circuits where the operating current is just in the order of several microamperes. In this regime, the switching as well as connection and leakage losses becomes predominant. Therefore, the 3-terminal harvester with the novel MPPT architecture could be implemented with ASIC in consultations with IC design engineers at ST Microelectronics in future to make it worthwhile. Finally, the application of EAWVS from a condition monitoring point of view, and ultimately conceptualization of the idea into a viable product can be explored. The three terminal MPPT concept can be implemented with the EAWS to improve its Limit of Detection (LoD). Finally, the EAWVS needed to be tested in the real environment under various conditions such as varying frequency and amplitude. This would essentially lead to the optimization of the performance in real environment.

Résumé

Cette thèse présente de travaux de recherche relatifs au matériau, à la conception, la réalisation, la caractérisation et l'application du dispositif. Elle est divisée en six sections avec quatre chapitres.

Le schéma de chacun est le suivant :

- **Introduction générale :** Définit les perspectives générales de cette thèse et discute des principaux objectifs.
- **Chapitre 1 :** Donne une revue de la littérature, identifiant les dispositifs de récupération d'énergie de pointe actuels à l'échelle microscopique en mettant l'accent sur la récupération d'énergie vibratoire et les défis à relever. Différentes applications et sources d'énergie pour la sont discutées avant d'entrer plus en détails dans la récupération d'énergie piézoélectrique. Des stratégies et des perspectives vers un récupérateur d'énergie piézoélectrique sans plomb sont présentées.
- **Chapitre 2 :** Ce chapitre porte sur la caractérisation à l'échelle microscopique de nouveaux matériaux piézoélectriques sans plomb déposés par un procédé sol-gel. Le tantalate de lithium (LT), le niobate de sodium et de potassium (KNN), les couches minces et les fibres de niobate de sodium et de potassium dopés au tantale (KNNT) sont étudiés et leurs propriétés électromécaniques et leurs valeurs de récupération d'énergie sont comparées au monocristal de niobate de lithium (LN). Les techniques qui ont été utilisées pour caractériser les propriétés piézoélectriques et leur les morphologies telles que la Microscopie à Force Atomique (AFM) sont détaillées. En outre, une brève discussion sur le traitement et le dépôt de ces matériaux piézoélectriques sont discutés.
- **Chapitre 3 :** Discute de la fabrication et de la caractérisation d'un microgénérateur sans plomb basé sur une plaquette monocristalline de niobate de lithium sans plomb. Dans ce chapitre, nous développons un modèle de circuit équivalent électromécanique du récupérateur d'énergie piézoélectrique et, en outre, le conditionnement de tension et l'interfaçage du dispositif pour une sortie CC contrôlée et stable sont discutés. Une architecture efficace pour maximiser la puissance transférée à la charge avec un Maximum

Power Point Tracking (MPPT) est également étudiée, avec un accent particulier sur les circuits à faible puissance.

- **Chapitre 4 :** La possibilité d'alimenter un WSN IoT sans batterie basé sur la connectivité Bluetooth Low Energy (BLE) avec vibration ambiante est démontrée. En outre, le principe de fonctionnement et la mise en œuvre du système du capteur sans fil autonome en énergie (EAWVS) basé sur le microcontrôleur commercial STM32 sont détaillés. La capacité de la moissonneuse à détecter l'accélération d'entrée est démontrée. Enfin, le scénario d'application de l'EAWVS est présenté.
- **Bilan et perspectives :** Enfin, les conclusions générales de la thèse sont exposées et les perspectives sont brièvement discutées.

Introduction générale

L'objectif général de ce travail de doctorat dans le cadre du projet ITN-ENHANCE est l'étude de la puissance électrique récoltée à partir de vibrations ambiantes à des fréquences relativement basses (< 500 Hz) en utilisant des matériaux sans plomb pour des capteurs ou des actionneurs de faible puissance utilisés dans l'automobile. Le marché mondial de l'IoT est évalué à près de 250 milliards d'euros en 2019, et avec un intérêt croissant pour des domaines tels que les structures intelligentes, l'agriculture de précision, les véhicules autonomes et l'intelligence artificielle (IA).

Pour obtenir un statut entièrement autonome pour les WSN, il est très important qu'ils soient alimentés indépendamment et, par conséquent, il est nécessaire de remplacer l'énergie puisée dans les batteries. Exploiter et stocker l'énergie ambiante disponible dans l'environnement pour alimenter ces WSN aiderait à remplacer les batteries nécessaires aux WSN et à les rendre autonomes. Dans cette situation, l'utilisation de vibrations mécaniques ambiantes omniprésentes pour générer de l'électricité pour alimenter les WSN est un choix prometteur par rapport au système d'alimentation conventionnel à base de batterie qui nécessite un remplacement intermittent. De plus, l'approche sans batterie aide à réduire les problèmes environnementaux causés par les batteries. Parmi diverses techniques pour convertir les vibrations en électricité: les techniques piézoélectriques, électromagnétiques et électrostatiques, la récupération d'énergie piézoélectrique. Cette dernière est la plus pratique pour la récupération de micro-énergie en raison de la densité

d'énergie élevée ($300\mu\text{W}/\text{cm}^2/\text{g}^2$) et de la compatibilité du dépôt de matériau avec le processus MEMS. Cependant, les collecteurs d'énergie piézoélectriques (PEH) de pointe tels que le PZT sont principalement basés sur des matériaux à base de plomb, un élément toxique qui n'est pas conforme à REACH (enregistrement, évaluation, autorisation et restriction des produits chimiques) et RoHS (réglementation sur la limitation des substances dangereuses). Pour cette raison, il existe un besoin croissant dans l'industrie électronique d'explorer de nouveaux matériaux et procédés respectueux de l'environnement pour les PEH "verts" de nouvelle génération basés sur des matériaux sans plomb. Dans cette thèse,

Projet ITN-ENHANCE

Le projet EU-ENHANCE se concentre sur le développement de sources d'alimentation pour des capteurs sans fil autonomes et auto-alimentés qui peuvent être pratiques dans des endroits difficiles d'accès ou dans des conditions de travail difficiles. L'un des meilleurs moyens possibles pour la mise en œuvre d'un tel concept de capteur de type installer et oublier consiste à exploiter la puissance de l'environnement ambiant, comme les vibrations, les énergies thermiques ou solaires. Pour obtenir une puissance de sortie élevée avec des collecteurs piézoélectriques, une valeur de couplage électromécanique K^2 élevée est requise.

En plus d'assurer une haute (Figure of Merit) FoM des matériaux, il est également nécessaire d'avoir une conception appropriée des pièces mécaniques et électriques pour avoir une meilleure performance du système de récupération d'énergie. Actuellement, la plupart de ces PEH avec un K^2 plus élevé utilisent du $\text{PbZr}_{1-x}\text{Ti}_x\text{O}_3$ (PZT). Cependant, à l'avenir, le PZT devra être remplacé par des matériaux sans plomb, même pour les couches minces en raison des préoccupations environnementales croissantes.

Le projet ENHANCE se concentre donc sur le développement de récupérateurs d'énergie pour les capteurs automobiles basés sur des matériaux sans plomb ; cependant, les résultats du projet pourraient également être importants pour d'autres industries telles que l'aérospatiale et les industries lourdes. Le matériau ferroélectrique sans plomb, tel que le LiNbO_3 (LN) présente une FoM similaire à celle du PZT et est compatible avec les applications à haute température (jusqu'à 500°C). L'une des densités de puissance notables les plus élevées ($300\mu\text{W}/\text{cm}^2/\text{g}^2$) obtenues parmi les micro-PEH à large bande passante ($\sim 10\text{ Hz}$) a été obtenue par EH à base de films de niobate

de sodium et de potassium (KNN) sans plomb. Cependant, ces matériaux sont relativement nouveaux par rapport au PZT standard industriel et l'application de ces matériaux dans les PEH est encore mal étudiée. Dans cette thèse, nous avons pour objectif de développer un micro PEH sans plomb avec une valeur de couplage électromécanique K^2 élevée et une récupération large bande.

Chapitre 1 : Revue de la littérature

Ce chapitre traite des dispositifs de récupération d'énergie de pointe actuels à l'échelle microscopique, tels que la récupération d'énergie piézoélectrique, électrostatique et électromagnétique, en mettant l'accent sur la récupération d'énergie vibratoire. Des stratégies et des perspectives vers un récupérateur d'énergie piézoélectrique sans plomb sont présentées.

Le WSN autonome se compose d'un capteur, d'un microcontrôleur, d'une section de transmission et enfin du transducteur. La principale consommation électrique du WSN provient du microcontrôleur et de la section émettrice. La quantité totale d'énergie requise pour le traitement et la transmission sans fil des WSN est généralement de l'ordre de 40 à 500 μJ et peut varier en fonction du protocole RF utilisé pour la transmission. La consommation électrique totale de tous les composants réunis (capteurs, émetteurs et microcontrôleurs) dans un WSN pendant un cycle de service peut être de l'ordre de 100 μW à 1 mW selon le rapport cyclique de fonctionnement.

Bien que les récupérateurs d'énergie ambiante à l'échelle microscopique puissent ne pas être en mesure de fournir l'alimentation pour un fonctionnement continu, il suffit d'alimenter ces nœuds WSN de manière intermittente. Par exemple, le système passe en mode veille lorsque l'énergie est stockée dans un condensateur et peut être utilisée pour se décharger dès que suffisamment d'énergie est stockée pour le mode opérationnel. Pour un capteur IoT en état de veille, sa puissance consommée peut être extrêmement faible (quelques microwatts). Par conséquent, le WSN est conçu intelligemment avec une faible consommation d'énergie lorsqu'il est éveillé et une consommation d'énergie négligeable en mode veille.

L'énergie ambiante disponible dans l'environnement peut être largement classée en sources mécaniques (vibrations, contraintes), sources rayonnantes (solaire, infrarouge et RF) et sources thermiques (gradients ou fluctuations de température). Dans le cas de l'énergie solaire, bien que la densité de puissance de l'énergie solaire soit élevée, la récupération n'est pas possible dans certains

domaines d'application pratiques des capteurs tels que l'intérieur des machines, où les rayonnements solaires ne peuvent pas atteindre. De même, il est également difficile de récupérer de l'énergie thermique là où il y a une absence de gradient de température. De même, la récupération d'énergie RF présente également certaines limitations dans la mise en œuvre en raison de la forte absorption de l'énergie RF par les métaux, limitant ainsi la densité de puissance disponible. Par conséquent, la récupération d'énergie ambiante est strictement spécifique à l'application, en fonction de la disponibilité de la source d'alimentation à l'emplacement de la cible d'installation. Par conséquent, pour alimenter de tels réseaux de capteurs, qui doivent être installés notamment dans des applications intérieures, des structures automobiles et mécaniques, l'énergie mécanique ambiante peut être un choix judicieux.

La récupération d'énergie vibratoire est la technique permettant de convertir les vibrations en énergie électrique utilisable par une conversion en deux étapes. Dans un premier temps, la vibration est transformée en un mouvement relatif entre deux éléments, à l'aide d'un système masse-ressort équivalent. Le mouvement relatif est ensuite converti en énergie électrique par un mécanisme de conversion mécanique-électrique (principalement piézoélectrique, électromagnétique ou électrostatique). L'énergie mécanique ambiante peut être transformée en énergie électrique par des mécanismes principaux, à savoir des récupérateurs d'énergie piézoélectriques, électrostatiques, électromagnétiques et triboélectriques. Les micro-récupérateurs d'énergie électromagnétique (EMEH) ont tendance à produire des tensions alternatives très faibles de l'ordre du millivolt. De plus, la tension de sortie diminue au fur et à mesure que la taille est réduite. Tout d'abord, nous avons comparé la puissance de sortie de toutes les technologies de récupération d'énergie vibratoire. Nous mettons en avant que les récupérateurs d'énergie électrostatique (EEH) ont une limitation de mise en œuvre lorsque l'appareil vibre avec une magnitude de plusieurs centaines de microns tout en maintenant un espacement en électrodes minimum de 0,5 mm pour produire des performances similaires. Pour les générateurs piézoélectriques et électrostatiques, le courant diminuera avec la surface en raison de la réduction de la capacité du dispositif. Les générateurs piézoélectriques ont l'avantage de produire des tensions élevées. Parmi toutes ces récupérations d'énergie vibratoire à l'échelle microscopique, les PEH ont donc un avantage supérieur en raison d'une tension de sortie relativement élevée, d'une densité de puissance de sortie relativement élevée et d'une conception simple par rapport à leurs homologues tels que les EMEH et les EEH.

Pendant plusieurs décennies, les céramiques piézoélectriques à base de plomb, telles que le PZT, ont été considérées comme les matériaux piézoélectriques les plus utilisés en raison de leurs fortes constantes piézoélectriques, de leur température de Curie élevée T_c et de leurs étapes de traitement relativement matures. L'existence d'une limite de phase morphotrope (MPB) entre deux phases ferroélectriques contribue à leur polarisation efficace, ce qui améliore les propriétés électromécaniques. Néanmoins, le plomb et ses dérivés, comme l'oxyde de plomb (PbO), ont été signalés comme présentant une toxicité et sont donc considérés comme des matières dangereuses. Récemment, l'Union européenne a également mis en œuvre la législation sur la restriction des substances dangereuses, qui a établi une norme stricte limitant l'utilisation de matériaux piézoélectriques à base de plomb dans les futurs appareils électroniques. En conséquence, plusieurs approches sont étudiées vers les matériaux céramiques sans plomb ces dernières années. Par exemple, telles que les monocristaux piézoélectriques et les céramiques ferroélectriques à structure pérovskite et les ferroélectriques à structure en couche de bismuth, ont fait l'objet de recherches approfondies. Également, plusieurs ferroélectriques à structure pérovskite BaTiO_3 [BT], $(\text{Bi}_{1/2}\text{Na}_{1/2})\text{TiO}_3$ [BNT], $(\text{Bi}_{1/2}\text{K}_{1/2})\text{TiO}_3$ [BKT], KNbO_3 [KN], $(\text{K},\text{Na})\text{NbO}_3$ [KNN]) ont fait l'objet de nombreuses recherches.

Sur la base de la relation entre la contrainte appliquée et la direction de polarisation du matériau piézoélectrique, les PEH peuvent être classés en modes de fonctionnement d_{31} , d_{33} et d_{15} . Dans les modes d_{31} et d_{33} , le matériau piézoélectrique est soumis à une contrainte de flexion alors que dans le mode d_{15} c'est la contrainte de cisaillement qui entre en jeu. Les PEH possèdent des électrodes à plaques parallèles en mode d_{31} avec la direction de polarisation perpendiculaire à la direction de la contrainte appliquée. Un PEH en mode d_{33} est constitué d'électrodes interdigitées car la direction de polarisation est parallèle à la direction de la contrainte appliquée. Le mode d_{31} est plus couramment mis en œuvre que le mode d_{33} en raison de sa simplicité de fabrication. Cependant, d_{33} est normalement supérieur au coefficient d_{31} dans les matériaux piézoélectriques. Ainsi, le mode d_{33} génère une tension de sortie plus élevée. Précisons qu'un PEH génère une tension alternative à la sortie. Par conséquent, un circuit de gestion de l'alimentation (PMC) est nécessaire pour rectifier, stocker et réguler la sortie CA avant qu'elle ne puisse être utilisée pour alimenter les WSN. Étant donné que les microgénérateurs produisent de l'énergie de l'ordre des microwatts, ce qui est juste suffisant pour alimenter les nœuds IoT, ces dispositifs doivent être efficaces pour les applications à faible consommation. Les PMC avec les solutions de circuits intégrés (IC) sur puce

obtiennent de meilleures performances que les implémentations avec des composants discrets prêts à l'emploi. PMC agit comme une interface entre le récupérateur d'énergie piézoélectrique (PEH) et la charge connectée.

Chapitre 1 : Caractérisation électromécanique des matériaux piézoélectriques

Dans ce chapitre, l'extraction de propriétés électromécaniques telles que d_{33} et la figure de mérite (FoM) de récupération d'énergie de matériaux piézoélectriques sans plomb à l'échelle microscopique, pour développer des dispositifs de récupération d'énergie vibratoire sont discutées. Les résultats sont comparés au monocristal de niobate de lithium sans plomb disponible dans le commerce, pour la fabrication de récupérateurs d'énergie. Les techniques qui ont été utilisées pour caractériser les propriétés piézoélectriques, les morphologies telles que la Microscopie à Force Atomique (AFM) sont détaillées.

La microscopie à force de réponse piézoélectrique (PFM) est devenue un outil puissant pour étudier les propriétés électromécaniques, le mécanisme de commutation des domaines ferroélectriques et la réponse piézoélectrique dans les matériaux de faible dimension ces dernières années. La technique PFM est basée sur la microscopie à sonde à balayage (SPM) en mode contact, où le SPM est équipé d'un générateur de fonctions, d'un amplificateur de verrouillage et d'un porte-à-faux conducteur. Dans la technique PFM, une pointe AFM conductrice agit comme une électrode supérieure, tandis que l'autre côté de l'échantillon est connecté électriquement au mandrin conducteur qui est mis à la terre et agit comme l'électrode inférieure.

Le PFM peut donc mesurer à la fois les composants hors plan et dans le plan de la réponse piézoélectrique, souvent également appelés PFM vertical (VPFM) et PFM latéral (LPFM). VPFM indique les mouvements verticaux de la position du laser sur le photodétecteur sensible à la position (PSD), associés au mouvement hors plan de l'échantillon. La caractérisation à l'échelle microscopique de nouveaux matériaux piézoélectriques sans plomb déposés par un procédé sol-gel est réalisée. Le tantalate de lithium (LT), le niobate de sodium et de potassium (KNN), les couches minces et les fibres de niobate de sodium et de potassium dopés au tantale (KNNT) sont étudiés et leurs propriétés électromécaniques et leurs potentiels de récupération d'énergie sont comparées au monocristal de niobate de lithium (LN).

Les principales propriétés piézoélectriques telles que d_{33} et la figure de mérite (FoM) de récupération d'énergie sont extraites. Les propriétés électromécaniques et la commutation de polarisation des matériaux ferroélectriques sans plomb, à savoir le tantalate de lithium LT (films minces), le niobate de sodium et de potassium (KNN) et le KNN dopé au Ta (films et fibres) ont été étudiés à l'aide de PFM. Le tantalate de lithium (LiTaO_3)-(LT) est une pérovskite à température de Curie élevée (650 °C) qui peut être utilisée à température élevée pour la récupération d'énergie électromécanique. De même, Le niobate de potassium et de sodium (KNN) sont des céramiques piézoélectrique biocompatibles respectueuses de l'environnement avec un coefficient piézoélectriques (d_{33}) comparables au titanate de zirconate de plomb (PZT) dans le transducteur. Bien que les films KNN n'aient montré aucune amélioration de d_{33} par polarisation sous pointe AFM à 3 kV/mm (20 V V_{tip}), la polarisation à des températures élevées à 4 kV/mm s'est avérée augmenter le coefficient piézoélectrique (d_{33}) à partir de 23 pm /V à 22h/V. Bien que les valeurs de d_{33} des échantillons non polarisés soient inférieures aux valeurs de pointe qui ont été rapportées jusqu'à présent, l'augmentation de d_{33} lors de la polarisation est un signe prometteur de l'utilisation de ces matériaux dans les applications de récupération d'énergie. De plus, l'étude des films de KNNT montre que la substitution du site B par Ta peut conduire à une augmentation significative du d_{33} par rapport aux échantillons de KNN purs. Le d_{33} du porte-à-faux KNNT non polarisé s'est avéré être de 48 pm/V, qui a augmenté à 221 pm/V lors de la polarisation à 3 kV/mm. Ces valeurs sont proches des valeurs d_{33} des films KNNT rapportées jusqu'à présent et peuvent donc être exploitées pour être utilisées dans des applications de récupération d'énergie à l'avenir. Cette étude de la réponse piézoélectrique de ces films pourrait être utile pour la compréhension et l'optimisation des propriétés piézoélectriques des PTF pour diverses applications et ainsi permettre d'évaluer les performances des dispositifs PTF. De plus, les propriétés ferroélectriques et la commutation de polarisation (hystérésis et courbes papillon) des fibres KNN et KNNT ont été étudiées avant et après la polarisation par AFM. Les fibres KNNT ont montré un coefficient piézoélectrique d_{33} (~130 pm/V) par rapport aux fibres KNN non dopées (28 pm/V). Les bonnes propriétés piézoélectriques des fibres KNN/KNNT suggèrent qu'elles pourraient être utilisées pour fabriquer de nouveaux dispositifs PEH flexibles. Il a été observé que le FoM des porte-à-faux au tantalate de lithium augmente avec l'épaisseur, ce qui est dû à l'augmentation de la permittivité diélectrique. Parmi tous les films traités sol-gel, le film KNNT présente une FoM plus élevée en raison de ses valeurs de permittivité diélectrique plus élevées. Enfin, le FoM des films sans plomb

traités sol-gel a été déterminé pour une éventuelle évaluation en tant que candidat pour des applications de récupération d'énergie. Les FoM de ces films traités sol-gel sur acier sont comparés au monocristal de niobate de lithium sans plomb disponible dans le commerce. En comparaison, le FoM du monocristal de niobate de lithium est supérieur aux films KNN et KNNT traités sol-gel, grâce à leur faible permittivité diélectrique. Bien que les cristaux de niobate de lithium soient largement utilisés pour les applications optiques et RF, leur application dans la récupération d'énergie vibratoire est rarement étudiée. Pour cette raison, un récupérateur d'énergie piézoélectrique sans plomb basé sur un monocristal de niobate de lithium sera exploré dans le chapitre suivant.

Chapitre 3 : Microgénérateur piézoélectrique à base de monocristal de niobate de lithium sans plomb

Dans ce chapitre, la fabrication et la caractérisation d'un microgénérateur sans plomb basé sur une plaquette monocristalline de niobate de lithium sans plomb sont discutées. En outre, un modèle de circuit équivalent électromécanique du récupérateur d'énergie piézoélectrique est développé et, en outre, le conditionnement de tension et l'interfaçage du dispositif pour une sortie CC contrôlée et stable sont discutés. Une architecture efficace pour maximiser la puissance transférée à la charge avec un Maximum Power Point Tracking (MPPT) est également étudiée, avec un accent particulier sur les circuits à faible puissance. Concernant le LiNbO_3 piézoélectrique (niobate de lithium - LN), il a été démontré que les propriétés électromécaniques des monocristaux de LN dépendent fortement de l'orientation, et sont comparables aux céramiques PZT. Le LN (YXl)/128 a été peu étudié dans le domaine de la récupération d'énergie, même s'il présente une constante diélectrique beaucoup plus faible que la famille PZT ($\epsilon_{33} = 50,5$) et un coefficient piézoélectrique plus élevé par rapport aux autres matériaux sans Pb ($d_{23}=27 \text{ pC/N}$). Un autre défi majeur auquel sont confrontés les PEH est la bande passante étroite de la fréquence de fonctionnement, car la tension et la puissance de sortie diminuent considérablement en s'éloignant de la fréquence de résonance. Le PEH produit une tension de sortie CA en phase avec la fréquence appliquée de la force mécanique et la tension doit être redressée avant de pouvoir être stockée pour une application pratique. Ainsi, si la tension générée est inférieure à la chute de seuil de diode du redresseur, la puissance n'est pas utilisée. Étant donné que la fréquence des sources de vibrations environnementales ambiantes typiques est faible (moins de 300 Hz) et susceptible de varier dans

une certaine mesure, des PEH avec de faibles fréquences de résonance et des capacités de fonctionnement à large bande sont nécessaires pour des performances fiables. Il existe plusieurs rapports de microgénérateurs piézoélectriques avec diverses configurations complexes telles qu'une structure de membrane, plusieurs couches piézoélectriques empilées, etc. pour forcer la non-linéarité dans le système et pousser vers un régime de fréquence plus large. Cependant, ces approches à plusieurs degrés de liberté ont généralement des limitations telles qu'une densité de puissance réduite en raison d'un facteur Q de faible qualité. Récemment, un nouvel intérêt est apparu avec le réglage de la fréquence de fonctionnement des PEH en exploitant l'effet de couplage électromécanique élevé. Les PEH fortement couplés sont donc considérés comme une solution pour améliorer la bande passante en fréquence des PEH. Pour les PEH avec un grand K^2 , la division de résonance donne deux pics de puissance de sortie bien séparés entre eux, étendant ainsi la plage de récolte. Badel et Lefeuvre [180] ont montré qu'il est possible d'ajuster largement la fréquence de résonance des récupérateurs d'énergie piézoélectriques fortement couplés pour obtenir une récupération d'énergie à large bande à l'aide de circuits d'interface. De telles perspectives prometteuses pour la récupération d'énergie vibratoire à large bande ne peuvent être atteintes que par la conception et la fabrication de PEH avec un fort coefficient de couplage électromécanique global K . Cependant, la plupart des PEH hautement couplés signalés jusqu'à présent sont basés sur des matériaux à base de plomb tels que le PZT et le PMN-PT. Les « PEH verts » sans plomb avec une configuration simple, fonctionnant à de basses fréquences ambiantes avec un couplage K élevé et présentant une capacité opérationnelle à large bande sont rarement reparties dans la littérature. Par conséquent, ce chapitre aborde l'étude d'un microgénérateur PEH vert avec du niobate de lithium comme matériau piézoélectrique actif qui fonctionne à basse fréquence de résonance (~ 200 Hz) sur une large plage de fréquences de fonctionnement. L'aspect de conception et les considérations telles que la géométrie, le choix de la tension en circuit ouvert et la ou circuit de récupération d'un point de vue d'application d'un capteur de vibrations sans fil autonome en énergie (EAWVS), seront détaillés au chapitre 5. La caractérisation des performances de l'appareil telles que la tension de sortie, la puissance à charge optimale à différentes accélérations est présentée ainsi que l'extraction de paramètres internes tels que le couplage électromécanique K et le facteur de qualité mécanique Q_m . En outre, le modèle électromécanique global de Masons de l'appareil est dérivé de l'analyse d'impédance et les résultats sont comparés aux simulations LT-SPICE. Le modèle est validé en comparant les résultats expérimentaux avec la simulation LT-SPICE. Ensuite,

la résistance de charge optimale pour la récupération de puissance maximale est obtenue par des méthodes expérimentales et est comparée à la simulation à l'aide du circuit équivalent électromécanique. Enfin, le redresseur doubleur de tension est mis en œuvre et les résultats sont comparés avec le modèle LT-Spice sous une excitation de base et une fréquence de fonctionnement données pour une charge donnée. Les modèles de circuits équivalents avec une impédance globale Z_{in} peuvent être utilisés pour l'analyse et la conception de systèmes piézoélectriques. Le modèle de circuit équivalent est basé sur une analogie entre les variables d'état mécaniques et électriques. Enfin, une sortie de circuit de redressement appropriée est choisie pour convertir la tension alternative en courant continu en fonction des paramètres extraits de l'appareil (K^2Q_m). En prenant une plage de fréquences étroite, proche de la résonance (f_r), le facteur de qualité (Q_R) est évalué à 44. Le facteur de couplage électromécanique $k_{31} = 0,26$ est obtenu, ce qui donne un $K^2Q_m = 3$. Pour le pic de résonance à la charge optimale $R_{opt} = 550 \text{ k}\Omega$, la tension de crête $V_{\hat{e}t}$ et la puissance RMS (P_{RMS}) à 1 g d'accélération se trouvent respectivement proches de 6 V et 35 μW . Dans plusieurs scénarios d'application, le spectre de vibration d'entrée du PEH fluctue. Par conséquent, la largeur de bande de puissance BW, qui est un paramètre important pour déterminer la plage de fréquences de fonctionnement, est définie par les fréquences de coupure à mi-puissance. L'appareil a une demi-bande passante maximale pleine largeur de 10,8 % à la résonance. C'est un avantage évident car il peut être utilisé pour extraire l'énergie d'un spectre plus large de la fréquence d'entrée. La densité de puissance globale du PEH-PM peut être estimée à 36 $\mu\text{W}/\text{cm}^2/\text{g}^2$.

De plus, un nouveau concept de circuit à trois bornes avec suivi du point de puissance maximale (MPPT) pour les applications à très faible puissance a été exploré. La quantité de puissance générée à partir d'un système PEH dépend principalement de facteurs tels que la fréquence d'entrée et l'amplitude de la vibration d'entrée. Les variations des vibrations d'entrée modifient considérablement le point de fonctionnement optimal ou le suivi du point de puissance maximale (MPPT) d'un PEH avec le temps. Étant donné que les microgénérateurs produisent une puissance de l'ordre du microwatt, ce qui est juste suffisante pour alimenter les nœuds IoT, son fonctionnement au MPP, (quelles que soient les conditions d'entrée telles que la fréquence, l'accélération ou les variations de charge) doit être assuré. Pour rendre le MPPT intéressant dans les applications de récupération d'énergie à très faible puissance, une partie négligeable de la puissance récupérée doit être prise en compte dans la mise en œuvre de cette fonction. Étant donné que cela peut représenter un défi difficile pour les concepteurs de circuits intégrés, nous proposons

un nouveau récupérateur d'énergie piézoélectrique à trois bornes avec l'une des bornes exclusivement dédiées à la détection de la tension en circuit ouvert (V_{oc}). Ainsi, nous explorons une nouvelle approche de la méthode FOC pour déterminer la tension en circuit ouvert (V_{oc}) en temps réel à l'aide d'une troisième borne supplémentaire qui agit comme un capteur V_{oc} . Cette approche peut être avantageuse tant que la cellule de détection de V_{oc} est conçue avec une occupation de zone plus petite ou même négligeable par rapport au collecteur principal, de sorte que la zone utilisée à des fins de mesure, plutôt que pour la production d'énergie, est insignifiante. Selon cette conception, la perte de puissance produite par la récolteuse, due à la présence de la cellule de détection, est inférieure à 1 %. Du point de vue du système, cette perte de puissance et la présence d'une borne supplémentaire peuvent être compensées par divers avantages, dont la simplification de l'architecture du circuit associée aux fonctions MPPT (comme la pré-régulation, l'échantillonnage, le commutateur série et la logique), et la réduction relative de l'absorption de puissance. Avec ce nouveau concept, le circuit intégré de gestion de l'alimentation peut être grandement simplifié en un simple comparateur ultra-basse consommation, utilisé pour comparer la tension fournie par le circuit principal avec la tension fournie par la cellule de détection utilisée comme référence.

Chapitre 5 : Capteur de vibrations sans fil autonome en énergie basé sur un microgénérateur piézoélectrique

Dans ce chapitre, il est démontré que le circuit de récupération d'énergie alimente un IOT-WSN sans batterie basé sur la connectivité Bluetooth Low Energy (BLE) avec vibration ambiante. Nous explorons un système sans batterie - Energy Autonomous Wireless Vibration Sensor (EAWVS) pour surveiller les vibrations et les défauts qui se composent d'un PEH et d'un système de transmission radio basé sur un schéma Bluetooth Low Energy (BLE) qui est auto-déclenché et entièrement autonome. Étant donné que les pièces défectueuses ont un profil d'accélération plus prononcé que les pièces non défectueuses, ce travail introduit une méthodologie de détection de défaillance basée sur la mesure de l'accélération et sur son écart par rapport aux valeurs nominales des pièces non défectueuses. L'EAWVS se compose uniquement d'un PEH pour l'alimentation et d'une radio Bluetooth Low Energy (BLE) pour la connectivité. Le nœud du capteur peut être connecté sans fil à une station de base (BS) qui effectue le traitement des données et transfère les données vers le cloud. BLE est utilisé comme norme de communication en raison de

sa faible consommation d'énergie et de la compatibilité et de la facilité d'utilisation de BLE dans les appareils portables pour communiquer avec les WSN. Le nœud de capteur est conçu pour transmettre des ondes par intermittence, et ainsi la radio est arrêtée après chaque transmission pour minimiser la consommation d'énergie globale. La particularité de ce système est que le PEH joue le double rôle de transducteur d'énergie et de capteur vibratoire. La fabrication et la caractérisation du PEH à base de niobate de lithium sont abordées au chapitre 4. Le suivi de la vibration d'entrée est réalisé en mesurant le temps entre balises successives, également appelé advertising time (t_{adv}), émis par la radio EAWVS vers la BS. Et ainsi la radio est arrêtée après chaque transmission pour minimiser la consommation d'énergie globale.

L'EAWVS offre une flexibilité supplémentaire, qui permet la lecture des mesures à distance et sans fil en exploitant la communication BLE et en transmettant des balises à une BS distante avec la lecture du capteur basée sur la lecture dans le domaine temporel facile à mettre en œuvre en mesurant le t_{adv} . Le PEH remplit la double fonction de collecteur d'énergie et de capteur de vibration et, comme le montrent les résultats expérimentaux, il peut effectuer une détection de vibration dans la plage d'accélération [0,5 g - 1,2 g] avec une Limit of Detection (LoD) de 0,6 g. De plus, des tests expérimentaux ont montré que le système, basé sur l'EAWVS et la BS, a des capacités de détection reproductibles et précises dans une limite d'erreur de 11 %. Il a été démontré comment la simplicité de l'architecture EAWVS se traduit par plusieurs avantages tels que le respect de l'environnement, la taille, le coût, et surtout son utilisation comme dispositif «installation et oubli» sans entretien dans pratiquement toutes les applications où l'énergie de vibration est disponible. Enfin, toutes les mesures expérimentales ont été réalisées sur un PCB de 2 cm x 2 cm d'une épaisseur de 0,45 cm, implémenté, à l'exception du PEH, avec des composants standards uniquement pour démontrer la faisabilité d'une preuve de concept dont les performances opérationnelles pourraient être encore améliorées par de prochains progrès que la recherche des matériaux et des composants électroniques apportera à l'avenir.

Conclusion et perspectives

Le travail réalisé au cours de la thèse aborde plusieurs aspects de la récupération d'énergie piézoélectrique, du point de vue des matériaux, des dispositifs, des systèmes et des applications. Les propriétés électromécaniques à l'échelle microscopique telles que le coefficient

piézoélectrique (d_{33}) et le facteur de mérite peuvent être des informations précieuses pour l'optimisation des propriétés et également un outil pour la sélection de matériaux sans plomb pour les futurs dispositifs et applications de récupération d'énergie. Aussi, il explore les moyens d'améliorer ces propriétés par dopage et « poling ». Un récupérateur d'énergie piézoélectrique monobloc unimorphe basé sur un cristal de niobate de lithium sans plomb a été conçu et ses performances ont été évaluées. Pour assurer une efficacité de conversion maximale dans les systèmes d'alimentation sous le microwatt, un PEH à trois bornes a été proposé qui consiste en une nouvelle architecture MPPT dont le but principal est de rendre le MPPT intéressant. Avec l'architecture MPPT, le circuit intégré de gestion de l'alimentation (PMIC) et le circuit de récupération d'énergie peuvent être simplifiés en un comparateur de puissance ultra-faible minimal sans oscillateurs, circuits de détection ou de pré-régulation. Enfin, un circuit de récupération est utilisée pour alimenter un nouveau capteur sans fil auto-alimenté et sans pile pour la surveillance des vibrations qui peut effectuer une détection vibratoire dans la plage d'accélération [0,5 g - 1,2 g], dans une limite d'erreur de 11 %. Le présent travail offre plusieurs perspectives. Tout d'abord, il propose de améliorations des performances du récupérateur d'énergie piézoélectrique par une meilleure conception et une éventuelle miniaturisation du récupérateur qui pourraient être explorées par de nouvelles étapes de procédés de fabrication compatibles avec l'industrie MEMS/microélectronique. L'amélioration du rendement de l'abatteuse peut ainsi améliorer la LoD de l'EAWS. De plus, les performances d'autres collecteurs basées sur des matériaux sans plomb tels que le KNN et le tantalate de lithium peuvent être explorées du point de vue de l'application d'un capteur. Deuxièmement, les voies possibles de mise en œuvre physique des trois collecteurs de terminaux basés sur la nouvelle architecture MPPT, dont la preuve de concept a été détaillée dans cette thèse, doivent être explorées. Il n'est pas judicieux de mettre en œuvre des circuits d'interface avec des composants électroniques discrets dans le cas de circuits microélectroniques où le courant de fonctionnement est juste de l'ordre de quelques microampères. Par conséquent, le moissonneur à 3 terminaux avec la nouvelle architecture MPPT pourrait être mis en œuvre avec l'ASIC en consultation avec les ingénieurs de conception de circuits intégrés de ST Microelectronics à l'avenir pour le rendre intéressant. Enfin, l'application de l'EAWVS du point de vue de la surveillance de l'état et, finalement, la conceptualisation de l'idée en un produit viable sont explorées. Le collecteur à 3 terminaux avec la nouvelle architecture MPPT pourrait être mis

en œuvre avec l'ASIC en consultation avec les ingénieurs de conception de circuits intégrés de ST Microelectronics à l'avenir pour le rendre intéressant.

References

- [1] S. M. R. Islam, J. Lloret, and Y. B. Zikria, “Internet of things (IoT)-Based wireless health: Enabling technologies and applications,” *Electronics*, vol. 10, no. 2, 2021, doi: 10.3390/electronics10020148.
- [2] A. S. Adila, A. Husam, and G. Husi, “Towards the self-powered Internet of Things (IoT) by energy harvesting: Trends and technologies for green IoT,” in *2018 2nd International Symposium on Small-scale Intelligent Manufacturing Systems (SIMS)*, Cavan, Apr. 2018, pp. 1–5. doi: 10.1109/SIMS.2018.8355305.
- [3] R. Fedele, M. Merenda, and F. Giammaria, “Energy harvesting for IoT road monitoring systems,” *isi*, vol. 18, no. 4, pp. 605–623, Dec. 2018, doi: 10.3166/i2m.17.605-623.
- [4] “Market Research Report, 2020 July, pp 140, <https://www.fortunebusinessinsights.com/industry-reports/internet-of-things-iot-market-100307>.”
- [5] S. Bhalla, S. Moharana, V. Talakokula, and N. Kaur, *Piezoelectric Materials: Applications in SHM, Energy Harvesting and Bio-mechanics*. Chichester, UK: John Wiley & Sons, Ltd, 2016. doi: 10.1002/9781119265139.
- [6] M. M. Ahmad and F. U. Khan, “Review of vibration-based electromagnetic–piezoelectric hybrid energy harvesters,” *Int J Energy Res*, vol. 45, no. 4, pp. 5058–5097, Mar. 2021, doi: 10.1002/er.6253.
- [7] S. Boisseau, G. Despesse, and B. Ahmed, “Electrostatic Conversion for Vibration Energy Harvesting,” in *Small-Scale Energy Harvesting*, M. Lallart, Ed. InTech, 2012. doi: 10.5772/51360.
- [8] S. Naifar, S. Bradai, C. Viehweger, and O. Kanoun, “Survey of electromagnetic and magnetoelectric vibration energy harvesters for low frequency excitation,” *Measurement*, vol. 106, pp. 251–263, Aug. 2017, doi: 10.1016/j.measurement.2016.07.074.
- [9] M. Iqbal, M. M Nauman, F.U. Khan, P. E Abas, Q. Cheok, A. Iqbal, B. Aissa “Vibration-based piezoelectric, electromagnetic, and hybrid energy harvesters for microsystems applications: A contributed review,” *Int J Energy Res*, vol. 45, no. 1, pp. 65–102, Jan. 2021, doi: 10.1002/er.5643.

- [10] M.-G. Kang, W.-S. Jung, C.-Y. Kang, and S.-J. Yoon, "Recent Progress on PZT Based Piezoelectric Energy Harvesting Technologies," *Actuators*, vol. 5, no. 1, p. 5, Feb. 2016, doi: 10.3390/act5010005.
- [11] M. A. Albreem, A. M. Sheikh, M. H. Alsharif, M. Jusoh, and M. N. Mohd Yasin, "Green Internet of Things (GloT): Applications, Practices, Awareness, and Challenges," *IEEE Access*, vol. 9, pp. 38833–38858, 2021, doi: 10.1109/ACCESS.2021.3061697.
- [12] "STMicroelectronics. Ultra-Low-Power 32-Bit MCU Arm-Based Cortex-M0+, up to 64 KB Flash Memory, 8 KB SRAM, 2 KB EEPROM, USB, ADC, DAC, STM32L052x6 STM32L052x8 datasheet. Available online: <https://www.st.com> (accessed on June 20th, 2020). STMicro386 electronics Geneva, Switzerland, 2014.".
- [13] S. Roundy, P. K. Wright, and J. Rabaey, "A study of low level vibrations as a power source for wireless sensor nodes," *Computer Communications*, vol. 26, no. 11, pp. 1131–1144, Jul. 2003, doi: 10.1016/S0140-3664(02)00248-7.
- [14] X. Fu, T. Bu, C. Li, G. Liu, and C. Zhang, "Overview of micro/nano-wind energy harvesters and sensors," *Nanoscale*, vol. 12, no. 47, pp. 23929–23944, 2020, doi: 10.1039/D0NR06373H.
- [15] Q. Liu, X. Wang, W. Song, H. Qiu, J. Zhang, Z. Fan, M. Yu, Y. Long, "Wireless Single-Electrode Self-Powered Piezoelectric Sensor for Monitoring," *ACS Appl. Mater. Interfaces*, vol. 12, no. 7, pp. 8288–8295, Feb. 2020, doi: 10.1021/acsami.9b21392.
- [16] P. Micek and D. Grzybek, "Wireless stress sensor based on piezoelectric energy harvesting for a rotating shaft," *Sensors and Actuators A: Physical*, vol. 301, p. 111744, Jan. 2020, doi: 10.1016/j.sna.2019.111744.
- [17] "<http://www.iba-industrial.com/industry-solutions/wire-and-cable-e-beam-crosslinking>."
- [18] "D. Shen et al., 'Micromachined PZT cantilever based on SOI structure for low frequency vibration energy harvesting,' *Sensors Actuators, A Phys.*, vol. 154, no. 1, pp. 103–108, Aug. 2009".
- [19] J. Wu, "Perovskite lead-free piezoelectric ceramics," *Journal of Applied Physics*, vol. 127, no. 19, p. 190901, May 2020, doi: 10.1063/5.0006261.
- [20] G. Clementi, S. Margueron, M. A. Suarez, T. Baron, B. Dulmet, and A. Bartasyte, "Piezoelectric and Pyroelectric Energy Harvesting from Lithium Niobate Films," *J. Phys.: Conf. Ser.*, vol. 1407, p. 012039, Nov. 2019, doi: 10.1088/1742-6596/1407/1/012039.

- [21] C. Sun, X. Chen, J. Wang, G. Yuan, J. Yin, and Z. Liu, "Structure and piezoelectric properties of BiFeO₃ and Bi_{0.92}Dy_{0.08}FeO₃ multiferroics at high temperature," *Solid State Communications*, vol. 152, no. 14, pp. 1194–1198, Jul. 2012, doi: 10.1016/j.ssc.2012.04.067.
- [22] L. Van Minh, M. Hara, and H. Kuwano, "High performance nonlinear micro energy harvester integrated with (K, Na)NbO₃/Si composite quad-cantilever," in *2014 IEEE 27th International Conference on Micro Electro Mechanical Systems (MEMS)*, San Francisco, CA, USA, Jan. 2014, pp. 397–400. doi: 10.1109/MEMSYS.2014.6765660.
- [23] R. La Rosa, P. Livreri, C. Trigona, L. Di Donato, and G. Sorbello, "Strategies and Techniques for Powering Wireless Sensor Nodes through Energy Harvesting and Wireless Power Transfer," *Sensors*, vol. 19, no. 12, p. 2660, Jun. 2019, doi: 10.3390/s19122660.
- [24] Q. Liu *et al.*, "Wireless Single-Electrode Self-Powered Piezoelectric Sensor for Monitoring," *ACS Appl. Mater. Interfaces*, vol. 12, no. 7, pp. 8288–8295, Feb. 2020, doi: 10.1021/acsami.9b21392.
- [25] V. Dertimanis and E. Chatzi, "Sensor Networks in Structural Health Monitoring: From Theory to Practice," *JSAN*, vol. 9, no. 4, p. 47, Oct. 2020, doi: 10.3390/jsan9040047.
- [26] "8-pin mcu with high-precision 16-bit pwms. [Online]. Available: <http://ww1.microchip.com/downloads/en/DeviceDoc/40001723D.pdf>."
- [27] "Msp432p401r, msp432p401m mixed-signal microcontrollers. [Online]. Available: <http://www.ti.com/lit/ds/symlink/msp432p401r.pdf>."
- [28] "STMicroelectronics. Bluetooth® Low Energy wireless system-on-chip. Available online: 388 <https://www.Bluetooth.com/specifications> (accessed on June 20th, 2020). STMicroelectron389 ics Geneva, Switzerland, 2010."
- [29] A. R. M. Siddique, S. Mahmud, and B. V. Heyst, "A comprehensive review on vibration based micro power generators using electromagnetic and piezoelectric transducer mechanisms," *Energy Conversion and Management*, vol. 106, pp. 728–747, Dec. 2015, doi: 10.1016/j.enconman.2015.09.071.
- [30] "Kehoe MW, Freudinger LC. Aircraft ground vibration testing at the NASA dryden flight research facility. NASA Technical Memorandum, 104275; 1993."
- [31] E. B Hameyie, M. A. Bitetto, , N. Thambi, & K. A Cook-Chennault, , "Piezoelectric Energy Harvesting: A Green and Clean Alternative for Sustained Power Production.," 2008.

- [32] S. Roundy, “On the Effectiveness of Vibration-based Energy Harvesting,” *Journal of Intelligent Material Systems and Structures*, vol. 16, no. 10, pp. 809–823, Oct. 2005, doi: 10.1177/1045389X05054042.
- [33] M. Li and X. Jing, “Novel tunable broadband piezoelectric harvesters for ultralow-frequency bridge vibration energy harvesting,” *Applied Energy*, vol. 255, p. 113829, Dec. 2019, doi: 10.1016/j.apenergy.2019.113829.
- [34] M. Zhou, M. S. H. Al-Furjan, J. Zou, and W. Liu, “A review on heat and mechanical energy harvesting from human – Principles, prototypes and perspectives,” *Renewable and Sustainable Energy Reviews*, vol. 82, pp. 3582–3609, Feb. 2018, doi: 10.1016/j.rser.2017.10.102.
- [35] S. P. Beeby, L. Wang, D. Zhu, A. S. Weddel, G. V. Merrett, B. Stark, G. Szarka, B.M. Al-Hashimi “A micro electromagnetic generator for vibration energy harvesting,” *J. Micromech. Microeng.*, vol. 17, no. 7, pp. 1257–1265, Jul. 2007, doi: 10.1088/0960-1317/17/7/007.
- [36] Y. Liu, X. Zhang, S. Niu, W. Fu, and X. Guo, “Design and Analysis of a Linear Memory Machine for Ocean Wave Power Generation,” *Energies*, vol. 13, no. 19, p. 5216, Oct. 2020, doi: 10.3390/en13195216.
- [37] M. Gao, P. Wang, Y. Cao, R. Chen, and D. Cai, “Design and Verification of a Rail-Borne Energy Harvester for Powering Wireless Sensor Networks in the Railway Industry,” *IEEE Trans. Intell. Transport. Syst.*, pp. 1–14, 2016, doi: 10.1109/TITS.2016.2611647.
- [38] U. Erturun, A. A. Eisape, S. H. Kang, and J. E. West, “Energy harvester using piezoelectric nanogenerator and electrostatic generator,” *Appl. Phys. Lett.*, vol. 118, no. 6, p. 063902, Feb. 2021, doi: 10.1063/5.0030302.
- [39] T. Nakanishi, T. Miyajima, K. Chokawa, M. Aradidai, H. Toshiyoshi, T. Sugiyama, G. Hashiguchi, K. Shiraishi, “Negative-charge-storing mechanism of potassium-ion SiO_2 -based electrets for vibration-powered generators,” *Appl. Phys. Lett.*, vol. 117, no. 19, p. 193902, Nov. 2020, doi: 10.1063/5.0029012.
- [40] P. R. Adhikari, N. T. Tasneem, R. C. Reid, and I. Mahbub, “Electrode and electrolyte configurations for low frequency motion energy harvesting based on reverse electrowetting,” *Sci Rep*, vol. 11, no. 1, p. 5030, Dec. 2021, doi: 10.1038/s41598-021-84414-3.

- [41] M. Salem, M. Salem, D.-A. Borca-Tasciuc, and M. M. Hella, “Electrostatic MEMS converters with a switchable dielectric constant for micro-scale power generation,” in *2007 International Conference on Microelectronics*, Cairo, Egypt, Dec. 2007, pp. 205–208. doi: 10.1109/ICM.2007.4497694.
- [42] S. Roundy *Energy Scavenging for Wireless Sensor Nodes with a Focus on Vibration to Electricity Conversion. PhD Thesis. University of California, Berkeley, 2003.*
- [43] P. Basset, D. Galayko, F. Cottone, E. Blokhina, F. Marty, T. Bourouina “Electrostatic vibration energy harvester with combined effect of electrical nonlinearities and mechanical impact,” *J. Micromech. Microeng.*, vol. 24, no. 3, p. 035001, Mar. 2014, doi: 10.1088/0960-1317/24/3/035001.
- [44] M. Martins, V. Correia, J. M. Cabral, S. Lanceros-Mendez, and J. G. Rocha, “Optimization of piezoelectric ultrasound emitter transducers for underwater communications,” *Sensors and Actuators A: Physical*, vol. 184, pp. 141–148, Sep. 2012, doi: 10.1016/j.sna.2012.06.008.
- [45] F. Akasheh, T. Myers, J. D. Fraser, S. Bose, and A. Bandyopadhyay, “Development of piezoelectric micromachined ultrasonic transducers,” *Sensors and Actuators A: Physical*, vol. 111, no. 2–3, pp. 275–287, Mar. 2004, doi: 10.1016/j.sna.2003.11.022.
- [46] R. Proksch, “Piezoresponse Force Microscopy with Asylum Research AFMs,” p. 24.
- [47] G. Ivensky, S. Bronstein, and S. Ben-Yaakov, “A Comparison of Piezoelectric Transformer AC/DC Converters with Current Doubler and Voltage Doubler Rectifiers,” *IEEE Trans. Power Electron.*, vol. 19, no. 6, pp. 1446–1453, Nov. 2004, doi: 10.1109/TPEL.2004.836646.
- [48] W. Tian, Z. Ling, W. Yu, and J. Shi, “A Review of MEMS Scale Piezoelectric Energy Harvester,” *Applied Sciences*, vol. 8, no. 4, Art. no. 4, Apr. 2018, doi: 10.3390/app8040645.
- [49] S. Saxena, R. Sharma, and B. D. Pant, “Design and development of guided four beam cantilever type MEMS based piezoelectric energy harvester,” *Microsyst Technol*, vol. 23, no. 6, pp. 1751–1759, Jun. 2017, doi: 10.1007/s00542-016-2940-1.
- [50] M. Huang, “A Low-Frequency MEMS Piezoelectric Energy Harvesting System Based on Frequency Up-Conversion Mechanism,” *Micromachines*, vol. 10, no. 10, p. 639, Sep. 2019, doi: 10.3390/mi10100639.

- [51] A. Chamuah, “Piezoelectric Energy Harvester Using MEMS Structures: A Review,” vol. 4, no. 2, p. 6, 2018.
- [52] N. Panayanthatta, L. Montes, E. Bano, C. Trigona, and R. L. Rosa, “Three terminal piezoelectric energy harvester based on novel MPPT design,” in *2019 19th International Conference on Micro and Nanotechnology for Power Generation and Energy Conversion Applications (PowerMEMS)*, Krakow, Poland, Dec. 2019, pp. 1–7. doi: 10.1109/PowerMEMS49317.2019.92321107155.
- [53] X. Sun, P. Wang, Z. Wang, Z. Xia, X. Yue, X Ding, S Shi,. "A piezoelectric vibration energy harvester with the adjustable frequency". *Micronanoelectronic Technol.* 2014, 51, 518–522”.
- [54] L. Tang, Y. Yang, A nonlinear piezoelectric energy harvester with magnetic oscillator. *Appl. Phys. Lett.* 2012, 101, 094102”.
- [55] N. Zhao, J. Yang, Q. Yu, J Zhao,. J. Liu Y. Wen, P. Li, "Three-dimensional piezoelectric vibration energy harvester using spiral-shaped beam with triple operating frequencies". *Rev. Sci. Instrum.* 2016, 87, 1316–11324”.
- [56] B. Andò, S. Baglio, A. R. Bulsara, V. Marletta, "A bistable buckled beam based approach for vibrational energy harvesting". *Sens. Actuators A Phys.* 2014, 211, 153–161”.
- [57] M. Dorfmeister, B. Kössl, M. Schneider, and U. Schmid, “A Novel Bi-Stable MEMS Membrane Concept Based on a Piezoelectric Thin Film Actuator for Integrated Switching,” *Proceedings*, vol. 2, no. 13, p. 912, Jan. 2019, doi: 10.3390/proceedings2130912.
- [58] F. Costache, B. Pawlik, and A. Rieck, “Development of a Compact, Low-Frequency Vibration, Piezoelectric MEMS Energy Harvester,” *Proceedings*, vol. 1, no. 4, Art. no. 4, Aug. 2017, doi: 10.3390/proceedings1040588.
- [59] E. C. N. Silva and N. Kikuchi, “Design of piezoelectric transducers using topology optimization,” *Smart Materials and Structures*, vol. 8, no. 3, pp. 350–364, Jun. 1999, doi: 10.1088/0964-1726/8/3/307.
- [60] E. L. Pradeesh and S. Udhayakumar, “Investigation on the geometry of beams for piezoelectric energy harvester,” *Microsyst Technol*, vol. 25, no. 9, pp. 3463–3475, Sep. 2019, doi: 10.1007/s00542-018-4220-8.

- [61] Y. Fenglin, M. Wengjun, Z. Jie, and Y. Hang, “Cantilever beam based piezoelectric energy harvester,” *International Journal on Smart Sensing and Intelligent Systems*, vol. 8, no. 4, pp. 2018–2041, 2015, doi: 10.21307/ijssis-2017-841.
- [62] M. I. Friswell and S. Adhikari, “Sensor shape design for piezoelectric cantilever beams to harvest vibration energy,” *Journal of Applied Physics*, vol. 108, no. 1, p. 014901, Jul. 2010, doi: 10.1063/1.3457330.
- [63] X. Gao, W.-H. Shih, and W. Y. Shih, “Vibration energy harvesting using piezoelectric unimorph cantilevers with unequal piezoelectric and nonpiezoelectric lengths,” *Appl. Phys. Lett.*, vol. 97, no. 23, p. 233503, Dec. 2010, doi: 10.1063/1.3521389.
- [64] E. Dechant, F. Fedulov, L. Fetisov, and M. Shamonin, “Bandwidth Widening of Piezoelectric Cantilever Beam Arrays by Mass-Tip Tuning for Low-Frequency Vibration Energy Harvesting,” *Applied Sciences*, vol. 7, no. 12, p. 1324, Dec. 2017, doi: 10.3390/app7121324.
- [65] X. Chen, S. Xu, N. Yao, and Y. Shi, “1.6 V Nanogenerator for Mechanical Energy Harvesting Using PZT Nanofibers,” *Nano Letters*, vol. 10, no. 6, pp. 2133–2137, Jun. 2010, doi: 10.1021/nl100812k.
- [66] M. Riaz, J. Song, O. Nur, Z. L. Wang, and M. Willander, “Study of the Piezoelectric Power Generation of ZnO Nanowire Arrays Grown by Different Methods,” *Advanced Functional Materials*, vol. 21, no. 4, pp. 628–633, Feb. 2011, doi: 10.1002/adfm.201001203.
- [67] A. Romani, R. P. Paganelli, and M. Tartagni, “Fast and Reliable Modeling of Piezoelectric Transducers for Energy Harvesting Applications,” *Procedia Engineering*, vol. 25, pp. 1345–1348, 2011, doi: 10.1016/j.proeng.2011.12.332.
- [68] B. Kumar and S.-W. Kim, “Energy harvesting based on semiconducting piezoelectric ZnO nanostructures,” *Nano Energy*, vol. 1, no. 3, Art. no. 3, May 2012, doi: 10.1016/j.nanoen.2012.02.001.
- [69] H. Y. S. Al-Zahrani, “Non Linear Piezoelectricity in Wurtzite Semiconductor Core-Shell Nanowires: An Atomistic Modelling Approach,” p. 144.
- [70] R. Agrawal, B. Peng, E. E. Gdoutos, and H. D. Espinosa, “Elasticity Size Effects in ZnO Nanowires—A Combined Experimental-Computational Approach,” *Nano Letters*, vol. 8, no. 11, Art. no. 11, Nov. 2008, doi: 10.1021/nl801724b.

- [71] Z. L. Wang, “Splendid One-Dimensional Nanostructures of Zinc Oxide: A New Nanomaterial Family for Nanotechnology,” *ACS Nano*, vol. 2, no. 10, pp. 1987–1992, Oct. 2008, doi: 10.1021/nn800631r.
- [72] R. Agrawal and H. D. Espinosa, “Giant Piezoelectric Size Effects in Zinc Oxide and Gallium Nitride Nanowires. A First Principles Investigation,” *Nano Letters*, vol. 11, no. 2, pp. 786–790, Feb. 2011, doi: 10.1021/nl104004d.
- [73] D. Faust and R. Lakes, “Temperature and Substrate Dependence of Piezoelectric Sensitivity for PVDF Films,” *Ferroelectrics*, vol. 481, no. 1, pp. 1–9, Jun. 2015, doi: 10.1080/00150193.2015.1048149.
- [74] L. Serairi, L. Gu, Y. Qin, Y. Lu, P. Basset, and Y. Leprince-Wang, “Flexible piezoelectric nanogenerators based on PVDF-TrFE nanofibers,” *Eur. Phys. J. Appl. Phys.*, vol. 80, no. 3, p. 30901, Dec. 2017, doi: 10.1051/epjap/2017170288.
- [75] J. Ryu *et al.*, “Ubiquitous magneto-mechano-electric generator,” *Energy Environ. Sci.*, vol. 8, no. 8, pp. 2402–2408, 2015, doi: 10.1039/C5EE00414D.
- [76] F. Dell’Anna *et al.*, “State-of-the-Art Power Management Circuits for Piezoelectric Energy Harvesters,” *IEEE Circuits Syst. Mag.*, vol. 18, no. 3, pp. 27–48, 2018, doi: 10.1109/MCAS.2018.2849262.
- [77] E. Lefeuvre, D. Audigier, C. Richard, and D. Guyomar, “Buck-Boost Converter for Sensorless Power Optimization of Piezoelectric Energy Harvester,” *IEEE Trans. Power Electron.*, vol. 22, no. 5, pp. 2018–2025, Sep. 2007, doi: 10.1109/TPEL.2007.904230.
- [78] A. Tabesh and L. G. Frechette, “A Low-Power Stand-Alone Adaptive Circuit for Harvesting Energy From a Piezoelectric Micropower Generator,” *IEEE Trans. Ind. Electron.*, vol. 57, no. 3, Art. no. 3, Mar. 2010, doi: 10.1109/TIE.2009.2037648.
- [79] G. Ivensky, M. Shvartsas, and S. Ben-Yaakov, “Analysis and Modeling of a Voltage Doubler Rectifier Fed by a Piezoelectric Transformer,” *IEEE Trans. Power Electron.*, vol. 19, no. 2, pp. 542–549, Mar. 2004, doi: 10.1109/TPEL.2003.823179.
- [80] A. Toprak, “MEMS Scale CMOS Compatible Energy Harvesters Using Piezoelectric Polymers for Sustainable Electronics,” p. 160.
- [81] I. C. Lien, Y. C. Shu, W. J. Wu, S. M. Shiu, and H. C. Lin, “Revisit of series-SSHI with comparisons to other interfacing circuits in piezoelectric energy harvesting,” *Smart Mater. Struct.*, vol. 19, no. 12, p. 125009, Dec. 2010, doi: 10.1088/0964-1726/19/12/125009.

- [82] D. Guyomar and M. Lallart, “Recent Progress in Piezoelectric Conversion and Energy Harvesting Using Nonlinear Electronic Interfaces and Issues in Small Scale Implementation,” *Micromachines*, vol. 2, no. 2, pp. 274–294, Jun. 2011, doi: 10.3390/mi2020274.
- [83] K. Wang and J.-F. Li, “Domain Engineering of Lead-Free Li-Modified (K,Na)NbO₃ Polycrystals with Highly Enhanced Piezoelectricity,” *Adv. Funct. Mater.*, vol. 20, no. 12, Art. no. 12, May 2010, doi: 10.1002/adfm.201000284.
- [84] J. Cho, M. Anderson, R. Richards, D. Bahr, and C. Richards, “Optimization of electromechanical coupling for a thin-film PZT membrane: II. Experiment,” *J. Micromech. Microeng.*, vol. 15, no. 10, pp. 1804–1809, Oct. 2005, doi: 10.1088/0960-1317/15/10/003.
- [85] T. M. Kamel and G. de With, “Poling of hard ferroelectric PZT ceramics,” *Journal of the European Ceramic Society*, vol. 28, no. 9, Art. no. 9, Jan. 2008, doi: 10.1016/j.jeurceramsoc.2007.11.023.
- [86] K. Yako, H. Kakemoto, T. Tsurumi, and S. Wada, “Domain size dependence of d₃₃ piezoelectric properties for barium titanate single crystals with engineered domain configurations,” *Materials Science and Engineering: B*, vol. 120, no. 1–3, pp. 181–185, Jul. 2005, doi: 10.1016/j.mseb.2005.02.031.
- [87] R. Agrawal and H. D. Espinosa, “Giant Piezoelectric Size Effects in Zinc Oxide and Gallium Nitride Nanowires. A First Principles Investigation,” *Nano Letters*, vol. 11, no. 2, pp. 786–790, Feb. 2011, doi: 10.1021/nl104004d.
- [88] R. Galos *et al.*, “Electrical Impedance Measurements of PZT Nanofiber Sensors,” *Journal of Nanomaterials*, vol. 2017, pp. 1–9, 2017, doi: 10.1155/2017/8275139.
- [89] J. V. Vidal *et al.*, “Dual Vibration and Magnetic Energy Harvesting With Bidomain LiNbO₃-Based Composite,” vol. 67, no. 6, p. 11, 2020.
- [90] M. Gürbüz, Ü. Çelik, H. Sakurai, Y. Kuromitsu, and A. Oral, “Structural and Electrical Characterization of Electro Spray Deposited PZT Sol-PZT Nanopowder Composite Thick Films,” p. 4.
- [91] C. D. Richards, M. J. Anderson, D. F. Bahr, and R. F. Richards, “Efficiency of energy conversion for devices containing a piezoelectric component,” *J. Micromech. Microeng.*, vol. 14, no. 5, pp. 717–721, May 2004, doi: 10.1088/0960-1317/14/5/009.

- [92] I. Kanno, H. Kotera, and K. Wasa, "Measurement of transverse piezoelectric properties of PZT thin films," *Sensors and Actuators A: Physical*, vol. 107, no. 1, pp. 68–74, Oct. 2003, doi: 10.1016/S0924-4247(03)00234-6.
- [93] A. Safari and M. Abazari, "Lead-free piezoelectric ceramics and thin films," *IEEE Trans. Ultrason., Ferroelect., Freq. Contr.*, vol. 57, no. 10, pp. 2165–2176, Oct. 2010, doi: 10.1109/TUFFC.2010.1674.
- [94] C. Qin, Z. Shen, W. Luo, F. Song, Y. Hong, Z. Wang, Y. Li "Effect of excess Bi on the structure and electrical properties of $\text{CaBi}_2\text{Nb}_2\text{O}_9$ ultrahigh temperature piezoceramics," *J Mater Sci: Mater Electron*, vol. 29, no. 9, pp. 7801–7804, May 2018, doi: 10.1007/s10854-018-8778-9.
- [95] M. Cernea, A. C. Galca, M. C. Cioanher, C. Dragoi, and G. Ioncea, "Piezoelectric BNT-BT0.11 thin films processed by sol–gel technique," *J Mater Sci*, vol. 46, no. 17, Art. no. 17, Sep. 2011, doi: 10.1007/s10853-011-5512-x.
- [96] E. D. Politova, N. V. Golubko, G. M. Kaleva, A. V. Mosunov, N. V Sadovskaya, E. A . Fortalnova, D. A Kiselev, T. S Ilina, A. M. Kislyuk, S. Y Stefanovich, P. K. Panda, "Ferroelectric and local piezoelectric properties of modified KNN ceramics," *Integrated Ferroelectrics*, vol. 196, no. 1, Art. no. 1, Feb. 2019, doi: 10.1080/10584587.2019.1591955.
- [97] M. Zgonik, R. Schlessler, I. Biaggio, E. Voit, J. Tscherry, and P. Günter, "Materials constants of KNbO_3 relevant for electro- and acousto-optics," *Journal of Applied Physics*, vol. 74, no. 2, pp. 1287–1297, Jul. 1993, doi: 10.1063/1.354934.
- [98] J. Fuentes, J. Portelles, M.D. Durrthy Rodrigue, H. H Mok, O. Raymond, J. Heiras, M. P Cruz, J. M. Siqueiros, "Dielectric and piezoelectric properties of the KNN ceramic compound doped with Li, La and Ta," *Appl. Phys. A*, vol. 118, no. 2, pp. 709–715, Feb. 2015, doi: 10.1007/s00339-014-8783-7.
- [99] V. Ya. Shur, "Nano- and Microdomain Engineering of Lithium Niobate and Lithium Tantalate for Piezoelectric Applications," in *Advanced Piezoelectric Materials*, Elsevier, 2017, pp. 235–270. doi: 10.1016/B978-0-08-102135-4.00006-0.
- [100] S. Murakami, T. Yoshimura, K. Satoh, K. Wakazono, K. Kariya, and N. Fujimura, "Development of Piezoelectric MEMS Vibration Energy Harvester Using (100) Oriented BiFeO_3 Ferroelectric Film," *J. Phys.: Conf. Ser.*, vol. 476, p. 012007, Dec. 2013, doi: 10.1088/1742-6596/476/1/012007.

- [101] J. Yang *et al.*, “Large piezoelectric properties in KNN-based lead-free single crystals grown by a seed-free solid-state crystal growth method,” *Appl. Phys. Lett.*, vol. 108, no. 18, Art. no. 18, May 2016, doi: 10.1063/1.4948642.
- [102] S. Dunn, “Determination of Cross Sectional Variation of Ferroelectric Properties for Thin Film (Ca. 500 nm) PZT (30/70) via PFM,” *Integrated Ferroelectrics*, vol. 59, no. 1, pp. 1505–1512, Sep. 2003, doi: 10.1080/10584580390259993.
- [103] T. Li, L. Chen, and K. Zeng, “In situ studies of nanoscale electromechanical behavior of nacre under flexural stresses using band excitation PFM,” *Acta Biomaterialia*, vol. 9, no. 4, pp. 5903–5912, Apr. 2013, doi: 10.1016/j.actbio.2013.01.003.
- [104] E. Soergel, “Piezoresponse force microscopy (PFM),” *J. Phys. D: Appl. Phys.*, vol. 44, no. 46, p. 464003, Nov. 2011, doi: 10.1088/0022-3727/44/46/464003.
- [105] D. Denning, J. Guyonnet, and B. J. Rodriguez, “Applications of piezoresponse force microscopy in materials research: from inorganic ferroelectrics to biopiezoelectrics and beyond,” *International Materials Reviews*, vol. 61, no. 1, Art. no. 1, Jan. 2016, doi: 10.1179/1743280415Y.0000000013.
- [106] “Model: Bruker AFM ICON 2018, <https://www.bruker.com/en/products-and-solutions/microscopes/materials-afm/dimension-icon-afm.htm>.”
- [107] “<https://www.brukerafmprobes.com/p-3692-pfm-smpl.aspx>.”
- [108] A. Verma, N. Panayanthatta, A. Ichangi, T. Fischer, L. Montes, E. Bano, S. Mathur, “Interdependence of piezoelectric coefficient and film thickness in LiTaO₃ cantilevers,” p. 12.
- [109] V.Ya. Shur, “Nano- and Microdomain Engineering of Lithium Niobate and Lithium Tantalate for Piezoelectric Applications,” in *Advanced Piezoelectric Material*, 2nd ed., Woodhead Publishing in Materials, 2017, pp. 235–270. doi: <https://doi.org/10.1016/C2015-0-01989-X>.
- [110] A. Bartasyte, S. Margueron, T. Baron, S. Oliveri, and P. Boulet, “Toward High-Quality Epitaxial LiNbO₃ and LiTaO₃ Thin Films for Acoustic and Optical Applications,” *Advanced Materials Interfaces*, vol. 4, no. 8, p. 1600998, Apr. 2017, doi: 10.1002/admi.201600998.
- [111] “U. A. A. Azlan, N. A. Azmi, M. A. M. Hatta, M. W. A. Rashid, and M. A. A. M. Abid, ‘Optimization of Sodium Potassium Niobate Thin Films with Different Deposition Layers,’ *J. Phys*, p. 12053, 2018.”.

- [112] K. UCHINO, *Advanced piezoelectric materials*. Woodhead Publishing Limited, 2008. doi: 10.1201/b15882-1.
- [113] “T. Osugi, Yukihiisa and Yoshino, Takashi and Suzuki, Kenji and Hirai, ‘Single crystal FBAR with LiNbO₃ and LiTaO₃ piezoelectric substance layers,’ in Microwave Symposium, IEEE, 2007, pp. 873–876”.
- [114] K. Kitamura, Y. Furukawa, K. Niwa, V. Gopalan, and T. E. Mitchell, “Crystal growth and low coercive field 180° domain switching characteristics of stoichiometric LiTaO₃,” *Appl. Phys. Lett.*, vol. 73, no. 21, Art. no. 21, Nov. 1998, doi: 10.1063/1.122676.
- [115] K. Uchino, “Piezoelectric Energy Harvesting Systems-Essentials to Successful Developments,” *Energy Technology*, vol. 6, no. 5, pp. 829–848, May 2018, doi: 10.1002/ente.201700785.
- [116] A. C. Busacca *et al.*, “Surface periodic poling in congruent lithium tantalate,” *Electron. Lett.*, vol. 42, no. 9, Art. no. 9, 2006, doi: 10.1049/el:20060518.
- [117] F. Akasheh, T. Myers, J. D. Fraser, S. Bose, and A. Bandyopadhyay, “Development of piezoelectric micromachined ultrasonic transducers,” *Sensors and Actuators A: Physical*, vol. 111, no. 2–3, Art. no. 2–3, Mar. 2004, doi: 10.1016/j.sna.2003.11.022.
- [118] A. Arnau Vives, Ed., *Piezoelectric transducers and applications*, 2. ed. Berlin: Springer, 2008.
- [119] M. Alhawari, B. Mohammad, H. Saleh, and M. Ismail, *Energy harvesting for self-powered wearable devices*. 2018. Accessed: Sep. 12, 2019. [Online]. Available: <http://public.ebib.com/choice/publicfullrecord.aspx?p=4941454>
- [120] B. Andò, S. Baglio, C. Trigona, N. Dumas, L. Latorre, and P. Nouet, “Nonlinear mechanism in MEMS devices for energy harvesting applications,” *J. Micromech. Microeng.*, vol. 20, no. 12, Art. no. 12, Dec. 2010, doi: 10.1088/0960-1317/20/12/125020.
- [121] R. Calìo *et al.*, “Piezoelectric Energy Harvesting Solutions,” *Sensors*, vol. 14, no. 3, Art. no. 3, Mar. 2014, doi: 10.3390/s140304755.
- [122] M. Kohli and P. Muralt, “Poling of ferroelectric thin films,” *Ferroelectrics*, vol. 225, no. 1, Art. no. 1, Mar. 1999, doi: 10.1080/00150199908009123.
- [123] M. Hagiwara, S. Takahashi, T. Hoshina, H. Takeda, O. Sakurai, and T. Tsurumi, “Nonlinear Shear Response in (K,Na)NbO₃-Based Lead-Free Piezoelectric Ceramics,” *KEM*, vol. 445, pp. 47–50, Jul. 2010, doi: 10.4028/www.scientific.net/KEM.445.47.

- [124] V. J. and M. I., “Predicting Macroscale Effects Through Nanoscale Features,” in *Atomic Force Microscopy - Imaging, Measuring and Manipulating Surfaces at the Atomic Scale*, V. Bellitto, Ed. InTech, 2012. doi: 10.5772/37219.
- [125] F.-Z. Yao, Q. Yu, K. Wang, Q. Li, and J.-F. Li, “Ferroelectric domain morphology and temperature-dependent piezoelectricity of (K,Na,Li)(Nb,Ta,Sb)O₃ lead-free piezoceramics,” *RSC Adv.*, vol. 4, no. 39, Art. no. 39, 2014, doi: 10.1039/C4RA01697A.
- [126] P. Val-Gómez, A. del Campo, F. Rubio-Marcos, J. F. Fernández, and A. Moure, “Poling and depoling influence on the micro-stress states and phase coexistence in KNN-based piezoelectric ceramics,” *Journal of the European Ceramic Society*, vol. 39, no. 4, Art. no. 4, Apr. 2019, doi: 10.1016/j.jeurceramsoc.2018.10.011.
- [127] “<http://gwyddion.net/>.”
- [128] S. Priya and S. Nahm, Eds., *Lead-free piezoelectrics*. New York, NY: Springer, 2012.
- [129] H. J. Seog *et al.*, “Recent Progress in Potassium Sodium Niobate Lead-free Thin Films,” *J. Korean Phys. Soc.*, vol. 72, no. 12, pp. 1467–1483, Jun. 2018, doi: 10.3938/jkps.72.1467.
- [130] P. Val-Gómez, A. del Campo, F. Rubio-Marcos, J. F. Fernández, and A. Moure, “Poling and depoling influence on the micro-stress states and phase coexistence in KNN-based piezoelectric ceramics,” *Journal of the European Ceramic Society*, vol. 39, no. 4, pp. 1011–1019, Apr. 2019, doi: 10.1016/j.jeurceramsoc.2018.10.011.
- [131] H.-C. Thong, C. Zhao, Z. Zhu, C. Wu, Y. Liu, Z-Z Du, J-F Li, W. Gong, K. Wang “Technology transfer of lead-free (K, Na)NbO₃-based piezoelectric ceramics,” *Materials Today*, vol. 29, pp. 37–48, 2019, doi: <https://doi.org/10.1016/j.mattod.2019.04.016>.
- [132] D.-T. Le *et al.*, “Effects of the Domain Size on Local d₃₃ in Tetragonal (Na_{0.53}K_{0.45}Li_{0.02})(Nb_{0.8}Ta_{0.2})O₃ Ceramics,” *Journal of the American Ceramic Society*, vol. 96, no. 1, pp. 174–178, 2013, doi: 10.1111/j.1551-2916.2012.05445.x.
- [133] Q. Li *et al.*, “Poling engineering of (K,Na)NbO₃ -based lead-free piezoceramics with orthorhombic–tetragonal coexisting phases,” *J. Mater. Chem. C*, vol. 5, no. 3, pp. 549–556, 2017, doi: 10.1039/C6TC04723H.
- [134] L.-Q. Cheng, K. Wang, J.-F. Li, Y. Liu, and J. Li, “Piezoelectricity of lead-free (K, Na)NbO₃ nanoscale single crystals,” *J. Mater. Chem. C*, vol. 2, no. 43, pp. 9091–9098, 2014, doi: 10.1039/C4TC01745E.

- [135] Y. Huan, X. Wang, Z. Shen, J. Kim, H. Zhou, and L. Li, “Nanodomains in KNN-Based Lead-Free Piezoelectric ceramics: Origin of Strong Piezoelectric Properties,” *J. Am. Ceram. Soc.*, vol. 97, no. 3, pp. 700–703, Mar. 2014, doi: 10.1111/jace.12850.
- [136] K. Wang, J.-F. Li, and J.-J. Zhou, “High Normalized Strain Obtained in Li-Modified (K,Na)NbO₃ Lead-Free Piezoceramics,” *Appl. Phys. Express*, vol. 4, no. 6, Art. no. 6, May 2011, doi: 10.1143/APEX.4.061501.
- [137] J. S. Park *et al.*, “Effect of A-site Excess on the Piezoelectric Properties of (K_{0.48}Na_{0.52})_{1+x}(Nb_{0.55}Ta_{0.45})O₃ Thin Films,” *Ferroelectrics*, vol. 465, no. 1, Art. no. 1, Jun. 2014, doi: 10.1080/00150193.2014.893808.
- [138] S. Gupta, A. Belianinov, M. Baris Okatan, S. Jesse, S. V. Kalinin, and S. Priya, “Fundamental limitation to the magnitude of piezoelectric response of $\langle 001 \rangle_{\text{pc}}$ textured K_{0.5}Na_{0.5}NbO₃ ceramic,” *Appl. Phys. Lett.*, vol. 104, no. 17, p. 172902, Apr. 2014, doi: 10.1063/1.4874648.
- [139] D. A. Ochoa *et al.*, “Extensive domain wall contribution to strain in a (K,Na)NbO₃-based lead-free piezoceramics quantified from high energy X-ray diffraction,” *Journal of the European Ceramic Society*, vol. 36, no. 10, pp. 2489–2494, Aug. 2016, doi: 10.1016/j.jeurceramsoc.2016.03.022.
- [140] “knn STRAIN PIEZOELETRIC COEFFICIENT.pdf.”
- [141] J. S. Park *et al.*, “Effect of A-site Excess on the Piezoelectric Properties of (K_{0.48} Na_{0.52})_{1+x} (Nb_{0.55} Ta_{0.45})O₃ Thin Films,” *Ferroelectrics*, vol. 465, no. 1, pp. 60–67, Jun. 2014, doi: 10.1080/00150193.2014.893808.
- [142] Y. Shindo, F. Narita, K. Sato, and T. Takeda, “Nonlinear electromechanical fields and localized polarization switching of piezoelectric macrofiber composites,” *J. Mech. Mater. Struct.*, vol. 6, no. 7–8, pp. 1089–1102, Dec. 2011, doi: 10.2140/jomms.2011.6.1089.
- [143] Y. G. Lv, C. L. Wang, J. L. Zhang, L. Wu, M. L. Zhao, and J. P. Xu, “Tantalum influence on physical properties of (K_{0.5}Na_{0.5})(Nb_{1-x}Ta_x)O₃ ceramics,” *Materials Research Bulletin*, vol. 44, no. 2, pp. 284–287, Feb. 2009, doi: 10.1016/j.materresbull.2008.06.019.
- [144] J. Fuentes *et al.*, “Dielectric and piezoelectric properties of the KNN ceramic compound doped with Li, La and Ta,” *Appl. Phys. A*, vol. 118, no. 2, Art. no. 2, Feb. 2015, doi: 10.1007/s00339-014-8783-7.

- [145] N. Kondo *et al.*, “Improvement in Ferroelectric Properties of Chemically Synthesized Lead-Free Piezoelectric (K,Na)(Nb,Ta)O₃ Thin Films by Mn Doping,” *Jpn. J. Appl. Phys.*, p. 7, 2010.
- [146] T. Li *et al.*, “Electrical properties of lead-free KNN films on SRO/STO by RF magnetron sputtering,” *Ceramics International*, vol. 40, no. 1, Art. no. 1, Jan. 2014, doi: 10.1016/j.ceramint.2013.07.005.
- [147] T. Lusiola, A. Hussain, M. Kim, T. Graule, and F. Clemens, “Ferroelectric KNNT Fibers by Thermoplastic Extrusion Process: Microstructure and Electromechanical Characterization,” *Actuators*, vol. 4, no. 2, pp. 99–113, May 2015, doi: 10.3390/act4020099.
- [148] X. Chen, S. Xu, N. Yao, and Y. Shi, “1.6 V Nanogenerator for Mechanical Energy Harvesting Using PZT Nanofibers,” *Nano Letters*, vol. 10, no. 6, Art. no. 6, Jun. 2010, doi: 10.1021/nl100812k.
- [149] M.-H. Zhang *et al.*, “Determination of polarization states in (K,Na)NbO₃ lead-free piezoelectric crystal,” *J Adv Ceram*, vol. 9, no. 2, pp. 204–209, Apr. 2020, doi: 10.1007/s40145-020-0360-2.
- [150] J. Xiao, T. S. Herng, J. Ding, and K. Zeng, “Polarization rotation in copper doped zinc oxide (ZnO:Cu) thin films studied by Piezoresponse Force Microscopy (PFM) techniques,” *Acta Materialia*, vol. 123, pp. 394–403, Jan. 2017, doi: 10.1016/j.actamat.2016.10.051.
- [151] Y. Huan, X. Wang, Z. Shen, J. Kim, H. Zhou, and L. Li, “Nanodomains in KNN-Based Lead-Free Piezoelectric ceramics: Origin of Strong Piezoelectric Properties,” *J. Am. Ceram. Soc.*, vol. 97, no. 3, pp. 700–703, Mar. 2014, doi: 10.1111/jace.12850.
- [152] H. Y. S. Al-Zahrani, “Non Linear Piezoelectricity in Wurtzite Semiconductor Core-Shell Nanowires: An Atomistic Modelling Approach,” p. 144.
- [153] V. Koval, G. Viola, and Y. Tan, “Biasing Effects in Ferroic Materials,” in *Ferroelectric Materials - Synthesis and Characterization*, A. Peláiz-Barranco, Ed. InTech, 2015. doi: 10.5772/60764.
- [154] D. Damjanovic, “Stress and frequency dependence of the direct piezoelectric effect in ferroelectric ceramics,” *Journal of Applied Physics*, vol. 82, no. 4, Art. no. 4, Aug. 1997, doi: 10.1063/1.365981.
- [155] X. Meng, W. Wang, H. Ke, J. Rao, D. Jia, and Y. Zhou, “Synthesis, piezoelectric property and domain behaviour of the vertically aligned K_{1-x} Na_x NbO₃ nanowire with a

- morphotropic phase boundary,” *J. Mater. Chem. C*, vol. 5, no. 3, pp. 747–753, 2017, doi: 10.1039/C6TC04629K.
- [156] R. Xu and S. G. Kim, “figures of merits of piezoelectric materials in energy harvesters,” p. 5.
- [157] J. I. Roscow, Y. Zhang, M. J. Krasny, R. W. C. Lewis, J. Taylor, and C. R. Bowen, “Freeze cast porous barium titanate for enhanced piezoelectric energy harvesting,” *J. Phys. D: Appl. Phys.*, vol. 51, no. 22, p. 225301, Jun. 2018, doi: 10.1088/1361-6463/aabc81.
- [158] S. Priya *et al.*, “A Review on Piezoelectric Energy Harvesting: Materials, Methods, and Circuits,” *Energy Harvesting and Systems*, vol. 4, no. 1, pp. 3–39, Aug. 2019, doi: 10.1515/ehs-2016-0028.
- [159] J. I. Roscow, J. Taylor, and C. R. Bowen, “Manufacture and characterization of porous ferroelectrics for piezoelectric energy harvesting applications,” *Ferroelectrics*, vol. 498, no. 1, pp. 40–46, Aug. 2016, doi: 10.1080/00150193.2016.1169154.
- [160] S. H. Baek *et al.*, “Giant Piezoelectricity on Si for Hyperactive MEMS,” *Science*, vol. 334, no. 6058, pp. 958–961, Nov. 2011, doi: 10.1126/science.1207186.
- [161] J. I. Roscow, R. W. C. Lewis, J. Taylor, and C. R. Bowen, “Modelling and fabrication of porous sandwich layer barium titanate with improved piezoelectric energy harvesting figures of merit,” *Acta Materialia*, vol. 128, pp. 207–217, Apr. 2017, doi: 10.1016/j.actamat.2017.02.029.
- [162] J. I. Roscow, H. Pearce, H. Khanbarez, S. Kar-Narayan, and C. R. Bowen, “Modified energy harvesting figures of merit for stress- and strain-driven piezoelectric systems,” *Eur. Phys. J. Spec. Top.*, vol. 228, no. 7, pp. 1537–1554, Aug. 2019, doi: 10.1140/epjst/e2019-800143-7.
- [163] A. Bani Milhim and R. Ben-Mrad, “Fabrication of Lead-Free Piezoelectric (K, Na)NbO₃ Thin Film on Nickel-Based Electrodes,” *J. Microelectromech. Syst.*, vol. 25, no. 2, Art. no. 2, Apr. 2016, doi: 10.1109/JMEMS.2016.2515058.
- [164] J.-J. Zhou, J.-F. Li, K. Wang, and X.-W. Zhang, “Phase structure and electrical properties of (Li,Ta)-doped (K,Na)NbO₃ lead-free piezoceramics in the vicinity of Na/K = 50/50,” *J Mater Sci*, vol. 46, no. 15, pp. 5111–5116, Aug. 2011, doi: 10.1007/s10853-011-5442-7.
- [165] “<http://www.roditi.com/>.”

- [166] S. M. Kostritskii, P. Bourson, M. Aillerie, M. D. Fontana, and D. Kip, “Quantitative evaluation of the electro-optic effect and second-order optical nonlinearity of lithium tantalate crystals of different compositions using Raman and infrared spectroscopy,” *Appl. Phys. B*, vol. 82, no. 3, pp. 423–430, Mar. 2006, doi: 10.1007/s00340-005-2046-4.
- [167] K. Shibata, F. Oka, A. Ohishi, T. Mishima, and I. Kanno, “Piezoelectric Properties of (K,Na)NbO₃ Films Deposited by RF Magnetron Sputtering,” *Appl. Phys. Express*, vol. 1, no. 1, p. 011501, Jan. 2008, doi: 10.1143/APEX.1.011501.
- [168] J. Pavlič, B. Malič, and T. Rojac, “Small Reduction of the Piezoelectric d₃₃ Response in Potassium Sodium Niobate Thick Films,” *Journal of the American Ceramic Society*, vol. 97, no. 5, pp. 1497–1503, 2014, doi: <https://doi.org/10.1111/jace.12797>.
- [169] “Lee, Y. H.; Cho, J. H.; Kim, B. I.; Choi, D. K. Piezoelectric Properties and Densification Based on Control of Volatile Mass of Potassium and Sodium in (K_{0.5}Na_{0.5})NbO₃ Ceramics. *Jpn. J. Appl. Phys.* 2008, 47 (6 PART 1), 4620–4622. <https://doi.org/10.1143/JJAP.47.4620>.”
- [170] V. Ion *et al.*, “Impact of thickness variation on structural, dielectric and piezoelectric properties of (Ba,Ca)(Ti,Zr)O₃ epitaxial thin films,” *Sci Rep*, vol. 8, no. 1, p. 2056, Dec. 2018, doi: 10.1038/s41598-018-20149-y.
- [171] *Nalwa HS. Handbook of thin films. H Nalwa, editor. Handbook of Thin Films. Elsevier. 2002;100–60.*
- [172] S. Bhalla, S. Moharana, V. Talakokula, and N. Kaur, *Piezoelectric Materials: Applications in SHM, Energy Harvesting and Bio-mechanics*. Chichester, UK: John Wiley & Sons, Ltd, 2016. doi: 10.1002/9781119265139.
- [173] R. Calìo *et al.*, “Piezoelectric Energy Harvesting Solutions,” *Sensors*, vol. 14, no. 3, pp. 4755–4790, Mar. 2014, doi: 10.3390/s140304755.
- [174] H. Elbahr, T. A. Ali, A. Badawi, and S. Sedky, “Simulation of a New PZT Energy Harvester with a Lower Resonance Frequency Using COMSOL Multiphysics®,” p. 8, 2014.
- [175] G. Clementi *et al.*, “LiNbO₃ films – A low-cost alternative lead-free piezoelectric material for vibrational energy harvesters,” *Mechanical Systems and Signal Processing*, vol. 149, p. 107171, Feb. 2021, doi: 10.1016/j.ymssp.2020.107171.

- [176] K. Nakamura, H. Ando, and H. Shimizu, "Bending Vibrator Consisting of a LiNbO₃ Plate with a Ferroelectric Inversion Layer," *Jpn. J. Appl. Phys.*, vol. 26, no. S2, p. 198, Jan. 1987, doi: 10.7567/JJAPS.26S2.198.
- [177] A. Chamuah, "Piezoelectric Energy Harvester Using MEMS Structures: A Review," vol. 4, no. 2, p. 6, 2018.
- [178] D. Gibus, "Strongly coupled piezoelectric cantilevers for broadband vibration energy harvesting," *Applied Energy*, p. 17, 2020.
- [179] A. Morel, A. Badel, R. Grézaud, P. Gasnier, G. Despesse, and G. Pillonnet, "Resistive and reactive loads' influences on highly coupled piezoelectric generators for wideband vibrations energy harvesting," *Journal of Intelligent Material Systems and Structures*, vol. 30, no. 3, pp. 386–399, Feb. 2019, doi: 10.1177/1045389X18810802.
- [180] A. Badel and E. Lefeuvre, "Wideband Piezoelectric Energy Harvester Tuned Through its Electronic Interface Circuit," *J. Phys.: Conf. Ser.*, vol. 557, p. 012115, Nov. 2014, doi: 10.1088/1742-6596/557/1/012115.
- [181] "R. Holland: IEEE Trans. Sonics and Ultrasonics, 14, (1967) 18."
- [182] J. Cho, M. Anderson, R. Richards, D. Bahr, and C. Richards, "Optimization of electromechanical coupling for a thin-film PZT membrane: II. Experiment," *J. Micromech. Microeng.*, vol. 15, no. 10, pp. 1804–1809, Oct. 2005, doi: 10.1088/0960-1317/15/10/003.
- [183] "ANSI/IEEE Std 176-1987 An American National Standard IEEE Standard on Piezoelectricity," p. 74.
- [184] K. Uchino *et al.*, "Loss mechanisms and high power piezoelectrics," *J Mater Sci*, vol. 41, no. 1, pp. 217–228, Jan. 2006, doi: 10.1007/s10853-005-7201-0.
- [185] "S. Hirose, M. Aoygi, Y. Tomikawa, S. Takahashi and K. Uchino: High power characteristics at anti-resonance frequency of piezoelectric transducers, Ultrasonics, 34, (1996) 213."
- [186] K. Uchino, Y. Zhuang, and S. O. Ural, "loss determination methodology for a piezoelectric ceramic: new phenomenological theory and experimental proposals," *J. Adv. Dielect.*, vol. 01, no. 01, pp. 17–31, Jan. 2011, doi: 10.1142/S2010135X11000033.
- [187] "A.V. Mezheritky: Quality Factor of Piezoceramics, Ferroelectrics, 266, (2002) 277."
- [188] S. Johansson, J.-Å. Schweitz, L. Tenerz, and J. Tirén, "Fracture testing of silicon microelements in situ in a scanning electron microscope," p. 6.

- [189] F. Ericson and J. Schweitz, “Micromechanical fracture strength of silicon,” *Journal of Applied Physics*, vol. 68, no. 11, pp. 5840–5844, Dec. 1990, doi: 10.1063/1.346957.
- [190] B. Richter, J. Twiefel, and J. Wallaschek, “Piezoelectric Equivalent Circuit Models,” in *Energy Harvesting Technologies*, S. Priya and D. J. Inman, Eds. Boston, MA: Springer US, 2009, pp. 107–128. doi: 10.1007/978-0-387-76464-1_4.
- [191] W. G. Cady, “The Piezo-Electric Resonator,” *Proc. IRE*, vol. 10, no. 2, pp. 83–114, Apr. 1922, doi: 10.1109/JRPROC.1922.219800.
- [192] K. S. V. Dyke, “The Piezo-Electric Resonator and Its Equivalent Network,” p. 23.
- [193] A. Bybi, “One-Dimensional Electromechanical Equivalent Circuit for Piezoelectric Array Elements,” p. 5.
- [194] D. Guyomar, A. Badel, E. Lefeuvre, and C. Richard, “Toward energy harvesting using active materials and conversion improvement by nonlinear processing,” *IEEE Trans. Ultrason., Ferroelect., Freq. Contr.*, vol. 52, no. 4, pp. 584–595, Apr. 2005, doi: 10.1109/TUFFC.2005.1428041.
- [195] S. P. Beeby *et al.*, “A comparison of power output from linear and nonlinear kinetic energy harvesters using real vibration data,” *Smart Mater. Struct.*, vol. 22, no. 7, p. 075022, Jul. 2013, doi: 10.1088/0964-1726/22/7/075022.
- [196] G. Sebald, H. Kuwano, D. Guyomar, and B. Ducharne, “Experimental Duffing oscillator for broadband piezoelectric energy harvesting,” *Smart Mater. Struct.*, vol. 20, no. 10, p. 102001, Oct. 2011, doi: 10.1088/0964-1726/20/10/102001.
- [197] A. Morel, R. Grézaud, G. Pillonnet, P. Gasnier, G. Despesse, and A. Badel, “Active AC/DC control for wideband piezoelectric energy harvesting,” *J. Phys.: Conf. Ser.*, vol. 773, p. 012059, Nov. 2016, doi: 10.1088/1742-6596/773/1/012059.
- [198] Y. Kuang, Z. J. Chew, J. Dunville, J. Sibson, and M. Zhu, “Strongly coupled piezoelectric energy harvesters: Optimised design with over 100 mW power, high durability and robustness for self-powered condition monitoring,” *Energy Conversion and Management*, vol. 237, p. 114129, Jun. 2021, doi: 10.1016/j.enconman.2021.114129.
- [199] D. Gibus, P. Gasnier, A. Morel, S. Boisseau, and A. Badel, “Modelling and design of highly coupled piezoelectric energy harvesters for broadband applications,” *J. Phys.: Conf. Ser.*, vol. 1407, p. 012009, Nov. 2019, doi: 10.1088/1742-6596/1407/1/012009.

- [200] D. Motter, J. V. Lavarda, F. A. Dias, and S. da Silva, "Vibration energy harvesting using piezoelectric transducer and non-controlled rectifiers circuits," *J. Braz. Soc. Mech. Sci. & Eng.*, vol. 34, no. spe, Art. no. spe, 2012, doi: 10.1590/S1678-58782012000500006.
- [201] M. Lallart, "Nonlinear technique and self-powered circuit for efficient piezoelectric energy harvesting under unloaded cases," *Energy Conversion and Management*, vol. 133, pp. 444–457, Feb. 2017, doi: 10.1016/j.enconman.2016.10.065.
- [202] Y.-Y. Chen, "Piezoelectric power transducers and its interfacing circuitry on energy harvesting and structural damping applications," p. 224.
- [203] A. Brenes, A. Morel, J. Juillard, E. Lefeuvre, and A. Badel, "Maximum power point of piezoelectric energy harvesters: a review of optimality condition for electrical tuning," *Smart Mater. Struct.*, vol. 29, no. 3, p. 033001, Mar. 2020, doi: 10.1088/1361-665X/ab6484.
- [204] X.-D. Do, S.-K. Han, and S.-G. Lee, "Optimization of piezoelectric energy harvesting systems by using a MPPT method," in *2014 IEEE Fifth International Conference on Communications and Electronics (ICCE)*, Danang, Vietnam, Jul. 2014, pp. 309–312. doi: 10.1109/CCE.2014.6916720.
- [205] S. Fan, L. Zhao, R. Wei, L. Geng, and P. X.-L. Feng, "An ultra-low quiescent current power management ASIC with MPPT for vibrational energy harvesting," in *2017 IEEE International Symposium on Circuits and Systems (ISCAS)*, Baltimore, MD, USA, May 2017, pp. 1–4. doi: 10.1109/ISCAS.2017.8050865.
- [206] A. D. T. Elliott and P. D. Mitcheson, "Piezoelectric energy harvester interface with real-time MPPT," *J. Phys.: Conf. Ser.*, vol. 557, p. 012125, Nov. 2014, doi: 10.1088/1742-6596/557/1/012125.
- [207] M. Balato, L. Costanzo, A. Lo Schiavo, and M. Vitelli, "Optimization of both Perturb & Observe and Open Circuit Voltage MPPT Techniques for Resonant Piezoelectric Vibration Harvesters feeding bridge rectifiers," *Sensors and Actuators A: Physical*, vol. 278, pp. 85–97, Aug. 2018, doi: 10.1016/j.sna.2018.05.017.
- [208] D. D. Gaikwad and M. S. Chavan, "Implementation of DC-DC Converter for MPPT by Direct Control Method," *International Journal of Engineering Research*, vol. 3, no. 9, p. 5, 2014.
- [209] M. Balato, L. Costanzo, A. Lo Schiavo, and M. Vitelli, "Optimization of both Perturb & Observe and Open Circuit Voltage MPPT Techniques for Resonant Piezoelectric Vibration

- Harvesters feeding bridge rectifiers,” *Sensors and Actuators A: Physical*, vol. 278, pp. 85–97, Aug. 2018, doi: 10.1016/j.sna.2018.05.017.
- [210] C. Lu, C.-Y. Tsui, and W.-H. Ki, “Vibration Energy Scavenging System With Maximum Power Tracking for Micropower Applications,” *IEEE Trans. VLSI Syst.*, vol. 19, no. 11, pp. 2109–2119, Nov. 2011, doi: 10.1109/TVLSI.2010.2069574.
- [211] R. Dayal, K. Modepalli, and L. Parsa, “A New Optimum Power Control Scheme for Low-Power Energy Harvesting Systems,” *IEEE Trans. on Ind. Applicat.*, vol. 49, no. 6, pp. 2651–2661, Nov. 2013, doi: 10.1109/TIA.2013.2264043.
- [212] G. K. Ottman, H. F. Hofmann, A. C. Bhatt, and G. A. Lesieutre, “Adaptive piezoelectric energy harvesting circuit for wireless remote power supply,” *IEEE Trans. Power Electron.*, vol. 17, no. 5, Art. no. 5, Sep. 2002, doi: 10.1109/TPEL.2002.802194.
- [213] N. Kong and D. S. Ha, “Low-Power Design of a Self-powered Piezoelectric Energy Harvesting System With Maximum Power Point Tracking,” *IEEE Trans. Power Electron.*, vol. 27, no. 5, pp. 2298–2308, May 2012, doi: 10.1109/TPEL.2011.2172960.
- [214] Y. Hu *et al.*, “An Adaptable Interface Conditioning Circuit Based on Triboelectric Nanogenerators for Self-Powered Sensors,” *Micromachines*, vol. 9, no. 3, Art. no. 3, Mar. 2018, doi: 10.3390/mi9030105.
- [215] A. Tabesh and L. G. Frechette, “A Low-Power Stand-Alone Adaptive Circuit for Harvesting Energy From a Piezoelectric Micropower Generator,” *IEEE Trans. Ind. Electron.*, vol. 57, no. 3, pp. 840–849, Mar. 2010, doi: 10.1109/TIE.2009.2037648.
- [216] A. D. T. Elliott and P. D. Mitcheson, “Piezoelectric energy harvester interface with real-time MPPT,” *J. Phys.: Conf. Ser.*, vol. 557, p. 012125, Nov. 2014, doi: 10.1088/1742-6596/557/1/012125.
- [217] Z. J. Chew and M. Zhu, “Microwatt power consumption maximum power point tracking circuit using an analogue differentiator for piezoelectric energy harvesting,” *J. Phys.: Conf. Ser.*, vol. 660, p. 012022, Dec. 2015, doi: 10.1088/1742-6596/660/1/012022.
- [218] G. K. Ottman, H. F. Hofmann, A. C. Bhatt, and G. A. Lesieutre, “Adaptive piezoelectric energy harvesting circuit for wireless remote power supply,” *IEEE Trans. Power Electron.*, vol. 17, no. 5, pp. 669–676, Sep. 2002, doi: 10.1109/TPEL.2002.802194.
- [219] “ANSIIEEE Std 176-1987 An American National Standard.pdf.”

- [220] X. Li, W. Y. Shih, I. A. Aksay, and W.-H. Shih, “Electromechanical Behavior of PZT-Brass Unimorphs,” *Journal of the American Ceramic Society*, vol. 82, no. 7, pp. 1733–1740, Jul. 1999, doi: 10.1111/j.1151-2916.1999.tb01993.x.
- [221] S. Saadon and O. Sidek, “Micro-Electro-Mechanical System (MEMS)-Based Piezoelectric Energy Harvester for Ambient Vibrations,” *Procedia - Social and Behavioral Sciences*, vol. 195, pp. 2353–2362, Jul. 2015, doi: 10.1016/j.sbspro.2015.06.198.
- [222] H. Liu, J. Zhong, C. Lee, S.-W. Lee, and L. Lin, “A comprehensive review on piezoelectric energy harvesting technology: Materials, mechanisms, and applications,” *Applied Physics Reviews*, vol. 5, no. 4, p. 041306, Dec. 2018, doi: 10.1063/1.5074184.
- [223] *COMSOL Multiphysics 5.4*.
- [224] J. H. Kim *et al.*, “Development of a hybrid type smart pen piezoelectric energy harvester for an IoT platform,” *Energy*, p. 119845, Jan. 2021, doi: 10.1016/j.energy.2021.119845.
- [225] J. M. Rabaey *et al.*, “PicoRadios for wireless sensor networks: the next challenge in ultra-low power design,” in *2002 IEEE International Solid-State Circuits Conference. Digest of Technical Papers (Cat. No.02CH37315)*, San Francisco, CA, USA, 2002, vol. 1, pp. 200–201. doi: 10.1109/ISSCC.2002.993005.
- [226] R. La Rosa, C. Dehollain, and P. Livreri, “Advanced Monitoring Systems Based on Battery-Less Asset Tracking Modules Energized through RF Wireless Power Transfer,” *Sensors*, vol. 20, no. 11, p. 3020, May 2020, doi: 10.3390/s20113020.
- [227] J. K. Lee, “Magnetostrictive patch sensor system for battery-less real-time measurement of torsional vibrations of rotating shafts,” *Journal of Sound and Vibration*, p. 14, 2018.
- [228] Y. Kim and Y. Y. Kim, “A novel Terfenol-D transducer for guided-wave inspection of a rotating shaft,” p. 10, 2007.
- [229] D. Zappalá, M. Bezziccheri, C. J. Crabtree, and N. Paone, “Non-intrusive torque measurement for rotating shafts using optical sensing of zebra-tapes,” *Meas. Sci. Technol.*, vol. 29, no. 6, p. 065207, Jun. 2018, doi: 10.1088/1361-6501/aab74a.
- [230] J. S. Kim and G.-W. Kim, “New non-contacting torque sensor based on the mechanoluminescence of ZnS:Cu microparticles,” *Sensors and Actuators A: Physical*, vol. 218, pp. 125–131, Oct. 2014, doi: 10.1016/j.sna.2014.07.023.
- [231] R. L. Rosa, C. Dehollain, P. Livreri, and C. Trigona, “An Energy Autonomous and Battery-Free Measurement System for Ambient Light Power with Time Domain Readout,” p. 24.

- [232] A. Homayouni-Amlashi, A. Mohand-Ousaid, and M. Rakotondrabe, “Analytical Modelling and Optimization of a Piezoelectric Cantilever Energy Harvester with In-Span Attachment,” *Micromachines*, vol. 11, no. 6, p. 591, Jun. 2020, doi: 10.3390/mi11060591.
- [233] Z. Li *et al.*, “An Energy Harvesting System with Reconfigurable Piezoelectric Energy Harvester Array for IoT Applications,” in *2020 IEEE International Symposium on Circuits and Systems (ISCAS)*, Seville, Spain, Oct. 2020, pp. 1–5. doi: 10.1109/ISCAS45731.2020.9180965.
- [234] T. Tsuchiya, T. Ikeda, A. Tsunematsu, K. Sugano, and O. Tabata, “Tensile Testing of Single-Crystal Silicon Thin Films at 600°C Using Infrared Radiation Heating,” *Sensors and Materials*, vol. 22, no. 1, p. 11, 2010.
- [235] C. R. Bowen, H. A. Kim, P. M. Weaver, and S. Dunn, “Piezoelectric and ferroelectric materials and structures for energy harvesting applications,” *Energy Environ. Sci.*, vol. 7, no. 1, pp. 25–44, 2014, doi: 10.1039/C3EE42454E.
- [236] D. Zabek, R. Pullins, M. Pearson, A. Grzebielec, and T. Skoczkowski, “Piezoelectric-silicone structure for vibration energy harvesting: experimental testing and modelling,” *Smart Mater. Struct.*, vol. 30, no. 3, p. 035002, Mar. 2021, doi: 10.1088/1361-665X/abd964.

APPENDIX 1

ABBREVIATIONS

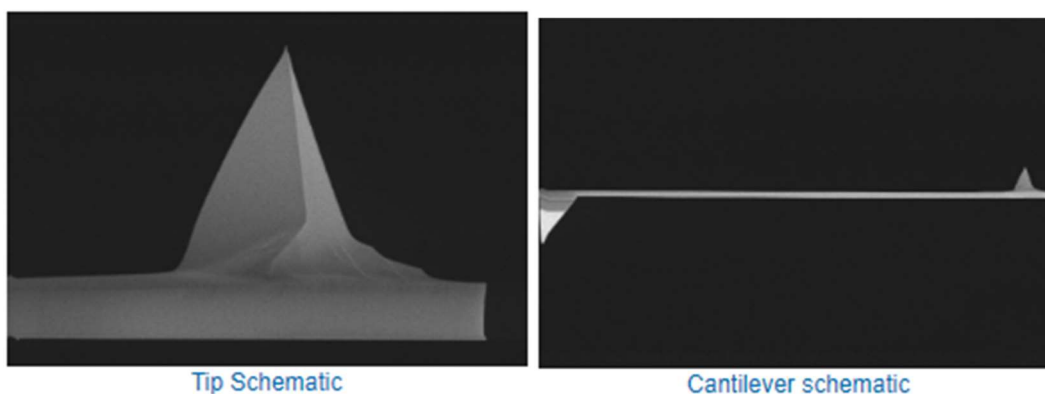
<i>Internet of Things</i>	<i>IoT</i>
<i>wireless sensor nodes</i>	<i>WSNs</i>
<i>Maximum Power Point Tracking</i>	<i>MPPT</i>
<i>Bluetooth Low Energy</i>	<i>BLE</i>
<i>Atomic Force Microscopy</i>	<i>AFM</i>
<i>Figure of Merit</i>	<i>FoM</i>
<i>Energy Autonomous Wireless Vibration Sensor</i>	<i>EAWVS</i>
<i>Micro Electro Mechanical Systems</i>	<i>MEMS</i>
<i>Piezoelectric Energy Harvesters</i>	<i>PEH</i>
<i>Vibrational Energy Harvesters</i>	<i>Vi-EH</i>
<i>Sodium Potassium Niobate</i>	<i>KNN</i>
<i>Lead Zirconate Tantalate</i>	<i>PZT</i>
<i>Lithium Niobate</i>	<i>LN</i>
<i>Radio Frequency</i>	<i>RF</i>
<i>System-on-Chip</i>	<i>SoC</i>
<i>Vi-Energy Harvester</i>	<i>ViEH</i>
<i>Electromagnetic Energy Harvesters</i>	<i>EMEHs</i>
<i>Electrostatic energy harvesters</i>	<i>EEHs</i>
<i>cyclic transparent optical polymer</i>	<i>CYTOP</i>
<i>Piezoelectric Materials</i>	<i>PM</i>
<i>Polyvinylidene fluoride</i>	<i>PVDF</i>
<i>Alternating Current</i>	<i>AC</i>
<i>Single Degree of Freedom</i>	<i>SDOF</i>
<i>Poly(methyl methacrylate)</i>	<i>PMMA</i>
<i>Polydimethylsiloxane</i>	<i>PDMS</i>
<i>Liquid Crystal Display</i>	<i>LCD</i>
<i>Power-Management Circuit</i>	<i>PMC</i>

<i>Full-Bridge Rectifiers</i>	<i>FBR</i>
<i>Standard Energy Transfer</i>	<i>SET</i>
<i>Complementary Metal Oxide Semiconductor</i>	<i>CMOS</i>
<i>Metal Oxide Semiconductor Field Effect Transistor</i>	<i>MOSFET</i>
<i>Piezoresponse</i>	<i>PR</i>
<i>Scanning Probe Microcopy</i>	<i>SPM</i>
<i>Piezoresponse Force Microcopy</i>	<i>PFM</i>
<i>Lateral Piezoresponse Force Microcopy</i>	<i>LPFM</i>
<i>Vertical Piezoresponse Force Microcopy</i>	<i>VPFM</i>
<i>Lock-in Amplifier</i>	<i>LIA</i>
<i>Position Sensitive Photodetector</i>	<i>PSD</i>
<i>inverse optical lever sensitivity</i>	<i>inv-OLS</i>
<i>Periodically Poled Lithium Niobate</i>	<i>PPLN</i>
<i>Lithium tantalate</i>	<i>LT</i>
<i>Piezoelectric Thin Films</i>	<i>PTFs</i>
<i>High Temperature</i>	<i>HT</i>
<i>Sodium Potassium Niobate Tantalate</i>	<i>KNNT</i>
<i>Printed Circuit Board</i>	<i>PCB</i>
<i>Finite Element Method</i>	<i>FEM</i>
<i>Root Mean Square</i>	<i>RMS</i>
<i>Synchronized Switch Harvesting on Inductor</i>	<i>SSHI</i>
<i>Double synchronized switch harvesting</i>	<i>DSSH</i>
<i>Fractional Open-Circuit</i>	<i>FOC</i>
<i>Silicon on Insulator</i>	<i>SOI</i>
<i>Integrated Circuit</i>	<i>IC</i>
<i>Power Management IC</i>	<i>PMIC</i>
<i>Application-Specific Integrated Circuit</i>	<i>ASIC</i>
<i>Base Station</i>	<i>BS</i>
<i>Limit of Detection</i>	<i>LOD</i>
<i>Programmable Voltage Detector</i>	<i>PVD</i>
<i>General-Purpose Input/Output</i>	<i>GPIO</i>

APPENDIX 2

AFM tip and cantilever qualifications: Model SCM PIT V2 from Bruker*

*Source: Bruker website

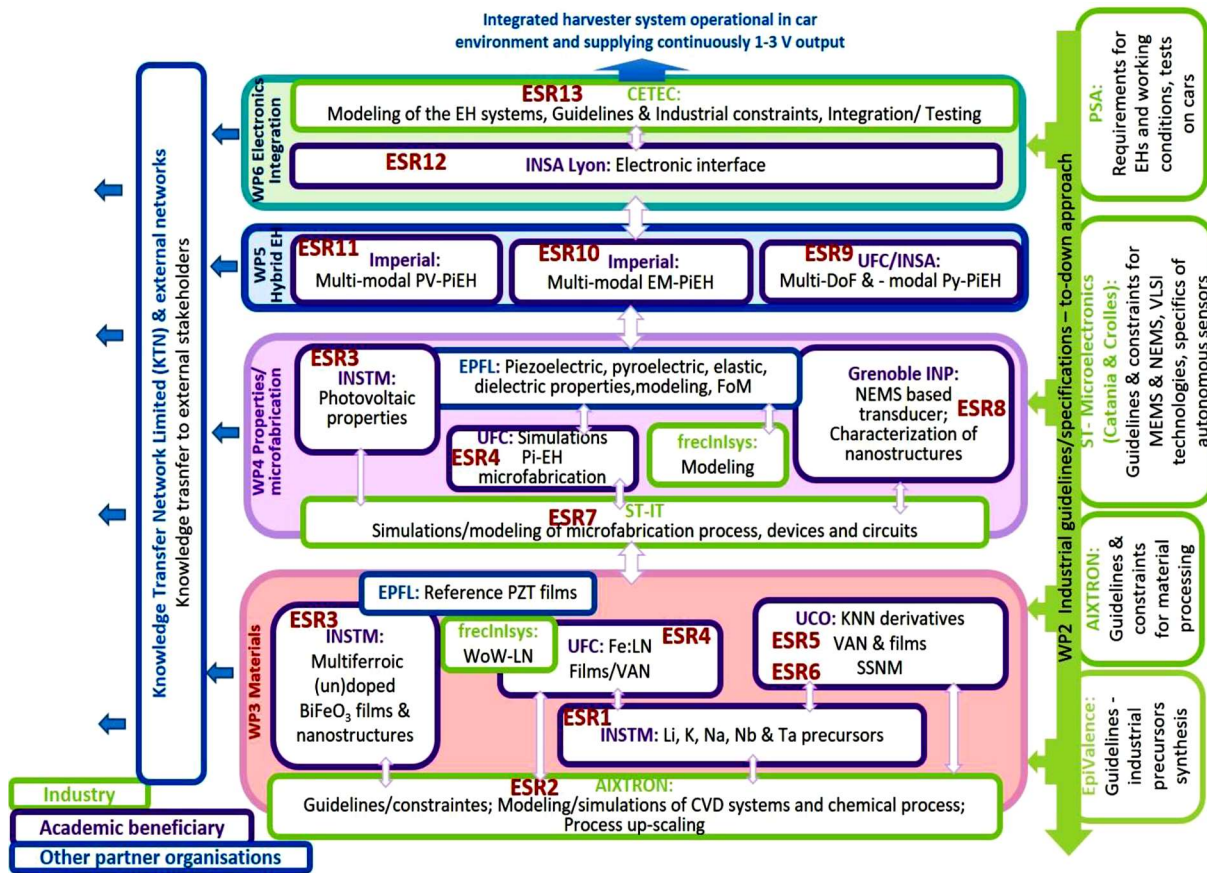


CL Shape	Resonant Freq. (kHz)			Spring Const. K (N/m)			Length (μm)			Width (μm)		
	Nom	Min	Max	Nom	Min.	Max.	Nom.	Min.	Max.	Nom.	Min.	Max
Rectangular	75	50	100	3.0	1.5	6.0	225	215	235	35	33	37

Tip Geometry	Tip Height (h) (μm)	Tip Radius (nm):	Tip Coating	Material Properties	Electrical Sp. (Ωcm)	CL Thickness (μm)
Rotated	10 - 15	25	Pt/Ir	N doped-Si Antimony (n) doped Si	0.01 - 0.025	2.80 ± 0.75

:

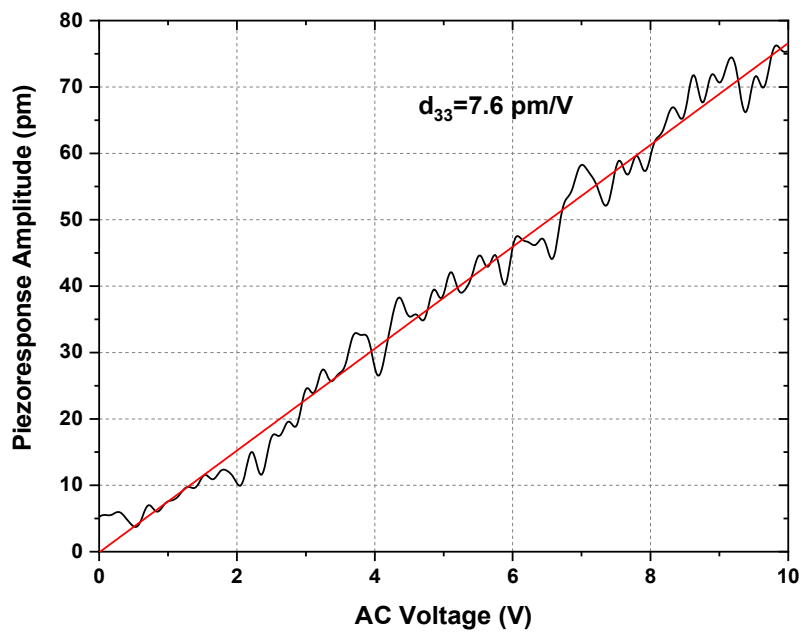
APPENDIX 3



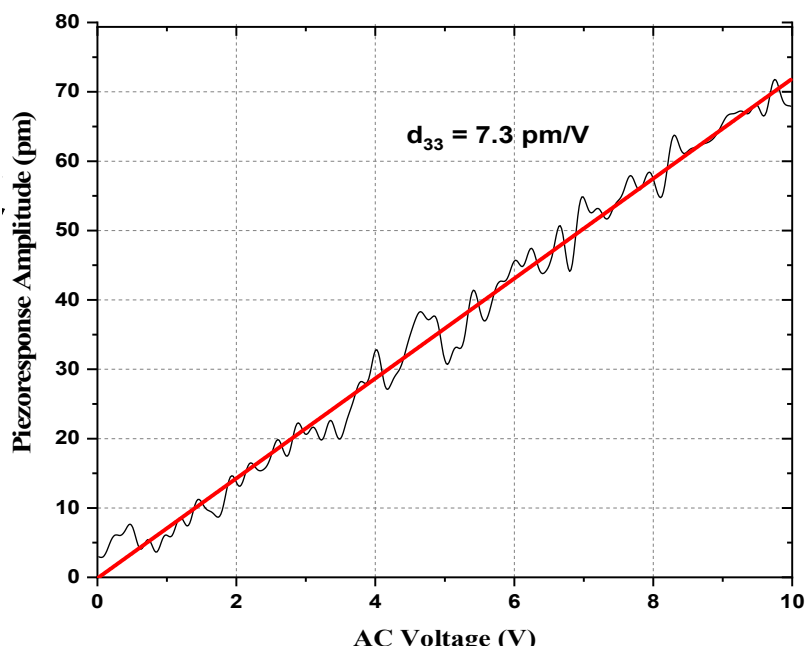
Research interactions between consortium members and partner organizations of ENHANCE

The main aim of the ENHANCE project is to spur a multidisciplinary joint research activity involving chemistry, materials science, physics, mechanics, engineering and electronics to fabricate harvesters with high-power density and their systems offering stabilized output voltage in 1-3 V range, and adapted to specific needs of sensors, with high autonomy and working in elevated temperature ranges from room temperature to 600 °C in vehicles. In a nutshell, the project aims to develop methods of scavenging of energies available in the ambient atmosphere such as heat (pyroelectric), light (photovoltaic), vibrations and/or to use a combination of hybrid sources (piezoelectric-pyroelectric-electromagnetic- photovoltaic) with sufficient power at a reasonable price for real industrial applications such as automotive industry.

APPENDIX 4



d_{33} of PPLN reference sample at 15 kHz



d_{33} of PPLN reference samples at 50 kHz

APPENDIX 5

List of Publications:

1. N. Panayanthatta, L. Montes, E. Bano, C. Trigona and R. L. Rosa, "*Three terminal piezoelectric energy harvester based on novel MPPT design*," 2019 19th International Conference on Micro and Nanotechnology for Power Generation and Energy Conversion Applications (PowerMEMS), Krakow, Poland, 2019, IEEE, pp. 1-7, doi: 10.1109/PowerMEMS49317.2019.92321107155.
2. A. Verma A., N. Panayanthatta, N., A. Ichangi, T. Fischer, L. Montes, E. Bano, & S. MathurS. *Interdependence of Piezoelectric Coefficient and Film Thickness in LiTaO₃ Cantilevers*. Journal of the American Ceramic Society, 104(5), 1966-1977, 2021. doi.org/10.1111/jace.17606.
3. N. Panayanthatta, G. Clementi, M. Ouhabaz, M. Costanza, S. Margueron, A. Bartasyte, S. Basrour, E. Bano, L. Montes, C. Dehollain and R. La Rosa, *A Self-Powered and Battery-Free Vibrational Energy to Time Converter for Wireless Vibration Monitoring*, Sensors, 21 (22), 2021.
4. N. Panayanthatta, G. Clementi, M. Ouhabaz, A. Bartasyte, M. Lallart, S. Basrour, R. La Rosa E. Bano, L. Montes, *Lead free Piezoelectric Microgenerator with high K and broadband frequency for low frequency vibrations*, under preparation.
5. A. Verma A., N. Panayanthatta, N., A. Ichangi., T. Fischer, L. Montes, E. Bano, & S. Mathur. *Isomorphous substitution in (K,Na)NbO₃ for superior piezoelectric performance and energy harvesting*, under preparation.

List of Conferences and Symposiums:

1. N. Panayanthatta, R La Rosa, S. Basrour, E. Bano, L. Montes, *A Battery free wireless sensor node design for vibration monitoring*, International conference on advances in energy harvesting technology ICAEHT 2021, India, March 2021.
2. N. Panayanthatta, X. Mescot, E. Bano, L. Montes, *Nanocharacterization of spin coated piezomaterials for energy harvesting devices*, Symposium and workshop on Knowledge transfer, patenting & commercialization, Knowledge Transfer Network UK, July 2020.

3. N. Panayanthatta, R. La Rosa, C. Trigona, E. Bano, L. Montes, *Optimization of the geometry of MEMS Piezoelectric Energy Harvester cantilevers*, COMSOL conference Europe, 2020.
- N. Panayanthatta, L. Montès, E. Bano, C. Trigona and R. L. Rosa, "*Three terminal piezoelectric energy harvester based on novel MPPT design*," PowerMEMS conference 2019, Krakow.
4. N. Panayanthatta, E. Bano, L. Montes, *study of spin coated KNN thin films*, IWPMA 2019, Lyon.
5. N. Panayanthatta, E. Bano, L. Montes, *AFM characterization of Ferroelectric materials*, International Symposium "From Molecular Engineering to Advanced Materials" at University of Cologne, Germany from May, 2019.
6. N. Panayanthatta, E. Bano, L. Montes, *Study of Piezoelectric Nanogenerators*, Journées de la Matière Condensée, Grenoble, France, August 27-31, 2018.
7. N. Panayanthatta, E. Bano, L. Montes, *Piezoelectric Nanogenerators*, RJP - Rencontres Jeunes Physicien, Grenoble, France, July 2018

List of Trainings

1. Training on "***Mechatronics and Electronics for EHs***"_ CEDRAT Technologies-Grenoble, September 2020.
2. **European School on Nanoscience and Nanotechnology (ESONN) school** 2020, August 23 - September 12, Grenoble, France.
3. Training and workshop on ***Knowledge transfer, patenting & commercialization***, Knowledge Transfer Network UK, July 2020.
4. ***POWERMEMS school on ambient energy harvesting***, December 2-6, 2019 in Krakow, Poland.
5. Workshop and Symposium "***From Molecular Engineering to Advanced Materials***" at University of Cologne, Germany from May 19 -26, 2019
6. Training School in "***Career Opportunities***", hosted by EPFL - EPFL, Lausanne, Switzerland, September 5-6, 2018,
7. Training in ***advanced microelectronic characterization*** by AFM modes in Bruker AFM ICON by Bruker (Tapping mode, contact mode, TUNA, PFM), April 2019

8. Training on *clean room* facilities and fabrication of MEMS pressure sensor on Silicon, August 2018.
9. Training on *piezoelectric Energy harvesting* - 2018, UFC Besancon, France, May 16th to 18th.

Other Contributions:

1. Prepared report on optimized design of piezoelectric transducers, submitted to EU commission as part of ITN-ENHANCE Project, November 2018.
2. Created Open access database of piezoelectric materials, accessible at:
https://en.wikipedia.org/wiki/List_of_piezoelectric_materials

